UNIVERSITÉ DE LORRAINE | BIBLIOTHÈQUES UNIVERSITAIRES

AVERTISSEMENT
DROIT D'AUTEUR

Ce document est le fruit d'un long travail approuvé par le jury de soutenance et mis à disposition de l'ensemble de la communauté universitaire élargie.

Il est soumis à la propriété intellectuelle de l'auteur. Ceci implique une obligation de citation et de référencement lors de l'utilisation de ce document. Toute contrefaçon, plagiat ou reproduction illicite encourt une poursuite pénale.

Contact bibliothèque : ddoc-theses-contact@univ-lorraine.fr
(Cette adresse ne permet pas de contacter les auteurs)

Code de la Propriété Intellectuelle. articles L 122. 4
Code de la Propriété Intellectuelle. articles L 335.2- L 335.10

UNIVERSITÉ DE LORRAINE
34 COURS LÉOPOLD — CS 25233
54052 NANCY CEDEX
TÉL : 03 54 50 54 00
CONTACT@UNIV-LORRAINE.FR
WWW.UNIV-LORRAINE.FR

Thèse de Doctorat

UNIVERSITE DE LORRAINE

Nonlinear Dynamic Buckling of Thin-Shell Structures: Seven-Parameter Shell Elements with Mortar Coupling, Elasto-Plasticity, Implicit and Explicit Solvers

par

Anh-Khoa CHAU

Ecole Doctorale C2MP

Spécialité :

MÉCANIQUE DES MATÉRIAUX

Soutenue le 28 janvier 2026

Membres du jury :

Directeurs de thèse :	M. Michaël BRUN	Professeur, LEM3, Université de Lorraine, Metz
	M. Pascal Ventura	Ingénieur de recherche, LEM3, Metz
Co-encadrant :	M. Florent DE MARTIN	Ingénieur de recherche, BRGM, Orléans
Président :	M. Jean-Louis BATOZ	Professeur, Laboratoire Roberval, UTC, Compiègne
Rapporteurs :	Mme. Delphine BRANCHERIE	Professeur, Laboratoire Roberval, UTC, Compiègne
	M. Robin BOUCLIER	Professeur, INSA Toulouse / ICA&IMT, Toulouse
Examinateurs :	M. Benjamin RICHARD	Chef du Bureau B2EM/SES/PSN-EXP, ASNR, Paris
	M. Nahiene HAMILA	Professeur, IRDL, Bretagne INP, Bretagne
Invité :	M. Hamid ZAHROUNI	Professeur, LEM3, Université de Lorraine, Metz

Laboratoire LEM3 UMR CNRS 7239
7 rue Félix Savart, 57000 METZ, FRANCE

Remerciements

Je tiens tout d'abord à exprimer ma profonde gratitude à mon directeur de thèse, Michaël Brun, pour son encadrement, sa disponibilité et son enthousiasme. Sa confiance, son expérience et sa rigueur scientifique m'ont accompagné dans la maturation des idées et leur valorisation tout au long de cette thèse.

Je remercie Pascal Ventura, co-directeur de thèse, ainsi que Hamid Zahrouni et Michel Potier-Ferry, pour leur accompagnement scientifique, leurs échanges stimulants et leurs retours précieux, qui ont contribué aux publications issues de ce travail. Je remercie également Florent De Martin pour son accueil au BRGM et pour m'avoir fait découvrir son code `EFISPEC3D`.

Je remercie chaleureusement les membres de mon jury : Delphine Brancherie et Robin Bouclier, rapporteurs, pour la lecture attentive du manuscrit et la qualité de leurs commentaires ; Jean-Louis Batoz, président, ainsi que Nahiene Hamila et Benjamin Richard, examinateurs, pour leurs remarques constructives et leurs mots bienveillants lors de la soutenance. J'ai été très honoré de présenter mes travaux devant vous.

Je remercie ensuite l'ensemble de mes collègues et amis du LEM3 pour l'excellente ambiance au laboratoire. Merci à Laura Litscher, Aurore Hanson, Souksavanh Carballo et à l'équipe de secrétariat pour leur soutien administratif, toujours précieux. Merci aussi à Paul, Joé, Mickaël, Flora, Mélaine, Julien, Momo, et à tous les autres, pour l'aide au quotidien et les bons moments partagés.

Je remercie enfin mes amis proches pour leur soutien constant, notamment Cyril et Anne, Quang Thong et Minh Ngoc, Van Anh et Damien, ainsi que Minh Nhat. Merci également aux amis du groupe sportif RER B et à mes amis vietnamiens à Metz, pour leur énergie et leur présence, même à distance.

Enfin, je remercie ma femme, Hanh Pham, pour être toujours à mes côtés, pour sa confiance et pour m'encourager à poursuivre ma passion. Merci d'avoir partagé ce chemin avec moi, d'avoir grandi ensemble, et pour le bonheur de notre famille, notamment avec l'arrivée de Lucas.

Résumé étendu

Cette thèse développe un cadre numérique (éléments finis et éléments spectraux) dédié à l'analyse du flambage dynamique non linéaire de structures minces, en présence de non-linéarités géométriques (grandes déformations) et matériau (élasto-plasticité multiplicative), ainsi qu'à la simulation de la propagation d'ondes en domaines non bornés. Le fil conducteur est de proposer une chaîne de modélisation et de résolution cohérente et robuste : une formulation de coque "continuum-based" permettant l'usage direct de lois constitutives tridimensionnelles, la stratégie de mortar pour le couplage coque–coque et coque–solide adaptées aux maillages non conformes, et des solveurs implicites et explicites capables de traiter des régimes transitoires sévères (snap-through, post-flambement avec changement de branches, chargements impulsionnels).

Formulation de coque à 7 paramètres. Pour modéliser les structures minces, on retient une formulation de coque en déplacement dite à 7 paramètres, issue de l'approche du solide dégénéré. Elle étend une cinématique de type Reissner–Mindlin en introduisant l'extensibilité d'épaisseur, de manière à s'inscrire naturellement dans un cadre de grandes déformations. La formulation est construite pour autoriser l'utilisation directe de lois constitutives 3D, sans condensation, ce qui constitue un avantage décisif dès lors que l'on vise des matériaux non linéaires ou des états de contrainte complexes.

Dans le système d'équations global, seules six inconnues nodales interviennent : (i) le déplacement de la surface moyenne (trois composantes) et (ii) la variation des vecteurs directeurs de la coque (trois composantes). Le septième paramètre intervient sous la forme d'un champ de déformation incompatible introduit par la méthode EAS ("Enhanced Assumed Strain"). Cet enrichissement vise spécifiquement la déformation normale transverse afin de réduire le verouillage de Poisson en épaisseur ("Poisson thickness locking"). Le champ EAS est contrôlé au niveau élémentaire par une condition d'orthogonalité, permettant de conserver une taille globale minimale (pas d'inconnue EAS globale) tout en apportant la souplesse nécessaire pour atténuer le verrouillage.

Au-delà du verrouillage d'épaisseur, les verrouillages membrane et cisaillement sont traités par des choix de discrétisation cohérents avec la littérature : utilisation d'éléments

quadratiques (ou d'ordre supérieur) et intégration réduite. Dans les applications de la thèse, la discrétisation repose principalement sur des quadrilatères à 8 nœuds, intégrés avec une quadrature 2×2 sur la surface moyenne, ce compromis s'avérant efficace pour la dynamique et suffisamment robuste pour les instabilités.

Elasto-plasticité en grandes déformations. La thèse étend le cadre à une plasticité isotrope en grandes déformations basée sur la décomposition multiplicative du gradient de transformation. Un point méthodologique important est l'intégration de cette loi matériau dans la coque à 7 paramètres : (i) la formulation de coque, initialement construite en configuration de référence, est exprimée en configuration courante, afin de faciliter l'incorporation des relations constitutives non linéaires ; (ii) une stratégie est proposée pour prendre en compte le champ EAS dans ce cadre de matériau non linéaire et le rendre compatible avec la formulation variationnelle de coque. Dans les cas élasto-plastiques, un soin particulier est apporté à la vérification du champ de la déformation plastique afin d'éviter des phénomènes de verrouillage volumique.

Afin d'évaluer la performance de la coque et d'investiguer la crédibilité des résultats, un élément solide hexaédrique est développé en parallèle et sert de référence numérique. Cette approche coque/solide offre une lecture claire des approximations induites par la réduction coque, tout en permettant de partager une bibliothèque commune de lois matériaux.

Méthode de mortar. De nombreuses structures minces réalistes combinent plusieurs sous-domaines (structures raidies) et conduisent naturellement à des interfaces où les maillages ne sont pas conformes. Pour traiter ces situations, la thèse met en œuvre la méthode de mortar afin d'imposer des contraintes de continuité/collage à l'interface, au moyen de multiplicateurs de Lagrange.

Sur cette base, une formulation EF globale en déplacements est dérivée, intégrant les contraintes cinématiques linéaires (conditions de Dirichlet et collages mortar) par des multiplicateurs de Lagrange. Cette construction permet de faire coexister, dans un même modèle global monolithique, des éléments de coque et des éléments solides, et de les coupler de manière cohérente au niveau variationnel.

Solveurs implicites. En dynamique non linéaire, la thèse développe deux solveurs implicites. Le premier est le solveur Newton–Raphson (NR), qui couvre les non-linéarités géométriques et matériau. Le second explore la Méthode Asymptotique Numérique (ANM) comme alternative, en particulier dans des problèmes géométriquement non linéaires incluant des chargements de pression non conservatifs.

La stratégie d'intégration en temps côté implicite s'appuie sur des schémas de type α (Generalized–α et les variantes), dont l'intérêt est d'introduire une dissipation numérique

contrôlée ciblant principalement les hautes fréquences. Cet aspect est crucial pour les coques minces, qui peuvent exciter des modes haute fréquence susceptibles d'accumuler une énergie non physique et de déstabiliser la simulation si elles ne sont pas correctement amorties. Un pas de temps adaptatif est également utilisé afin d'optimiser la charge de calcul : l'idée est de conserver de grands pas lorsque la réponse est relativement régulière, et de raffiner l'intégration lorsqu'un événement fortement non linéaire survient (snap-through, transition post-flambement).

L'ANM est formulée dans un cadre dynamique à partir d'une construction homotopique et d'un développement en série : à chaque pas de temps, les équations gouvernantes sont transformées en une suite de problèmes linéaires partageant le même opérateur tangent, de sorte qu'une seule factorisation est nécessaire par pas. La thèse propose un pas de temps adaptatif en ordre (lié aux critères de convergence de la série) permettant d'adopter un compromis optimal entre précision et coût. L'un des objectifs méthodologiques est de mener une comparaison entre NR et ANM en dynamique du flambage : NR peut bénéficier de grands pas mais au prix de reconstructions/factorisations tangentes répétées, tandis que l'ANM réduit ces opérations mais requiert davantage d'évaluations de forces, ce qui rend l'équilibre coût/précision dépendant du contexte logiciel et de la taille des problèmes visés.

Solveurs explicites. En complément des solveurs implicites, la thèse développe deux solveurs explicites basés sur le schéma classique de Différence Centrée, particulièrement attractifs pour des dynamiques rapides et des non-linéarités sévères. Le premier solveur explicite est un schéma monolithique standard. Le second introduit une stratégie multi-pas de temps fondée sur l'approche GC, développée dans un cadre de décomposition de domaine (famille HATI), permettant d'utiliser des pas différents selon les sous-domaines. Cette approche vise les problèmes à échelles de temps multiples (maillages hétérogènes, zones localement raffinées, vitesses d'ondes différentes), où un pas global unique serait inutilement pénalisant.

L'emploi d'éléments de coque à 7 paramètres en explicite soulève deux verrous. Le premier est le pas de temps critique, fortement contrôlé par l'épaisseur et par la présence de modes haute fréquence qui n'influencent pas nécessairement la réponse d'intérêt. Pour atténuer cette restriction, une stratégie de "Selective Mass Scaling" (SMS) est adaptée à la coque à 7 paramètres grâce à un paramètre contrôlable, de manière à réduire les fréquences critiques tout en préservant au mieux l'exactitude sur les modes bas fréquence et les propriétés de conservation du schéma. Le second verrou est le traitement du champ EAS. Une condensation statique exacte peut imposer une résolution de type Newton au niveau élémentaire pour mettre à jour le champ EAS, ce qui annule l'avantage de

l'explicite. La thèse étudie donc des stratégies de condensation simplifiée issues de la littérature et propose un traitement explicite de la condition d'orthogonalité, conçu pour préserver l'efficacité computationnelle des schémas explicites tout en maintenant l'effet anti-verrouillage de l'EAS.

Pour sécuriser l'usage de ces approximations en explicite, des contrôles a posteriori sont proposés : suivi énergétique (pour détecter une accumulation non physique d'énergie) et suivi de l'erreur associée à la condition d'orthogonalité (pour évaluer la qualité du traitement EAS). Ces outils fournissent une vérification opérationnelle de la qualité de la solution dans des régimes fortement transitoires.

Validation numérique. La validation du cadre méthodologique s'appuie sur plusieurs familles de tests. Une première famille porte sur les propriétés de conservation (quantité de mouvement, énergie) en présence de maillages non conformes, afin d'évaluer la pertinence du couplage mortar en dynamique et la stabilité du cadre monolithique à multiplicateurs de Lagrange. Une deuxième famille cible des instabilités dynamiques de type snap-through et des situations de post-flambement avec changement de branches, incluant des forces suiveuses, afin d'exercer les solveurs implicites (NR/ANM) dans des scénarios où la réponse est particulièrement sensible et non linéaire. Une troisième famille de tests vise la dynamique élasto-plastique en grandes déformations sous chargements impulsionnels, afin de valider l'incorporation de la loi élasto-plastique en grandes déformations dans l'élément de coque et d'évaluer les performances des solveurs (NR implicite et schémas explicites mono-domaine et multi-pas).

Les investigations montrent que la coque à 7 paramètres reproduit fidèlement les solutions de référence (notamment celles obtenues par l'élément solide développé en parallèle), et que les stratégies de résolution proposées sont globalement robustes. Les solveurs implicites NR et ANM se révèlent précis ; l'ANM présente l'intérêt de réduire le nombre de constructions et factorisations de tangentes, même si son coût global peut dépendre du nombre d'évaluations de forces et donc de l'environnement d'implémentation. Les solveurs explicites, incluant le schéma multi-pas de temps et le traitement explicite de l'orthogonalité, apparaissent précis, robustes et stables sur les cas test considérés ; la stratégie SMS et les contrôles a posteriori jouent un rôle important pour concilier efficacité et fiabilité.

PML en éléments spectraux pour domaines non bornés. En parallèle du cœur « flambage dynamique des coques », une étude complémentaire porte sur les couches parfaitement appariées (PML) pour la propagation d'ondes en domaines non bornés, dans un cadre d'éléments spectraux. Une PML non décomposée ("unsplit"), non convolutionnelle et formulée en déplacement est développée puis implémentée dans EFISPEC3D (code

open-source massivement parallèle dédié à la sismologie). Les validations numériques incluent le problème de Lamb, des configurations de guide d'ondes et un milieu stratifié à deux couches. Les résultats mettent en évidence une excellente stabilité à long terme et une bonne précision, y compris dans des situations difficiles d'incidence rasante. Bien que cette contribution soit en dehors du périmètre initial principal, elle constitue un premier jalon vers des problèmes d'interaction sol–structure, où des structures minces peuvent être excitées par des ondes transitoires et développer des instabilités dynamiques.

Bilan. L'ensemble des développements aboutit à un cadre général et cohérent, couvrant à la fois des aspects de dynamique linéaire (propagation d'ondes) et de dynamique non linéaire géométrique et matériau pour des structures minces sensibles au flambage. Les choix méthodologiques — coque "continuum-based" à 7 paramètres avec EAS, plasticité multiplicative, couplages mortar, formulation monolithique à multiplicateurs de Lagrange, solveurs implicites α (NR/ANM) et solveurs explicites (différence centrée, multi-pas GC/HATI, SMS, traitement EAS dédié) — forment une base immédiatement mobilisable pour des cas académiques et des applications d'ingénierie de taille moyenne, et ouvrent naturellement vers des extensions telles que le contact, le calcul explicite haute performance, et les problématiques d'interaction structure–milieu en domaine non borné.

Résumé

Dans ce travail de thèse, est développé un code aux éléments finis et aux éléments spectraux pour le flambage dynamique non linéaire géométrique et matériau de structures minces, ainsi que pour la propagation d'ondes. Pour les structures minces, nous adoptons une formulation de coque à 7 paramètres, en déplacement, qui comporte six inconnues cinématiques (déplacement de la surface moyenne et variation des vecteurs directeurs de la coque) et un champ de déformation additionnelle incompatible ("Enhanced Assumed Strain"), piloté au niveau élémentaire par une condition d'orthogonalité afin de limiter les problèmes de verrouillage. Cette formulation de coque permet l'utilisation de lois constitutives tridimensionnelles, sans condensation, dans le cadre des grandes déformations.

Pour les matériaux élasto-plastiques en grandes déformations, nous adoptons le cadre de la décomposition multiplicative du tenseur gradient de la transformation. Les couplages entre éléments finis coque–coque et coque–solide sont traités selon la méthode de mortar. Comme solution de référence, un élément fini solide hexaédrique est développé en parallèle à l'élément coque. Une formulation générale monolithique est proposée de sorte que le code de simulation développé permette la coexistence d'éléments coques et solides ainsi que leur couplage via l'utilisation de multiplicateurs de Lagrange pour l'ensemble des contraintes cinématiques du problème (conditions de Dirichlet et collages).

Nous développons ensuite les solveurs, basés sur des schémas d'intégration temporelle implicite et explicite. Côté implicite, les méthodes α, introduisant une dissipation numérique contrôlée, considèrent un pas de temps adaptatif afin d'optimiser l'intégration temporelle. Deux stratégies implicites de résolution sont mises en œuvre : la méthode classique de Newton–Raphson et la Méthode Asymptotique Numérique ("Asymptotic Numerical Method"). Côté explicite, outre le schéma classique de la Différence Centrée, nous proposons un solveur explicite multi-pas de temps basé sur la méthode GC, permettant le couplage en temps entre sous-domaines. Pour l'élément de coque à 7 paramètres, un traitement original de la condition d'orthogonalité est proposé, permettant de préserver l'efficacité des solveurs explicites.

Le code est validé sur des cas tests exigeants : tests de conservation des quantités de mouvement et d'énergie pour des modèles avec des maillages non-conformes, flambage dynamique (snap-through) et changement de branches en post-flambement, présence de forces suiveuses, ainsi que des tests sous chargements impulsionnels et grandes déformations pour des structures minces élasto-plastiques. Les résultats montrent que l'élément coque à 7 paramètres reproduit fidèlement les solutions de référence. Les solveurs NR et ANM sont à la fois précis et robustes ; l'ANM a l'avantage de réduire le nombre de constructions et factorisations de matrices tangentes. Les solveurs explicites, incluant l'algorithme explicite dédié à l'élément coque à 7 paramètres, s'avèrent performants, précis, robustes et stables.

Dans le cadre des éléments spectraux et des problèmes de propagation d'ondes dans des milieux tridimensionnels, la technique des PML ("Perfectly Matched Layers") pour des domaines non bornés est également explorée. Une PML non décomposée, non convolutionnelle, formulée en déplacement, est dévelopée et est implémentée dans `EFISPEC3D`, un code libre et massivement parallèle dédié à la propagation d'ondes pour des problèmes de sismologie. L'étude numérique — comprenant le test de Lamb pour un milieu élastique homogène, des problèmes de guide d'onde et un milieu stratifié à deux couches — met en évidence l'excellent comportement de la PML, en termes de stabilité à long terme et de précision pour des problèmes avec des ondes en incidence rasante.

Ce travail de thèse propose un cadre général et cohérent, couvrant de nombreux aspects de la dynamique linéaire (propagation d'ondes) et non linéaire géométrique et matériau pour les structures minces sensibles aux phénomènes de flambage. Le cadre théorique et le code qui en sont issus sont immédiatement mobilisables pour des études académiques et des applications d'ingénierie de taille moyenne, constituant une base solide pour des extensions vers la mécanique du contact, des calculs explicites hautes performances, et des problèmes de film-substrat ou d'interaction sol–structure dans des milieux non-bornés.

Abstract

This thesis develops a finite-element and spectral-element code for the nonlinear dynamic buckling of thin-shell structures with geometric and material nonlinearities, as well as for wave-propagation problems. For thin shells, we adopt a displacement-based 7-parameter formulation with six kinematic unknowns (mid-surface displacement and the variation of shell directors) and an additional incompatible strain field (Enhanced Assumed Strain, EAS) enforced at the element level by an orthogonality condition to mitigate locking. This shell formulation enables the direct use of three-dimensional constitutive laws, without condensation, in a finite-strain setting.

To extend our investigation to material nonlinearity, we adapt an isotropic multiplicative elasto-plastic framework in the shell formulation. Shell–shell and shell–solid couplings are handled with the mortar method. As a reference, the solid finite element is developed in parallel to the shell element. A displacement-based finite element formulation that enables shell and solid elements to coexist in a monolithic global model is derived.

We then develop the solvers, based on implicit and explicit time-integration schemes. On the implicit side, α-methods with controlled numerical dissipation are combined with adaptive time stepping to optimize the time integration. Two implicit strategies are implemented: the classical Newton–Raphson method and the Asymptotic Numerical Method (ANM). On the explicit side, in addition to the classical Central-Difference scheme, we propose a multi-time-step explicit solver based on the GC method, enabling time coupling between subdomains. For the 7-parameter shell element, we introduce an original treatment of the orthogonality condition that preserves the efficiency of the explicit solvers.

The code is validated against demanding benchmarks: momentum- and energy-conservation tests for nonconforming meshes, dynamic buckling (snap-through) and branch switching in post-buckling with the presence of follower loads, and dynamic elasto-plastic response of thin structures under impulsive loading and severe deformation. The results show that the 7-parameter shell element reproduces the reference solutions with high fidelity. Both NR and ANM solvers are accurate and robust; ANM has the

advantage of reducing the number of tangent-matrix constructions and factorizations. The explicit solvers, including the proposed algorithm dedicated to the 7-parameter shell, are accurate, robust, and stable.

Within the spectral-element framework and three-dimensional wave-propagation problems, the Perfectly Matched Layer (PML) technique for unbounded domains is also explored. An unsplit, non-convolutional, displacement-based PML is developed and implemented in `EFISPEC3D`, a massively parallel and open-source code for wave propagation in seismology. The numerical study, including Lamb's problem for a homogeneous elastic medium, waveguide problems, and a two-layer stratified medium, demonstrates the excellent behavior of the PML in terms of long-term stability and accuracy for grazing-incidence waves.

Overall, this thesis proposes a general, coherent framework that covers many aspects of linear dynamics (wave propagation) and of geometric and material nonlinear dynamics for thin-shell, buckling-sensitive structures. The resulting theory and code are immediately applicable to academic studies and medium-scale engineering applications, and provide a solid basis for extensions to contact mechanics, high-performance computations, and film–substrate or soil–structure interaction problems in unbounded media.

Contents

List of Figures xvii

List of Tables xxiii

1 Introduction 1
- 1.1 Motivation . . . 1
- 1.2 State of the art . . . 2
  - 1.2.1 Finite element modeling of shell structures . . . 2
  - 1.2.2 Nonlinear dynamic analysis of shell structures . . . 5
- 1.3 Objectives of the thesis . . . 10
- 1.4 Publications related to the thesis work . . . 13
- 1.5 Outline of the thesis . . . 13

2 Finite Deformation Solid Mechanics 15
- 2.1 Kinematics and Deformation . . . 16
- 2.2 Stress Measures and Constitutive Relation . . . 18
- 2.3 Strong Form of Governing Equations . . . 20
- 2.4 Reference Configuration Formulation . . . 21
  - 2.4.1 Variational description. . . . 21
  - 2.4.2 Tangent stiffness . . . 24
- 2.5 Current Configuration Formulation . . . 25
- 2.6 Displacement-based Finite Element Formulation . . . 27

3 7-parameter Shell Formulation 33
- 3.1 Shell's Geometry and Kinematics . . . 33
- 3.2 Poisson Thickness Locking . . . 37
- 3.3 Enhanced Variational and Finite Element Formulations . . . 39
  - 3.3.1 Reference configuration formulation . . . 39
  - 3.3.2 Current configuration formulation . . . 44

3.4 Explicit Through-thickness Integration . . . 45
3.5 Non-Conservative Loads - Pressure Loads . . . 47
3.6 Isotropic Elasto-plasticity at Finite Strains . . . 48
3.6.1 Constitutive governing equations . . . 49
3.6.2 Elastic trial and return-mapping algorithm . . . 52
3.6.3 Exact algorithmic tangent moduli . . . 54
3.6.4 Introduction of EAS variable into the trial elastic strain . . . 58
3.7 Coupling Problem between Shell Components . . . 60
3.7.1 Pre-processing strategy for the shell directors at the interface . . . 60
3.7.2 Mortar approach . . . 61

4 Nonlinear Dynamic Analysis of Shell Structures 67
4.1 High-Frequency Modes of 3D-Shell Elements . . . 69
4.1.1 Modal analysis of a thin plate . . . 69
4.1.2 Selective Mass Scaling technique. . . . 72
4.2 Implicit Nonlinear Dynamic Analysis . . . 74
4.2.1 Modified α-methods for nonlinear dynamics . . . 74
4.2.2 Newton-Raphson resolution procedure . . . 76
4.3 Asymptotic Numerical Method for Implicit Geometrically Nonlinear Dynamics . . . 79
4.3.1 ANM development for three-dimensional solid elements . . . 80
4.3.2 ANM development for 7-parameter shell elements . . . 85
4.3.3 ANM solver for geometrically nonlinear dynamics . . . 89
4.3.4 Comparison between ANM and Newton–Raphson method . . . 93
4.4 Explicit Nonlinear Dynamic Analysis . . . 94
4.4.1 Explicit solver using Central Difference scheme . . . 95
4.4.2 Multi-time step explicit solver . . . 97
4.4.3 Treatment of the EAS field in 7-parameter shell elements . . . 103

5 Numerical validation 107
5.1 Intersecting Plates . . . 108
5.2 Snap-through of Cylindrical Roof . . . 112
5.2.1 Implicit computations . . . 114
5.2.2 Explicit computations . . . 118
5.2.3 Computations with standard mortar coupling . . . 120
5.3 Implicit Buckling of Thin Shells . . . 123
5.3.1 Axially loaded cylinder . . . 123

5.3.2 Closed cylinder under pressure load . . . 126
5.3.3 Conclusion . . . 131
5.4 Finite-Strain Elasto-plastic Dynamics . . . 131
5.4.1 Quasi-static pinched hemisphere . . . 133
5.4.2 Plate under uniform pressure . . . 134
5.4.3 Roof loaded by velocity impulse . . . 136
5.4.4 Pinched cylinder . . . 138
5.4.5 Twisted cylinder . . . 140
5.4.6 Stiffened roof . . . 143
5.4.7 Conclusion . . . 146

6 Spectral Element Perfectly Matched Layers for Transient Elastodynamics 149
6.1 Introduction . . . 149
6.2 Time-domain Governing Equations . . . 151
6.2.1 Stretching function . . . 151
6.2.2 Strong form of governing equations . . . 153
6.2.3 Continuous weak form of governing equations . . . 155
6.3 Displacement-based Spectral Element PML . . . 156
6.3.1 Spectral element method . . . 156
6.3.2 Displacement-based weak form . . . 158
6.3.3 Explicit algorithm . . . 162
6.4 Numerical Validation . . . 165
6.4.1 Wave propagation in a homogeneous half-space . . . 166
6.4.2 Homogeneous waveguide . . . 170
6.4.3 Two-layered half-space . . . 175
6.5 Conclusion . . . 178

7 Conclusions and Perspectives 181
7.1 Summary of the thesis work . . . 181
7.2 Perspectives . . . 184

Bibliography 187

Appendix A FINITE ELEMENT DISCRETIZATION FOR PROBLEMS AT FINITE STRAIN 201
A.1 Three-dimensional elements . . . 201
A.1.1 Matrix form . . . 201

A.1.2 Spatial discretization 201
A.1.3 Finite element formulation in the reference configuration 202
A.1.4 Finite element formulation in the current configuration 205
A.2 7-parameter shell formulation 207
A.2.1 Matrix form 207
A.2.2 Spatial discretization 208
A.2.3 Finite element formulation in the reference configuration 209
A.2.4 Finite element formulation in the current configuration 212

Appendix B MECHANICAL ENERGY AND MOMENTUM 217
B.1 Discrete mechanical energy 217
B.2 Linear and angular momentum 218

List of Figures

2.1 Reference (undeformed) and current (deformed) configurations in finite deformation problems 17

3.1 Shell geometry and kinematics 34
3.2 Discontinuity of the nodal shell directors for L-shaped and T-shaped coupling problems 60
3.3 Spatial discretization of the shell directors $\boldsymbol{a}_3$ for two adjacent 8-node shell elements: (a) L-shaped cross-section; (b) T-profile cross-section 61
3.4 Mortar coupling surfaces (in red) for L-shaped and T-shaped cross-section thin-walled beams 62
3.5 Overconstraint in the coupling problem of four bodies. 64

4.1 Model and eigenfrequency spectra of the thin plate using 7-parameter shell and 3D solid elements with consistent (CMM) and lumped (LMM) mass matrices. 70
4.2 Eigenmodes obtained from modal analysis for the 7p-shell model and the consistent mass matrix (CMM). The modes correspond to the red points on the spectrum displayed in Figure 4.1. 70
4.3 Thin plate described in Figure 4.1a: Effect of the parameter β_0 on the eigenvalue spectra and the critical time step 74
4.4 Coupling problem of four subdomains. 97

5.1 Three intersecting plates: problem description. 108
5.2 Snapshots during the motion of the three intersecting plates. 109
5.3 Three intersecting plates — implicit Constant Average Acceleration (CAA) computation with $\Delta t = 5.00\,\mathrm{ms}$: time histories of mechanical energies, linear momentum, and angular momentum. 110

5.4 Three intersecting plates - Implicit computations using α–methods with $\Delta t = 5.00\,\text{ms}$: Energies $[J]$ versus time $[s]$ for different α–methods. Solid line: total energy, dashed: kinetic, dash-dot: internal energy. 111
5.5 Three intersecting plates — multi-time-step explicit computations with $\Delta t_m = m\,\Delta t_j$: mechanical energies [J] vs time [s] for step ratios $m \in \{1, 10, 35\}$. Solid: total; dashed: kinetic; dash–dot: internal. 112
5.6 Three intersecting plates — multi-time-step explicit computations with $\Delta t_m = 35\,\Delta t_j = 70.0\,\mu\text{s}$: time histories of mechanical energies, linear momentum, and angular momentum. 113
5.7 Cylindrical roof: Problem description (both sides of the roof are pinned). 113
5.8 Cylindrical roof: Displacement U on the deformed configuration at different times: (a) $t = 0.01s$, (b) $t = 0.07s$, (c) $t = 0.14s$, (d) $t = 0.16s$, (e) $t = 0.20s$, (f) $t = 0.25s$. 114
5.9 Cylindrical roof — CAA computations with $\Delta t = 0.50\,\text{ms}$: time history of the loaded-point displacement and the number of NR iterations / ANM order per step. 115
5.10 Cylindrical roof — computations with $\Delta t = 0.50\,\text{ms}$: time history of the kinetic energy (CAA versus HAM). 115
5.11 Cylindrical roof — Hilber–α method (HAM, $\rho_\infty = 0.8$) with $\Delta t = 0.50\,\text{ms}$: time history of the loaded-point displacement and the number of NR iterations / ANM order per step. 116
5.12 Cylindrical roof - Hilber–α method computations with adaptive Δt: Time history of the displacement of the loaded point, and number of NR iterations / ANM order required for each time step. 116
5.13 Cylindrical roof - Hilber–α method computations with adaptive Δt: Time history of the time step size and the kinetic energy. 117
5.14 Cylindrical roof — explicit computations (with/without Rayleigh damping): time history of the loaded-point displacement and mechanical energy error ϵ_W. 118
5.15 Cylindrical roof — explicit computations (with/without Rayleigh damping): time histories of internal and kinetic energies. 119
5.16 Cylindrical roof — explicit computations with $\Delta t = 30\,\mu\text{s}$ and with no Rayleigh damping: time histories of internal and kinetic energies. Comparison between static condensation and the proposed EAS treatment. 119
5.17 Cylindrical roof — subdomain partition and discretizations 120

5.18 Cylindrical roof (asymmetric loading): snapshots of the displacement field U on the deformed configuration at selected times: (a) $t = 0.11\,\mathrm{s}$, (b) $t = 0.12\,\mathrm{s}$, (c) $t = 0.13\,\mathrm{s}$, (d) $t = 0.17\,\mathrm{s}$, (e) $t = 0.18\,\mathrm{s}$, (f) $t = 0.26\,\mathrm{s}$. 121
5.19 Cylindrical roof — implicit computations with domain decomposition: time histories of the loaded-point displacement and the adaptive time step size. 121
5.20 Cylindrical roof — explicit computations with $\Delta t_m = 25.0\,\mu\mathrm{s}$, $\Delta t_j = 2.5\,\mu\mathrm{s}$ $(m = 10)$ and Rayleigh damping $\mathbf{C} = 5.0\,\hat{\mathbf{M}}$: time histories of the loaded-point displacement and the mechanical-energy error ϵ_W. 122
5.21 Axially loaded cylinder - problem description. 123
5.22 Axially loaded cylinder — experimental results [164]: deformation (left) and load–displacement curve (right). n denotes the number of circumferential waves. 124
5.23 Axially loaded cylinder - Cartography of perturbation values ΔR (a) and deformed configurations (b-h) corresponding to the black points in Figure 5.24. n denotes the number of circumferential waves. 125
5.24 Axially loaded cylinder - Load-displacement curves from the experiment (Asymmetric and Symmetric curves) and the numerical solutions using NR and ANM solvers. 125
5.25 Axially loaded cylinder - Evolution of time step size during the simulation of NR and ANM solvers. 126
5.26 Closed cylinder under pressure load: problem description. 127
5.27 Closed cylinder under pressure load: The first three buckling modes obtained from the linear eigen-buckling analysis. 127
5.28 Closed cylinder under pressure load — implicit computations with $\Delta t = 0.01\,\mathrm{ms}$: time histories of the maximal radial displacement and the relative residual error. 128
5.29 Closed cylinder under pressure load — maximal radial displacement on the deformed configuration at: (a) $t = 0.75\,\mathrm{ms}$, (b) $t = 1.50\,\mathrm{ms}$, (c) $t = 3.20\,\mathrm{ms}$, (d) $t = 3.80\,\mathrm{ms}$. 128
5.30 Closed cylinder under pressure — implicit computations with $\Delta t \leq 0.05\,\mathrm{ms}$: time histories of the maximal radial displacement and the time step size. 129
5.31 Closed cylinder under pressure — implicit computations with $\Delta t \leq 0.05\,\mathrm{ms}$ and a symmetric tangent operator: time histories of the maximal radial displacement and the relative residual error. 130
5.32 Pinched hemisphere: problem description and force-displacement curve . 133

5.33 Pinched hemisphere: hardening variable ξ (at the midplane surface) at various loading stages on the deformed configuration. (a)–(c) loading with $u_A = 42.0\,\text{mm}$, $77.7\,\text{mm}$, $96.5\,\text{mm}$; (d)–(f) unloading with $u_A = 85.8\,\text{mm}$, $69.3\,\text{mm}$, $26.8\,\text{mm}$ 134
5.34 Plate under uniform pressure: problem description. 135
5.35 Plate under uniform pressure: time histories of center point displacement obtained from the 8×8-element mesh (M1) and 16×16 element-mesh (M2). 135
5.36 Plate under uniform pressure: time histories of energy errors ϵ_{EAS} and ϵ_W 136
5.37 Cylindrical roof: problem description. 136
5.38 Cylindrical roof: vertical displacement U_z on the deformed configuration at selected times: (a) $t = 1.0\,\mu\text{s}$, (b) $t = 0.20\,\text{ms}$, (c) $t = 0.40\,\text{ms}$, (d) $t = 0.80\,\text{ms}$. 137
5.39 Cylindrical roof (Mesh 1): time history of the center-point displacement on the crown line for computations with Mesh 1. 138
5.40 Cylindrical roof (Mesh 2): time history of the center-point displacement on the crown line and the evolution of the EAS error ϵ_{EAS}. 138
5.41 Pinched cylinder: problem description. 139
5.42 Pinched cylinder: time histories of the reaction force on the crown line obtained from different computations. 139
5.43 Pinched cylinder: time histories of the EAS error ϵ_{EAS} and the mechanical-energy error ϵ_W obtained from different computations. 140
5.44 Pinched cylinder: hardening variable at various loading stages on the deformed configuration. (a–c) outer surface of the shell ($\theta^3 = 1$) from the 7-parameter shell explicit computation at $t = 0.6\,\text{ms}$, $1.0\,\text{ms}$, and $2.2\,\text{ms}$; (d) solid explicit computation at $t = 2.2\,\text{ms}$. 141
5.45 Twisted cylinder: problem description. 142
5.46 Twisted cylinder: displacement U_{norm} and reaction versus twist angle. . . 142
5.47 Twisted cylinder: hardening variable ξ at various twist angles on the deformed configuration. (a–d) mid-surface of the shell ($\theta^3 = 0$) from the 7-parameter shell explicit computation at $\phi = 30°, 60°, 90°, 120°$; (e) solid explicit computation at $\phi = 120°$. 143
5.48 Twisted cylinder: time histories of the EAS error ϵ_{EAS} and the mechanical-energy error ϵ_W obtained from different computations. 143
5.49 Stiffened roof: problem description. 144
5.50 Stiffened roof: Meshes. (a) Roof mesh 16×16 (M1), (b) Roof mesh 32×32 (M2), (c) Mesh of 2×40 elements for each stiffener (both M1 and M2). . 145

5.51 Stiffened roof: time histories of the center-point displacement on the crown line. . . . 145
5.52 Stiffened roof: time histories of the EAS error ϵ_{EAS} and the mechanical-energy error ϵ_W. . . . 146
5.53 Stiffened roof: hardening variable ξ at different times on the deformed configuration of the roof. (a–c) outer surface ($\theta^3 = 1$) from 7-parameter shell explicit computation (M2) at $t = 5.0\,\text{ms}$, $10.0\,\text{ms}$, and $45.0\,\text{ms}$; (d) solid explicit computation at $t = 45.0\,\text{ms}$. . . . 147
5.54 Stiffened roof: hardening variable ξ at different times on the deformed configuration of stiffener A (see Figure 5.49). (a–c) outer surface ($\theta^3 = 1$) from 7-parameter shell explicit computation (M2) at $t = 5.0\,\text{ms}$, $10.0\,\text{ms}$, and $45.0\,\text{ms}$; (d) solid explicit computation at $t = 45.0\,\text{ms}$. . . . 148

6.1 Truncated body Ω consisting of the elastic domain Ω_{el} and the nonphysical PML domain Ω_{PML}. The outer boundary of the PML is fixed. . . . 151
6.2 Homogeneous medium case: PML model description. . . . 166
6.3 Homogeneous medium case: Snapshots of vertical displacement obtained from Model 1. . . . 168
6.4 Homogeneous medium case: Time history of the vertical displacement at receiver A [50.0; 0.0; 0.0] and receiver B [50.0; 0.0; −100.0], obtained from Model 1. . . . 169
6.5 Homogeneous medium case: Time histories of kinetic energy in the elastic domain from different PML models. . . . 169
6.6 Pseudo-2D homogeneous waveguide: PML model description. . . . 170
6.7 Pseudo-2D homogeneous waveguide: Time history of the horizontal displacements at receiver A [200.0; 0.0; 0.0] and receiver B [200.0; 0.0; −20.0] from the PML models with $\alpha_{0X} = 0.0$ and $\alpha_{0X} = 4.0$. . . . 170
6.8 Pseudo-2D homogeneous waveguide: Time history of the kinetic energy in the elastic domain from the PML models with $\alpha_{0X} = 0.0$, $\alpha_{0X} = 2.0$, and $\alpha_{0X} = 4.0$. . . . 171
6.9 Pseudo-2D homogeneous waveguide: Snapshots of vertical displacement obtained from Model 1. . . . 172
6.10 3D homogeneous waveguide: PML model description. . . . 173
6.11 3D homogeneous waveguide: Time history of the displacement at receiver A [100.0; 0.0; 0.0] and receiver B $[200, 0, -20]\,\text{m}$ from PML models with $\alpha_{0Y} = 0.0$ and $\alpha_{0Y} = 3.0$ . . . 174
6.12 3D homogeneous waveguide: Energy in the elastic domain. . . . 174

6.13 3D homogeneous waveguide: Snapshots of vertical displacement obtained from PML model with $\alpha_{0Y} = 0.0$. 175
6.14 Two-layered half-space: PML model description. 176
6.15 Two-layered half-space: Mesh of PML model. 176
6.16 Two-layered half-space: Time history of the displacement at receiver A [200.0; 0.0; 0.0] from the PML models with $\alpha_{0X} = 0.0$ and $\alpha_{0X} = 4.0$. . . 177
6.17 Two-layered half-space: Time history of the displacement at point B [200.0; 0.0; −10.0] from the PML models with $\alpha_{0X} = 0.0$ and $\alpha_{0X} = 4.0$. 178
6.18 Two-layered half-space: Time histories of kinetic energy in the elastic domain from PML models. 178
6.19 Two-layered half-space: Snapshots of vertical displacement obtained from PML model with $\alpha_{0X} = 0.0$. 179

List of Tables

4.1 Thin plate: Mode participation factor obtained from the modal analysis of 7-parameter shell model using CMM 71
4.2 Applied time integration parameters as a function of the spectral radius ρ_∞ 75
4.3 Summary of matrix 98

5.1 Three intersecting plates – explicit computations: Summary of SMS parameter β_0, the critical time step $\Delta t_{\text{cr.}}$, and the chosen time step sizes for subdomain 1 (vertical plate) and subdomain 2 (horizontal plates). . . 110
5.2 Cylindrical roof — Time-stepping performance of implicit solvers. 117
5.3 Axially loaded cylinder — computational time-stepping workload (adaptive, $\Delta t \leq 0.01\,\text{s}$). 124
5.4 Closed cylinder under pressure — computational time-stepping workload. 130
5.5 Finite-strain elasto-plastic dynamics — time-stepping workload of *implicit NR* computations. 132

6.1 Homogeneous medium case: stretching function parameters and the time-step-sizes for PML models 167
6.2 Homogeneous medium case: relative error in displacement over the time interval $[0.0, 4.0\,\text{s}]$ at receiver A, located on the free surface at $[50, 0, 0]\,\text{m}$, and receiver B, located at the PML–elastic interface at $[50, 0, -100]\,\text{m}$ . . 167
6.3 Pseudo-2D homogeneous waveguide: relative error in displacement over the time interval $[0.0, 4.0\,\text{s}]$ at receiver A $[200, 0, 0]\,\text{m}$, and receiver B $[200, 0, -20]\,\text{m}$ 171
6.4 3D homogeneous waveguide: relative error in displacement over the time interval $[0, 4.0\,\text{s}]$ at receiver A $[200, 0, 0]\,\text{m}$, and receiver B $[200, 0, -20]\,\text{m}$ 173
6.5 Two-layered half-space: relative error in displacement over the time interval $[0, 10.0\,\text{s}]$ at receiver A $[200, 0, 0]\,\text{m}$, and receiver B $[200, 0, -10]\,\text{m}$ 177

Chapter 1

Introduction

1.1 Motivation

Shell structures are widely used in engineering applications ranging from aerospace components and ship hulls to civil infrastructure and energy systems. Their high strength-to-weight ratio and geometric efficiency make them ideal for carrying loads over large spans or surfaces. However, these advantages also make them susceptible to complex nonlinear behaviors under severe loading conditions. Large deformations can trigger phenomena such as buckling, material yielding, and strongly coupled dynamic effects, leading to failure modes that are challenging to predict.

Accurate simulations of such nonlinear phenomena are essential for ensuring structural safety, optimizing designs, and avoiding excessive conservatism in engineering practice. To this end, the finite element method (FEM) offers a flexible and powerful numerical framework, capable of representing complex geometries and capturing nonlinearities.

The *Laboratoire d'Étude des Microstructures et de Mécanique des Matériaux* (LEM3) has developed strong expertise in finite element buckling analysis in the quasi-static regime using the Asymptotic Numerical Method (ANM) [62, 165, 166], an alternative resolution strategy to the classical Newton–Riks method. ANM enables efficient tracing of complex equilibrium paths, including highly nonlinear post-buckling branches, while requiring minimal computational effort for nonlinear resolution.

Extending this expertise from the quasi-static to the dynamic regime introduces new challenges. The coupling between inertia, stiffness, and damping over time can produce instabilities that go beyond a static loss of equilibrium, being driven or amplified by inertial effects and the time-varying nature of the loading. Such phenomena are particularly pronounced during buckling or post-buckling stages and under impulsive or high-rate loading, where the structural response may be dominated by short-duration,

high-frequency components. Therefore, the choice of a suitable time integration strategy is crucial:

- Implicit schemes provide unconditional stability and are advantageous for problems with slow or moderate transients, but require iterative solvers and can become computationally expensive in highly nonlinear dynamics.
- Explicit schemes avoid global iterations, making them well-suited for short-duration, high-frequency, or impulsive events; however, they require very small time steps to maintain stability.

The motivation for this work is to build upon LEM3's established expertise in quasi-static buckling and extend it to the nonlinear dynamic analysis of shell structures, with a primary focus on geometric and material nonlinearities. Particular attention is given to the design of solvers for both implicit and explicit time integration schemes, enabling robust simulations under impulsive and transient loading.

1.2 State of the art

1.2.1 Finite element modeling of shell structures

The nonlinear analysis of thin shell structures requires a consistent combination of shell theory and a finite element (FE) formulation. The two classical shell theories are the Kirchhoff–Love (KL) theory [99, 119] and the Reissner–Mindlin (RM) theory [142, 143, 124]. Both theories are derived from continuum mechanics, assuming that normals to the mid-surface remain straight and inextensible during deformation. The KL theory further ensures that the normals remain orthogonal to the mid-surface, which is particularly suitable for thin shells, leading to a relatively simple formulation that can be naturally embedded in a finite strain framework as shown in [98, 4]. By contrast, the RM theory relaxes the normality condition by allowing transverse shear deformation, making it more versatile and applicable to moderately thick shells. The RM formulation can account for large displacements and finite rotations of the mid-surface, but its classical form is not derived in a finite strain framework, which complicates its direct extension to problems involving large strains and nonlinear constitutive behavior.

Direct approach. Applying the Finite Element Method (FEM) directly to the governing equations of shell theories is known as the direct approach to modeling thin shell structures. In practice, the RM theory is often preferred since it requires only C^0

continuity of the shell's mid-surface [148–150, 79, 145, 91, 93, 158]. Because the governing equations are expressed in terms of stress resultants, the finite element discretization involves only the two-dimensional mid-surface of the shell. Elements obtained in this way are often referred to as geometrically exact, since no additional assumptions or numerical integration are required through the thickness [31, 92].

Degenerated solid approach. Developed in parallel with the direct approach and dominating the literature, the degenerated solid approach derives shell finite elements directly from the three-dimensional continuum. The essential idea is that the finite element discretization is applied to the 3D continuum, which is then reduced using shell kinematic assumptions, rather than the governing equations of an existing shell theory. In this way, complex analytical stress-resultant formulations can be avoided and replaced with the numerical through-the-thickness approximation and integration.

Büchter and Ramm [47] showed that, under equivalent assumptions, parameterizations, and interpolations, degenerated shell elements are mathematically equivalent to direct-approach elements. Early formulations [90, 68, 139, 133] assume straight directors, constant thickness, and vanishing transverse normal stress, yielding a 5-parameter Reissner–Mindlin-type shell element. The 5 parameters denote 5 nodal degrees of freedom: 3 translational degrees of freedom for the motion of the mid-surface and 2 rotational degrees of freedom for the directors. However, the 5-parameter formulation requires condensing the 3D constitutive law, which becomes complex in the case of nonlinear materials, and the assumption of a straight director does not hold in laminates or composites.

To overcome these limitations, the degenerated solid approach was extended to six-parameter formulations without rotational degrees of freedom, accounting for thickness extensibility. However, using the full 3D constitutive law leads to Poisson thickness locking. The locking comes from the inability of the element's interpolation in the thickness direction to capture the Poisson effect in the element under bending. To overcome this locking, Parish [134] proposed introducing an extra displacement-like parameter to ensure the quadratic variation of the displacement field in the thickness direction, leading to the 7-parameter shell element. At the same time, Büchter and Ramm [46], Büchter et al. [48] employed the Enhanced Assumed Strain (EAS) method [151] to introduce a strain-like variable to the 6-parameter formulation, which can enhance the approximated strain and make it compatible with the 3D constitutive law, leading also to the 7-parameter formulation. The strain-like 7th parameter can be eliminated at the element level, thus the 7-parameter formulation with EAS provides only 6 degrees of freedom at the global level.

These strategies were investigated and extended in [144, 30, 40, 38]. The 7-parameter formulation can be extended to higher-order formulations for multi-layered shells, such as laminates or composites [42, 100, 159, 160].

Solid-shell approach. The solid-shell, or shell-like solid, is a variant of the degenerated solid approach, as it is also based on a continuum formulation. Originally proposed by Hauptmann and Schweizerhof [83], this method employs standard solid finite elements with a single layer of elements through the thickness and low-order interpolation in the thickness direction. To recover shell kinematics, the formulation is often expressed in isoparametric (curvilinear) coordinates, which requires particular care during mesh generation. Although Hauptmann and Schweizerhof [83] demonstrated that Reissner–Mindlin-type kinematics could be incorporated into solid-shell elements, in most of the subsequent literature the term *solid-shell* refers to three-dimensional formulations with extensible thickness [160, 159, 65], in which the complete 3D constitutive laws are employed without any modifications or manipulation.

Locking Phenomena

Locking is one of the central challenges in the development of shell finite elements. According to the reason that leads to the locking phenomenon, we can categorize locking into two groups as follows [31]:

- *Shear locking*, *membrane locking*, and *curvature-thickness (trapezoidal) locking*. These effects arise from the intrinsic ill-conditioning of thin-shell kinematics, where small discretization errors can lead to significant artificial stiffness [31]. In principle, they vanish with mesh refinement, but in practice, they severely deteriorate the performance of low-order (high-order for membrane locking) or coarse meshes.
- *Poisson thickness locking* and *volumetric locking* result from incompatibilities between the interpolation functions and the material behavior (Poisson effect and nearly incompressible or incompressible material), and therefore do not vanish under mesh refinement.

A variety of remedies have been developed to alleviate locking, including: (selective) reduced integration [88, 18, 19, 65, 141], assumed strain methods [68, 15, 25, 29], enhanced assumed strain [151, 46, 48], B-bar methods [90], and the discrete strain gap (DSG) method [32, 108, 69].

NURBS-based shell elements The advent of isogeometric analysis (IGA) [89] introduced a new paradigm for shell modeling. By employing NURBS basis functions, IGA provides exact geometry representation, high inter-element continuity, and direct compatibility with CAD descriptions. The first IGA shell formulation based on Kirchhoff–Love theory was proposed by Kiendl et al. [97], with subsequent extensions to hyperelastic and elastoplastic materials at finite strains [98, 4]. In parallel, Reissner–Mindlin-type IGA shells were developed by Benson et al. [21], followed by further improvements and applications [70, 66]. Numerous works have explored solid-like and solid-shell formulations in the IGA framework [87, 33–35, 49, 50].

1.2.2 Nonlinear dynamic analysis of shell structures

In engineering practice, the analysis and design of shell structures is usually carried out under the quasi-static regime, as in EN 1993-1-6 [1]. The equilibrium path is typically traced using path-following techniques, such as the Riks arc-length method [63, 138, 137], to obtain the load-displacement curve. The nonlinear behavior of the structure, including large displacements, large rotations, and material nonlinearities, can then be investigated along this equilibrium path.

Nevertheless, dynamic analysis is often required as a complementary tool. Numerous studies have demonstrated the efficiency of dynamic simulations in capturing the post-buckling process when quasi-static solvers fail to converge [103, 94, 114]. A second situation arises when the external actions themselves are dynamic: under pulse loading, for example, the instability threshold depends not only on the load amplitude but also on its duration, requiring dedicated criteria to characterize the dynamic response [109]. Another case occurs when the structural response is intrinsically transient, such as blast and impact on protective structures [71], seismic excitations in civil engineering, or transient fluid–structure interaction [96]. In such contexts, nonlinear dynamic simulations extend the scope of quasi-static approaches by accounting for inertia and transient phenomena that govern the actual structural response.

In dynamic analysis, the continuous governing equations of motion are discretized in time, replacing the continuous response by a sequence of discrete instants. The solution is then advanced step by step, a process referred to as *time integration*. Two major classes of time integration schemes are commonly used: implicit schemes and explicit schemes, with the choice depending on the nature of the problem under consideration.

Implicit schemes

The implicit schemes are often preferred for problems governed by smooth nonlinearities, such as geometric or material nonlinearities. In elasto-plasticity, for instance, the response is smooth within either the elastic or plastic regime, with nonsmoothness arising only at the transition between these states [2]. In such schemes, the solution is defined *implicitly* through the discrete governing equations and must therefore be solved at each time step. When the governing equations are nonlinear, this resolution requires iterative strategies—most commonly the Newton–Raphson method—which may become computationally demanding or even fail to converge under severe nonlinear conditions. The principal advantage of implicit schemes lies in their ability to use relatively large time steps.

Numerically dissipative schemes. An important aspect of implicit computations is controlling spurious high-frequency modes, which is particularly critical in shell structures [161, 140]. In most engineering applications, the response of shell structures is governed by bending and a few fundamental membrane modes, all of which lie in the low-frequency range. However, the finite element model also introduces high-frequency modes, such as transverse shear or thickness-stretching (in three-dimensional shell) modes, whose number increases with mesh refinement. Properly resolving these modes would require small time steps, and when they are not adequately damped, they tend to accumulate non-physical energy during the simulation. This artificial energy growth can contaminate the solution and eventually destabilize the computation.

The need to suppress non-physical high-frequency modes led to the development of numerically dissipative implicit schemes. The central idea is to embed numerical damping directly into the time integration scheme so that it primarily attenuates high-frequency components while leaving the low-frequency response essentially unaffected. Early contributions include the Hilber–α method [84], the Bossak–α method [162], and the Generalized-α method [56], originally proposed for linear elastoplastic problems but found to be less efficient in nonlinear dynamics. Thus, Energy- and Momentum-conserving schemes were later introduced, many of which specifically target shell structures [152, 153, 39, 26]. This line of development led to the Generalized Energy–Momentum method [112, 113], which encompasses special cases such as modified α-methods (Newmark-dissipative, Hilber–α, Bossak–α, and Generalized-α), as well as the Energy–Momentum conserving schemes. Although the Generalized Energy–Momentum method does not strictly conserve momenta and its dissipation is not always confined to the high-frequency range, it has shown excellent performance in shell problems [159, 114]. More advanced formulations,

such as the energy-decaying schemes, extend this framework by providing controllable high-frequency dissipation while ensuring momentum conservation [5, 6, 41].

The Asymptotic Numerical Method. As mentioned above, implicit schemes lead to nonlinear algebraic equations that must be solved iteratively at each time step. In practice, the Newton–Raphson (NR) method is the standard approach, and is implemented in all commercial finite element codes due to its quadratic convergence under favorable conditions [2]. The procedure consists in linearizing the residual equations around the current estimate of the solution, solving the resulting system using the tangent stiffness matrix, and updating the solution iteratively until the residual is smaller than a given tolerance. Despite its efficiency in many problems, Newton–Raphson requires repeated assembly and factorization of the tangent operator, which becomes particularly severe in large-scale models. Simplified alternatives, such as modified or quasi-Newton methods, reduce computational cost by reusing or approximating the tangent matrix, but they tend to perform poorly in buckling situations. This limitation has motivated the development of the Asymptotic Numerical Method (ANM) as an alternative numerical method to the NR.

The Asymptotic Numerical Method (ANM) was first introduced by Cochelin [59], Cochelin et al. [61, 62] as a path-following technique for quasi-static elastic nonlinear problems. The main difference with the Newton–Raphson (NR) procedure is that NR iteratively *guesses* the solution through successive linearizations, whereas ANM *approximates* the solution using the power series expansion based on the perturbation technique. This approach transforms the original nonlinear system into a sequence of linear problems involving the same tangent operator. As a result, only one tangent matrix needs to be assembled and factorized in each resolution process, making ANM particularly attractive for large-scale nonlinear analyses. In addition, in the path-following setting, Cochelin [59] proposed using the load factor, an unknown of the governing equations, as the expansion parameter of the power series, resulting an algorithm that is highly efficient in terms of computational effort. These advantages have been confirmed in numerous studies [166, 165, 125]. In the context of quasi-static buckling, ANM has also shown excellent performance for the identification of bifurcation points and branch switching [8, 9, 37], and has been extended to nonlinear materials [127, 126, 7] as well as unilateral contact problems [3].

The extension of ANM to dynamics was initiated by Cochelin and Compain [60], followed by several variants [95, 36], leading to high-order implicit algorithms for nonlinear dynamic problems. In this framework, a homotopy parameter ϵ is introduced into the

governing equations and used as the expansion parameter for a power series. This transforms the nonlinear system into a sequence of linear systems with the same tangent operator, and the solution of the original problem is recovered by setting $\epsilon = 1$. This strategy was further developed in fluid mechanics, where Guevel et al. [80, 81, 82] applied ANM to the Navier-Stokes equations and proposed efficient algorithms for incompressible flows. In particular, Guevel et al. [81] conducted a detailed comparison between NR and ANM in terms of computational time, demonstrating a significant reduction in cost with ANM. More recently, Claude et al. [57] investigated an alternative approach in which the time t itself was used as the expansion parameter. However, their study revealed that the time steps required by this method were considerably smaller than those typically used in classical NR-based solvers.

In summary, implicit schemes allow for large time steps and are well-suited for problems governed by smooth nonlinearities, with dissipative variants of the α-methods providing robust control of spurious high-frequency modes. The Asymptotic Numerical Method (ANM) offers an attractive alternative to the Newton–Raphson method by reducing the number of tangent factorizations. While several works have demonstrated its efficiency in quasi-static problems and in some academic nonlinear dynamic cases, systematic comparisons between ANM and Newton–Raphson in the context of dynamic buckling of shell structures are still lacking.

Explicit schemes

Explicit schemes provide an attractive alternative for the nonlinear dynamic analysis of shell structures, particularly for short-duration, high-speed loadings or severe nonlinearities [20]. In explicit computations, the solution at a given time step is computed *explicitly* from the known solution at the previous step, without the need to solve any linear or nonlinear systems of equations. The most widely used explicit algorithm is the central difference method [17, 20].

Critical time step. Explicit schemes are conditionally stable: the time step must remain below a critical value governed by the highest natural frequency of the discretized model. In shell formulations, unphysical high-frequency modes can therefore impose unnecessarily small time steps, reducing computational efficiency. A widely adopted remedy is the *Selective Mass Scaling* (SMS) technique, first proposed by Olovsson et al. [131, 130] for thin-walled structures with solid elements. The principle is to add artificial mass selectively to certain components, thereby reducing the eigenvalues associated with high-frequency modes while minimizing the influence on the low-frequency response.

Building on this idea, Cocchetti et al. [58] introduced an SMS version tailored to solid-shell elements, which was further investigated in [132, 123]. More recently, Oesterle et al. [129], Hoffmann et al. [85] proposed an SMS approach based on the Discrete Strain Gap method for shear-deformable shell and solid-shell elements. A comprehensive comparison of these techniques was reported in Hoffmann et al. [86], who demonstrated that the formulation of Cocchetti et al. [58] offers the best compromise between accuracy and computational cost.

Explicit algorithms for shell elements. The main contribution to explicit dynamics of shell structures is the pioneering work of Belytschko et al. [16, 18, 19], who introduced and investigated the linear four-node shell element based on Reissner–Mindlin kinematics, equipped with reduced integration and hourglass control and shear-locking free. Building on these developments, Benson et al. [21] proposed a NURBS-based explicit shell element inspired by the Belytschko et al. [16] element. The investigations demonstrated excellent performance under large rotations, large distortion, elasto-plasticity, and complex contact conditions.

However, the use of 3D-shell and solid-shell elements in explicit computations is not straightforward. Since low-order elements (both in the mid-surface and through the thickness) are typically preferred in explicit analysis, these formulations are particularly prone to locking, which necessitates the use of the Enhanced Assumed Strain (EAS) method. The issue was first reported by Tan and Vu-Quoc [156], who noted that a *static condensation* was performed at the beginning of each time step to update the EAS fields, although the procedure was not detailed. Subsequent investigations by Mattern et al. [122, 123], Pagani et al. [132] clarified that static condensation requires a Newton-type resolution process at the element level to solve for the EAS fields, thereby losing the computational efficiency of an *explicit* formulation. To overcome this difficulty, the authors proposed simplified condensation strategies and demonstrated that these lead to very good performance while retaining the advantages of explicit integration.

In summary, explicit schemes have proven highly effective for shell dynamics under severe nonlinearities and transient loadings. Their main limitations remain the small critical time step and the treatment of the EAS field in the solid-like shell elements, which aim to obtain robust and efficient explicit algorithms. For the latter, the EAS treatment proposed in [132] needs to be investigated, especially in cases of fast loading, severe deformation and material plasticity.

1.3 Objectives of the thesis

This thesis aims to extend LEM3's expertise in quasi-static buckling analysis to the nonlinear dynamic regime of thin-walled structures. Particular emphasis is placed on finite-strain theory to capture large-strain effects, buckling phenomena, and elasto-plasticity. The work seeks to consolidate and adapt existing methods from the literature into an in-house software environment developed during the PhD work. This platform is designed not only to serve as a research tool for addressing advanced academic problems, but also as a foundation for high-performance computing (HPC) codes dedicated to engineering applications.

7-parameter shell formulation. This work adopts the 7-parameter shell formulation of Büchter and Ramm [46], Büchter et al. [48], which extends the classical Reissner–Mindlin kinematics by including thickness extensibility. Based on the degenerated solid approach, the formulation allows consistent use of full three-dimensional constitutive laws within a finite-strain framework. Bischoff and Ramm [30] confirmed that this formulation is optimal in the sense that only six nodal unknowns appear in the global governing equations.

The seventh parameter is introduced through the Enhanced Assumed Strain (EAS) method, which enriches the transverse normal strain field to alleviate Poisson thickness locking. Shear and membrane locking are avoided by restricting the formulation to quadratic or higher-order elements and by employing reduced integration, as recommended in Bischoff et al. [31]. In practice, the thesis primarily employs 8-node quadrilateral elements with 2×2 quadrature points on the mid-surface. For problems involving elasto-plasticity, the plastic strain field is systematically verified to prevent volumetric locking as recommended in [2].

Since the formulation is continuum-based, solid elements are used as a numerical reference. This dual perspective clarifies how shell elements formulated in curvilinear coordinates relate to their solid counterparts in Cartesian coordinates, while also enabling the reuse of a common material model library. We also employ the standard mortar approach [170] to handle the coupling between solid and shell elements as well as between the shell's components in certain situations, such as shell structures with stiffeners. On this basis, both the 7-parameter shell and solid element serve as the foundation for the development of both implicit and explicit dynamic solvers.

Implicit dynamics. For implicit dynamic analysis, both geometric and material nonlinearities are considered. The governing equations also include Lagrange multipliers to enforce linear kinematic constraints such as imposed displacements and mortar coupling. To control spurious high-frequency modes, we employ modified α-methods, represented by the modified Generalized-α method, a simplified variant of the Generalized Energy–Momentum method. These schemes avoid the complexity of computing consistent internal forces and stiffness tangent under nonlinear material behavior, while retaining favorable dissipative properties. Their performance has been assessed in Vu-Quoc and Tan [159], Lavrencic and Brank [114]. Moreover, the Hilber–α method, a version of the modified Generalized-α method, is also implemented as a standard implicit operator in ABAQUS [2].

The Newton–Raphson method is adopted as the baseline nonlinear solver, combined with an adaptive time-step algorithm based on convergence rate, to maximize efficiency. In parallel, the Asymptotic Numerical Method (ANM) is mobilized, only for geometrically nonlinear problems. The objective is to conduct a fair comparison with the Newton–Raphson method in terms of time-stepping efficiency and computational performance in buckling dynamics.

Explicit dynamics. For explicit dynamics, the central difference scheme is adopted. As in the implicit case, both geometric and material nonlinearities are considered. To address the stability restriction, the Selective Mass Scaling strategy of Cocchetti et al. [58], originally proposed for solid-shell elements, is adapted here to the 7-parameter shell formulation, ensuring accuracy while preserving the conservation properties of the central difference scheme.

A particular focus is placed on the treatment of the EAS field in the explicit context. We investigate the simplified static condensation approach of Pagani et al. [132] specifically tailored to maintain explicit efficiency while alleviating locking. The accuracy and robustness of the algorithm are studied through benchmark tests involving pulse loading and large-strain elasto-plasticity.

In addition to the mono-domain explicit solver, we also adopt the Hybrid Asynchronous Time Integrator (HATI) framework [78, 43, 44] to develop a multi-time step explicit solver within the context of domain decomposition. This approach allows for the efficient treatment of large-scale problems with heterogeneous spatial discretizations and multiple characteristic time scales.

Spectral Element Perfectly Matched Layers (PML). Perfectly Matched Layers (PML) are among the most effective techniques for simulating wave propagation in unbounded domains. The basic principle is to surround the computational domain of interest with a nonphysical absorbing layer of finite thickness that can attenuate outgoing waves without generating spurious reflections at the interface with the physical domain. Since their introduction by Bérenger [22] for electromagnetic waves, PML formulations have been successfully adapted to elastodynamics in both finite element [12, 14, 11, 110, 111, 45, 116, 76, 167–169] and spectral element contexts [107, 104, 163].

Although not originally planned as part of the thesis, I had the opportunity to collaborate with Dr. Florent De Martin at BRGM on the implementation of PML in `EFISPEC3D` [120], an open-source spectral element software dedicated to the solution of three-dimensional wave equations. The objective was to extend the code with an absorbing boundary condition that efficiently attenuates outgoing waves.

Before this collaboration, we had already investigated the displacement-based PML formulation proposed in [12, 14, 11], in the context of isogeometric analysis (IGA). We proposed a two-dimensional hybrid asynchronous IGA-PML [51], which allows different spatial and temporal discretizations in the PML and the finite-element physical domain. Building on this experience, our strategy within the spectral element framework is to extend the investigation to three-dimensional problems using the same PML formulation.

While this development lies outside the main objectives of the present thesis, it represents a first step toward exploring three-dimensional soil-structure interaction problems, such as the seismic response of steel storage tanks undergoing dynamic buckling. Beyond its direct relevance to seismic engineering, this line of investigation also demonstrates how the numerical techniques developed in the thesis can be extended to broader wave propagation and structural-interaction problems.

In summary, the objectives of this thesis are to develop and assess advanced finite element formulations and solvers for the nonlinear dynamic analysis of thin-walled structures. A primary focus is on the 7-parameter shell elements. Solid elements are employed in parallel as reference solutions, providing a consistent basis for evaluating the performance of shell formulations. The Asymptotic Numerical Method is investigated as an alternative solver to the classical Newton-Raphson method for implicit geometrically nonlinear dynamics, whereas a robust and efficient explicit algorithm for shell elements is developed. Finally, the complementary study on Perfectly Matched Layers opens the door to future investigations of soil–structure interaction beyond the scope of this thesis.

1.4 Publications related to the thesis work

The results of this thesis have been disseminated through several peer-reviewed journal articles. We provide below the list of publications related to the thesis:

- A. Chau, M. Brun, T. Elguedj. *Hybrid Asynchronous isogeometric Perfectly Matched Layer for transient elastodynamics*, Computers and Geotechnics. 158 (2023) 105387.
- A. Chau, M. Brun, P Ventura, H. Zahrouni, M. Potier-Ferry. *Nonlinear buckling analysis of thin-walled beams modeled with 7-parameter shell elements*, Thin-Walled Structures. 201 (2024) 111994.
- A. Chau, M. Brun, P Ventura, H. Zahrouni, M. Potier-Ferry. *Asymptotic Numerical Method for dynamic buckling of shell structures with follower pressure*, International Journal of Solids and Structures. 308 (2025) 113135.
- A. Chau, M. Brun, P Ventura, H. Zahrouni, M. Potier-Ferry. *Explicit dynamics and buckling simulations with 7-p shell elements and enhanced assumed strain*, Finite Elements in Analysis & Design. 247 (2025) 104346.

1.5 Outline of the thesis

This thesis is structured in six chapters. After presenting the theoretical foundations of finite deformation solid mechanics and displacement-based finite elements, attention is given to the development of a 7-parameter shell formulation, with emphasis on Poisson's thickness locking, elasto-plastic behavior, and coupling strategies between shells and between shells and solids. Building on these formulations, general solvers for nonlinear dynamic analysis are proposed, encompassing both implicit and explicit time integration schemes, as well as an alternative solver based on the Asymptotic Numerical Method (ANM). The performance of the formulations and solver using benchmark problems that cover geometric and material nonlinearities under transient and impulsive loading. Finally, a complementary study on Perfectly Matched Layers (PML) for 3D transient elastodynamics is presented, illustrating the potential extension of the developed methods to soil–structure interaction problems. The detailed outline is as follows.

Chapter 2 introduces the theoretical foundations of finite deformation solid mechanics. The strong form of the governing equations is presented, along with their variational weak formulations, in both the Total Lagrangian and Updated Lagrangian frameworks. The fundamental principles of displacement-based finite elements are recalled, including

standard solid elements and a nonlinear solution procedure based on the Newton–Raphson method. Additional details on the discretization of solid elements are provided in Appendix A.1. The numerical results obtained with solid elements serve as reference solutions for assessing the performance of the 7-parameter shell formulation developed in this work.

Chapter 3 is devoted to the 7-parameter shell formulation. Special attention is given to the issue of Poisson's thickness locking and its treatment through the Enhanced Assumed Strain (EAS) method. The finite element implementation is described at the element level (with complementary details in Appendix A.2) and shown to be compatible with the global finite element framework established in the previous chapter. The treatment of non-conservative loads and the extension to elasto-plasticity at finite strains are also addressed. Coupling between shell components is discussed through two strategies: a pre-processing approach and the classical mortar method, the latter being applicable to solid–shell coupling.

Chapter 4 develops solvers for the nonlinear dynamic analysis of shell structures, building on the formulations established in the preceding chapters. Topics covered include the influence of high-frequency modes in thin shells, implicit time integration schemes based on α-methods with Newton–Raphson iterations, and the development of an ANM-based solver. Explicit solvers are also introduced, with particular emphasis on the treatment of the EAS field in an explicit setting.

Chapter 5 presents the numerical validation of the proposed formulations and solvers. The first two academic benchmarks, which consist of three intersecting plates and the dynamic snap-through of a cylindrical roof, demonstrate the basic capabilities of the developed solvers. Comparisons between the Newton–Raphson method and the ANM are conducted using two implicit buckling analyses: an axially loaded cylinder and a closed cylinder under external pressure. The explicit algorithm for the 7-parameter shell elements, as well as the NR-based implicit solver, are then examined in the context of finite strain elasto-plasticity through a series of impulsive loading cases.

Chapter 6 reports on a complementary study carried out in collaboration with BRGM on Perfectly Matched Layers (PML) for transient elastodynamics using spectral elements. After presenting the governing equations and weak formulation of the displacement-based PML, the chapter provides numerical validations, including Lamb's test in homogeneous and heterogeneous media and a waveguide configuration. Although this exploratory work lies outside the main scope of the thesis, it illustrates the potential for extending the numerical methods developed here to problems of soil–structure interaction under seismic loading.

Chapter 2

Finite Deformation Solid Mechanics

This chapter focuses on geometric nonlinearity in solid mechanics, which is fundamental for modeling large-deformation problems. The concepts presented here form the basis for the shell formulation discussed later in the thesis.

Solid Mechanics concerns the behavior of continuous solid materials, particularly their motion, deformation, and resistance to external actions such as forces or prescribed displacements. These external actions, commonly referred to as boundary conditions, cause a deformable body to undergo displacement and deformation until it reaches a mechanically balanced configuration. At equilibrium, all material points within the body, including those at the boundaries, must satisfy the local equilibrium equations.

To analyze this mechanical response, we begin by defining the displacement field, which characterizes how each material point in the body moves in response to external loading. From the displacement field, we derive the strain, which quantifies the deformation of infinitesimal elements, and the stress, which quantifies the internal resistance of the material to that deformation. Solving a solid mechanics problem thus involves establishing and coupling these three fields—displacement, strain, and stress—while enforcing equilibrium throughout the body under the imposed boundary conditions.

We commonly classify the primary sources of nonlinearity in solid mechanics problems into four categories:

- **Geometric nonlinearity**: Arises when the deformation is significant, and it becomes necessary to distinguish between the initial (reference) and the current (deformed) configurations. The relation between strain and displacement becomes nonlinear in this case.
- **Material nonlinearity**: Occurs when the stress-strain relationship is nonlinear, as in hyperelastic or elasto-plastic materials.

- **Force nonlinearity**: Introduced when external loads (such as pressure or follower forces) depend on the current configuration, hence making them deformation-dependent.
- **Kinematic (or displacement) nonlinearity**: Appears in problems where the boundary conditions are applied on surfaces whose location depends on the deformation, such as in contact mechanics or rigid body motions.

Among these, this chapter focuses on geometric nonlinearity. We begin by introducing the fundamental theory of finite strains in three dimensions, followed by the strong and weak forms of the governing equations. The basic principles of finite element discretization, with emphasis on solid elements, are then presented to derive the discrete governing equations. This chapter thus establishes the theoretical framework and provides reference numerical results that will serve as benchmarks for the 7-parameter shell elements.

2.1 Kinematics and Deformation

In finite deformation theory, we allow the possibility that deformation can become large during loading. In such cases, it is necessary to distinguish between the reference configuration, in which the initial shape of the body or bodies to be analyzed is known, and the current configuration after loading. Figure 2.1 shows the two configurations and the coordinate frames that will be used to describe each one. We note that the body's current configuration is unknown at the start of the analysis; therefore, it must be determined as part of the solution process.

The fundamental kinematic relationships describing the deformation of a homogeneous body are presented here, as shown in Figure 2.1. A body has material points whose positions are given by the vector $\boldsymbol{X}$ in a fixed reference configuration, Ω, in three-dimensional space. After the body is loaded, each material point is described by its position vector, $\boldsymbol{x}$, in the current configuration, ω. In Cartesian coordinates, the position vectors are described in terms of their components as:

$$\boldsymbol{X} = X_I \, \boldsymbol{e}_I, \qquad \boldsymbol{x} = x_I \, \boldsymbol{e}_I, \qquad I = 1, 2, 3 \tag{2.1}$$

where $\boldsymbol{e}_I$ are unit base vectors and the summation convention is used for repeated indices of like kind. The indices are written in capital letters and refer to the Cartesian coordinates. The position vector at the current configuration is related to the position vector in the reference configuration through the displacement vector, as shown in Figure 2.1.

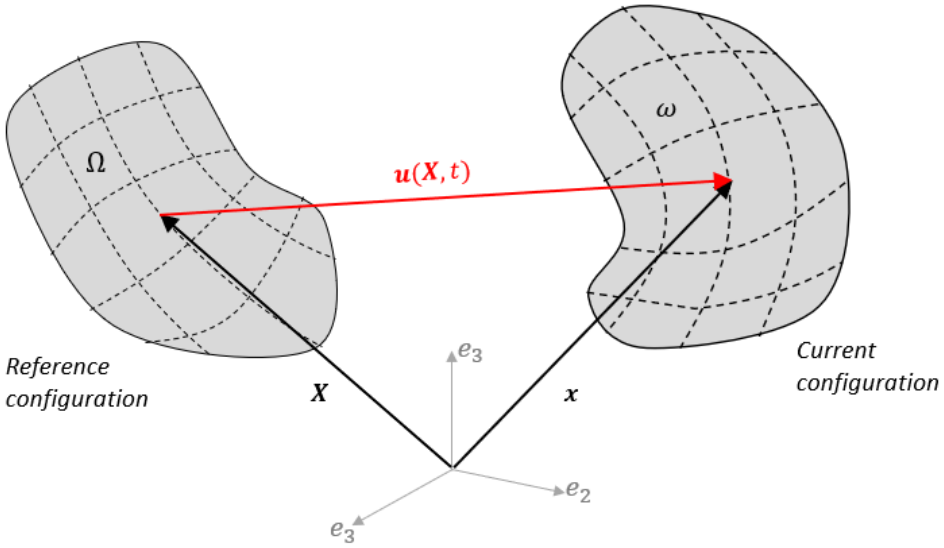

Figure 2.1 Reference (undeformed) and current (deformed) configurations in finite deformation problems

Accordingly,

$$\boldsymbol{u}(\boldsymbol{X},t) = \boldsymbol{x}(\boldsymbol{X},t) - \boldsymbol{X} \tag{2.2}$$

Determination of the displacement $\boldsymbol{u}(\boldsymbol{X},t)$ is required as part of any solution.

Deformation gradient. A fundamental measure of deformation is described by the deformation gradient given by:

$$\boldsymbol{F} = \frac{\partial \boldsymbol{x}}{\partial \boldsymbol{X}}, \qquad F_{IJ} = \frac{\partial x_I}{\partial X_J} \tag{2.3}$$

To ensure that the material volume elements remain positive, the deformation gradient is subject to the constraint:

$$J = \det \boldsymbol{F} > 0 \tag{2.4}$$

As seen in Eq. (2.3), the deformation gradient is a two-point tensor with one basis defined in the current configuration and the other in the reference configuration. It is a direct measure that maps a differential line element in the reference configuration $d\boldsymbol{X}$ into one in the current configuration $d\boldsymbol{x}$:

$$d\boldsymbol{x} = \boldsymbol{F} \cdot d\boldsymbol{X} \tag{2.5}$$

Thus, we can use it to determine the change in length and direction of a differential line element. The deformation gradient is also used for the mapping of a differential volume

or an oriented area between the reference and the current configurations:

$$d\omega = J\, d\Omega \qquad\qquad d\mathbf{a} = J\boldsymbol{F}^{-T}.d\mathbf{A} \tag{2.6}$$

where $d\Omega$ and $d\omega$ denote the differential volumes, $d\boldsymbol{A} = \boldsymbol{N}.dA$ and $d\mathbf{a} = \boldsymbol{n}.da$ denote the differential areas with $\boldsymbol{N}$ and $\boldsymbol{n}$ as the unit normal vectors, respectively, in the reference and current configurations.

Strain measures For the development of constitutive equations, it is common to introduce deformation measures that are more suitable for either the reference or the current configuration. In the reference configuration, the right Cauchy-Green deformation tensor is introduced as:

$$\mathbf{C} = \boldsymbol{F}^{\mathrm{T}}\boldsymbol{F}, \qquad C_{IJ} = F_{KI}\, F_{KJ} \tag{2.7}$$

Alternatively, we can use the Green-Lagrange strain tensor, $\boldsymbol{E}$, given as:

$$\boldsymbol{E} = \frac{1}{2}\Big(\mathbf{C} - \boldsymbol{I}\Big) \tag{2.8}$$

where $\boldsymbol{I}$ is the second-order identity tensor. The Green-Lagrange strain tensor may be expressed in terms of displacement as:

$$\boldsymbol{E} = \frac{1}{2}\left(\frac{\partial \boldsymbol{u}}{\partial \boldsymbol{X}} + \frac{\partial \boldsymbol{u}}{\partial \boldsymbol{X}}^{\mathrm{T}} + \frac{\partial \boldsymbol{u}}{\partial \boldsymbol{X}}^{\mathrm{T}}.\frac{\partial \boldsymbol{u}}{\partial \boldsymbol{X}}\right) \tag{2.9}$$

Eq. (2.9) shows the quadratic form of the Green-Lagrange strain tensor in terms of the displacement field $\boldsymbol{u}$. When the displacement is small, we can neglect the quadratic term of displacement, and thus the Green-Lagrange strain tensor becomes the infinitesimal strain tensor.

In the current configuration, a common deformation measure is the left Cauchy-Green deformation tensor $\boldsymbol{b}$, expressed as:

$$\boldsymbol{b} = \boldsymbol{F}\,\boldsymbol{F}^{\mathrm{T}}, \qquad b_{IJ} = F_{IK}\, F_{JK} \tag{2.10}$$

2.2 Stress Measures and Constitutive Relation

Stress is the force per unit area. In finite deformation problems, it is essential to clarify the configuration for which a stress is measured. Indeed, depending on the area under consideration, the definition of stress varies. In the current configuration, let us consider

a force $\Delta \boldsymbol{f}$ acting on a differential area $\Delta \boldsymbol{a} = \boldsymbol{n}\,\Delta a$, where $\boldsymbol{n}$ is the unit normal vector at a material point. The traction vector $\boldsymbol{t}$ acting on this point is defined as:

$$\boldsymbol{t} = \lim_{\Delta a \to 0} \frac{\Delta \boldsymbol{f}}{\Delta a} = \boldsymbol{\sigma n} \tag{2.11}$$

where $\boldsymbol{\sigma}$ is known as the Cauchy stress tensor with a dimension of 3×3. The Cauchy stress tensor refers to the current deformed geometry as a reference for both the force and the area of interest. Thus, it is often referred to as the true stress. Another common stress measure defined in the current configuration, which can also be used in the formulation in the reference configuration, is the Kirchhoff stress $\boldsymbol{\tau}$:

$$\boldsymbol{\tau} = J\boldsymbol{\sigma} \qquad \longrightarrow \int_{\omega} \boldsymbol{\sigma}\, d\omega = \int_{\Omega} \boldsymbol{\sigma}\, J\, d\Omega = \int_{\Omega} \boldsymbol{\tau}\, d\Omega \tag{2.12}$$

A different traction vector, denoting as $\boldsymbol{T}$, can be defined by considering the same force $\Delta \boldsymbol{f}$, but with the differential area in the reference configuration $\Delta \boldsymbol{A} = \boldsymbol{N}\,\Delta A$ ($\boldsymbol{N}$ is the unit normal vector):

$$\boldsymbol{T} = \lim_{\Delta a \to 0} \frac{\Delta \boldsymbol{f}}{\Delta a} = \boldsymbol{P}^{\mathrm{T}} \boldsymbol{N} \tag{2.13}$$

where $\boldsymbol{P}$ is known as the first Piola-Kirchhoff stress tensor (PK1) with a dimension of 3×3. As the force and the differential area are not defined in the same configuration, the PK1 is a two-point tensor. Here, it is worth noting from the two measures of traction that:

$$d\boldsymbol{f} = \boldsymbol{t}\, da = \boldsymbol{T}\, dA \tag{2.14}$$

Substituting Eq. (2.13) and Eq. (2.11) into the above relation, and using Eq. (2.6), we can derive the relation between the Cauchy stress tensor and the PK1 tensor as follows:

$$\boldsymbol{P} = J\boldsymbol{F}^{-1}\boldsymbol{\sigma} = \boldsymbol{F}^{-1}\boldsymbol{\tau} \tag{2.15}$$

Unlike the Cauchy and Kirchhoff stress tensors, the PK1 tensor is not symmetric. By post-multiplying $\boldsymbol{P}$ with the transpose of the inverse of the deformation gradient, a symmetric tensor can be defined. This pseudo stress tensor is known as the second Piola-Kirchhoff (PK2) stress tensor, denoted by $\mathbf{S}$. Thus, from the definition:

$$\mathbf{S} = \boldsymbol{P}\boldsymbol{F}^{-T} = J\boldsymbol{F}^{-1}\boldsymbol{\sigma}\boldsymbol{F}^{-T} = \boldsymbol{F}^{-1}\boldsymbol{\tau}\boldsymbol{F}^{-T} \tag{2.16}$$

Constitutive relation With the measures of both strains and stresses presented previously, constitutive relations or material models, which provide the relation between

the kinematics and the material response, are presented here. First, let us assume the existence of a so-called strain energy density function or elastic potential ψ. Considering a strain energy density expressed in terms of the right Cauchy-Green deformation tensor $\mathbf{C}$ or the Green-Lagrange deformation tensor $\boldsymbol{E}$, the second Piola-Kirchhoff stress is computed as follows:

$$\mathbf{S} = 2\frac{\partial \psi}{\partial \mathbf{C}} = \frac{\partial \psi}{\partial \boldsymbol{E}} \tag{2.17}$$

Through a standard transformation, we can also obtain the Kirchhoff stress as [170]:

$$\boldsymbol{\tau} = \boldsymbol{F}\,\mathbf{S}\,\boldsymbol{F}^{\mathrm{T}} = 2\frac{\partial \psi}{\partial \boldsymbol{b}}\,\boldsymbol{b} \tag{2.18}$$

2.3 Strong Form of Governing Equations

Equilibrium equations The local equilibrium equation (balance of linear momentum) in the current configuration is obtained as a force balance on a small differential volume of deformed solid and is given by:

$$\operatorname{div}\boldsymbol{\sigma} + \rho\,\boldsymbol{b} = \rho\,\ddot{\boldsymbol{u}} \tag{2.19}$$

where ρ is the mass density in the current configuration, $\boldsymbol{b}$ is the body force per unit mass, and $div(\cdot)$ is the material divergence operator. The mass density in the current configuration may be related to the reference configuration mass density, ρ_0, using the balance of mass principle and yields:

$$\rho_0 = J\,\rho \tag{2.20}$$

The local equilibrium equation may also be written in the reference configuration using relations between stress measures and the chain rule of differentiation as follows:

$$\operatorname{Div}\boldsymbol{P} + \rho_0\,\boldsymbol{b} = \rho_0\,\ddot{\boldsymbol{u}} \tag{2.21}$$

where $Div(\cdot)$ is the spatial divergence operator.

The local moment equilibrium (balance of angular momentum) gives the symmetry requirement for the Cauchy and PK2 stresses:

$$\boldsymbol{\sigma}^{\mathrm{T}} = \boldsymbol{\sigma}, \quad \boldsymbol{S}^{\mathrm{T}} = \boldsymbol{S} \tag{2.22}$$

Boundary conditions and initial conditions We may categorize the basic boundary conditions into two types: displacement boundary conditions and traction boundary conditions. For the definition of boundary conditions, the boundary of the body Γ is decomposed into two sets: Γ_N represents the Neumann boundary, where the traction $\boldsymbol{T}$ is given, and Γ_D denotes the Dirichlet boundary, where displacement $\mathbf{q}$ is prescribed:

$$\Gamma = \Gamma_D \cup \Gamma_N, \qquad \Gamma_D \cap \Gamma_N = \varnothing \tag{2.23}$$

The two basic boundary conditions can be summarized as follows:

$$\begin{aligned} \boldsymbol{u} &= \hat{\mathbf{u}}(t) && \text{on } \Gamma_D \times [0,T] \\ \boldsymbol{P} \cdot \boldsymbol{N} &= \boldsymbol{T}(\boldsymbol{u}, t) && \text{on } \Gamma_N \times [0,T] \end{aligned} \tag{2.24}$$

Herein, $[0,T]$ denotes the time interval of interest. Due to the time dependency of the local equilibrium in Eq. (2.19) and Eq. (2.21), which contains the second derivatives with respect to time, a suitable set of initial conditions for the displacement and velocity at time $t = 0$ is needed:

$$\begin{aligned} \boldsymbol{u}(\boldsymbol{X}, t=0) &= \boldsymbol{u}_0(\boldsymbol{X}) \quad \text{in } \Omega \\ \dot{\boldsymbol{u}}(\boldsymbol{X}, t=0) &= \dot{\boldsymbol{u}}_0(\boldsymbol{X}) \quad \text{in } \Omega \end{aligned} \tag{2.25}$$

2.4 Reference Configuration Formulation

To construct finite element approximations for finite deformation problems, the governing equations must be expressed in the weak form. This can be done either in the reference configuration or the current configuration. We begin with the reference configuration so that the domain remains fixed during deformation, simplifying the integration and linearization. The results can later be mapped to the current configuration.

2.4.1 Variational description.

The weak form can be derived using methods such as the Galerkin method, the Principle of Virtual Work, or the Principle of Minimum Potential Energy. We use the latter here. The total potential energy Π of the elastic body is defined as the difference between the internal strain energy Π_{int} and the external work Π_{ext}. For dynamic problems, inertial effects are included via the d'Alembert principle [170], modeling inertia as a body force

$\boldsymbol{b}^{(\text{inertia})} = -\ddot{\boldsymbol{u}}$. Thus, the potential energy functional becomes:

$$\Pi = \Pi_{\text{kin}} + \Pi_{\text{int}} - \Pi_{\text{ext}} \tag{2.26}$$

with each term defined as:

$$\begin{aligned} \Pi_{\text{kin}} &= \int_\Omega \rho_0 \, \boldsymbol{u} \cdot \ddot{\boldsymbol{u}} \, d\Omega, \quad \Pi_{\text{int}} = \int_\Omega \psi(\boldsymbol{E}(\boldsymbol{u})) \, d\Omega, \\ \Pi_{\text{ext}} &= \int_\Omega \rho_0 \, \boldsymbol{u} \cdot \boldsymbol{b} \, d\Omega + \int_{\Gamma_N} \boldsymbol{u} \cdot \boldsymbol{T} \, d\Gamma \end{aligned} \tag{2.27}$$

Using the Principle of Minimum Potential Energy, we seek a displacement field $\boldsymbol{u}(\boldsymbol{X}, t)$ that minimizes the Potential Energy $\Pi(\boldsymbol{u})$. The first variation of the potential energy functional in Eq. (2.26) yields the weak form as follows:

$$\delta\Pi = \delta\Pi_{\text{kin}} + \delta\Pi_{\text{int}} - \delta\Pi_{\text{ext}} = 0 \tag{2.28}$$

With the variations defined as:

$$\begin{aligned} \delta\Pi_{\text{kin}} &= \int_\Omega \rho_0 \, \delta\boldsymbol{u} \cdot \ddot{\boldsymbol{u}} \, d\Omega, \quad \delta\Pi_{\text{int}} = \int_\Omega \delta\boldsymbol{E} : \boldsymbol{S} \, d\Omega, \\ \delta\Pi_{\text{ext}} &= \int_\Omega \rho_0 \, \delta\boldsymbol{u} \cdot \boldsymbol{b} \, d\Omega + \int_{\Gamma_N} \delta\boldsymbol{u} \cdot \boldsymbol{T} \, d\Gamma \end{aligned} \tag{2.29}$$

The weak form in Eq. (2.28) is the same as the Principle of Virtual Work, in which $\delta\Pi_{\text{int}}$, $\delta\Pi_{\text{kin}}$, and $\delta\Pi_{\text{ext}}$ denote respectively the internal virtual work, the virtual kinetic energy and the external virtual work. In this context, the variation $\delta\boldsymbol{u}$ is considered as a virtual displacement.

At this stage, the Dirichlet boundary condition on Γ_D has not yet been enforced in the continuous weak form. Several enforcement strategies exist (see [170]), many of which are applied after spatial discretization (as presented later in Section 2.6). In this work, we prefer to introduce the Dirichlet condition in the continuous weak form using the Lagrange multiplier method. Indeed, the Dirichlet condition is a kinematic constraint to the minimization of the potential energy functional. Therefore, it is common to introduce in Eq. (2.26), in addition to the potential energy, the Lagrange multiplier functional as follows:

$$\Pi_{\text{cons}} = \int_{\Gamma_D} \boldsymbol{\lambda} \cdot (\boldsymbol{u} - \hat{\boldsymbol{u}}_D) \, d\Gamma = 0 \tag{2.30}$$

in which the Lagrange multipliers $\boldsymbol{\lambda}(\boldsymbol{X})$ represent the reaction traction on the Dirichlet boundary:

$$\boldsymbol{\lambda}(\boldsymbol{X}) = \boldsymbol{P} \cdot \boldsymbol{N} \quad \text{on } \Gamma_D \tag{2.31}$$

The variation of the above functional gives two terms. The first term is the Lagrange multiplier virtual work, or the virtual work due to the reaction force at the Dirichlet boundary, defined as:

$$\delta\Pi_{\text{cons}} = \int_{\Gamma_D} \delta\boldsymbol{u} \cdot \boldsymbol{\lambda}\, d\Gamma \tag{2.32}$$

This virtual work is added to the weak form in Eq. (2.28) as follows:

$$\delta\Pi = \delta\Pi_{\text{kin}} + \delta\Pi_{\text{int}} - \delta\Pi_{\text{ext}} - \delta\Pi_{\text{cons}} = 0 \tag{2.33}$$

The second term gives the weak form of the Dirichlet condition, given as:

$$\int_{\Gamma_D} \delta\boldsymbol{\lambda} \cdot \left(\boldsymbol{u} - \hat{\boldsymbol{u}}_D\right) d\Gamma = 0 \tag{2.34}$$

After obtaining the continuous weak form in Eq. (2.33), it is interesting to see how the weak form relates to the strong form presented in Section 2.3. To do that, we first write the increment of the Green-Lagrange strain from its definition in Eq. (2.8) using the deformation gradient tensor in Eq. (2.3) as follows:

$$\delta\boldsymbol{E} = \frac{1}{2}\left(\boldsymbol{F}^{\mathrm{T}}\frac{\partial\delta\boldsymbol{u}}{\partial\boldsymbol{X}} + \frac{\partial\delta\boldsymbol{u}}{\partial\boldsymbol{X}}^{\mathrm{T}}\boldsymbol{F}\right) \tag{2.35}$$

Substituting Eq. (2.35) into the virtual internal work in Eq. (2.29), and using the relation in Eq. (2.16), we obtain:

$$\begin{aligned}\delta\Pi_{\text{int}} &= \int_\Omega \frac{1}{2}\left(F_{KI}\frac{\partial\delta u_K}{\partial X_J} + \frac{\partial\delta u_K}{\partial X_J}F_{KJ}\right) S_{IJ}\, d\Omega = \int_\Omega \frac{\partial\delta u_K}{\partial X_J} S_{IJ} F_{KJ}\, d\Omega \\ &= \int_\Omega \frac{\partial\delta u_K}{\partial X_J}\, P_{IK}\, d\Omega\end{aligned} \tag{2.36}$$

Integrating by parts and applying the *Divergence Theorem*, the virtual internal work becomes:

$$\begin{aligned}\delta\Pi_{\text{int}} &= \int_\Omega \frac{\partial}{\partial X_I}\left(\delta u_K\, P_{IK}\right) d\Omega - \int_\Omega \delta u_K \frac{\partial P_{IK}}{\partial X_I}\, d\Omega \\ &= \int_\Omega \text{Div}\left(\boldsymbol{P}\cdot\delta\boldsymbol{u}\right) d\Omega - \int_\Omega \delta\boldsymbol{u}\cdot\text{Div}\boldsymbol{P}\, d\Omega \\ &= \int_{\Gamma_D\cup\Gamma_N} \delta\boldsymbol{u}\cdot\boldsymbol{P}\,\boldsymbol{N}\, d\Gamma - \int_\Omega \delta\boldsymbol{u}\cdot\text{Div}\boldsymbol{P}\, d\Omega\end{aligned} \tag{2.37}$$

Thus, the weak form in Eq. (2.33) can be rewritten as follows:

$$\begin{aligned}\delta\Pi = &\int_\Omega \delta\boldsymbol{u}\cdot(-\mathrm{Div}(\boldsymbol{P})+\rho_0(\ddot{\boldsymbol{u}}-\boldsymbol{b}))\,d\Omega \;\; ... \\ &+\int_{\Gamma_N}\delta\boldsymbol{u}\cdot(\boldsymbol{P}\boldsymbol{N}-\boldsymbol{T})\,d\Gamma+\int_{\Gamma_D}\delta\boldsymbol{u}\cdot(\boldsymbol{P}\boldsymbol{N}-\boldsymbol{\lambda})\,d\Gamma=0\end{aligned} \tag{2.38}$$

As the above equation must be satisfied for any $\delta\boldsymbol{u}$, we can recover the strong form of balance of linear momentum and Neumann boundary condition in the reference configuration as presented in Section 2.3.

2.4.2 Tangent stiffness

The weak form in Eq. (2.33) is a nonlinear equation with respect to the displacement field $\boldsymbol{u}(\boldsymbol{X},t)$. To solve this nonlinear problem, the Newton–Raphson method is commonly employed, where tangent operators naturally arise. While this iterative procedure can be applied directly to the discrete weak form (as presented in Section 2.6), it is instructive to derive it at the variational (continuous) level. This approach not only reveals how the tangent operators emerge in continuous formulation but also facilitates their subsequent formulation in the current configuration.

Linearization. Linearization is a standard process in the Newton-Raphson procedure. For simplicity, we consider the static problem by neglecting the virtual kinetic energy. The weak form in Eq. (2.33) is now expressed in only the displacement field $\boldsymbol{u}$ and the Lagrange multipliers $\boldsymbol{\lambda}$ as variables, and the nonlinearity arises only in the internal virtual work:

$$\delta\Pi(\boldsymbol{u},\boldsymbol{\lambda})=\delta\Pi_{\mathrm{int}}(\boldsymbol{u})-\delta\Pi_{\mathrm{ext}}(\boldsymbol{u})-\delta\Pi_{\mathrm{cons}}(\boldsymbol{\lambda})=0 \tag{2.39}$$

Let us denote $\mathrm{d}(\cdot)$ the Newton increment (not a differential) of $(\cdot)$. The linearization of the above equation at the $(k+1)^{th}$ iteration writes:

$$\begin{aligned}\delta\Pi(\boldsymbol{u}^{k+1},\boldsymbol{\lambda}^{k+1}) &\approx \delta\Pi(\boldsymbol{u}^{k},\boldsymbol{\lambda}^{k})+\mathrm{d}\delta\Pi=0\\ \boldsymbol{u}^{k+1}&=\boldsymbol{u}^{k}+\mathrm{d}\boldsymbol{u}\\ \boldsymbol{\lambda}^{k+1}&=\boldsymbol{\lambda}^{k}+\mathrm{d}\boldsymbol{\lambda}\end{aligned} \tag{2.40}$$

with:

$$\begin{aligned} \mathrm{d}\delta\Pi = \frac{\partial\delta\Pi}{\partial \boldsymbol{u}}\mathrm{d}\boldsymbol{u} + \frac{\partial\delta\Pi}{\partial \boldsymbol{\lambda}}\mathrm{d}\boldsymbol{\lambda} &= \frac{\partial\delta\Pi_{\mathrm{int}}}{\partial \boldsymbol{u}}\mathrm{d}\boldsymbol{u} - \frac{\partial\delta\Pi_{\mathrm{ext}}}{\partial \boldsymbol{u}}\mathrm{d}\boldsymbol{u} - \frac{\partial\delta\Pi_{\mathrm{cons}}}{\partial \boldsymbol{\lambda}}\mathrm{d}\boldsymbol{\lambda} \\ &= \mathrm{d}\delta\Pi_{\mathrm{int}} - \mathrm{d}\delta\Pi_{\mathrm{ext}} - \mathrm{d}\delta\Pi_{\mathrm{cons}} \end{aligned} \tag{2.41}$$

This iterative process stops when the residual $\delta\Pi(\boldsymbol{u}^{k+1}, \boldsymbol{\lambda}^{k+1})$ vanishes up to numerical accuracy.

Tangent stiffness. Here, we focus only on the tangent stiffness that arises from the nonlinearity of the internal virtual work. Using Eq. (2.29), the Newton increment of the internal virtual work writes:

$$\mathrm{d}\delta\Pi_{\mathrm{int}} = \int_\Omega \delta\boldsymbol{E} : \boldsymbol{\mathcal{D}} : \mathrm{d}\boldsymbol{E}\, d\Omega + \int_\Omega \mathrm{d}\delta\boldsymbol{E} : \boldsymbol{S}\, d\Omega \tag{2.42}$$

In Eq. (2.42), the first integral gives the material tangent stiffness, in which $\boldsymbol{\mathcal{D}}$ is the material tangent modulus tensor:

$$\boldsymbol{\mathcal{D}} = \frac{\partial \boldsymbol{S}}{\partial \boldsymbol{E}} = \frac{\partial^2 \psi}{\partial \boldsymbol{E}\, \partial \boldsymbol{E}}, \quad \mathcal{D}_{IJKL} = \frac{\partial^2 \psi}{\partial E_{IJ}\, \partial E_{KL}} \tag{2.43}$$

The second integral in Eq. (2.42) gives a tangent term arising from the nonlinear form of the strain-displacement relation, and is often called the geometric stiffness. From the definition in Eq. (2.9), the increment of the Green-Lagrange strain is given as:

$$\mathrm{d}\boldsymbol{E} = \frac{1}{2}\left(\frac{\partial \mathrm{d}\boldsymbol{u}}{\partial \boldsymbol{X}} + \frac{\partial \mathrm{d}\boldsymbol{u}}{\partial \boldsymbol{X}}^{\mathrm{T}} + \frac{\partial \boldsymbol{u}}{\partial \boldsymbol{X}}^{\mathrm{T}} \cdot \frac{\partial \mathrm{d}\boldsymbol{u}}{\partial \boldsymbol{X}} + \frac{\partial \mathrm{d}\boldsymbol{u}}{\partial \boldsymbol{X}}^{\mathrm{T}} \cdot \frac{\partial \boldsymbol{u}}{\partial \boldsymbol{X}}\right) \tag{2.44}$$

From Eq. (2.35), the increment of the variation of the Green-Lagrange strain tensor writes:

$$\mathrm{d}\delta\boldsymbol{E} = \frac{1}{2}\left(\frac{\partial \mathrm{d}\boldsymbol{u}}{\partial \boldsymbol{X}}^{\mathrm{T}} \cdot \frac{\partial \delta\boldsymbol{u}}{\partial \boldsymbol{X}} + \frac{\partial \delta\boldsymbol{u}}{\partial \boldsymbol{X}}^{\mathrm{T}} \cdot \frac{\partial \mathrm{d}\boldsymbol{u}}{\partial \boldsymbol{X}}\right) \tag{2.45}$$

2.5 Current Configuration Formulation

Variational description. The transformation from the reference configuration to the current configuration is made in two steps. First, we replace terms defined in the reference configuration with ones in the current configuration. Second, we convert the integrals over the undeformed body to ones in the current configuration.

The weak form presented in Eq. (2.33) is expressed in terms of the variation of the Green-Lagrange strain, $\delta\boldsymbol{E}$, and the second Piola-Kirchhoff stress $\boldsymbol{S}$. To obtain the weak form in the current configuration, we replace these quantities with the variation of the so-called engineering strain $\delta\boldsymbol{\epsilon}$ and the Cauchy stress $\boldsymbol{\sigma}$, which are measured in the current configuration. Applying the chain rule to Eq. (2.35), the variation of the Green-Lagrange tensor writes:

$$\begin{aligned}\delta\boldsymbol{E} = \frac{1}{2}\left(\boldsymbol{F}^{\mathrm{T}}\frac{\partial\delta\boldsymbol{u}}{\partial\boldsymbol{x}}\boldsymbol{F} + \boldsymbol{F}^{\mathrm{T}}\frac{\partial\delta\boldsymbol{u}}{\partial\boldsymbol{x}}^{\mathrm{T}}\boldsymbol{F}\right) &= \frac{1}{2}\boldsymbol{F}^{\mathrm{T}}\left(\frac{\partial\delta\boldsymbol{u}}{\partial\boldsymbol{x}} + \frac{\partial\delta\boldsymbol{u}}{\partial\boldsymbol{x}}^{\mathrm{T}}\right)\boldsymbol{F} \\ &= \boldsymbol{F}^{\mathrm{T}}\,\delta\boldsymbol{\epsilon}\,\boldsymbol{F}\end{aligned} \tag{2.46}$$

Similarly, we can rewrite the increment of the Green-Lagrange strain tensor:

$$\mathrm{d}\boldsymbol{\epsilon} = \frac{1}{2}\left(\frac{\partial\mathrm{d}\boldsymbol{u}}{\partial\boldsymbol{x}} + \frac{\partial\mathrm{d}\boldsymbol{u}}{\partial\boldsymbol{x}}^{\mathrm{T}}\right) \tag{2.47}$$

as well as the increment of the variation of the Green-Lagrange strain tensor in Eq. (2.45):

$$\begin{aligned}\mathrm{d}\delta\boldsymbol{E} &= \frac{1}{2}\boldsymbol{F}^{\mathrm{T}}\left(\frac{\partial\mathrm{d}\boldsymbol{u}}{\partial\boldsymbol{x}}^{\mathrm{T}}\cdot\frac{\partial\delta\boldsymbol{u}}{\partial\boldsymbol{x}} + \frac{\partial\delta\boldsymbol{u}}{\partial\boldsymbol{x}}^{\mathrm{T}}\cdot\frac{\partial\mathrm{d}\boldsymbol{u}}{\partial\boldsymbol{x}}\right)\boldsymbol{F} \\ &= \frac{1}{2}\boldsymbol{F}^{\mathrm{T}}\,\mathrm{d}\delta\boldsymbol{\epsilon}\,\boldsymbol{F}\end{aligned} \tag{2.48}$$

as well as the variation of the strain. Using Eq. (2.46) and Eq. (2.16), we can rewrite the variation of the strain energy presented in Eq. (2.33) as follows:

$$\delta\Pi_{\mathrm{int}} = \int_\Omega \delta\boldsymbol{E} : \boldsymbol{S}\,d\Omega = \int_\Omega \delta\boldsymbol{\epsilon} : \boldsymbol{F}\,\boldsymbol{S}\,\boldsymbol{F}^{\mathrm{T}}\,d\Omega = \int_\Omega \delta\boldsymbol{\epsilon} : \boldsymbol{\tau}\,d\Omega = \int_\Omega \delta\boldsymbol{\epsilon} : J\boldsymbol{\sigma}\,d\Omega \tag{2.49}$$

The second step is now performed using the transformation of volume and area in Eq (2.6) to convert the integrals in the reference configuration to the current configuration:

$$\delta\Pi_{\mathrm{int}} = \int_\omega \delta\boldsymbol{\epsilon} : \boldsymbol{\sigma}\,d\omega \tag{2.50}$$

Similarly, we may also transform the virtual kinetic energy and external virtual work:

$$\delta\Pi_{\mathrm{kin}} = \int_\omega \rho\,\delta\boldsymbol{u}.\ddot{\boldsymbol{u}}\,d\omega\,, \qquad \delta\Pi_{\mathrm{ext}} = \int_\omega \rho\,\delta\boldsymbol{u}.\boldsymbol{b}\,d\omega + \int_{\gamma_N} \delta\boldsymbol{u}.\boldsymbol{t}\,d\gamma \tag{2.51}$$

The Lagrange multiplier virtual work is written in the current configuration in the same form as in the reference configuration, as follows:

$$\delta\Pi_{cons} = \int_{\gamma_D} \delta\boldsymbol{u} \cdot \boldsymbol{\lambda}\, d\gamma \tag{2.52}$$

where $\boldsymbol{\lambda}$ is now considered as the reaction traction on the boundary γ_D in the current configuration.

Tangent Stiffness. Using Eq. (2.46) and Eq. (2.48), the Newton increment of the internal virtual work in Eq. (2.42) may be written in the current configuration as follows:

$$\begin{aligned} \mathrm{d}\delta\Pi_{\text{int}} &= \int_\Omega \boldsymbol{F}^{\mathrm{T}}\, \delta\boldsymbol{\epsilon}\, \boldsymbol{F} : \boldsymbol{\mathcal{D}} : \boldsymbol{F}^{\mathrm{T}}\, \mathrm{d}\boldsymbol{\epsilon}\, \boldsymbol{F}\, d\Omega + \int_\Omega \boldsymbol{F}^{\mathrm{T}}\, \mathrm{d}\delta\boldsymbol{\epsilon}\, \boldsymbol{F} : \boldsymbol{S}\, d\Omega \\ &= \int_\Omega \delta\boldsymbol{\epsilon} : \boldsymbol{\mathcal{C}} : \mathrm{d}\boldsymbol{\epsilon}\, d\Omega + \int_\omega \mathrm{d}\delta\boldsymbol{\epsilon} : \boldsymbol{\sigma}\, d\omega \\ &= \int_\Omega \delta\boldsymbol{\epsilon} : \boldsymbol{\mathcal{C}} : \mathrm{d}\boldsymbol{\epsilon}\, d\Omega + \int_\Omega \mathrm{d}\delta\boldsymbol{\epsilon} : \boldsymbol{\tau}\, d\Omega \end{aligned} \tag{2.53}$$

The increase in internal virtual work in the current configuration is expressed similarly to that in the reference configuration. The first integral gives the material tangent operator, where the fourth-order tensor $\boldsymbol{\mathcal{C}}$ is the material moduli in the current configuration. The relation between the material modulus in the two configurations is given as:

$$\mathcal{C}_{IJKL} = F_{IR}\, F_{JS}\, F_{KM}\, F_{LN}\, D_{RSMN} \tag{2.54}$$

The second integral yields the tangent term arising from the nonlinear strain measure.

2.6 Displacement-based Finite Element Formulation

As discussed previously, the problem at hand involves finding the displacement field $\boldsymbol{u} = \boldsymbol{u}(\boldsymbol{X}, t)$ that satisfies the variational formulation derived from minimizing the potential energy in Eq. (2.26), and equivalently, the weak form in Eq. (2.33). In this context, the finite element method provides a practical framework for reformulating the continuous equation into a more manageable discrete form. In the following, we present the key concept of the displacement-based finite element approach for the nonlinear problems in solid mechanics.

Domain Partitioning. The approximation starts by dividing the domain Ω into a collection of n^e non-overlapping subregions, or elements Ω^e, such that:

$$\Omega \approx \bigcup_{e}^{n^e} \Omega^e \tag{2.55}$$

Thus, any boundary $\Gamma \in \Omega$ is also divided into parts within elements Γ^e:

$$\Gamma \approx \bigcup_{e}^{n^e} (\Gamma \cap \Omega^e) \tag{2.56}$$

The same concept is also applied to the current configuration. This partitioning allows the integrals in the weak form to be computed as sums over each element:

$$\begin{aligned} \delta\Pi &= \int_\Omega (\cdot)\, d\Omega + \int_\Gamma (\cdot)\, d\Gamma = \sum_{e=1}^{n^e} \left[\int_{\Omega^e} (\cdot)\, d\Omega + \int_{\Gamma \cap \Omega^e} (\cdot)\, d\Gamma \right] \\ &= \int_\omega (\cdot)\, d\Omega + \int_\gamma (\cdot)\, d\Gamma = \sum_{e=1}^{n^e} \left[\int_{\omega^e} (\cdot)\, d\Omega + \int_{\gamma \cap \omega^e} (\cdot)\, d\gamma \right] \\ &= \sum_{e=1}^{n^e} \delta\Pi^e = 0 \end{aligned} \tag{2.57}$$

Approximation of the Field Variables. Within each element, the displacement field is approximated using a finite set of shape functions $N^{(k)}(\boldsymbol{X})$. Considering solid elements, the approximation writes:

$$\boldsymbol{u}(\boldsymbol{X}, t) \approx \boldsymbol{u}^h(\boldsymbol{X}, t) = \sum_{k=1}^{n^e} N^{(k)}(\boldsymbol{X})\, \mathbf{q}^{(k)}(t) \tag{2.58}$$

Where the notation $(\cdot)^h$ denotes the approximated field, $\mathbf{q}^{(k)}(t)$ are the nodal displacement values that evolve in time, and n^e is the number of nodes belonging to the eth element. This effectively reduces the original problem, defined over a continuum, to a formulation involving a finite number of unknowns at nodes. In finite element implementation, it is common to approximate the solution in the isoparametric setting, which gives the same shape functions used to represent the geometry:

$$\boldsymbol{X}^h(\boldsymbol{\xi}) = \sum_{k=1}^{n^e} N^{(k)}(\boldsymbol{\xi})\, \mathbf{X}^{(k)}, \qquad \boldsymbol{u}^h(\boldsymbol{\xi}, t) = \sum_{k=1}^{n^e} N^{(k)}(\boldsymbol{\xi})\, \mathbf{q}^{(k)}(t) \tag{2.59}$$

where $\boldsymbol{\xi}$ are the coordinates in the parametric element, and $\mathbf{X}^{(k)}$ are the nodal positions. The approximations apply not only to displacement, but also to velocities and accelerations, which are all interpolated using the same basis. It is worth noting that within an element, the shape function associated with a node equals 1.0 at that node and vanishes at all other nodes. This property ensures that the displacement field is continuous across element boundaries.

Concerning the spatial discretization of the Lagrange multipliers for the Dirichlet condition, it is common to employ the approximation used for the displacement for one of the Lagrange multipliers. Thus, the approximation of the field writes:

$$\boldsymbol{\lambda}^h(\boldsymbol{\xi}) = \sum_k N^{(k)}(\boldsymbol{\xi})\, \boldsymbol{\lambda}^{(k)} \tag{2.60}$$

Element-Level Weak Form. Using the above approximations, let us introduce the element-level discrete contributions to the weak form as follows:

$$\delta\Pi^e = \delta\mathbf{q}^{e\mathrm{T}}\Big(\mathbf{M}^e\,\ddot{\mathbf{q}}^e + \mathbf{f}^e_{\mathrm{int}} - \mathbf{f}^e_{\mathrm{ext}} - \mathbf{f}^e_{\mathrm{cons}}\Big) \tag{2.61}$$

where $\delta\mathbf{q}^e$ and $\ddot{\mathbf{q}}^e$ are the elementary vectors of nodal virtual displacements and nodal acceleration, and $\mathbf{M}^e$, $\mathbf{f}^e_{\mathrm{int}}$, $\mathbf{f}^e_{\mathrm{ext}}$, and $\mathbf{f}^e_{\mathrm{cons}}$ represent the element mass matrix, and the vectors of internal force, external force, reaction force respectively. The construction of these matrices and vectors is detailed in Appendix A.1.

Global Assembly. As the approximated displacement field is continuous across elements, the discrete element contribution to the weak form can be arranged into a global one by using an assembly operator:

$$\begin{aligned}
\delta\Pi &\approx \int_\Omega (\cdot)^h\, d\Omega + \int_\Gamma (\cdot)^h\, d\Gamma = \bigwedge_{e=1}^{N^e} \int_{\Omega^e} (\cdot)^h\, d\Omega + \bigwedge_{e=1}^{N^e} \int_{\Omega^e \cap \Gamma} (\cdot)^h\, d\Gamma \\
&\approx \int_\omega (\cdot)^h\, d\omega + \int_\gamma (\cdot)^h\, d\gamma = \bigwedge_{e=1}^{N^e} \int_{\omega^e} (\cdot)^h\, d\omega + \bigwedge_{e=1}^{N^e} \int_{\omega^e \cap \gamma} (\cdot)^h\, d\gamma
\end{aligned} \tag{2.62}$$

Thus, we obtain the global weak form over the entire domain as follows:

$$\delta\mathbf{q}^{\mathrm{T}}\left(\mathbf{M}\ddot{\mathbf{q}} + \mathbf{f}_{\mathrm{int}} - \mathbf{f}_{\mathrm{ext}} - \mathbf{f}_{\mathrm{cons}}\right) = 0 \tag{2.63}$$

Where the global mass matrix $\mathbf{M}$, and force vectors $\mathbf{f}_{\mathrm{int}}$, $\mathbf{f}_{\mathrm{ext}}$, and $\mathbf{f}_{\mathrm{cons}}$ are assembled from their element-level counterparts using the assembly operator. The global reaction force

vector is expressed explicitly in terms of the Lagrange multipliers as:

$$\mathbf{f}_{\text{cons}} = \mathbf{L}^{\mathrm{T}}\,\boldsymbol{\Lambda} \tag{2.64}$$

And the kinematic constraint of the Dirichlet condition writes:

$$\delta\boldsymbol{\Lambda}\Big(\mathbf{L}\,\mathbf{q} - \mathbf{B}(\hat{\boldsymbol{u}}_D)\Big) = 0 \tag{2.65}$$

Where $\boldsymbol{\Lambda}$ is the global vector of nodal Lagrange multipliers, and the matrix $\mathbf{L}$ and vector $\mathbf{B}(\hat{\boldsymbol{u}}_D)$ are detailed in Appendix A.1. Here, we consider only the linear Dirichlet conditions. Moreover, for most of the classical Dirichlet conditions, such as fixed conditions or displacement-imposing, the Dirichlet boundary is often properly discretized by the boundaries of elements. In this case, the *Dirac delta function* can be used to approximate the Lagrange multipliers instead of the element's shape function as done in Eq. (2.60). Thus, the matrix $\mathbf{L}$ become a Boolean matrix, so that:

$$\delta\Pi_{\text{cons}} = \delta\mathbf{q}^{\mathrm{T}}\,\mathbf{L}^{\mathrm{T}}\,\boldsymbol{\Lambda} = \sum_k \delta\mathbf{q}^{(k)\mathrm{T}}\,\boldsymbol{\Lambda}^{(k)} \tag{2.66}$$

and:

$$\delta\boldsymbol{\Lambda}^{\mathrm{T}}\,\Big(\mathbf{L}\mathbf{q} - \mathbf{B}\Big) = \sum_k \delta\boldsymbol{\Lambda}^{(k)\mathrm{T}}\Big(\mathbf{q}^{(k)} - \hat{\boldsymbol{u}}_D(\mathbf{X}^{(k)})\Big) \tag{2.67}$$

where k is the index for the nodes on the Dirichlet boundary.

Since Eq. (2.63) and Eq. (2.65) must hold for any values of $\delta\mathbf{q}$ and $\delta\boldsymbol{\Lambda}$, we may rewrite these equations as follows:

$$\begin{cases} \mathbf{M}\ddot{\mathbf{q}} + \mathbf{f}_{\text{int}} - \mathbf{f}_{\text{ext}} - \mathbf{L}^{\mathrm{T}}\,\boldsymbol{\Lambda} = \mathbf{0} \\ \mathbf{L}\,\mathbf{q} - \mathbf{B}(\hat{\boldsymbol{u}}_D) = \mathbf{0} \end{cases} \tag{2.68}$$

The above system is known as the semi-discrete governing equations of the classical dynamic problem, consisting of the equation of motion and the kinematic constraints. For the sake of completeness, we introduce the well-known and widely used Rayleigh viscous damping model into Eq. (2.68) as:

$$\mathbf{M}\ddot{\mathbf{q}} + \mathbf{C}\dot{\mathbf{q}} + \mathbf{f}_{\text{int}} - \mathbf{f}_{\text{ext}} - \mathbf{L}^{\mathrm{T}}\,\boldsymbol{\Lambda} = \mathbf{0} \tag{2.69}$$

where $\dot{\mathbf{q}}$ is the global vector of nodal velocities, and $\mathbf{C}$ denotes the global Rayleigh damping matrix, which is defined as:

$$\mathbf{C} = \alpha_R \mathbf{M} + \beta_R \mathbf{K}_0 \tag{2.70}$$

$\mathbf{K}_0$ is the initial global tangent stiffness matrix (presented in the following), α_R and β_R are the user-defined parameters. More details of these parameters can be found in [2].

Tangent operators. Using the same build-from-element process, the discrete form of the Newton increment of the internal virtual work in Eq. (2.42) writes:

$$\mathrm{d}\delta\Pi_{\text{int}} = \delta\mathbf{q}^{\mathrm{T}} \frac{\partial \mathbf{f}_{\text{int}}}{\partial \mathbf{q}} \,\mathrm{d}\mathbf{q} = \delta\mathbf{q}^{\mathrm{T}} \left(\mathbf{K}_M + \mathbf{K}_S\right) \mathrm{d}\mathbf{q} = \delta\mathbf{q}^{\mathrm{T}} \mathbf{K}_T \,\mathrm{d}\mathbf{q} \tag{2.71}$$

The form of the above equation is the same as the continuous version in Eq. (2.42): $\mathbf{K}_M$ represents the global material tangent stiffness matrix, $\mathbf{K}_S$ represents the geometric stiffness matrix that is related to the nonlinear strain-displacement relation, and $\mathbf{K}_T$ is called the global tangent stiffness matrix. Similarly, the linearized virtual work of the external force writes:

$$\mathrm{d}\delta\Pi_{\text{ext}} = \delta\mathbf{q}^{\mathrm{T}} \frac{\partial \mathbf{f}_{\text{ext}}}{\partial \mathbf{q}} \,\mathrm{d}\mathbf{q} = \delta\mathbf{q}^{\mathrm{T}} \mathbf{K}_L \,\mathrm{d}\mathbf{q} \tag{2.72}$$

where $\mathbf{K}_L$ is the loading tangent matrix.

Now, considering the nonlinear static problem, the equilibrium equation can be deduced from Eq. (2.68) as follows:

$$\begin{cases} \mathbf{R}_m = \mathbf{f}_{\text{int}} - \mathbf{f}_{\text{ext}} - \mathbf{L}^{\mathrm{T}} \boldsymbol{\Lambda} = \mathbf{0} \\ \mathbf{R}_c = \mathbf{L}\,\mathbf{q} - \mathbf{B}_D = \mathbf{0}; \end{cases} \tag{2.73}$$

where $\mathbf{R}_m$ and $\mathbf{R}_c$ are respectively the residual of the equilibrium equation and the one of the Dirichlet condition. The linearization of the above system, which is equivalent to the discrete form in Eq. (2.40), writes:

$$\begin{bmatrix} \mathbf{R}_m^k \\ \mathbf{R}_c^k \end{bmatrix} + \begin{bmatrix} \mathbf{K}_T - \mathbf{K}_L & \mathbf{L}^{\mathrm{T}} \\ \mathbf{L} & \mathbf{0} \end{bmatrix} \begin{bmatrix} \mathrm{d}\mathbf{q} \\ \mathrm{d}\boldsymbol{\Lambda} \end{bmatrix} = \begin{bmatrix} \mathbf{R}_m^k \\ \mathbf{R}_c^k \end{bmatrix} + \mathbf{A}_T \begin{bmatrix} \mathrm{d}\mathbf{q} \\ \mathrm{d}\boldsymbol{\Lambda} \end{bmatrix} = \begin{bmatrix} \mathbf{0} \\ \mathbf{0} \end{bmatrix} \tag{2.74}$$

where $\mathbf{A}_T$ is called the global tangent operator. Details on the construction of the matrices are presented in Appendix A.1.

The displacement-based finite element framework established here forms the foundation for the 7-parameter shell formulation presented in Chapter 3. The element-level construction of the shell elements, together with the mortar-based coupling strategy, remains fully compatible with the same global solution procedures and supplies the operators required by the dynamic solvers introduced in Chapter 4.

Chapter 3

7-parameter Shell Formulation

This chapter focuses on the 7-parameter shell formulation in the context of finite strain. Building on the theory of finite strain presented in Chapter 2, we begin by revisiting the fundamental concepts of shell geometry and kinematics. We then address the issue of Poisson thickness locking, a common locking phenomenon in low-order solid-like shell formulations.

To overcome this problem, we introduce the *enhanced variational formulation* proposed by Büchter et al. [48, 46], which incorporates an additional field known as the *Enhanced Assumed Strain (EAS)*. The finite element formulation is subsequently discussed, with particular emphasis on its implementation at the element level. An advantage of this approach is that the EAS field can be *eliminated locally at the element level*, thereby avoiding any increase in the size of the global system. This makes the formulation particularly efficient and well-suited for use with a global *Newton–Raphson solver*. In addition, we highlight the formulation's capability for *explicit through-thickness integration*, which offers further flexibility and computational benefits.

Next, we present the formulation of non-conservative pressure load on the shell surface. An isotropy multiplicative elasto-plastic framework is adapted to the shell formulation to extend our investigation to material nonlinearity. The chapter concludes with a discussion on *coupling strategies* between shell components. Two distinct methods are presented: the *pre-processing of shell directors* and the *standard mortar method*. These two coupling approaches have been published in Chau et al. [52], devoted to quasi-static computations, comparing Newton–Riks and Asymptotic Numerical Methods.

3.1 Shell's Geometry and Kinematics

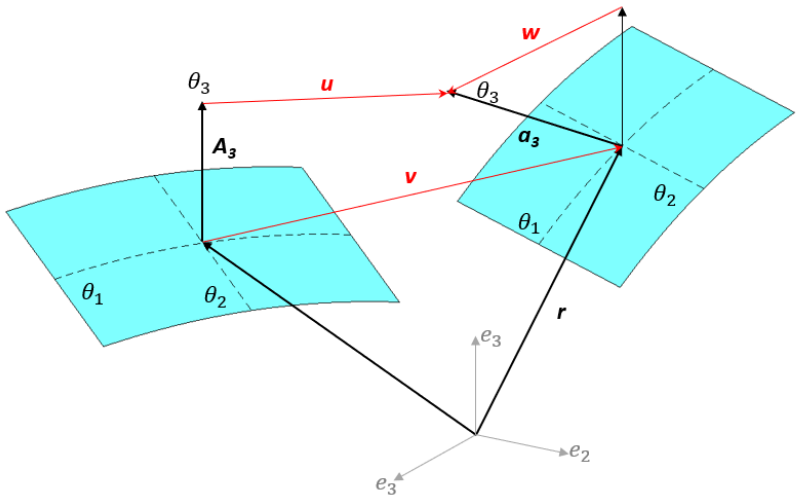

Figure 3.1 Shell geometry and kinematics

Shell geometry Let us consider a shell element in the reference configuration, as illustrated in Figure 3.1. The shell geometry is defined with respect to its mid-plane, which serves as the geometric and kinematic reference. This mid-surface is parameterized by curvilinear coordinates (θ^1, θ^2), and a point on it is described by the position vector:

$$\boldsymbol{R}(\theta^1, \theta^2) = R_I(\theta^1, \theta^2)\, e_I \tag{3.1}$$

where e_I is the basis vector in Cartesian coordinates. It is noted that the indices written in uppercase refer to the Cartesian coordinates, whereas the indices in lowercase in the following refer to curvilinear coordinates of the shell's element.

On the mid-plane, we prescribed a shell unit director field $\boldsymbol{d}(\theta^1, \theta^2)$ which represents the local thickness direction of the shell. This unit director is typically taken to be orthogonal to the mid-surface. The shell continuum is then constructed by extending a thickness $h(\theta^1, \theta^2)$ symmetrically along the shell director, such that a generic point in the shell is located at:

$$\begin{aligned} \boldsymbol{X}\left(\theta^1, \theta^2, \theta^3\right) &= \boldsymbol{R}\left(\theta^1, \theta^2\right) + \theta^3 \frac{h(\theta^1, \theta^2)}{2} \boldsymbol{d}\left(\theta^1, \theta^2\right), \qquad \text{with } \theta^3 \in [-1, 1] \\ &= \boldsymbol{R}\left(\theta^1, \theta^2\right) + \theta^3 \boldsymbol{A}_3\left(\theta^1, \theta^2\right) \end{aligned} \tag{3.2}$$

where $\boldsymbol{A}_3\left(\theta^1,\theta^2\right)$ denotes the shell director. Now let us consider a material point $\boldsymbol{X}\left(\theta^1,\theta^2\right)$ in the shell continuum, the local covariant base vectors, denoted by $\boldsymbol{G}_i$, are given as:

$$\begin{aligned}\boldsymbol{G}_\alpha &= \frac{\partial \boldsymbol{X}}{\partial \theta^i} = \boldsymbol{R}_{,\alpha} + \theta^3 \boldsymbol{A}_{3,\alpha} = \boldsymbol{A}_\alpha + \theta^3 \boldsymbol{A}_{3,\alpha}, \quad \alpha = 1,2 \\ \boldsymbol{G}_3 &= \frac{\partial \boldsymbol{X}}{\partial \theta^3} = \boldsymbol{A}_3\end{aligned} \tag{3.3}$$

We may also determine the metric coefficient as follows:

$$\begin{aligned}G_{\alpha\beta} &= \boldsymbol{G}_\alpha \cdot \boldsymbol{G}_\beta \\ &= \boldsymbol{A}_\alpha \cdot \boldsymbol{A}_\beta + \theta^3\Big(\boldsymbol{A}_{3,\alpha}\cdot\boldsymbol{A}_\beta + \boldsymbol{A}_{3,\beta}\cdot\boldsymbol{A}_\alpha\Big) + (\theta^3)^2 \boldsymbol{A}_{3,\alpha}\cdot\boldsymbol{A}_{3,\beta}\,, \quad \alpha,\beta = 1,2 \\ G_{\alpha 3} &= \boldsymbol{G}_\alpha \cdot \boldsymbol{G}_3 = \boldsymbol{A}_\alpha \cdot \boldsymbol{A}_3 + \theta^3 \boldsymbol{A}_{3,\alpha}\cdot\boldsymbol{A}_3 \\ G_{33} &= \boldsymbol{G}_3 \cdot \boldsymbol{G}_3 = \boldsymbol{A}_3 \cdot \boldsymbol{A}_3\end{aligned} \tag{3.4}$$

which can be gathered in matrix form as follows:

$$[G_{ij}] = \begin{bmatrix} G_{11} & G_{12} & G_{13} \\ G_{21} & G_{22} & G_{23} \\ G_{31} & G_{32} & G_{33} \end{bmatrix} \tag{3.5}$$

To obtain the contravariant base vectors $\boldsymbol{G}^i$, we first need to compute the contravariant metric coefficients, which can be obtained by the inverse matrix of the covariant coefficients, $[G^{ij}] = [G_{ij}]^{-1}$. Then, the contravariant base vector $\boldsymbol{G}^i$ can be obtained from the covariant base vector $\boldsymbol{G}_i$ by using the Kronecker property $\boldsymbol{G}^i \cdot \boldsymbol{G}_j = \delta^i_j$, as follows:

$$\boldsymbol{G}^i = G^{ij}\,\boldsymbol{G}_j \tag{3.6}$$

Shell kinematics The displacement field is assumed to vary linearly in the thickness direction as:

$$\boldsymbol{u}(\theta^1,\theta^2,\theta^3,t) = \boldsymbol{v}\left(\theta^1,\theta^2,t\right) + \theta^3 \boldsymbol{w}\left(\theta^1,\theta^2,t\right) \tag{3.7}$$

Where $\boldsymbol{v}$ provides the displacement of the mid-plane surface and $\boldsymbol{w}$ provides the change of the shell director between the reference and current configurations. Thus, as illustrated in Figure 3.1, the position vector $\boldsymbol{x}$ in the current configuration writes:

$$\boldsymbol{x} = \boldsymbol{X} + \boldsymbol{u} = (\boldsymbol{R} + \boldsymbol{v}) + \theta^3\,(\boldsymbol{A}_3 + \boldsymbol{w}) = \boldsymbol{r} + \theta^3\,\boldsymbol{a}_3 \tag{3.8}$$

This expression mirrors the reference configuration formulation in Eq. (3.2), showing that the shell's geometric and differential structure is preserved. Consequently, the base vectors and metric coefficients defined in Eq. (3.3) to Eq. (3.6) apply analogously in the current configuration.

Using the base vectors presented above, let us write the deformation gradient from its definition in Eq. (2.3):

$$\boldsymbol{F} = \frac{\partial \boldsymbol{x}}{\partial \boldsymbol{X}} = \frac{\partial \boldsymbol{x}}{\partial \boldsymbol{\theta}} \cdot \frac{\partial \boldsymbol{\theta}}{\partial \boldsymbol{X}} = \boldsymbol{g}_i \otimes \boldsymbol{G}^i = \left(\boldsymbol{G}_i + \frac{\partial \boldsymbol{u}}{\partial \theta^i}\right) \otimes \boldsymbol{G}^i = \boldsymbol{I} + \frac{\partial \boldsymbol{u}}{\partial \theta^i} \otimes \boldsymbol{G}^i \tag{3.9}$$

The strain tensors in the reference configuration may then be written in curvilinear coordinates. The right Cauchy strain tensor:

$$\boldsymbol{C} = \boldsymbol{F}^{\mathrm{T}}\boldsymbol{F} = g_{ij}\, \boldsymbol{G}^i \otimes \boldsymbol{G}^j = C_{ij}\, \boldsymbol{G}^i \otimes \boldsymbol{G}^j \tag{3.10}$$

From Eq. (2.8), the Green-Lagrange strain tensor may be expressed in terms of displacement as:

$$\begin{aligned}
\boldsymbol{E} &= \frac{1}{2}\Big(\boldsymbol{g}_{ij} - \boldsymbol{G}_{ij}\Big)\boldsymbol{G}^i \otimes \boldsymbol{G}^j \\
&= \frac{1}{2}\left[\left(\boldsymbol{G}_i + \frac{\partial \boldsymbol{u}}{\partial \theta^i}\right).\left(\boldsymbol{G}_j + \frac{\partial \boldsymbol{u}}{\partial \theta^j}\right) - \boldsymbol{G}_{ij}\right]\boldsymbol{G}^i \otimes \boldsymbol{G}^j \\
&= \frac{1}{2}\left(\frac{\partial \boldsymbol{u}}{\partial \theta^i} \cdot \boldsymbol{G}_j + \frac{\partial \boldsymbol{u}}{\partial \theta^j} \cdot \boldsymbol{G}_i + \frac{\partial \boldsymbol{u}}{\partial \theta^i} \cdot \frac{\partial \boldsymbol{u}}{\partial \theta^j}\right)\boldsymbol{G}^i \otimes \boldsymbol{G}^j \\
&= E_{ij}\, \boldsymbol{G}^i \otimes \boldsymbol{G}^j
\end{aligned} \tag{3.11}$$

Also, by substituting Eq. (3.3) and Eq. (3.7) into the above equation, the component of the Green-Lagrange strain can be expressed in terms of quantities defined on the mid-plane of the shell (α and β subscripts equal to 1 or 2):

$$\begin{aligned}
E_{\alpha\beta} &= \frac{1}{2}\Big[(\boldsymbol{v}_{,\alpha} + \theta^3 \boldsymbol{w}_{,\alpha}) \cdot (\boldsymbol{A}_\beta + \theta^3 \boldsymbol{A}_{3,\beta}) + (\boldsymbol{v}_{,\beta} + \theta^3 \boldsymbol{w}_{,\beta}) \cdot (\boldsymbol{A}_\alpha + \theta^3 \boldsymbol{A}_{3,\alpha}) \quad \ldots \\
&\qquad \ldots + (\boldsymbol{v}_{,\alpha} + \theta^3 \boldsymbol{w}_{,\alpha}) \cdot (\boldsymbol{v}_{,\beta} + \theta^3 \boldsymbol{w}_{,\beta})\Big] \\
E_{\alpha 3} &= \frac{1}{2}\Big[(\boldsymbol{v}_{,\alpha} + \theta^3 \boldsymbol{w}_{,\alpha}) \cdot \boldsymbol{A}_3) + \boldsymbol{w} \cdot (\boldsymbol{A}_\alpha + \theta^3 \boldsymbol{A}_{3,\alpha}) + (\boldsymbol{v}_{,\alpha} + \theta^3 \boldsymbol{w}_{,\alpha}) \cdot \boldsymbol{w}\Big] \\
E_{33} &= \frac{1}{2}\Big[2\,\boldsymbol{w} \cdot A_3 + \boldsymbol{w} \cdot \boldsymbol{w}\Big]
\end{aligned} \tag{3.12}$$

They may be decomposed into constant, linear, and quadratic terms with respect to θ^3:

$$E_{ij} = \alpha_{ij} + \beta_{ij}\theta^3 + \gamma_{ij}\left(\theta^3\right)^2 \tag{3.13}$$

with:

$$\begin{aligned}
\alpha_{\alpha\beta} &= \frac{1}{2}\Big(\boldsymbol{A}_\alpha \cdot \boldsymbol{v}_{,\beta} + \boldsymbol{A}_\beta \cdot \boldsymbol{v}_{,\alpha} + \boldsymbol{v}_{,\alpha} \cdot \boldsymbol{v}_{,\beta}\Big) \\
\alpha_{\alpha 3} &= \frac{1}{2}\Big(\boldsymbol{A}_\alpha \cdot \boldsymbol{w} + \boldsymbol{A}_3 \cdot \boldsymbol{v}_{,\alpha} + \boldsymbol{v}_{,\alpha} \cdot \boldsymbol{w}\Big) \\
\alpha_{33} &= \frac{1}{2}\Big(2\,\boldsymbol{w} \cdot A_3 + \boldsymbol{w} \cdot \boldsymbol{w}\Big) \\
\beta_{\alpha\beta} &= \frac{1}{2}\Big(\boldsymbol{A}_\alpha \cdot \boldsymbol{w}_{,\beta} + \boldsymbol{A}_\beta \cdot \boldsymbol{w}_{,\alpha} + \boldsymbol{A}_{3,\alpha} \cdot \boldsymbol{v}_{,\beta} + \boldsymbol{A}_{3,\beta} \cdot \boldsymbol{v}_{,\alpha} + \boldsymbol{v}_{,\alpha} \cdot \boldsymbol{w}_{,\beta} + \boldsymbol{v}_{,\beta} \cdot \boldsymbol{w}_{,\alpha}\Big) \\
\beta_{\alpha 3} &= \frac{1}{2}\Big(\boldsymbol{A}_3 \cdot \boldsymbol{w}_{,\alpha} + \boldsymbol{A}_{3,\alpha} \cdot \boldsymbol{w} + \boldsymbol{w} \cdot \boldsymbol{w}_{,\alpha}\Big) \\
\beta_{33} &= 0 \\
\gamma_{\alpha\beta} &= \frac{1}{2}\Big(\boldsymbol{A}_{3,\alpha} \cdot \boldsymbol{w}_{,\beta} + \boldsymbol{A}_{3,\beta} \cdot \boldsymbol{w}_{,\alpha} + \boldsymbol{w}_{,\alpha} \cdot \boldsymbol{w}_{,\beta}\Big) \\
\gamma_{\alpha 3} &= 0 \\
\gamma_{33} &= 0
\end{aligned} \tag{3.14}$$

It is apparent from the above equation that the in-plane strain components $E_{\alpha\beta}$ and $E_{\alpha 3}$ exhibit, respectively, quadratic and linear distributions through the thickness unless additional assumptions are imposed. In contrast, due to the linear variation of the displacement field through the thickness, the strain component E_{33} remains constant along the thickness direction. The latter leads to thickness Poisson locking, which will be discussed in the following.

3.2 Poisson Thickness Locking

To illustrate the phenomenon of Poisson thickness locking, consider a linear elastic Saint-Venant-Kirchhoff material, whose strain energy density function is given by:

$$\psi(\boldsymbol{E}) = \frac{1}{2}\boldsymbol{E} : \boldsymbol{D} : \boldsymbol{E} = \frac{1}{2}E_{ij}\, D^{ijkl}\, E_{kl} \tag{3.15}$$

Here, $\boldsymbol{E}$ denotes the Green–Lagrange strain tensor and $\boldsymbol{D}$ is the fourth-order elastic tensor, defined as:

$$\begin{aligned}\boldsymbol{\mathcal{D}} &= \mathcal{D}^{ijkl}\,\boldsymbol{G}_i \otimes \boldsymbol{G}_j \otimes \boldsymbol{G}_k \otimes \boldsymbol{G}_l \\ &= \left(\lambda G^{ij}G^{kl} + \mu(G^{ik}G^{jl} + G^{il}G^{jk})\right)\boldsymbol{G}_i \otimes \boldsymbol{G}_j \otimes \boldsymbol{G}_k \otimes \boldsymbol{G}_l\end{aligned} \tag{3.16}$$

where λ and μ are the Lamé constants. In Cartesian coordinates, this simplifies to:

$$\boldsymbol{\mathcal{D}} = \lambda\,\boldsymbol{I} \otimes \boldsymbol{I} + 2\mu\,\boldsymbol{\mathcal{I}} \tag{3.17}$$

where $\boldsymbol{I}$ is the second-order identity tensor and $\boldsymbol{\mathcal{I}}$ is the fourth-order symmetric identity tensor with components $\mathcal{I}_{IJKL} = 1/2\,(\delta_{IK}\delta_{JL} + \delta_{IL}\delta_{JK})$.

The second Piola–Kirchhoff stress tensor $\boldsymbol{S}$ is obtained from the energy function as:

$$\boldsymbol{S} = \frac{\partial \psi}{\partial \boldsymbol{E}} = D^{ijkl}E_{kl}\,\boldsymbol{G}_i \otimes \boldsymbol{G}_j = S^{ij}\,\boldsymbol{G}_i \otimes \boldsymbol{G}_j \tag{3.18}$$

Hence, the normal stress component S^{33} is:

$$S^{33} = \mathcal{D}^{33\alpha\beta}E_{\alpha\beta} + \mathcal{D}^{3333}E_{33} \tag{3.19}$$

In shell structures, the transverse normal stress S^{33} is typically small and nearly constant through the thickness. Imposing $\dfrac{\partial S^{33}}{\partial \theta^3} = 0$ (i.e., constant S^{33}) yields:

$$\begin{aligned}\frac{\partial S^{33}}{\partial \theta^3} &= \mathcal{D}^{33\alpha\beta}\,\frac{\partial E_{\alpha\beta}}{\partial \theta^3} + \mathcal{D}^{3333}\,\frac{\partial E_{33}}{\partial \theta^3} = 0 \\ \Rightarrow \frac{\partial E_{33}}{\partial \theta^3} &= -\frac{D^{33\alpha\beta}}{D^{3333}}\left(\beta_{\alpha\beta} + 2\theta^3\gamma_{\alpha\beta}\right)\end{aligned} \tag{3.20}$$

The above equation shows that if E_{33} is enforced to be constant, which is, in this case, because of the displacement assumption in Eq. (3.7), the necessary coupling with in-plane strains via the Poisson effect is artificially constrained. Since the in-plane strain $\beta_{ij} + 2\theta^3\gamma_{ij}$ cannot vanish independently from θ^3, this leads to an overstiff response—an effect known as Poisson thickness locking. To avoid this issue, E_{33} must be allowed to vary at least linearly through the thickness. A technique based on the concept of Enhanced Assumed Strain to overcome Poisson thickness locking will be presented in the next section.

3.3 Enhanced Variational and Finite Element Formulations

3.3.1 Reference configuration formulation

Enhanced Assumed Strain Field. To overcome Poisson thickness locking, it is necessary to augment the theory with an additional parameter (variable). One feasible approach is to introduce a strain variable, via the concept of Enhanced Assumed Strain as proposed by Büchter and Ramm [46], Büchter et al. [48], to ensure that the E_{33} component varies linearly in the thickness direction. Let us call the new strain variable $\tilde{\beta}_{33}$, then the enhanced Green-Lagrange strain $\boldsymbol{E}^*$ writes:

$$\boldsymbol{E}^*(\boldsymbol{u}, \tilde{\boldsymbol{E}}) = \boldsymbol{E}(\boldsymbol{u}) + \tilde{\boldsymbol{E}} \qquad \text{with} \qquad \tilde{\boldsymbol{E}} = \theta^3 \tilde{\beta}_{33}(\theta_1, \theta_2)\, \boldsymbol{G}^3 \otimes \boldsymbol{G}^3 \tag{3.21}$$

To introduce this extra variable properly in the general three-dimensional problem, we introduce the three-field Hu-Washizu functional defined as:

$$\begin{aligned} \Pi(\boldsymbol{u}, \tilde{\boldsymbol{E}}, \boldsymbol{S}) &= \Pi_{\text{int}}(\boldsymbol{u}, \tilde{\boldsymbol{E}}, \boldsymbol{S}) - \Pi_{\text{ext}}(\boldsymbol{u}) \\ &= \int_\Omega \Big(\psi(\boldsymbol{E} + \tilde{\boldsymbol{E}}) - \boldsymbol{S} : \tilde{\boldsymbol{E}} \Big)\, d\Omega - \Pi_{\text{ext}}(\boldsymbol{u}) \end{aligned} \tag{3.22}$$

Herein, $\tilde{\boldsymbol{E}}$ denotes the enhanced incompatible strain field and $\boldsymbol{S}$ an independent stress field. By construction, the enhanced incompatible strain field $\tilde{\boldsymbol{E}}$ satisfy the orthogonality condition:

$$\Pi_{\text{EAS}}(\tilde{\beta}_{33}, \boldsymbol{S}) = \int_\Omega \boldsymbol{S} : \tilde{\boldsymbol{E}}\, d\Omega = \int_\Omega S^{33}\, \theta^3\, \tilde{\beta}_{33}\, d\Omega = 0 \tag{3.23}$$

Thus, the functional in Eq. (3.22) reduces to:

$$\begin{aligned} \Pi(\boldsymbol{u}, \tilde{\boldsymbol{E}}) &= \Pi_{\text{int}}(\boldsymbol{u}, \tilde{\boldsymbol{E}}) - \Pi_{\text{ext}}(\boldsymbol{u}) \\ &= \int_\Omega \psi(\boldsymbol{E} + \tilde{\boldsymbol{E}})\, d\Omega - \Pi_{\text{ext}}(\boldsymbol{u}) \end{aligned} \tag{3.24}$$

For dynamic problems, the kinetic energy functional can also be introduced in the above equation via the d'Alembert principle as done in Section 2.4.

As seen Eq. (3.24), the Green-Lagrange strain $\boldsymbol{E}$ in the stored energy function is replaced by the enhanced one $\boldsymbol{E} + \tilde{\boldsymbol{E}}$, thus the PK2 stress from Eq. (3.18) depends not

only on the compatible strain $\boldsymbol{E}$, but also on the extra variable $\tilde{\beta}_{33}$:

$$\boldsymbol{S}(\boldsymbol{E}, \tilde{\beta}_{33}) = \frac{\partial \psi(\boldsymbol{E} + \tilde{\boldsymbol{E}})}{\partial(\boldsymbol{E} + \tilde{\boldsymbol{E}})} \tag{3.25}$$

Variational Description. Before writing the variational form of the problem, let us detail the integral of the orthogonality condition in Eq. (3.23) as follows:

$$\Pi_{\text{EAS}}(\tilde{\beta}_{33}, \boldsymbol{S}) = \int_A \mu(\theta^1, \theta^2) \left[\int_{-1}^{1} S^{33}\, \theta^3 \tilde{\beta}_{33}\, d\theta^3 \right] dA = 0 \tag{3.26}$$

with:

$$\mu(\theta^1, \theta^2) = \frac{\det(\boldsymbol{J}_A)}{|\boldsymbol{A}_1 \times \boldsymbol{A}_2|}, \qquad \boldsymbol{J}_A = \begin{bmatrix} \boldsymbol{A}_1 & \boldsymbol{A}_2 & \boldsymbol{A}_3 \end{bmatrix}, \qquad \boldsymbol{A}_\alpha = \frac{\partial \boldsymbol{R}}{\partial \theta^\alpha} \tag{3.27}$$

where $\boldsymbol{J}_A$ is the Jacobian matrix evaluated at the mid-plane surface $\boldsymbol{X}(\theta^1, \theta^2, \theta^3 = 0)$, and $\boldsymbol{A}_\alpha$ are tangent vectors to the mid-surface, as defined in Section 3.1. It can be seen that the orthogonality condition holds if S^{33} is constant in θ^3. Therefore, the variational form of the orthogonality condition writes:

$$\delta\Pi_{\text{EAS}}(\delta\tilde{\beta}_{33}, \boldsymbol{S}) = \int_\Omega \delta\tilde{\boldsymbol{E}} : \boldsymbol{S}\, d\Omega = \int_\Omega \delta\tilde{\beta}_{33} \theta^3\, S^{33}\, d\Omega = 0 \tag{3.28}$$

Now, we may write the internal virtual work from its definition in Eq. (3.24), by taking into account the orthogonality condition, as follows:

$$\begin{aligned} \delta\Pi_{\text{int}}(\delta\boldsymbol{u}, \boldsymbol{u}, \tilde{\beta}_{33}) &= \int_\Omega \delta\boldsymbol{E}(\boldsymbol{u}, \delta\boldsymbol{u}) : \boldsymbol{S}(\boldsymbol{E}, \tilde{\beta}_{33})\, d\Omega \\ &= \int_\Omega \delta E_{ij}(\boldsymbol{u}, \delta\boldsymbol{u})\; S^{ij}(\boldsymbol{E}, \tilde{\beta}_{33})\, d\Omega \end{aligned} \tag{3.29}$$

The variation of the Green-Lagrange strain can be obtained from Eq. (3.11) as follows:

$$\delta E_{ij} = \frac{1}{2} \left(\frac{\partial \delta\boldsymbol{u}}{\partial \theta^i} \cdot \boldsymbol{G}_j + \frac{\partial \delta\boldsymbol{u}}{\partial \theta^j} \cdot \boldsymbol{G}_i + \frac{\partial \delta\boldsymbol{u}}{\partial \theta^i} \cdot \frac{\partial \boldsymbol{u}}{\partial \theta^j} + \frac{\partial \boldsymbol{u}}{\partial \theta^i} \cdot \frac{\partial \delta\boldsymbol{u}}{\partial \theta^j} \right) \tag{3.30}$$

It is worth noting that the orthogonality condition leads to, firstly, the constant transverse normal stress S^{33} in the thickness direction, and secondly, the non-generating-energy property of the assumed strain $\theta^3\, \tilde{\beta}_{33}$. Moreover, as Eq. (3.28) must hold for any arbitrary value of $\delta\tilde{\beta}_{33}$ at the element level, we may treat the unknown $\tilde{\beta}_{33}$ at the element level and avoid its involvement in the global finite element setting. This property is discussed in the following.

Finite Element Formulation. We focus here on the finite element formulation at the element level. Within the shell element, the material point $\boldsymbol{X}$ in the reference configuration, defined in Eqs. (3.2), is approximated as follows:

$$\boldsymbol{X} \approx \boldsymbol{X}^h = \sum_k N^{(k)}(\theta^1, \theta^2) \left(\mathbf{R}^{(k)} + \theta^3 \, \mathbf{A}_3^{(k)} \right) = \mathbf{N} \, \mathbf{X} \tag{3.31}$$

where $N^{(k)}$ is the shape function associated with the kth node and $(\cdot)^{(k)}$ is its nodal values. Similarly, the approximation of the displacement field in Eq. (3.7) is obtained:

$$\boldsymbol{u} \approx \boldsymbol{u}^h = \sum_k N^{(k)}(\theta^1, \theta^2) \left(\mathbf{v}^{(k)} + \theta^3 \, \mathbf{w}^{(k)} \right) = \mathbf{N} \, \mathbf{q}^e \tag{3.32}$$

The approximation above is also applied to the time derivatives of the displacement field.

For the field of EAS, thanks to the orthogonality condition, the variable can be handled only at the element level. Thus, the continuity of this field between elements may not be required. Therefore, a simple bilinear approximation for this field within an element is sufficient:

$$\tilde{\beta}_{33} = \alpha_1 + \theta^1 \, \alpha_2 + \theta^2 \, \alpha_3 + \theta^1 \, \theta^2 \, \alpha_4 \tag{3.33}$$

α_1, α_2, α_3, and α_4 are the extra unknown parameters that can be eliminated at the element level. The incompatible strain component can be approximated as:

$$\begin{aligned} \tilde{E}_{33} &= \theta^3 \, \tilde{\beta}_{33} \\ &= \theta^3 \begin{bmatrix} 1 & \theta^1 & \theta^2 & \theta^1 \theta^2 \end{bmatrix} \begin{bmatrix} \alpha_1 & \alpha_2 & \alpha_3 & \alpha_4 \end{bmatrix}^{\mathrm{T}} \\ &= \mathbf{B}_\alpha \, \boldsymbol{\alpha}^e \end{aligned} \tag{3.34}$$

In the following, the discrete formulations of the shell element are expressed in matrix form, which is detailed in Appendix A.2. The notation $(\cdot)^e$ is omitted for brevity. Using the finite element approximation, let us write the discrete internal virtual work of a 7-parameter shell element as follows:

$$\delta \Pi_{\text{int}} = \delta \mathbf{q}^{\mathrm{T}} \int_{\Omega^e} \bar{\mathbf{B}}^{\mathrm{T}} \, \mathbf{S}(\mathbf{q}, \boldsymbol{\alpha}) \, d\Omega = \delta \mathbf{q}^{\mathrm{T}} \, \mathbf{f}_{\text{int}} \tag{3.35}$$

where $\mathbf{f}_{\text{int}}^e$ denotes the elementary internal force vector. The discrete weak form of the orthogonality condition writes:

$$\delta \Pi_{EAS} = \delta \boldsymbol{\alpha}^{\mathrm{T}} \int_{\Omega^e} \mathbf{B}_\alpha^{\mathrm{T}} \, S^{33}(\mathbf{q}, \boldsymbol{\alpha}) \, d\Omega = 0 \tag{3.36}$$

The above equation must hold for an arbitrary $\delta\boldsymbol{\alpha}$; therefore, the semi-discrete form of the orthogonality condition at the element level becomes:

$$\mathbf{R}_\alpha = \int_{\Omega^e} \mathbf{B}_\alpha^{\mathrm{T}}\, S^{33}(\mathbf{q}, \boldsymbol{\alpha})\, d\Omega = 0 \tag{3.37}$$

Details on the finite element formulation for the 7-parameter shell element can be found in Appendix A.2.

Tangent Operators. Along the lines of Section 2.4, the Newton increment of the internal virtual work writes:

$$\mathrm{d}\delta\Pi_{\mathrm{int}} = \int_\Omega \delta E_{ij}\, \mathcal{D}^{ijkl}\, \mathrm{d}E_{kl}\, d\Omega + \int_\Omega \mathrm{d}\delta E_{ij}\, S^{ij}\, d\Omega + \int_\Omega \delta E_{ij}\, \mathcal{D}^{ij33}\, \theta^3 \mathrm{d}\tilde{\beta}_{33}\, d\Omega \tag{3.38}$$

where $\boldsymbol{\mathcal{D}}$ is the material moduli. From its definition in Eq. (2.43), it can be written in curvilinear base vectors as follows:

$$\boldsymbol{\mathcal{D}} = D^{ijkl} \boldsymbol{G}_i \otimes \boldsymbol{G}_j \otimes \boldsymbol{G}_k \otimes \boldsymbol{G}_l\,, \qquad D^{ijkl} = \frac{\partial S^{ij}}{\partial E_{kl}} \tag{3.39}$$

The increment quantities are given in terms of displacement $\boldsymbol{u}$ as follows:

$$\begin{aligned} \mathrm{d}E_{ij} &= \frac{1}{2}\left(\frac{\partial \mathrm{d}\boldsymbol{u}}{\partial\theta^i}\cdot\boldsymbol{G}_j + \frac{\partial \mathrm{d}\boldsymbol{u}}{\partial\theta^j}\cdot\boldsymbol{G}_i + \frac{\partial \boldsymbol{u}}{\partial\theta^i}\cdot\frac{\partial \mathrm{d}\boldsymbol{u}}{\partial\theta^j} + \frac{\partial \mathrm{d}\boldsymbol{u}}{\partial\theta^i}\cdot\frac{\partial \boldsymbol{u}}{\partial\theta^j}\right) \\ \mathrm{d}\delta E_{ij} &= \frac{1}{2}\left(\frac{\partial \delta\boldsymbol{u}}{\partial\theta^i}\cdot\frac{\partial \mathrm{d}\boldsymbol{u}}{\partial\theta^j} + \frac{\partial \mathrm{d}\boldsymbol{u}}{\partial\theta^i}\cdot\frac{\partial \delta\boldsymbol{u}}{\partial\theta^j}\right) \end{aligned} \tag{3.40}$$

Compared to the increment of the internal virtual work in the original three-dimensional problem in Eq. (2.42), the one for the 7-parameter shell contains, in addition, the increment terms relating to the EAS field $\tilde{\beta}_{33}$, which needs to be eliminated at each iteration in the Newton-Raphson resolution process. From Eq. (3.28), the Newton increment of the orthogonality condition is given as:

$$\mathrm{d}\delta\Pi_{\mathrm{EAS}} = \int_\Omega \delta\tilde{\beta}_{33}\theta^3\, \mathcal{D}^{33kl}\, \mathrm{d}E_{kl}\, d\Omega + \int_\Omega \delta\tilde{\beta}_{33}\theta^3\, \mathcal{D}^{3333}\, \theta^3 \mathrm{d}\tilde{\beta}_{33}\, d\Omega = 0 \tag{3.41}$$

Here, let us consider the linearization setting at the $(k+1)^{th}$ iteration as presented in Section 2.4.2. Using the finite element discretization presented previously (details can be found in Appendix A.2), we can write the linearization of the element's internal virtual

work as follows:

$$\begin{aligned}\delta\Pi_{\text{int}}(\mathbf{q}^{k+1},\boldsymbol{\alpha}^{k+1}) &= \delta\Pi_{\text{int}}(\mathbf{q}^{k},\boldsymbol{\alpha}^{k}) + \mathrm{d}\delta\Pi_{\text{int}} \\ &= \delta\mathbf{q}^{\mathrm{T}}\,\mathbf{f}_{\text{int}}(\mathbf{q}^{k},\boldsymbol{\alpha}^{k}) + \delta\mathbf{q}^{\mathrm{T}}\left(\mathbf{K}_{uu}\,\mathrm{d}\mathbf{q} + \mathbf{K}_{u\alpha}\,\mathrm{d}\boldsymbol{\alpha}\right)\end{aligned} \tag{3.42}$$

Similarly, the linearization of the discrete orthogonality condition writes:

$$\begin{aligned}\delta\Pi_{\text{EAS}}(\mathbf{q}^{k+1},\boldsymbol{\alpha}^{k+1}) &= \delta\Pi_{\text{EAS}}(\mathbf{q}^{k},\boldsymbol{\alpha}^{k}) + \mathrm{d}\delta\Pi_{\text{EAS}} \\ &= \delta\boldsymbol{\alpha}^{\mathrm{T}}\,\left(\mathbf{R}_{\alpha}(\mathbf{q}^{k},\boldsymbol{\alpha}^{k}) + \mathbf{K}_{\alpha\alpha}\,\mathrm{d}\boldsymbol{\alpha} + \mathbf{K}_{u\alpha}^{\mathrm{T}}\,\mathrm{d}\mathbf{q}\right) = 0\end{aligned} \tag{3.43}$$

The above condition holds for any arbitrary $\delta\boldsymbol{\alpha}$, thus yields:

$$\mathrm{d}\boldsymbol{\alpha} = -\mathbf{K}_{\alpha\alpha}^{-1}\left(\mathbf{R}_{\alpha}^{k} + \mathbf{K}_{u\alpha}^{\mathrm{T}}\,\mathrm{d}\mathbf{q}\right) \tag{3.44}$$

Therefore, we can eliminate the terms relating to $\mathrm{d}\boldsymbol{\alpha}$ in the linearization of the element's internal virtual work as follows:

$$\delta\Pi_{\text{int}}^{e}(\mathbf{q}^{k+1},\boldsymbol{\alpha}^{k+1}) = \delta\mathbf{q}^{\mathrm{T}}\left(\mathbf{f}_{\text{int}}(\mathbf{q}^{k},\boldsymbol{\alpha}^{k}) + \mathbf{K}_{T}\,\mathrm{d}\mathbf{q} + \mathbf{f}_{\alpha}\right) \tag{3.45}$$

where:

$$\mathbf{K}_{T} = \mathbf{K}_{uu} - \mathbf{K}_{u\alpha}\,\mathbf{K}_{\alpha\alpha}^{-1}\mathbf{K}_{u\alpha}^{\mathrm{T}}\,, \qquad \mathbf{f}_{\alpha} = -\mathbf{K}_{u\alpha}\,\mathbf{K}_{\alpha\alpha}^{-1}\,\mathbf{R}_{\alpha} \tag{3.46}$$

Eq. (3.44) also permits us to update $\boldsymbol{\alpha}^{k+1}$ for the computation at the next iteration:

$$\mathbf{q}^{k+1} = \mathbf{q}^{k+1} + \mathrm{d}\mathbf{q}\,, \qquad \boldsymbol{\alpha}^{k+1} = \boldsymbol{\alpha}^{k} - \mathbf{K}_{\alpha\alpha}^{-1}\left[\mathbf{R}_{\alpha}^{k} + \mathbf{K}_{u\alpha}^{\mathrm{T}}\left(\mathbf{q}^{k+1} - \mathbf{q}^{k}\right)\right] \tag{3.47}$$

We observe that once the solution converges, the residual of orthogonality $\mathbf{R}_{\alpha}$ vanishes; thus, the vector $\mathbf{f}_{\alpha}$ also vanishes. As shown in this section, the orthogonality condition, as well as the EAS field, can be treated explicitly at the element level during the Newton-Raphson resolution process. Thus, the tangent stiffness matrix $\mathbf{K}_{T}$ as well as the internal force vector $\mathbf{f}_{\text{int}}$ of a shell element contribute to the global system in Eq. (2.73) and Eq. (2.74). The construction of all the matrices in the above equations is detailed in Appendix A.2.

3.3.2 Current configuration formulation

Variational Description. To transform the weak form of the 7-parameter shell formulation in the reference configuration, we follow the procedure presented in Section 2.5. First, we employ the deformation gradient defined in Eq. (3.9) to transform quantities from the reference configuration to the current configuration. The compatible strain variation $\delta\boldsymbol{\epsilon}$ may be obtained using Eq. (2.46) as follows:

$$\begin{aligned}\delta\boldsymbol{\epsilon} = \delta\epsilon_{ij}\,\boldsymbol{g}^i \otimes \boldsymbol{g}^j = \boldsymbol{F}^{-T}\,\boldsymbol{E}\,\boldsymbol{F}^{-1} &= \left(\boldsymbol{g}^k \otimes \boldsymbol{G}_k\right)\left(\delta E_{ij}\,\boldsymbol{G}^i \otimes \boldsymbol{G}^j\right)\left(\boldsymbol{G}_l \otimes \boldsymbol{g}^l\right) \\ &= \delta E_{ij}\,\boldsymbol{g}^i \otimes \boldsymbol{g}^j\end{aligned} \tag{3.48}$$

and the variation of the assumed strain writes:

$$\delta\tilde{\boldsymbol{\epsilon}} = \delta\tilde{\epsilon}_{33}\,\boldsymbol{g}^3 \otimes \boldsymbol{g}^3 = \delta\tilde{E}_{33}\,\boldsymbol{g}^3 \otimes \boldsymbol{g}^3 = \theta^3\tilde{\beta}_{33}\boldsymbol{g}^3 \otimes \boldsymbol{g}^3 \tag{3.49}$$

It is worth noting that the component δE_{ij} expressed in the reference configuration as in Eq. (3.30) may also be written in the current configuration as follows:

$$\delta\epsilon_{ij} = \delta E_{ij} = \frac{1}{2}\left(\frac{\partial\delta\boldsymbol{u}}{\partial\theta^i}\cdot\boldsymbol{g}_j + \frac{\partial\delta\boldsymbol{u}}{\partial\theta^j}\cdot\boldsymbol{g}_i\right) \tag{3.50}$$

Similarly, using the relation in Eq. (2.16), the Kirchhoff stress tensor expressed in curvilinear coordinates writes:

$$\begin{aligned}\boldsymbol{\tau} = \tau^{ij}\,\boldsymbol{g}_i \otimes \boldsymbol{g}_j = \boldsymbol{F}\,\boldsymbol{S}\,\boldsymbol{F}^{\mathrm{T}} &= \left(\boldsymbol{g}_k \otimes \boldsymbol{G}^k\right)\left(S^{ij}\,\boldsymbol{G}_i \otimes \boldsymbol{G}_j\right)\left(\boldsymbol{G}^l \otimes \boldsymbol{g}_l\right) \\ &= S^{ij}\,\boldsymbol{g}_i \otimes \boldsymbol{g}_j\end{aligned} \tag{3.51}$$

It can be seen from Eq.(3.48) and Eq.(3.51) that the components in curvilinear coordinates of the strain variation $\delta\boldsymbol{\epsilon}$ and the Kirchhoff stress $\boldsymbol{\tau}$ are respectively identical to the ones of the Green-Lagrange strain tensor variation $\delta\boldsymbol{E}$ and the PK2 stress $\boldsymbol{S}$.

Using Eq.(3.48) and Eq.(3.51), let us write the variational form of the strain energy in Eq. (3.29):

$$\delta\Pi_{\mathrm{int}}(\delta\boldsymbol{u}, \boldsymbol{u}, \tilde{\beta}_{33}) = \int_\Omega \delta\epsilon_{ij}(\boldsymbol{u}, \delta\boldsymbol{u})\;\tau^{ij}(\boldsymbol{E}, \tilde{\beta}_{33})\,d\Omega \tag{3.52}$$

and the variational form of the orthogonality condition in Eq. (3.28):

$$\delta\Pi_{\mathrm{EAS}}(\delta\tilde{\beta}_{33}, \boldsymbol{\tau}) = \int_\Omega \delta\tilde{\beta}_{33}\theta^3\,\tau^{33}\,d\Omega = 0 \tag{3.53}$$

Tangent Operators. Using Eq.(3.48) and Eq.(3.51), the Newton increment of the strain energy variation for the Newton-type solver in Eq.(3.38) is expressed in the current configuration as follows:

$$\mathrm{d}\delta\Pi_{\text{int}} = \int_\Omega \delta\epsilon_{ij}\, \mathcal{C}^{ijkl}\, \mathrm{d}\epsilon_{kl}\, d\Omega + \int_\Omega \mathrm{d}\delta\epsilon_{ij}\, \tau^{ij}\, d\Omega + \int_\Omega \delta\epsilon_{ij}\, \mathcal{C}^{ij33}\, \theta^3 \mathrm{d}\tilde{\beta}_{33}\, d\Omega \tag{3.54}$$

where $\boldsymbol{\mathcal{C}}$ is the material moduli in the current configuration as defined in Eq. (2.54). Here, it is expressed in curvilinear coordinates as follows:

$$\boldsymbol{\mathcal{C}} = \mathcal{C}^{ijkl} \boldsymbol{g}_i \otimes \boldsymbol{g}_j \otimes \boldsymbol{g}_k \otimes \boldsymbol{g}_l\,, \qquad \mathcal{C}^{ijkl} = \frac{\partial S^{ij}}{\partial E_{kl}} = \mathcal{D}^{ijkl} \tag{3.55}$$

The linearized weak form of the orthogonality condition writes:

$$\mathrm{d}\delta\Pi_{\text{EAS}} = \int_\Omega \delta\tilde{\beta}_{33}\theta^3\, \mathcal{C}^{33kl}\, \mathrm{d}\epsilon_{kl}\, d\Omega + \int_\Omega \delta\tilde{\beta}_{33}\theta^3\, \mathcal{C}^{3333}\, \theta^3 \mathrm{d}\tilde{\beta}_{33}\, d\Omega = 0 \tag{3.56}$$

Using the finite element discretization presented in Appendix A.2, we can obtain the same discrete equation of the internal virtual work, the orthogonality condition, as well as their linearization as in the reference formulation.

3.4 Explicit Through-thickness Integration

The variational formulation presented previously closely resembles the standard 3D continuum approach, where the numerical integration of the weak form in Eq. (3.29) or Eq. (3.52) is typically carried out over the full three-dimensional domain. However, in shell formulations, the geometry naturally distinguishes the thickness direction from the in-plane directions. This allows the integration to be separated as follows:

$$\int_\Omega (\cdot)\, d\Omega = \int_A \mu(\theta^1, \theta^2) \int_{-1}^{1} (\cdot)\, d\theta^3\, dA \tag{3.57}$$

with:

$$\mu(\theta^1, \theta^2) = \frac{\det(\boldsymbol{J}_A)}{|\boldsymbol{A}_1 \times \boldsymbol{A}_2|}, \qquad \boldsymbol{J}_A = \begin{bmatrix} \boldsymbol{A}_1 & \boldsymbol{A}_2 & \boldsymbol{A}_3 \end{bmatrix}, \qquad \boldsymbol{A}_\alpha = \frac{\partial \boldsymbol{R}}{\partial \theta^\alpha} \tag{3.58}$$

where $\boldsymbol{J}_A$ is the Jacobian matrix evaluated at the mid-surface, and $\boldsymbol{A}_\alpha$ are tangent vectors to the mid-surface, as defined in Section 3.1.

Let us express explicitly the strain energy variation in Eq. (3.29) in terms of θ^3. From Eq. (3.13), we can obtain the variation of the Green-Lagrange strain component as

follows:

$$\delta E_{ij} = \delta\alpha_{ij} + \delta\beta_{ij}\theta^3 + \delta\gamma_{ij}\left(\theta^3\right)^2 , \quad \beta_{33} = \tilde{\beta}_{33}, \quad \delta\beta_{33} = \delta\tilde{\beta}_{33} \tag{3.59}$$

By substituting the above equation into Eq. (3.29), the strain energy variation writes:

$$\delta\Pi_{\text{int}} = \int_\Omega \delta E_{ij}\, S^{ij}\, d\Omega = \int_A \left(\delta\alpha_{ij}\, n^{ij} + \delta\beta_{ij}\, m^{(1)ij} + \delta\gamma_{ij}\, m^{(2)ij}\right) dA \tag{3.60}$$

with the second Piola-Kirchhoff stress resultants:

$$n^{ij} = \mu\int_{-1}^{1} S^{ij}\, d\theta^3 , \qquad m^{(K)ij} = \mu\int_{-1}^{1} (\theta^3)^K\, S^{ij}\, d\theta^3 , \qquad K = 1, 2 \tag{3.61}$$

Now let us consider the Saint-Venant-Kirchhoff material as presented in Section 3.2:

$$S^{ij} = \mathcal{D}^{ijkl}\, E_{kl} = \mathcal{D}^{ijkl}\left[\alpha_{kl} + \beta_{kl}\theta^3 + \gamma_{kl}\left(\theta^3\right)^2\right] \tag{3.62}$$

Thus, the internal virtual work in Eq. (3.60) is expressed as follows:

$$\delta\Pi_{\text{int}} = \int_A \begin{bmatrix}\delta\alpha_{ij}, & \delta\beta_{ij}, & \delta\gamma_{ij}\end{bmatrix} \begin{bmatrix} \mathcal{D}_0^{ijkl} & \mathcal{D}_1^{ijkl} & \mathcal{D}_2^{ijkl} \\ \mathcal{D}_1^{ijkl} & \mathcal{D}_2^{ijkl} & \mathcal{D}_3^{ijkl} \\ \mathcal{D}_2^{ijkl} & \mathcal{D}_3^{ijkl} & \mathcal{D}_4^{ijkl} \end{bmatrix} \begin{bmatrix}\alpha_{kl} \\ \beta_{kl} \\ \gamma_{kl}\end{bmatrix} dA \tag{3.63}$$

where the explicit integration across the thickness is:

$$\mathcal{D}_K^{ijkl} = \mu\int_{-1}^{1} (\theta^3)^K\, \mathcal{D}^{ijkl}\, d\theta^3 , \qquad K = 1, 2, 3, 4 \tag{3.64}$$

Similarly, the variational form of the orthogonality condition in Eq. (3.28) can be expressed as follows:

$$\delta\Pi_{\text{EAS}} = \int_A \delta\tilde{\beta}_{33} \begin{bmatrix}\mathcal{D}_1^{33ij} & \mathcal{D}_2^{33ij} & \mathcal{D}_3^{33ij}\end{bmatrix} \begin{bmatrix}\alpha_{ij} \\ \beta_{ij} \\ \gamma_{ij}\end{bmatrix} dA = 0 \tag{3.65}$$

It is evident that, when the material model is linear, the material moduli $\mathcal{D}^{ijkl}$ remain unchanged during deformation. Consequently, the explicit through-thickness integration in Eq. (3.64) can be performed before entering the resolution process. For multi-layered shell problems that require numerous integration points in the thickness direction, this pre-integration feature reduces the full 3D integration over the volume to a 2D numerical integration over the mid-surface, significantly reducing computational effort.

Nevertheless, when the material model is nonlinear, this pre-integration is no longer applicable. The general formulation for nonlinear material can be found in [48, 29, 161]. One might say that the formulation with explicit through-thickness integration directly provides the stress resultants, which offer insight into shell behavior and are often used for engineering interpretations. However, if the formulation without the through-thickness is used, the stress resultants may still be obtained in post-processing. In this thesis work, we do not employ the through-thickness integration property in the implementation of the shell element.

3.5 Non-Conservative Loads - Pressure Loads

In this section, we consider the pressure load acting on the shell surface. Since the pressure is always orthogonal to the shell surface, the load is considered to depend on the shell deformation. Therefore, it is convenient to formulate the pressure load in the current configuration. Considering the pressure $\boldsymbol{t}$ is applied on the boundary γ_N, the external virtual work due to the pressure load writes:

$$\delta\Pi_{\text{ext}} = \int_{\gamma_N} \delta\boldsymbol{u} \cdot \boldsymbol{t}\, d\gamma = \int_{\gamma_N} \delta\boldsymbol{u} \cdot (p\,\boldsymbol{n})\, d\gamma \tag{3.66}$$

where $p = |\boldsymbol{t}|$ is the pressure amplitude, and $\boldsymbol{n}$ is the unit vector orthogonal to the shell surface. In the isoparametric (curvilinear) setting, we can obtain the following:

$$\boldsymbol{n}\, d\gamma = k\, \frac{\partial \boldsymbol{x}}{\partial \theta^1} \times \frac{\partial \boldsymbol{x}}{\partial \theta^2}\, d\theta^1 d\theta^2 = k\, \boldsymbol{g}_1 \times \boldsymbol{g}_2\, d\theta^1 d\theta^2 \tag{3.67}$$

where $\boldsymbol{g}_\alpha$ are the covariant vectors in the current configuration defined in Eq. (3.3), and $k = \pm 1$ is the sign coefficient depending on the construction of the mesh to correct the direction of the nodal force depending on the cases of internal or external pressure. Thus, the continuous external virtual work writes:

$$\delta\Pi_{\text{ext}} = \int_{-1}^{1}\int_{-1}^{1} k\, p\, \delta\boldsymbol{u} \cdot (\boldsymbol{g}_1 \times \boldsymbol{g}_2)\, d\theta^1 d\theta^2 \tag{3.68}$$

For the Newton solution process, the increment of the external virtual work writes:

$$\begin{aligned} \mathrm{d}\delta\Pi_{\text{ext}} &= \int_{-1}^{1}\int_{-1}^{1} k\, p\, \delta\boldsymbol{u} \cdot \left(\mathrm{d}\boldsymbol{g}_1 \times \boldsymbol{g}_2 + \boldsymbol{g}_1 \times \mathrm{d}\boldsymbol{g}_2\right) d\theta^1 d\theta^2 \\ &= \int_{-1}^{1}\int_{-1}^{1} k\, p\, \delta\boldsymbol{u} \cdot \left(-\boldsymbol{g}_2 \times \mathrm{d}\boldsymbol{g}_1 + \boldsymbol{g}_1 \times \mathrm{d}\boldsymbol{g}_2\right) d\theta^1 d\theta^2 \end{aligned} \tag{3.69}$$

Let us discretize the above equations using the finite element approximation (detail in Appendix A.2). The following expression of the covariant vectors can be obtained:

$$\mathrm{d}\boldsymbol{g}_1 = \frac{\partial \mathrm{d}\boldsymbol{x}}{\partial \theta^1} = \frac{\partial \mathrm{d}\boldsymbol{u}}{\partial \theta^1} = \mathbf{G}^{1:3}\,\mathrm{d}\mathbf{q}\,, \qquad \mathrm{d}\boldsymbol{g}_2 = \frac{\partial \mathrm{d}\boldsymbol{x}}{\partial \theta^2} = \frac{\partial \mathrm{d}\boldsymbol{u}}{\partial \theta^2} = \mathbf{G}^{4:6}\,\mathrm{d}\mathbf{q} \tag{3.70}$$

where $\mathbf{G}^{i:j}$ denotes the matrix that collects the ith to the jth row of matrix $\mathbf{G}$ presented in Appendix A.2. Furthermore, the cross product $\boldsymbol{a} \times \boldsymbol{b}$, where $\boldsymbol{a}$ and $\boldsymbol{b}$ are two given vectors, is written in the matrix form as follows:

$$\boldsymbol{a} \times \boldsymbol{b} = \begin{bmatrix} 0 & -a_3 & a_2 \\ a_3 & 0 & -a_1 \\ -a_2 & a_1 & 0 \end{bmatrix} \boldsymbol{b} = \mathbf{T}(\boldsymbol{a})\,\boldsymbol{b} \tag{3.71}$$

Thus, by omitting the assembly operator $\bigwedge_{e=1}^{N^e}$ for brevity, we can write the discrete external virtual work as:

$$\delta\Pi_{\text{ext}} = \delta\mathbf{q}^{\mathrm{T}}\,\mathbf{f}_{\text{ext}} = \delta\mathbf{q}^{\mathrm{T}} \int_{-1}^{1}\int_{-1}^{1} k\,p(\theta^1,\theta^2)\,\mathbf{N}^{\mathrm{T}}\,\mathbf{T}(\boldsymbol{g}_1)\,\boldsymbol{g}_2 d\theta^1 d\theta^2 \tag{3.72}$$

and its Newton increment as:

$$\mathrm{d}\delta\Pi_{\text{ext}} = \delta\mathbf{q}^{\mathrm{T}}\,\mathbf{K}_L\,\mathrm{d}\mathbf{q} \tag{3.73}$$

where the tangent matrix $\mathbf{K}_L$ is given as:

$$\mathbf{K}_L = \int_{-1}^{1}\int_{-1}^{1} k\,p(\theta^1,\theta^2)\,\mathbf{N}^{\mathrm{T}} \Big(-\mathbf{T}(\boldsymbol{g}_2)\,\mathbf{G}^{1:3} + \mathbf{T}(\boldsymbol{g}_1)\,\mathbf{G}^{4:6} \Big)\, d\theta^1 d\theta^2 \tag{3.74}$$

The external force vector as well as the tangent matrix $\mathbf{K}_L$ contribute to the global system in Eq. (2.73) and Eq. (2.74).

3.6 Isotropic Elasto-plasticity at Finite Strains

In engineering practice for shell structures, accounting for the plastic behavior of materials is essential to ensure reliable designs under severe ultimate loading conditions. Within the context of the 7-parameter shell elements, stress-based three-dimensional plasticity models can be directly employed. In this work, we adopt the finite-strain isotropic elasto-plasticity framework originally proposed by Simo [147] and subsequently investigated by F. Auricchio [73]. A key advantage of this formulation is that it preserves the

classical return-mapping algorithms of infinitesimal elasto-plasticity theory, allowing it to be extended to various plastic yield criteria. This generality is achieved by assuming material isotropy and formulating the constitutive equations in terms of the principal stresses. In the following, we present its application to the von Mises (J_2-flow) theory. The constitutive governing equations are first summarized in Section 3.6.1, followed by the trial elastic – plastic correction (return-mapping) algorithm in Section 3.6.2 and the exact algorithmic tangent moduli in Section 3.6.3, without considering the 7-parameter shell elements. The introduction of the EAS variable into the framework is then presented in Section 3.6.4.

3.6.1 Constitutive governing equations

Multiplicative decomposition. Let us first introduce the basic assumption of the local multiplicative decomposition of the deformation gradient $\boldsymbol{F}$ proposed by Lee [115], which is motivated by the micromechanical description of single-crystal metal plasticity:

$$\boldsymbol{F} = \boldsymbol{F}^e \, \boldsymbol{F}^p \tag{3.75}$$

where $\boldsymbol{F}^e$ and $\boldsymbol{F}^p$ represent the elastic and plastic parts of the deformation gradient, respectively. Based on the composition in Eq. (3.75), the total and plastic right Cauchy-Green deformation tensors are given by:

$$\boldsymbol{C} = \boldsymbol{F}^{\mathrm{T}} \, \boldsymbol{F} \qquad \boldsymbol{C}^p = \boldsymbol{F}^{pT} \, \boldsymbol{F}^p \tag{3.76}$$

Similarly, the elastic left Cauchy-Green deformation tensor is writes:

$$\boldsymbol{b}^e = \boldsymbol{F}^e \, \boldsymbol{F}^{eT} = \boldsymbol{F} \boldsymbol{C}^{p-1} \boldsymbol{F}^{\mathrm{T}} \tag{3.77}$$

From Eq. (3.77), let us express the rate of the left Cauchy-Green tensor as follows:

$$\dot{\boldsymbol{b}}^e = \boldsymbol{L}\boldsymbol{b}^e + \boldsymbol{b}^e \boldsymbol{L}^{\mathrm{T}} + \mathcal{L}_v(\boldsymbol{b}^e) \quad \text{with } \mathcal{L}_v(\boldsymbol{b}^e) = \boldsymbol{F} \dot{\boldsymbol{C}}^{p-1} \boldsymbol{F}^{\mathrm{T}} \tag{3.78}$$

where $\boldsymbol{L} = \dot{\boldsymbol{F}} \boldsymbol{F}^{-1} = \partial \dot{\boldsymbol{x}} / \partial \boldsymbol{x}$ is the velocity gradient in the current configuration. The additional term $\mathcal{L}_v(\boldsymbol{b}^e)$ corresponds to the contribution from plastic flow and is often referred to as the Lie derivative of $\boldsymbol{b}^e$. Thus, the terms $\boldsymbol{L}\boldsymbol{b}^e + \boldsymbol{b}^e \boldsymbol{L}^{\mathrm{T}}$ describe the evolution of the elastic strain $\boldsymbol{b}^e$ assuming the absence of plastic flow (i.e., when $\dot{\boldsymbol{C}}^{p-1} = \boldsymbol{0}$).

Spectral decomposition. Assuming the material isotropy in the continuum, the principal directions of the Kirchhoff stress tensor $\boldsymbol{\tau}$ coincide with the ones of the elastic left Cauchy-Green tensor $\boldsymbol{b}^e$, and their spectral decompositions take the form:

$$\boldsymbol{b}^e = (\lambda^{(A)})^2\, \boldsymbol{n}^{(A)} \otimes \boldsymbol{n}^{(A)}, \qquad \boldsymbol{\tau} = \beta^{(A)}\, \boldsymbol{n}^{(A)} \otimes \boldsymbol{n}^{(A)} \tag{3.79}$$

where $\lambda^{(A)}$ are the principal stretches equal to the square root of the principal values of $\boldsymbol{b}^e$ and $\beta^{(A)}$ are the principal Kirchhoff stresses.

Free energy function. To describe the elasto-plastic stress-strain relation, let us introduce the free energy function ψ in a general form as follows:

$$\psi = \psi(\boldsymbol{b}^e, \boldsymbol{\xi}) = \psi^e(\boldsymbol{b}^e) + \psi^p(\xi) \tag{3.80}$$

where $\psi^e(\boldsymbol{b}^e)$ is the elastic strain energy density, $\psi^p(\xi)$ is the plastic strain energy density assuming isotropic hardening, and ξ is the internal hardening variable. To obtain a formulation in principal stresses, the strain energy function is preferred to be expressed in terms of logarithmic principal stretches $e^{(A)} = \ln(\lambda^{(A)})$ as follows:

$$\psi^e(\boldsymbol{b}^e) = \psi^e(e^{(A)}) \tag{3.81}$$

We adopt the following quadratic hyperelastic strain energy function:

$$\psi^e(e^{(A)}) = \frac{1}{2}\lambda \left(e^{(1)} + e^{(2)} + e^{(3)}\right)^2 + \mu \left((e^{(1)})^2 + (e^{(2)})^2 + (e^{(3)})^2\right) \tag{3.82}$$

where λ and μ are the Lamé constants. As discussed in [147, 170], the stored energy function in Eq. (3.82) cannot be accepted as a correct model of elasticity for extreme strains; however, it provides an excellent approximation for moderately large elastic strains, which is useful to model metal plasticity. The principal Kirchhoff stresses are computed from the elastic strain energy using the following relation:

$$\beta^{(A)} = \frac{\partial \psi}{\partial e^{(A)}} = \frac{\partial \psi^e}{\partial e^{(A)}} = \lambda^{(A)}\, \frac{\partial \psi^e}{\partial \lambda^{(A)}} \tag{3.83}$$

Let us introduce, for convenience, the following vector and matrix notations:

$$\boldsymbol{\beta} = \begin{pmatrix} \beta^{(1)} \\ \beta^{(2)} \\ \beta^{(3)} \end{pmatrix}, \quad \boldsymbol{e} = \begin{pmatrix} e^{(1)} \\ e^{(2)} \\ e^{(3)} \end{pmatrix}, \quad \boldsymbol{1} = \begin{pmatrix} 1 \\ 1 \\ 1 \end{pmatrix}, \quad \boldsymbol{I}_3 = \begin{bmatrix} 1 & 0 & 0 \\ 0 & 1 & 0 \\ 0 & 0 & 1 \end{bmatrix} \tag{3.84}$$

Thus, the matrix form of the stress-strain relation in Eq. (3.83) becomes $\boldsymbol{\beta} = \boldsymbol{c}\boldsymbol{e}$ with $\boldsymbol{c}$ is the elastic 3×3 constitutive tensor, that writes:

$$\boldsymbol{c} = (\lambda + \frac{2}{3}\mu)\,\mathbf{1} \otimes \mathbf{1} + 2\mu(\boldsymbol{I}_3 - \frac{1}{3}\mathbf{1} \otimes \mathbf{1}) = (\lambda + \frac{2}{3}\mu)\mathbf{1} \otimes \mathbf{1} + 2\mu\boldsymbol{I}_{\text{dev}} \tag{3.85}$$

Von Mises yield function. The von Mises yield function is given by:

$$\Phi(\boldsymbol{\tau}, \xi) = \| \bar{\boldsymbol{\tau}} \| - \sqrt{\frac{2}{3}}\left[\sigma_{Y0} + R(\xi)\right] \leq 0 \tag{3.86}$$

where $\sigma_Y \geq 0$ is the yield stress, $R(\xi) = \partial\psi^p(\xi)/\partial\xi$ is a function describing the isotropic hardening law and $\| \bar{\boldsymbol{\tau}} \|$ is the norm of the deviatoric part of $\boldsymbol{\tau}$. The yield function can be expressed in terms of principal stresses using the following relation:

$$\| \bar{\boldsymbol{\tau}} \| = \| \bar{\boldsymbol{\beta}} \| = \sqrt{\bar{\boldsymbol{\beta}} \cdot \bar{\boldsymbol{\beta}}}\,, \qquad \text{with } \bar{\boldsymbol{\beta}} = (\boldsymbol{I}_3 - \frac{1}{3}\mathbf{1} \otimes \mathbf{1})\boldsymbol{\beta} = \boldsymbol{I}_{\text{dev}}\,\boldsymbol{\beta} \tag{3.87}$$

with $\bar{\boldsymbol{\beta}}$ denotes the principal deviatoric Kirchhoff stress, and $\mathbf{1} = [1, 1, 1]^{\mathrm{T}}$.

The development of the governing equations requires the derivative of the yield function with respect to the Kirchhoff stress, which can be expressed in terms of principal stresses via the chain rule as follows:

$$\partial_\tau \Phi = \frac{\partial \Phi}{\partial \boldsymbol{\tau}} = \frac{\partial \Phi}{\partial \beta^{(A)}} \frac{\partial \beta^{(A)}}{\partial \boldsymbol{\tau}} = \frac{\partial \Phi}{\partial \beta^{(A)}}\, \boldsymbol{n}^{(A)} \otimes \boldsymbol{n}^{(A)} = \partial_{\beta^{(A)}} \Phi\, \boldsymbol{n}^{(A)} \otimes \boldsymbol{n}^{(A)} \tag{3.88}$$

where derivatives with respect to the principal stresses are obtained using Eq. (3.87):

$$\begin{aligned} \partial_{\boldsymbol{\beta}} \Phi = \frac{\partial \Phi}{\partial \boldsymbol{\beta}} &= \left[\partial_{\beta^{(1)}} \Phi \quad \partial_{\beta^{(2)}} \Phi \quad \partial_{\beta^{(3)}} \Phi\right]^{\mathrm{T}} \\ &= \frac{\partial(\| \bar{\boldsymbol{\beta}} \|)}{\partial \bar{\boldsymbol{\beta}}} \cdot \frac{\partial \bar{\boldsymbol{\beta}}}{\partial \boldsymbol{\beta}} = \boldsymbol{I}_{\text{dev}} \frac{\bar{\boldsymbol{\beta}}}{\| \bar{\boldsymbol{\beta}} \|} = \frac{\bar{\boldsymbol{\beta}}}{\| \bar{\boldsymbol{\beta}} \|} = \bar{\boldsymbol{\nu}} \end{aligned} \tag{3.89}$$

where the property of $\boldsymbol{I}_{\text{dev}}\bar{\boldsymbol{\beta}} = \bar{\boldsymbol{\beta}}$ is used, and $\bar{\boldsymbol{\nu}}$ is the unit normal to the Mises surface in the principal stress space.

Governing equations. The governing constitutive equations, resulting from the principle of maximum plastic dissipation, are shown to be [147, 155]:

$$\begin{aligned} \text{Associated flow rule:} \quad & -\frac{1}{2}\mathcal{L}_v(\boldsymbol{b}^e) = \dot{\gamma}\,\frac{\partial \Phi}{\partial \boldsymbol{\tau}}\boldsymbol{b}^e \\ \text{Evolution of hardening variable:} \quad & \dot{\xi} = \sqrt{\frac{2}{3}}\dot{\gamma} \\ \text{Kuhn-Tucker condition:} \quad & \dot{\gamma} \geq 0, \quad \Phi \leq 0, \quad \dot{\gamma}\,\Phi(\boldsymbol{\tau}, \xi) = 0 \end{aligned} \tag{3.90}$$

where $\dot{\gamma}$ denotes the plastic consistency factor. Using Eq. (3.78), the associated flow rule can be written as follows:

$$\dot{\boldsymbol{b}^e} - \left(\boldsymbol{L}\,\boldsymbol{b}^e + \boldsymbol{b}^e\,\boldsymbol{L}^{\mathrm{T}}\right) = -2\dot{\gamma}\,\frac{\partial \Phi}{\partial \boldsymbol{\tau}}\boldsymbol{b}^e \tag{3.91}$$

As discussed previously, $\dot{\boldsymbol{b}}^e$ gives the rate of elastic strain, and $\boldsymbol{L}\,\boldsymbol{b}^e + \boldsymbol{b}^e\,\boldsymbol{L}^{\mathrm{T}}$ is considered as the rate of elastic strain assuming the absence of plastic flow. Therefore, the strategy *elastic trial–plastic correction* in the classical infinitesimal elasto-plastic model can be applied to solve the governing equations, as presented in the following.

3.6.2 Elastic trial and return-mapping algorithm

Time integration. Solving the differential governing equations in Eq. (3.90) requires the time integration. Let us consider a typical time interval $[t_n, t_{n+1}]$. It is assumed that the solution at the time t_n, $(\boldsymbol{b}^e_n, \xi_n)$, is known. The objective is to find the solution at the time t_{n+1} under the prescribed displacement increment given as $\Delta\boldsymbol{u} = \boldsymbol{u}_{n+1} - \boldsymbol{u}_n$.

Under the prescribed displacement $\Delta\boldsymbol{u}$, the elastic strain is first assumed to evolve freely from the plasticity with the rate $\boldsymbol{L}\,\boldsymbol{b}^e + \boldsymbol{b}^e\,\boldsymbol{L}^{\mathrm{T}}$. This yields the elastic trial solution as follows [147]:

$$\boldsymbol{b}^e_{tr} = \boldsymbol{f}\,\boldsymbol{b}^e_n\,\boldsymbol{f}^{\mathrm{T}}, \qquad \xi_{tr} = \xi_n \tag{3.92}$$

with $\boldsymbol{f}$ denotes the relative deformation gradient defined as:

$$\boldsymbol{f} = \frac{\partial x_{n+1}}{\partial x_n} = \boldsymbol{I} + \frac{\partial \Delta\boldsymbol{u}}{\partial x_n} \tag{3.93}$$

The trial principal stresses $\boldsymbol{\beta}_{tr}$ can be evaluated from the trial solution via the constitutive matrix $\boldsymbol{c}$ defined in Eq.(3.85). If the trial solution satisfies the yield function in Eq. (3.86), $\dot{\gamma} = 0$, the trial solution is the final solution at the time t_{n+1}. If the trial solution is outside of the yield surface, the final solution is obtained by projecting the trial solution

onto the yield surface via the plastic consistency factor $\dot{\gamma} > 0$. The process is referred to as *plastic correction* or *return-mapping*, formulated by integrating in time the governing equations in Eq. (3.90) as follows:

$$\begin{aligned} \boldsymbol{b}^e_{n+1} &= \boldsymbol{b}^e_{tr} \exp\Big[-2\Delta\gamma\, \partial_{\boldsymbol{\tau}} \Phi(\boldsymbol{\tau}_{n+1}, \xi_{n+1}) \Big] \\ \xi_{n+1} &= \xi_n + \sqrt{\frac{2}{3}} \Delta\gamma \\ \Delta\gamma \geq 0, &\qquad \Phi(\boldsymbol{\tau}_{n+1}, \xi_{n+1}) \leq 0, \qquad \Delta\gamma\, \Phi(\boldsymbol{\tau}_{n+1}, \xi_{n+1}) = 0 \end{aligned} \tag{3.94}$$

where $\Delta\gamma = (t_{n+1} - t_n)\dot{\gamma} > 0$, and the exponential approximation $y = y_0 \exp(A\Delta t)$ for the differential equation $\dot{y} = Ay$ is used. This exponential approximation is shown to preserve the plastic volume change [147], which is not the case while using the backward-Euler approximation as done in [146, 155]. The exponential approximation also motivates formulating the governing equations in terms of principal stresses.

Return-mapping in principal stress space. Substituting the spectral decomposition in Eq. (3.79) and the derivative of the yield function in Eq. (3.88) into the first equation in Eq. (3.94), and using the uniqueness of the spectral decomposition, we obtain:

$$\boldsymbol{n}^{(A)}_{n+1} = \boldsymbol{n}^{(A)}_{tr}, \quad \text{and} \quad (\lambda^{(A)}_{n+1})^2 = (\lambda^{(A)}_{tr})^2 \exp\Big[-2\Delta\gamma\, \partial_{\beta^{(B)}} \Phi(\beta^{(B)}_{n+1}, \xi_{n+1}) \Big] \tag{3.95}$$

The above equation is obtained using the following relation:

$$\begin{aligned} \exp\Big[(\lambda^{(A)})^2\, \boldsymbol{n}^{(A)}_{n+1} \otimes \boldsymbol{n}^{(A)}_{n+1} \Big] &= \sum_{m=0}^{\infty} \frac{\Big[(\lambda^{(A)})^2\, \boldsymbol{n}^{(A)}_{n+1} \otimes \boldsymbol{n}^{(A)}_{n+1} \Big]^m}{m!} \\ &= \sum_{m=0}^{\infty} \frac{(\lambda^{(A)})^{2m}}{n!}\, \boldsymbol{n}^{(A)}_{n+1} \otimes \boldsymbol{n}^{(A)}_{n+1} \\ &= \exp\big[(\lambda^{(A)})^2 \big]\, \boldsymbol{n}^{(A)}_{n+1} \otimes \boldsymbol{n}^{(A)}_{n+1} \end{aligned} \tag{3.96}$$

As seen in Eq. (3.95), the principal directions of the final solution coincide with those defined by the elastic trial solution; thus, the return-mapping can be performed in this fixed principal stress space.

Taking the logarithm of Eq. (3.95) and pre-multiplying by the elastic constitutive tensor $\boldsymbol{c}$ defined in Eq. (3.85) yields the following return-mapping algorithm:

$$\begin{aligned}
&\boldsymbol{\beta}_{tr} = \boldsymbol{c}\,\boldsymbol{e}_{tr}\,, \quad \bar{\boldsymbol{\nu}}_{n+1} = \bar{\boldsymbol{\nu}}_{tr} = \frac{\bar{\boldsymbol{\beta}}_{tr}}{\parallel \bar{\boldsymbol{\beta}}_{tr} \parallel}\,, \quad \bar{\boldsymbol{\nu}}_{n+1} \cdot \mathbf{1} = 0 \\
&\boldsymbol{\beta}_{n+1} = \boldsymbol{\beta}_{tr} - 2\mu\Delta\gamma\bar{\boldsymbol{\nu}}_{n+1}\,, \quad \xi_{n+1} = \xi_n + \sqrt{\frac{2}{3}}\Delta\gamma \\
&\Delta\gamma \geq 0, \qquad \Phi_{n+1} \leq 0, \qquad \Delta\gamma\,\Phi_{n+1} = 0
\end{aligned} \tag{3.97}$$

followed by the consistency equation $\Phi_{n+1} = 0$ that writes:

$$\begin{aligned}
\Phi_{n+1} =& \parallel \boldsymbol{\beta}_{n+1} \parallel + \sqrt{\frac{2}{3}}\left[\sigma_{Y0} + R(\xi_{n+1})\right] \\
=& \Phi_{tr} - 2\mu\Delta\gamma - \sqrt{\frac{2}{3}}\left[R\left(\xi_{tr} + \sqrt{\frac{2}{3}}\Delta\gamma\right) - R(\xi_{tr})\right] = 0
\end{aligned} \tag{3.98}$$

Solving Eq. (3.98) for the scalar $\Delta\gamma$ may require a local Newton-Raphson method when the hardening law $R(\xi)$ is nonlinear. It can be seen that the return-mapping algorithm presented here is identical to that of infinitesimal plasticity. The elastic predictor and plastic corrector algorithm is outlined in Algorithm 1.

3.6.3 Exact algorithmic tangent moduli

The algorithmic tangent moduli expressed in the current configuration at the time t_{n+1} are obtained using Eqs.(2.54), (2.43) and (2.8) as follows:

$$(\mathcal{C}_{IJKL})\Big|_{t_{n+1}} = \left(2F_{IR}\,F_{JS}\,F_{KM}\,F_{LN}\,\frac{\partial S_{RS}}{\partial C_{MN}}\right)\Bigg|_{t_{n+1}} \tag{3.99}$$

where the $\boldsymbol{S}$ denotes the PK2 stress tensor. Using the relation between the PK2 stress and the Kirchhoff stress in Eq.(2.16) and the spectral decomposition of the Kirchhoff stress in Eq.(3.79), the tangent moduli can be expressed in the principal stress space as

Algorithm 1 J_2-plasticity at finite strain: Elastic trial/return-mapping algorithm

Require: $\boldsymbol{b}^e_n$, ξ_n, $\boldsymbol{f}$

(1) Trial state:

Compute: $\boldsymbol{b}^e_{tr} = \boldsymbol{f}\,\boldsymbol{b}^e_n\,\boldsymbol{f}^{\mathrm{T}}, \quad \xi_{tr} = \xi_n$

Compute eigenvalues $(\lambda_A)^2$ and eigenvectors $\boldsymbol{n}^{(A)}$ of $\boldsymbol{b}^e_{tr}$

Compute logarithmic stretches: $\boldsymbol{e}_{tr} = \begin{bmatrix}\log(\lambda_1) & \log(\lambda_2) & \log(\lambda_3)\end{bmatrix}^{\mathrm{T}}$

Compute trial principal stresses: $\boldsymbol{\beta}_{tr} = \boldsymbol{c}\,\boldsymbol{e}_{tr}$

(2) Check plastic admissibility:

if $\Phi_{tr} = \left\|\bar{\boldsymbol{\beta}}_{tr}\right\| - \sqrt{\frac{2}{3}}\,(\sigma_{Y0} + R(\xi_{tr})) \leq 0$ **then**

Set $(\cdot)_{n+1} = (\cdot)_{tr}$

Compute $\boldsymbol{\tau}_{n+1} = \sum_{A=1}^{3} \beta^{(A)}_{tr}\,\boldsymbol{n}^{(A)} \otimes \boldsymbol{n}^{(A)}$

Exit

else

Continue to plastic corrector (3)

end if

(3) Plastic corrector:

Solve for $\Delta\gamma > 0$ the nonlinear equation:

$$\Phi_{n+1} = \Phi_{tr} - 2\mu\Delta\gamma - \sqrt{\frac{2}{3}}\left[R\left(\xi_{tr} + \sqrt{\frac{2}{3}}\Delta\gamma\right) - R(\xi_{tr})\right] = 0$$

Compute

$$\bar{\nu} = \frac{\bar{\boldsymbol{\beta}}_{tr}}{\|\,\bar{\boldsymbol{\beta}}_{tr}\,\|}, \quad \boldsymbol{\beta} = \boldsymbol{\beta} - 2\mu\,\Delta\gamma\bar{\nu}, \quad \boldsymbol{e} = \boldsymbol{e}_{tr} - \Delta\gamma\bar{\nu}$$

$$\tau_{n+1} = \sum_{A=1}^{3} \beta^{(A)}\,\boldsymbol{n}^{(A)} \otimes \boldsymbol{n}^{(A)}, \quad \boldsymbol{b}^e_{n+1} = \sum_{A=1}^{3} \exp(2e)\,\boldsymbol{n}^{(A)} \otimes \boldsymbol{n}^{(A)}, \quad \xi_{n+1} = \xi_{tr} + \sqrt{\frac{2}{3}}\Delta\gamma$$

follows (the notation $(\cdot)\big|_{t_{n+1}}$ is omitted for brevity):

$$\begin{aligned}\mathcal{C}_{IJKL} &= 2F_{IR}F_{JS}F_{KM}F_{LN}\frac{\partial}{\partial C_{MN}}\left[F_{RU}^{-1}\left(\beta^{(A)}m_{UV}^{(A)}\right)F_{SV}^{-1}\right]\\ &= 2\beta^{(A)}\,F_{IR}F_{JS}F_{KM}F_{LN}\,\frac{\partial}{\partial C_{MN}}\left[F_{RU}^{-1}\,m_{UV}^{(A)}\,F_{SV}^{-1}\right]+2F_{KM}F_{LN}\,\frac{\partial\beta^{(A)}}{\partial C_{MN}}\,m_{IJ}^{(A)}\\ &= 2\beta^{(A)}\,\hat{\mathcal{C}}_{IJKL}^{(A)}+\mathcal{C}_{IJKL}^{ep},\end{aligned} \tag{3.100}$$

where the $\boldsymbol{m}^{(A)}$ are the second-order tensors defined as:

$$\boldsymbol{m}_{n+1}^{(A)}=\boldsymbol{n}_{n+1}^{(A)}\otimes\boldsymbol{n}_{n+1}^{(A)}\quad\text{or}\quad m_{IJ,n+1}^{(A)}=n_{I,n+1}^{(A)}\,n_{J,n+1}^{(A)} \tag{3.101}$$

The tangent moduli in Eq.(3.100) can also be rewritten equivalently in compact tensor form as follows:

$$\boldsymbol{\mathcal{C}}_{n+1}=2\beta_{n+1}^{(A)}\hat{\boldsymbol{\mathcal{C}}}_{n+1}^{(A)}+\boldsymbol{\mathcal{C}}_{n+1}^{ep} \tag{3.102}$$

As the principal stress space remains unchanged during the plastic flow, that is $\boldsymbol{n}_{n+1}^{(A)}\otimes\boldsymbol{n}_{n+1}^{(A)}=\boldsymbol{n}_{tr}^{(A)}\otimes\boldsymbol{n}_{tr}^{(A)}$, the tensors $\hat{\boldsymbol{\mathcal{C}}}_{n+1}^{(A)}$ are independent from the plastic flow, or the return-mapping process, and thus depend only on the hyperelastic strain energy in Eq.(3.81). Whereas, the tensor $\boldsymbol{\mathcal{C}}_{n+1}^{ep}$ is dependent on the plastic flow. Using the chain rule below:

$$\frac{\partial\beta^{(A)}}{\partial C_{MN}}=\frac{\partial\beta^{(A)}}{\partial e_{tr}^{(B)}}\,\frac{\partial e_{tr}^{(B)}}{\partial C_{MN}}=a_{ep}^{(AB)}\,\frac{\partial e_{tr}^{(B)}}{\partial C_{MN}} \tag{3.103}$$

and the following relation derived in [154] for the hyperelasticity in principal stretches:

$$2F_{KM}F_{LN}\frac{\partial e_{tr}^{(B)}}{\partial C_{MN}}=n_K^{(B)}\,n_L^{(B)} \tag{3.104}$$

the tensor $\boldsymbol{\mathcal{C}}_{n+1}^{ep}$ writes:

$$\boldsymbol{\mathcal{C}}_{n+1}^{ep}=a_{ep}^{(AB)}\,\boldsymbol{m}_{n+1}^{(A)}\otimes\boldsymbol{m}_{n+1}^{(B)} \tag{3.105}$$

where 3×3 matrix $\boldsymbol{a}^{ep}$ denotes the linearization of the stress-strain relation in principal stress space, defined as:

$$\boldsymbol{a}_{ep}=\frac{\partial\boldsymbol{\beta}_{n+1}}{\partial\boldsymbol{e}_{tr}}\quad\text{or}\quad a_{ep}^{(AB)}=\frac{\partial\beta_{n+1}^{(A)}}{\partial e_{tr}^{(B)}} \tag{3.106}$$

Thus, the exact algorithmic tangent moduli are expressed as follows:

$$\boldsymbol{\mathcal{C}}_{n+1} = 2\beta_{n+1}^{(A)}\,\hat{\boldsymbol{\mathcal{C}}}_{n+1}^{(A)} + a_{ep}^{(AB)}\,\boldsymbol{m}_{n+1}^{(A)} \otimes \boldsymbol{m}_{n+1}^{(B)} \tag{3.107}$$

Explicit form of $\boldsymbol{\mathcal{C}}_{n+1}$. Let us first detail the explicit expression of the matrix $\boldsymbol{a}^{ep}$ from the return-mapping algorithm in Section 3.6.2. Using Eq.(3.97), the matrix $\boldsymbol{a}^{ep}$ is given as follows:

$$\boldsymbol{a}^{ep} = \frac{\partial \boldsymbol{\beta}_{n+1}}{\partial \boldsymbol{e}_{tr}} = \frac{\partial \boldsymbol{\beta}_{tr}}{\partial \boldsymbol{e}_{tr}} - 2\mu \frac{\partial \Delta\gamma}{\partial \boldsymbol{e}_{tr}} \otimes \bar{\boldsymbol{\nu}}_{n+1} - 2\mu\Delta\gamma \frac{\partial \bar{\boldsymbol{\nu}}_{n+1}}{\partial \boldsymbol{e}_{tr}} \tag{3.108}$$

The first derivative in the above equation gives the elastic constitutive tensor $\boldsymbol{c}$ defined in Eq. (3.85):

$$\frac{\partial \boldsymbol{\beta}_{tr}}{\partial \boldsymbol{e}_{tr}} = \boldsymbol{c} = (\lambda + \frac{2}{3}\mu)\,\mathbf{1} \otimes \mathbf{1} + 2\mu \boldsymbol{I}_{\text{dev}} \tag{3.109}$$

The third derivative, which is the derivative of the deviatoric unit vector $\boldsymbol{\nu}_{n+1}$ with respect to the trial logarithmic principal stretches, can be obtained using the chain rule as follows:

$$\begin{aligned} \frac{\partial \bar{\boldsymbol{\nu}}_{n+1}}{\partial \boldsymbol{e}_{tr}} = \frac{\partial \bar{\boldsymbol{\nu}}_{n+1}}{\partial \bar{\boldsymbol{\beta}}_{tr}} \frac{\partial \bar{\boldsymbol{\beta}}_{tr}}{\partial \boldsymbol{e}_{tr}} &= \frac{2\mu}{\| \bar{\boldsymbol{\beta}}_{tr} \|} \left(\boldsymbol{I}_3 - \bar{\boldsymbol{\nu}}_{n+1} \otimes \bar{\boldsymbol{\nu}}_{n+1}\right) \boldsymbol{I}_{\text{dev}} \\ &= \frac{2\mu}{\| \bar{\boldsymbol{\beta}}_{tr} \|} \left(\boldsymbol{I}_{\text{dev}} - \bar{\boldsymbol{\nu}}_{n+1} \otimes \bar{\boldsymbol{\nu}}_{n+1}\right) \end{aligned} \tag{3.110}$$

where the property $\boldsymbol{I}_{\text{dev}}\,\bar{\boldsymbol{\nu}}_{n+1} = \bar{\boldsymbol{\nu}}_{n+1}$ is used for the last equality.

The second derivative follows from differentiating the consistency equation in Eq. (3.98) as follows:

$$\frac{\partial \Phi_{tr}}{\partial \boldsymbol{e}_{tr}} - (2\mu + \frac{2}{3}R') \frac{\partial \Delta\gamma}{\partial \boldsymbol{e}_{tr}} = 0 \quad \text{with} \quad R' = \frac{\partial R(\xi_{n+1})}{\partial \xi} \tag{3.111}$$

which yields:

$$\frac{\partial \Delta\gamma}{\partial \boldsymbol{e}_{tr}} = \frac{1}{2\mu + \frac{2}{3}R'} \frac{\partial \Phi_{tr}}{\partial \boldsymbol{e}_{tr}} = \frac{2\mu}{2\mu + \frac{2}{3}R'} \bar{\boldsymbol{\nu}}_{n+1} \tag{3.112}$$

with:

$$\frac{\partial \Phi_{tr}}{\partial \boldsymbol{e}_{tr}} = \frac{\partial}{\partial \boldsymbol{e}_{tr}} (\| \bar{\boldsymbol{\beta}}_{tr} \|) = 2\mu \bar{\boldsymbol{\nu}}_{n+1} \tag{3.113}$$

Using all the derivative terms above, the explicit expression of the matrix $\boldsymbol{a}^{ep}$ writes:

$$\boldsymbol{a}^{ep} = (\lambda + \frac{2}{3}\mu)\mathbf{1} \otimes \mathbf{1} + 2\mu \left(s_{n+1} \boldsymbol{I}_{\text{dev}} - \delta_{n+1} \bar{\boldsymbol{\nu}}_{n+1} \otimes \bar{\boldsymbol{\nu}}_{n+1}\right) \tag{3.114}$$

with:

$$s_{n+1} = 1 - \frac{2\mu\Delta\gamma}{\| \bar{\boldsymbol{\beta}}_{tr} \|}, \qquad \delta_{n+1} = \frac{1}{1 + \dfrac{R'}{3\mu}} - \frac{2\mu\Delta\gamma}{\| \bar{\boldsymbol{\beta}}_{tr} \|} \tag{3.115}$$

The explicit expression of $\hat{\boldsymbol{\mathcal{C}}}^{(A)}$ derived from the formulation of finite elasticity in principal stretches in [154] is given as:

$$\begin{aligned} \hat{\boldsymbol{\mathcal{C}}}^{(A)} =& \frac{1}{d_A}\Big[\boldsymbol{\mathcal{I}}^b - \boldsymbol{b}\otimes\boldsymbol{b} - I_3(\lambda^{(A)})^{-2}\Big[(\boldsymbol{I} - \boldsymbol{m}^{(A)})\otimes(\boldsymbol{I} - \boldsymbol{m}^{(A)})\Big]\Big] \\ &+ \frac{(\lambda^{(A)})^2}{d_A}\Big[(\boldsymbol{b}\otimes\boldsymbol{m}^{(A)} + \boldsymbol{m}^{(A)}\otimes\boldsymbol{b}) + (I_1 - 4\,(\lambda^{(A)})^2)\,\boldsymbol{m}^{(A)}\otimes\boldsymbol{m}^{(A)}\Big] \end{aligned} \tag{3.116}$$

with:

$$\begin{aligned} \mathcal{I}^b_{IJKL} &= \frac{1}{2}(b_{IK}b_{JL} + b_{IL}b_{JK}) \\ d_A &= [(\lambda^{(A)})^2 - (\lambda^{(B)})^2][(\lambda^{(A)})^2 - (\lambda^{(C)})^2] \\ I_1 &= (\lambda^{(1)})^2 + (\lambda^{(2)})^2 + (\lambda^{(3)})^2 \\ I_3 &= (\lambda^{(1)}\lambda^{(2)}\lambda^{(3)})^2 \end{aligned} \tag{3.117}$$

The tensor $\hat{\boldsymbol{\mathcal{C}}}^{(A)}_{n+1}$ is evaluated with $\boldsymbol{b} = \boldsymbol{b}_{tr}$, $\lambda^{(A)} = \lambda^{(A)}_{tr}$ and $\boldsymbol{m}^{(A)} = \boldsymbol{m}^{(A)}_{tr} = \boldsymbol{m}^{(A)}_{n+1}$. In case of $d_A = 0$, it is recommended to use $d_A = 10^{-8}$.

3.6.4 Introduction of EAS variable into the trial elastic strain

Applying the present framework of elasto-plasticity to the 7-parameter shell elements, we need to introduce the EAS variable $\tilde{\beta}_{33}$ into the stress-strain relation in Eq.(3.83). Suppose the material model is hyperelastic using the strain energy function in Eq. (3.82), we can naturally inroduce of the EAS variable into the stress-strain relation, noting that the eigenvalues of the right Cauchy strain $\boldsymbol{C}$ are identical to those of the left Cauchy strain $\boldsymbol{b}$. The EAS variable can be introduced into the right Cauchy strain using Eq. (3.21) and Eq. (2.8) as follows:

$$\boldsymbol{C}^* = \boldsymbol{C} + 2\theta^3\tilde{\beta}_{33}\,\boldsymbol{G}^3\otimes\boldsymbol{G}^3 \tag{3.118}$$

Nevertheless, in the context of multiplicative elasto-plasticity, the above manner cannot be applied as only the elastic part of the strain is required for an elastic increment, as done in Eq. (3.92) via the relative deformation gradient. Using the shell geometry

presented in Section 3.1, the relative deformation gradient is defined as follows:

$$\begin{aligned} \boldsymbol{f} = \frac{\partial \boldsymbol{x}_{n+1}}{\partial \boldsymbol{x}_n} &= \frac{\partial \boldsymbol{x}_{n+1}}{\partial \theta^i} \otimes \frac{\partial \theta^i}{\partial \boldsymbol{x}_n} = \boldsymbol{g}_{i,n+1} \otimes \boldsymbol{g}_n^i \\ &= \boldsymbol{J}(\boldsymbol{x}_{n+1})\, \boldsymbol{J}^{-1}(\boldsymbol{x}_n) \end{aligned} \tag{3.119}$$

The relative deformation gradient is independent of the EAS variable. Indeed, the EAS variable is introduced locally in the Green-Lagrange strain tensor and does not modify the shell metric. The same problem has been discussed in the work of Roehl and Ramm [144], but the solution remains unclear.

In the present work, to overcome this problem, we assume that the EAS field modifies the shell basis vectors in the deformed (current) configuration as follows:

$$\boldsymbol{g}_i^\star = \begin{cases} \boldsymbol{g}_i, & i = 1, 2, \\ \boldsymbol{g}_3 + \theta^3 \tilde{\beta}_{33}\, \boldsymbol{g}^3 \end{cases} \tag{3.120}$$

Thus, the relative deformation gradient can account for the EAS variable as follows:

$$\boldsymbol{f}^\star = \boldsymbol{J}^\star(\boldsymbol{x}_{n+1}, \tilde{\beta}_{33,n+1})\, \boldsymbol{J}^{\star -1}(\boldsymbol{x}_n, \tilde{\beta}_{33,n}) \tag{3.121}$$

with:

$$\boldsymbol{J}^\star(\boldsymbol{x}, \tilde{\beta}_{33}) = \left[\boldsymbol{g}_1, \quad \boldsymbol{g}_2, \quad \boldsymbol{g}_3 + \theta^3 \tilde{\beta}_{33} \boldsymbol{g}^3\right], \quad \boldsymbol{g}_i = \frac{\partial \boldsymbol{x}}{\partial \theta^i}, \quad \boldsymbol{g}^i = \frac{\partial \theta^i}{\partial \boldsymbol{x}} \tag{3.122}$$

The modification of the basis vector in the deformed configuration in Eq. (3.120) serves only to compute the relative deformation gradient. It does not modify the global shell geometry as in the original concept of EAS in 7-parameter shell elements.

Now, using the modified covariant basis vectors in Eq. (3.120), the Green-Lagrange strain tensor defined in Eq. (3.11) becomes:

$$\begin{aligned} \boldsymbol{E} &= \frac{1}{2}\Big(\boldsymbol{g}_{ij}^\star - \boldsymbol{G}_{ij}\Big)\boldsymbol{G}^i \otimes \boldsymbol{G}^j \\ &= \frac{1}{2}\Big(\boldsymbol{g}_{ij} - \boldsymbol{G}_{ij}\Big)\boldsymbol{G}^i \otimes \boldsymbol{G}^j + \Big(\theta^3 \tilde{\beta}_{33} + (\theta^3 \tilde{\beta}_{33})^2\, g^{33}\Big)\, \boldsymbol{G}^3 \otimes \boldsymbol{G}^3 \end{aligned} \tag{3.123}$$

In the above equation, the quadratic terms $(\theta^3 \tilde{\beta}_{33})^2\, g^{33}$ are small and can be neglected, and the Green-Lagrange strain incorporating the EAS field in Eq. (3.21) is retrieved. Therefore, we can incorporate the present framework of elasto-plasticity at finite strain in the shell formulation in the current (deformed) configuration presented in Section 3.3.2.

3.7 Coupling Problem between Shell Components

The problem of connecting two 7-parameter shell meshes arises when there is a discontinuity in the curvature at the interface of two meshes, as illustrated in Figure 3.2 for the cases of L-shaped and T-shaped coupling. We can see this coupling problem in thin-walled beams or shells reinforced by stiffeners. To handle this ambiguity, Baguet [8] proposed to add two cylindrical fitting shell elements to ensure the continuity of the shell director of the L-shaped, so that a unique shell director can be defined at each node. Nevertheless, this method requires considerable effort in meshing and is only feasible for simple L-shaped coupling. In this section, we present two strategies to address the coupling between shell components. The first approach is simple: a unique shell director is assigned to each node on the interface; thus, it is called the pre-processing approach. This approach was also discussed in [31]. The second strategy is based on the standard mortar method [23, 24, 44, 51], which uses Lagrange multipliers and computes the mortar matrices.

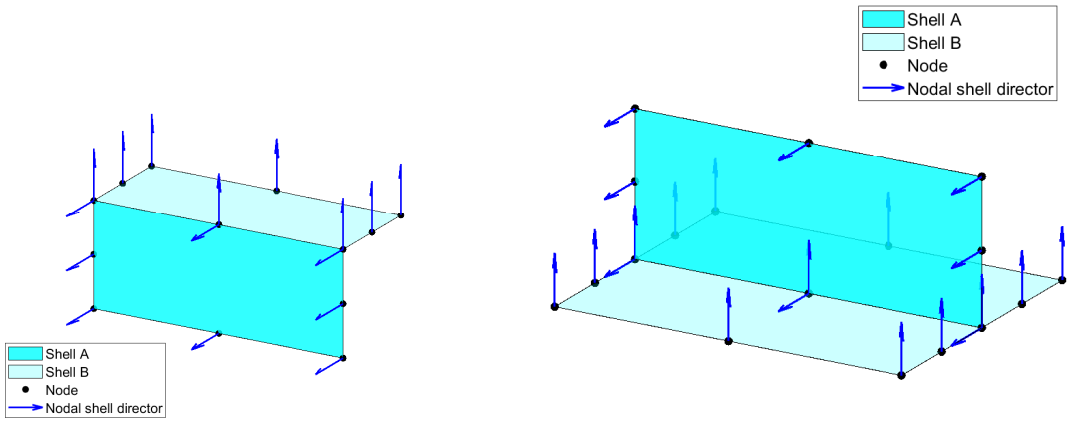

(a) L-shaped coupling (b) T-shaped coupling

Figure 3.2 Discontinuity of the nodal shell directors for L-shaped and T-shaped coupling problems

3.7.1 Pre-processing strategy for the shell directors at the interface

The idea of the pre-processing strategy is to choose unique shell directors for nodes on the common edge between the meshes of the shells. Considering two 8-node quadrilateral shell elements denoted as A and B as in Figure 3.2(a), we can easily choose unique shell

directors for the nodes on the intersection of the two shells as follows:

$$\boldsymbol{A}_3^{(\mathrm{k})} = \boldsymbol{A}_3^{A(k)} + \boldsymbol{A}_3^{B(k)} \tag{3.124}$$

where $\boldsymbol{A}_3^{A(k)}$ and $\boldsymbol{A}_3^{B(k)}$ are respectively the nodal original shell directors of the element A and B at the kth node, and $\boldsymbol{A}_3^{(\mathrm{k})}$ is the chosen common shell director for the kth node. The common shell directors will ensure the continuity of the shell director fields between the two elements as displayed in Figure 3.3(a), which illustrates the cross-section of the L-shaped coupling between two shell elements. The same procedure can be applied to the T-shaped coupling case as displayed in Figure 3.2(b) and Figure 3.3(b).

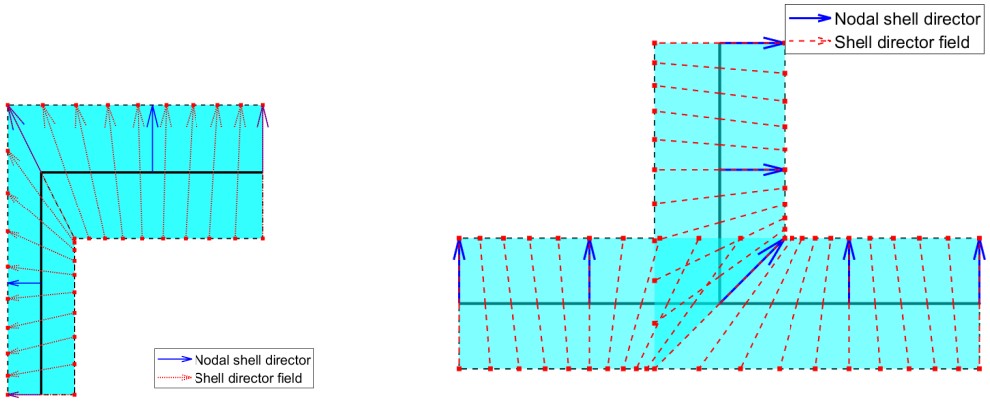

(a) L-shaped cross-section (b) T-profile cross-section

Figure 3.3 Spatial discretization of the shell directors $\boldsymbol{a}_3$ for two adjacent 8-node shell elements: (a) L-shaped cross-section; (b) T-profile cross-section

3.7.2 Mortar approach

The second approach to connecting the shell components is to use the standard mortar method. The mortar approach is commonly used for mesh tying (also called tied contact) problems. The principle is to impose the continuity of displacement between the shell components on the interface as illustrated in Figure 3.4. It can be seen that the coupling interface corresponds to the red rectangular surface, which is not the interface between the two mid-surfaces, but rather the interface between the two volumetric bodies managed by the two shells. Therefore, we can also apply this strategy to solid–shell coupling.

Variational Description. To formulate the mortar method, let us consider two bodies $\Omega^{(1)}$ and $\Omega^{(2)}$, whose interface is denoted as $\Gamma_h = \Omega^{(1)} \cap \Omega^{(2)}$. The boundary of each

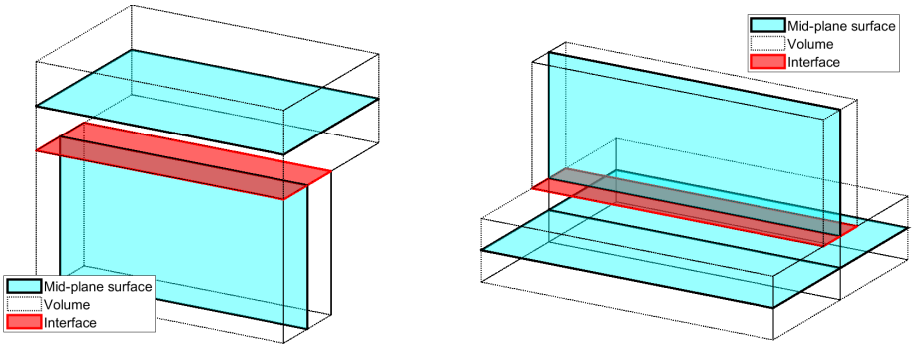

Figure 3.4 Mortar coupling surfaces (in red) for L-shaped and T-shaped cross-section thin-walled beams

body now consists of the Neumann and the Dirichlet boundaries, and also the interface boundary:

$$\begin{aligned} \partial\Omega^{(\cdot)} &= \Gamma_N^{(\cdot)} \cup \Gamma_D^{(\cdot)} \cup \Gamma_h \\ \Gamma_N^{(\cdot)} \cap \Gamma_D^{(\cdot)} &= \Gamma_N^{(\cdot)} \cap \Gamma_h = \Gamma_D^{(\cdot)} \cap \Gamma_h = \varnothing \end{aligned} \tag{3.125}$$

Here, let us call $\Omega^{(1)}$ the slave domain, and $\Omega^{(2)}$ the master domain. To ensure the tying condition between the two bodies, we may impose the continuity of displacement between the two bodies on the interface Γ_h:

$$\boldsymbol{u}^{(1)}(\boldsymbol{X}) - \boldsymbol{u}^{(2)}(\boldsymbol{X}) = \boldsymbol{0} \quad \text{on} \quad \Gamma_h \tag{3.126}$$

The above equation is considered as a constraint to the minimization problem of the potential energy presented in Eq. (2.26). Therefore, to take into account this condition in the weak form of the problem, it is common to introduce the Lagrange multiplier functional as follows:

$$\Pi_{\text{cons}} = \int_{\Gamma_h} \boldsymbol{\lambda} \cdot (\boldsymbol{u}^{(1)} - \boldsymbol{u}^{(2)})\, d\Gamma \tag{3.127}$$

in which the Lagrange multipliers $\boldsymbol{\lambda}(\boldsymbol{X})$ represent the traction on the interface:

$$\boldsymbol{\lambda}(\boldsymbol{X}) = \boldsymbol{P}^{(1)}(\boldsymbol{X}) \cdot \boldsymbol{N}^{(1)}(\boldsymbol{X}) = -\boldsymbol{P}^{(2)}(\boldsymbol{X}) \cdot \boldsymbol{N}^{(2)}(\boldsymbol{X}) \quad \text{on} \quad \Gamma_h \tag{3.128}$$

The variation of the functional in Eq. (3.127) provides two terms. The first term is the virtual work due to traction forces on the interface:

$$\delta\Pi_{\text{cons}} = \int_{\Gamma_h} (\delta\boldsymbol{u}^{(1)} - \delta\boldsymbol{u}^{(2)}) \cdot \boldsymbol{\lambda}\, d\Gamma \tag{3.129}$$

and the second term gives the weak form of the displacement continuity condition on the interface:

$$\int_{\Gamma_h} \delta\boldsymbol{\lambda} \cdot (\boldsymbol{u}^{(1)} - \boldsymbol{u}^{(2)})\, d\Gamma = 0 \tag{3.130}$$

It is worth noting that the above weak form may also be written in the current configuration as done to the Lagrange multiplier virtual work presented in Section 2.5. In this case, $\boldsymbol{\lambda}$ is considered as the traction in the current configuration on the interface Γ_h.

Standard mortar approach. For the discretization in space, we use the standard finite element to approximate the displacement $\boldsymbol{u}$ and its variation $\delta\boldsymbol{u}$ as presented in Eq. (2.58). For the Lagrange multipliers, there are two well-known discretization approaches: the standard and the dual mortar approaches. The first one employs the standard shape functions on the slave domain $\Omega^{(A)}$ to approximate the Lagrange multipliers. In contrast, the second approach employs a so-called biorthogonality condition to construct the dual shape functions with respect to the slave domain, then uses these dual shape functions to approximate the Lagrange multipliers. The advantage of the duality lies in the sparsity of the mortar matrices, thus making the coupling algorithm computationally efficient. More details about the dual mortar approach can be found in the thesis work of Popp [136]. In the present work, we employ the standard mortar approach. The semi-discrete virtual work of the interface forces writes:

$$\delta\Pi_{\text{cons}} = \int_{\Gamma_h} \left(\delta\mathbf{q}^{(1)\mathrm{T}}\, \mathbf{L}^{(1)\mathrm{T}} + \delta\mathbf{q}^{(2)\mathrm{T}}\, \mathbf{L}^{(2)\mathrm{T}} \right) \boldsymbol{\Lambda}\, d\Gamma \tag{3.131}$$

and the discrete condition of the continuity of displacement on the interface writes:

$$\delta\boldsymbol{\Lambda}^{\mathrm{T}} \left(\mathbf{L}^{(1)}\, \mathbf{q}^{(1)} + \mathbf{L}^{(2)}\, \mathbf{q}^{(2)} \right) = \mathbf{0} \tag{3.132}$$

In the above equations, $\mathbf{L}^{(1)}$ and $\mathbf{L}^{(2)}$ are the mortar matrices:

$$\mathbf{L}^{(1)} = \int_{\Gamma_h} \mathbf{N}^{(1)\mathrm{T}}\, \mathbf{N}^{(1)}\, d\Gamma\,, \qquad \mathbf{L}^{(2)} = -\int_{\Gamma_h} \mathbf{N}^{(1)\mathrm{T}}\, \mathbf{N}^{(2)}\, d\Gamma \tag{3.133}$$

In finite element implementation, we can consider that the two bodies are in the same domain by arranging $\mathbf{q}^{(1)}$ and $\mathbf{q}^{(2)}$ in a global nodal displacement vector without overlapping on the nodal values. Thus, the mortar matrices can also be put in a global mortar matrix as follows:

$$\begin{bmatrix} \mathbf{L}^{(1)} & \mathbf{L}^{(2)} \end{bmatrix} \begin{bmatrix} \mathbf{q}^{(1)} \\ \mathbf{q}^{(2)} \end{bmatrix} = \mathbf{L}\,\mathbf{q} = \mathbf{0} \tag{3.134}$$

and:

$$\delta\Pi_{\text{cons}} = \delta\mathbf{q}^{\mathrm{T}} \int_{\Gamma_h} \mathbf{L}^{\mathrm{T}} \boldsymbol{\Lambda}\, d\Gamma \tag{3.135}$$

It can be seen that the kinematic constraint now takes the same form as a linear Dirichlet condition, as introduced in Section 2.6 within the finite element framework. Therefore, the mortar-based kinematic constraint can be directly incorporated into the governing equations in Eq. (2.73) by treating it as an additional Dirichlet-type condition.

Overconstraint. An overconstraint occurs when multiple constraints are applied to the same degree of freedom. Overconstraints make the problem ill-conditioned, leading to inaccurate solutions or degrading the convergence rate during the resolution process. When using the mortar method for the mesh tying problem, there are two situations in which overconstraints commonly occur: at the crosspoints where more than two bodies meet, as the point A illustrated in Figure 3.5, and at the intersection between the Dirichlet boundary and the coupling interface, as the point B in Figure 3.5. These critical nodes exist in the discrete setting despite the condition in Eq. (3.125) in the continuous setting.

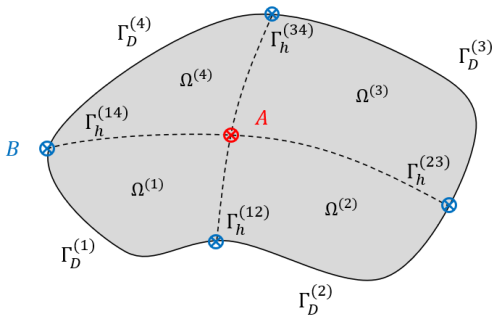

Figure 3.5 Overconstraint in the coupling problem of four bodies.

Some overconstraints can be handled automatically during the resolution process, especially when the element's shape functions are used to approximate the Lagrange multipliers for both the coupling and Dirichlet conditions. This observation is made based on our experience, and also reported in [2]. In other cases, the overconstraint can be avoided by carefully canceling the shape function of these critical points. To illustrate

this concept, let us consider the crosspoint A in Figure 3.5:

$$\begin{cases} \boldsymbol{u}^{(1)} = \boldsymbol{u}^{(2)} & \text{on} \quad \Gamma_h^{(12)} \\ \boldsymbol{u}^{(2)} = \boldsymbol{u}^{(3)} & \text{on} \quad \Gamma_h^{(23)} \\ \boldsymbol{u}^{(3)} = \boldsymbol{u}^{(4)} & \text{on} \quad \Gamma_h^{(34)} \\ \boldsymbol{u}^{(4)} = \boldsymbol{u}^{(1)} & \text{on} \quad \Gamma_h^{(14)} \end{cases} \longrightarrow \begin{cases} \boldsymbol{u}^{(1)} = \boldsymbol{u}^{(2)} & \text{on} \quad \Gamma_h^{(12)} \\ \boldsymbol{u}^{(2)} = \boldsymbol{u}^{(3)} & \text{on} \quad \Gamma_h^{(23)} \\ \boldsymbol{u}^{(3)} = \boldsymbol{u}^{(4)} & \text{on} \quad \Gamma_h^{(34)} \\ \boldsymbol{u}^{(4)} = \boldsymbol{u}^{(1)} & \text{on} \quad \Gamma_h^{(14)} \setminus \boldsymbol{X} = \boldsymbol{X}_A \end{cases} \tag{3.136}$$

Similarly, for point B:

$$\begin{cases} \boldsymbol{u}^{(1)} = \hat{\boldsymbol{u}}_D^{(1)} & \text{on} \quad \Gamma_D^{(1)} \\ \boldsymbol{u}^{(4)} = \hat{\boldsymbol{u}}_D^{(4)} & \text{on} \quad \Gamma_D^{(4)} \\ \boldsymbol{u}^{(1)} = \boldsymbol{u}^{(4)} & \text{on} \quad \Gamma_h^{(14)} \end{cases} \longrightarrow \begin{cases} \boldsymbol{u}^{(1)} = \hat{\boldsymbol{u}}_D^{(1)} & \text{on} \quad \Gamma_D^{(1)} \\ \boldsymbol{u}^{(4)} = \hat{\boldsymbol{u}}_D^{(4)} & \text{on} \quad \Gamma_D^{(4)} \setminus \boldsymbol{X} = \boldsymbol{X}_A \\ \boldsymbol{u}^{(1)} = \boldsymbol{u}^{(4)} & \text{on} \quad \Gamma_h^{(14)} \end{cases} \tag{3.137}$$

Conclusion of the chapter. This chapter reviews the formulation of the 7-parameter shell elements proposed by Büchter et al. [48] based on the Enhanced Assumed Strain concept. The formulation was originally developed in the reference configuration and is extended in this work to the current configuration. The latter permits us to adopt the framework of finite strain elasto-plasticity proposed by Simo [147] as presented in Section 3.6. We also discuss the coupling problem between the shell components, focusing on the standard mortar approach, which is also applicable for the shell–solid coupling. These two developments can be incorporated in the presented finite element formulation, and thus are ready for the solvers developed in Chapter 4.

Chapter 4

Nonlinear Dynamic Analysis of Shell Structures

In Chapters 2 and 3, we developed the element-level weak formulations for both three-dimensional solid elements and 7-parameter shell elements, which serve as the basis for constructing the semi-discrete governing equations in Eqs. (2.68) and (2.69). In this chapter, we focus on the development of solvers for nonlinear dynamic analysis, with particular emphasis on the 7-parameter shell elements. The objective is to formulate general solvers capable of capturing the nonlinear effects arising from finite strain theory, nonlinear material behavior, and time-dependent boundary conditions. A special case of kinematic nonlinearity will also be addressed in the solvers using an explicit time integrator. We begin by considering the time discretization of the governing equations.

Fully Discrete Governing Equations. For transient problems, variables such as displacement, velocity, acceleration, and Lagrange multipliers are time-dependent. Thus, the global governing equations in Eqs. (2.68) and (2.69) are expressed at arbitrary time t within a given time interval $[0, T]$. To solve dynamic problems, these equations must be discretized in time. A common approach is to subdivide the interval $t \in [0, T]$ into a sequence of smaller intervals $[t_n, t_{n+1}]$, with the corresponding time step $\Delta t = t_{n+1} - t_n$, where n is the time step index. Consequently, the spatially discretized solution $\mathbf{q}$, along with all other relevant quantities, is now approximated in time:

$$(\cdot)\Big|_{t_{n+1}} = (\cdot)_{n+1} \tag{4.1}$$

Thus, the fully discrete form of the equation of motion becomes:

$$\mathbf{M}\,\ddot{\mathbf{q}}_{n+1} + \mathbf{C}\,\dot{\mathbf{q}}_{n+1} + \mathbf{f}_{\text{int},n+1} - \mathbf{f}_{\text{ext},n+1} - \mathbf{L}^{\mathrm{T}}\boldsymbol{\Lambda}_{n+1} = \mathbf{0} \tag{4.2}$$

with the kinematic constraints:

$$\mathbf{L}\,\mathbf{q}_{n+1} - \mathbf{B}_{n+1} = \mathbf{0} \tag{4.3}$$

Eq. (4.2) represents the spatially discrete equation of motion at a discrete time t_{n+1}, combining inertia, damping, internal and external forces, and constraint reactions. Eq. (4.3) enforces the prescribed constraints exactly at that same time.

Newmark Time Integration Schemes. The integration of the system in Eqs. (4.2) and (4.3) requires the successive computation of displacement, velocity, and acceleration at each time step. A widely used approach is the approximate formulae of the Newmark time integration scheme, given as:

$$\begin{aligned}
\mathbf{q}_{n+1} &= \mathbf{q}_n + \Delta t\,\dot{\mathbf{q}}_n + \left(\frac{1}{2} - \beta\right)\Delta t^2\,\ddot{\mathbf{q}}_n + \beta\,\Delta t^2\,\ddot{\mathbf{q}}_{n+1} \\
\dot{\mathbf{q}}_{n+1} &= \dot{\mathbf{q}}_n + (1-\gamma)\Delta t\,\ddot{\mathbf{q}}_n + \gamma\,\Delta t\,\ddot{\mathbf{q}}_{n+1}
\end{aligned} \tag{4.4}$$

where β and γ are the Newmark parameters. These relations provide expressions for the unknown displacement, velocity, and acceleration at t_{n+1} in terms of the known solution at t_n. Two classical parameter choices yield well-known schemes: the implicit Constant Average Acceleration (CAA) scheme with $\beta = 0.25$ and $\gamma = 0.5$, and the explicit Newmark scheme with $\beta = 0.0$ and $\gamma = 0.5$, known as the Central Difference (CD) scheme.

Implicit schemes such as CAA allow for relatively large time steps. However, they lead to nonlinear systems requiring iterative solvers, such as the Newton–Raphson method. The efficiency of these solvers depends heavily on their convergence properties, which can be compromised by the presence of nonphysical high-frequency modes, an issue particularly pronounced in thin structures.

Explicit schemes, such as the Newmark scheme with $\beta = 0.0$ and $\gamma = 0.5$, allow for the direct computation of $\mathbf{q}_{n+1}$ from the previous time step, leading to straightforward solution procedures. This advantage permits us to easily consider all types of nonlinearity, including the kinematic nonlinearity that may arise in Eq. (4.3). However, explicit schemes are only conditionally stable; the time step must be smaller than a critical value to ensure stability. This critical time step is typically defined as [88]:

$$\Delta t_{crit} = \frac{2}{\omega_{max}} \tag{4.5}$$

where ω_{max} is the maximum eigenfrequency obtained from modal analysis of the considered discrete problem. In practice, nonphysical high-frequency modes in thin structures modeled by 7-parameter shell elements may unnecessarily reduce this critical time step, motivating a closer examination of these modes.

Outline of the Chapter. Section 4.1 analyzes nonphysical high-frequency modes in a thin plate using modal analysis. Section 4.2 introduces the Generalized-α method for high-frequency damping and revisits the implicit solver based on the Newton–Raphson method. Section 4.3 presents the Asymptotic Numerical Method (ANM) for geometrically nonlinear dynamics with non-conservative forces, employing homotopy and perturbation at the element level. Section 4.4 details the explicit Central Difference solvers.

It is worth noting that the ANM method for follower forces has been published in Chau et al. [53]. In Chau et al. [54], an explicit time integration approach with special treatment of EAS has been presented and investigated for linear elastic materials. Here, with respect to the two published papers, additional developments are provided, including implicit time integration with numerical damping (α-generalized methods), multi-time step aspects in explicit computations, and a more general organization of the different constraints in the developed solvers.

4.1 High-Frequency Modes of 3D-Shell Elements

4.1.1 Modal analysis of a thin plate

In this section, we investigate the high-frequency modes of a thin plate that is embedded on two of its edges. This benchmark structure is illustrated in Figure 4.1 and has been employed in earlier works by Wall et al. [161], Ramm and Wall [140], Kloppel et al. [102]. In these works, the authors analyzed the eigenvalues of the tangent stiffness matrix $\mathbf{K}_T$ to investigate how high-frequency modes impact the system conditioning. Here, we employ a different approach, utilizing a modal analysis in the context of dynamic problems, to gain a deeper understanding of these modes. We consider two different models: a shell model made of 10×10 8-node quadrilateral 7-parameter shell elements, and a solid model made of 10×10 20-node hexahedral elements.

The computed modal spectra for both models are shown in Figure 4.1b. Each model uses two types of mass matrices: a Consistent Mass Matrix (CMM) and a Lumped Mass Matrix (LMM), where the LMM is diagonal and is commonly used in explicit dynamic solvers. The construction of mass matrices can be found in Appendix A. We can see

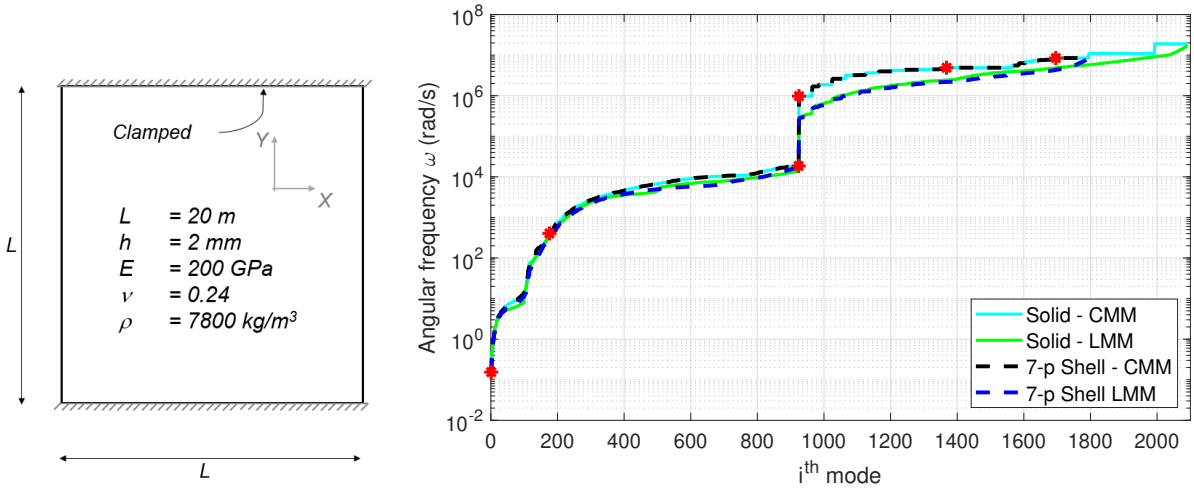

(a) Problem's description (b) Eigenvalue spectra

Figure 4.1 Model and eigenfrequency spectra of the thin plate using 7-parameter shell and 3D solid elements with consistent (CMM) and lumped (LMM) mass matrices.

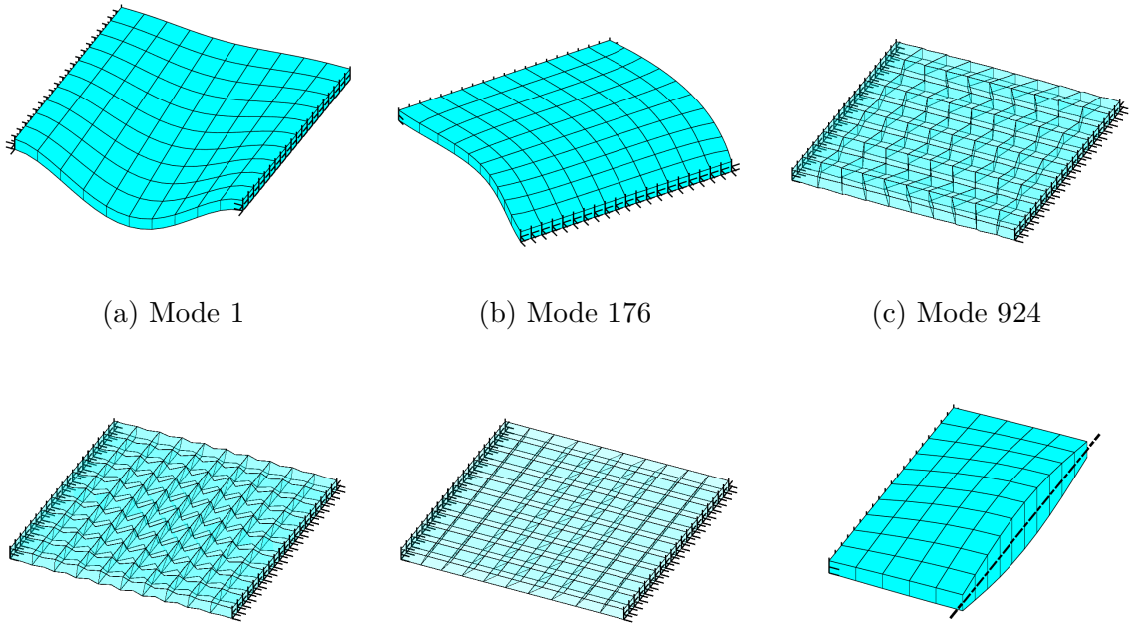

(a) Mode 1 (b) Mode 176 (c) Mode 924

(d) Mode 925 (e) Mode 1368 (f) Mode 1696

Figure 4.2 Eigenmodes obtained from modal analysis for the 7p-shell model and the consistent mass matrix (CMM). The modes correspond to the red points on the spectrum displayed in Figure 4.1.

Table 4.1 Thin plate: Mode participation factor obtained from the modal analysis of 7-parameter shell model using CMM

Mode	ω (rad/s)	Period (s)	Participation factor					
			V_X	V_Y	V_Z	W_X	W_Y	W_Z
1	20.3	1.5×10^{-1}	-	-	0.56	-	-	-
176	7.8×10^{-3}	4.0×10^{-2}	-	0.79	-	-	-	-
196	4.4×10^{-3}	4.0×10^{-3}	0.76	-	-	-	-	-
925	3.2×10^{-6}	9.8×10^{-5}	-	-	-	-	2.0×10^{-4}	-
1368	6.4×10^{-7}	4.9×10^{-6}	-	-	-	0.81	-	-
1373	6.4×10^{-7}	4.9×10^{-6}	-	-	-	-	0.81	-
1696	3.7×10^{-7}	8.5×10^{-6}	-	-	-	-	-	0.70

that the results from the shell model agree very well with the 3D model. Since the 3D model has more degrees of freedom, its spectrum is longer. One interesting feature is the clear jump in eigenvalues around the 900th mode, which is consistent with the findings in [161, 140].

Table 4.1 summarizes the mass participation factor of important modes from the shell model, and Figure 4.2 shows the corresponding deformed shape of these modes. The first modes are bending modes, which are expected as they represent the main behavior of the structure. The modes from about the 176th to the 924th are in-plane membrane modes. These modes involve mostly the motion of the mid-plane surface. However, after the jump, the modes become dominated by the shell directors without the mid-plane motion. They include transverse shear modes (e.g., 925th to 1695th) and eventually thickness-change modes from the 1696th mode. This behavior shows the 3D property of the 7-parameter shell elements. It is worth noting that this jump is not observed in 5-parameter shell models (Reissner-Mindlin shells), as investigated in [161, 140]. The primary reason for this jump in solid and solid-like shell models is that the numerical models exhibit significantly higher stiffness in the thickness direction compared to the in-plane direction, which is realistic for thin shells [161].

Impact on implicit solvers. In implicit solvers, achieving high convergence rates and utilizing large time steps is crucial for computational efficiency. However, the high-frequency modes after the jump, as seen in Figure 4.1(b), lead to poor conditioning of the tangent stiffness matrix. This makes the convergence of iterative solvers slower. This

issue was also studied in [161, 102], where two preconditioning techniques were proposed to eliminate the jump in the spectrum. Those are the *Scaled Director Conditioning* [161] and the *Scale Thickness Conditioning* [102].

Nevertheless, it is also important to mention that many membrane modes, such as the 925th, are already considered high-frequency modes in thin shells, and the above preconditioning techniques cannot filter them out in the solution process. These modes require unnecessarily small time steps to be captured. A common method to mitigate the impacts of high-frequency modes in implicit computations is to introduce numerical damping in the time integration scheme. In this work, we use the α-methods, represented by the Generalized-α scheme (see Section 4.2).

Impact on the critical time step. In explicit dynamic analysis, the critical time step depends on the highest eigenfrequency, as shown in Eq. (4.5). The jump in high frequencies leads to unnecessarily small time steps, which increases the computational time. To mitigate this issue, we can employ the preconditioning techniques mentioned previously. These methods modify the measure of the shell directors through a scale factor, thereby affecting the formulation of the internal force vector at the element level.

Another effective approach is the *Selective Mass Scaling* method, which was first proposed in Olovsson et al. [131, 130]. This technique modifies only specific parts of the mass matrix, primarily those associated with high-frequency modes, while preserving the low-frequency behavior. As a result, it is possible to add artificial mass without significantly altering the physical response. In this thesis work, we adopt a version of this method from Cocchetti et al. [58], which was conceptualized for linear solid elements, as detailed below.

4.1.2 Selective Mass Scaling technique.

It has been previously shown that the high modes are governed by the degrees of freedom associated with $\mathbf{w}$ representing the change of shell directors. Therefore, considering a 7-parameter shell element, the nodal masses associated with the degrees of freedom $\mathbf{w}$ are scaled by a factor $\beta \geq 1$ as follows:

$$\hat{\hat{\mathbf{M}}}^e = \begin{bmatrix} \hat{\mathbf{M}}^e_{\mathbf{v}} & \mathbf{0} \\ \mathbf{0} & \beta \hat{\mathbf{M}}^e_{\mathbf{w}} \end{bmatrix} \tag{4.6}$$

where β is the scale factor, $\hat{\mathbf{M}}^e_{\mathbf{v}}$ and $\hat{\mathbf{M}}^e_{\mathbf{w}}$ are respectively the diagonal elementary mass matrices associated to the degrees of freedom of $\mathbf{v}$ and $\mathbf{w}$ detailed in Appendix A.2.

To gain insight into the scale factor β, let us present another common approach to estimate the critical time-step size in explicit solvers. Considering a shell element, the critical time step is defined as the time it takes the fastest wave to propagate within the shortest length of the element, which is usually the shell thickness h^e, as follows:

$$\Delta t_{crit} \approx \frac{h^e}{c_p} \tag{4.7}$$

where c_p is the velocity of the fastest wave, corresponding to the speed of the P-wave, in the continuum. It is worth noting that the velocity c_p is equal to $\sqrt{(\lambda + 2\mu)/\rho}$, where ρ denotes the mass density, λ and μ are the Lamé coefficients of the continuum. Thus, the idea here is to modify the mass matrix by the scale factor β to decrease the wave velocity in the thickness direction and obtain the new critical time step as follows:

$$\Delta t_{crit,new} \approx \frac{h^e}{c_p}\sqrt{\beta} \leq \frac{l^e}{c_p} \tag{4.8}$$

The inequality in the above equation indicates that the new critical time step cannot exceed the time it takes the fastest wave to propagate within the distance l^e between the two closest nodes in the element. Therefore, we can parameterize the scale factor β using the following equation:

$$\beta = \beta_0 \, \frac{A^e}{(h^e)^2} \propto \left(\frac{l^e}{h^e}\right)^2 \tag{4.9}$$

Now, let us get back to the thin plate considered in Section 4.1. The plate thickness is 0.002 meters, and element size is 2.0×2.0 meters, which gives $A^e = 4$ and $l^e = 0.5 \times 2.0 = 1.0$ meter for 8-node quadrilateral elements. In Figure 4.3, several values of the β_0 parameter are considered to evaluate its effect on the eigenvalue spectra of the structure. It can be seen that when β_0 increases, the characteristic jump is less significant, but at the same time, the spectrum in the lower range (between the 100th and 200th eigenmodes) is affected more. Concerning the critical time step, with $\beta_0 = 0.2$, the critical time step is multiplied by a factor of 450, which is pretty much the ratio of l^e/h^e. Thus, for $\beta_0 > 0.2$, the multiplicative factor remains at about 450, as seen in Figure 4.3(b). It is worth noting that for 8-node quadrilateral elements whose sizes are equal, the value of β_0 between 0.20 and 0.25 is optimal as the ratio A^e/l^e is equal to 4.0.

As a conclusion, β_0 parameter should be carefully chosen to alleviate the jump in the eigenvalue spectrum while not altering the important eigenmodes in the transient

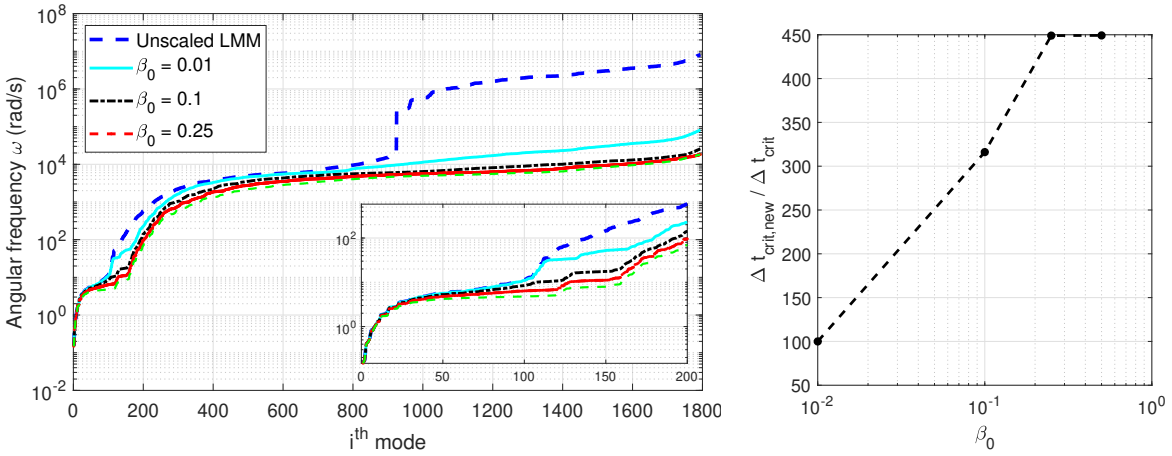

(a) Modal spectra obtained with different values of β_0 (b) Critical time step versus β_0

Figure 4.3 Thin plate described in Figure 4.1a: Effect of the parameter β_0 on the eigenvalue spectra and the critical time step

structural response. In practice, the ratio of l^e/h^e is approximately 5 to 10; therefore, the SMS technique can be employed to increase the critical time step by the same factor.

4.2 Implicit Nonlinear Dynamic Analysis

In this section, we detail the solver based on the Newton–Raphson method for implicit nonlinear dynamic analysis. We consider here the geometric and material nonlinearities, as well as the non-conservative pressure loads. As investigated in Section 4.1, it is desirable and necessary to filter out the high-frequency modes. To this goal, it is common to employ dissipative time integration schemes [113, 112]. Several methods have been developed initially for elastodynamics and investigated in the context of geometrically nonlinear dynamics, such as the Bossak-α Method (BAM), the Hilber-α Method (HHT), and the Generalized-α Method (G-α); the latter encompasses the former two as special cases. In the following, we employ the modified version of these implicit α-methods, which was investigated in Brank et al. [39], Lavrencic and Brank [114].

4.2.1 Modified α-methods for nonlinear dynamics

We consider the Generalized-α Method as the general case of the α-methods. The Generalized-α Method introduces the generalized mid-points $t_{n+1-\alpha_f}$ and $t_{n+1-\alpha_m}$ and shifts the acceleration, velocity, and displacement in the governing equations from t_{n+1}

Table 4.2 Applied time integration parameters as a function of the spectral radius ρ_∞

Method	α_m	α_f	β	γ
Newmark	0	0	$1/(1+\rho_\infty^2)$	$\frac{3-\rho_\infty}{2(1+\rho_\infty)}$
Hilber-α	0	$\frac{1-\rho_\infty}{\rho_\infty+1}$	$0.25(1+\alpha_f)^2$	$0.5+\alpha_f$
Bossak-α	$\frac{\rho_\infty-1}{\rho_\infty+1}$	0	$0.25(1-\alpha_m)^2$	$0.5-\alpha_m$
Generalized-α	$\frac{2\rho_\infty-1}{\rho_\infty+1}$	$\frac{\rho_\infty}{\rho_\infty+1}$	$0.25(1-\alpha_m+\alpha_f)^2$	$0.5-\alpha_m+\alpha_f$

to these mid-points as follows:

$$\begin{cases} \mathbf{M}\,\ddot{\mathbf{q}}_{n+1-\alpha_m} + \mathbf{C}\,\dot{\mathbf{q}}_{n+1-\alpha_f} + \mathbf{f}_{\text{int},n+1-\alpha_f} - \mathbf{f}_{\text{ext},n+1-\alpha_f} - \mathbf{L}^{\mathrm{T}}\boldsymbol{\Lambda}_{n+1-\alpha_f} = \mathbf{0} \\ \mathbf{L}\,\mathbf{q}_{n+1-\alpha_f} - \mathbf{B}_{n+1-\alpha_f} = \mathbf{0} \end{cases} \tag{4.10}$$

where the linear interpolation is used to determine the nodal values within $[t_n, t_{n+1}]$:

$$\begin{aligned} \ddot{\mathbf{q}}_{n+1-\alpha_m} &= (1-\alpha_m)\,\ddot{\mathbf{q}}_{n+1} + \alpha_m\,\ddot{\mathbf{q}}_n \\ \dot{\mathbf{q}}_{n+1-\alpha_f} &= (1-\alpha_f)\,\dot{\mathbf{q}}_{n+1} + \alpha_f\,\dot{\mathbf{q}}_n \\ \boldsymbol{\Lambda}_{n+1-\alpha_f} &= (1-\alpha_f)\,\boldsymbol{\Lambda}_{n+1} + \alpha_f\,\boldsymbol{\Lambda}_n \\ \mathbf{B}_{n+1-\alpha_f} &= (1-\alpha_f)\,\mathbf{B}_{n+1} + \alpha_f\,\mathbf{B}_n \end{aligned} \tag{4.11}$$

The time integration parameters β, γ, α_f and α_m are given as functions of spectral radius $\rho_\infty \in [0,1]$ which is used to control the high-frequency dissipation. In the present work, we adopt the functions as given in Table 4.2, which are derived in [56] as optimal for minimizing numerical dissipation at the low-frequency range and maximizing it in the high-frequency range in elastodynamics.

In the present work, we employ the simplification on the computation of $\mathbf{f}_{\text{int},n+1-\alpha_f}$ that was investigated in [39, 114], given as follows:

$$\mathbf{f}_{\text{int},n+1-\alpha_f} \approx (1-\alpha_f)\,\mathbf{f}_{\text{int},n+1} + \alpha_f\,\mathbf{f}_{\text{int},n} \tag{4.12}$$

It is worth noting that the same simplification is also employed with the Hilber-α Method in ABAQUS [2]. This simplification is the reason for the word "modified" in the title of

this section. A similar simplification is made on the external force vector as follows:

$$\mathbf{f}_{\text{ext},n+1-\alpha_f} \approx (1-\alpha_f)\,\mathbf{f}_{\text{ext}}(t_{n+1},\mathbf{q}_{n+1}) + \alpha_f\,\mathbf{f}_{\text{ext}}(t_n,\mathbf{q}_n) \tag{4.13}$$

4.2.2 Newton-Raphson resolution procedure

Iterative procedure. Using the Generalized-α Method presented previously, the residual of the equation of motion writes:

$$\begin{aligned}\mathbf{R}_m = &\left(\frac{1-\alpha_m}{\beta\Delta t^2}\,\mathbf{M} + \frac{(1-\alpha_f)\,\gamma}{\beta\Delta t}\mathbf{C}\right)\Delta\mathbf{q} \;\; ... \\ &+ (1-\alpha_f)\left(\mathbf{f}_{\text{int},n+1} - \mathbf{f}_{\text{ext},n+1} - \mathbf{L}^{\mathrm{T}}\boldsymbol{\Lambda}_{n+1}\right) + \mathbf{f}_n = \mathbf{0}\end{aligned} \tag{4.14}$$

followed by the residual of the linear kinematic constraint:

$$\mathbf{R}_c = (1-\alpha_f)\,\mathbf{L}\,\mathbf{q}_{n+1} - (1-\alpha_f)\,\mathbf{B}_{n+1} = \mathbf{0} \tag{4.15}$$

In Eq. (4.14), the global vector $\mathbf{f}_n$ is defined as:

$$\mathbf{f}_n = \mathbf{M}\,\ddot{\mathbf{q}}_{pn} + \mathbf{C}\,\dot{\mathbf{q}}_{pn} + \alpha_f\,(\mathbf{f}_{\text{int},n} - \mathbf{f}_{\text{ext},n} - \mathbf{L}^{\mathrm{T}}\boldsymbol{\Lambda}_n) \tag{4.16}$$

where

$$\begin{aligned}\ddot{\mathbf{q}}_{pn} &= -\frac{1-\alpha_m}{\beta\Delta t}\dot{\mathbf{q}}_n - \frac{1-\alpha_m-2\beta}{2\beta}\ddot{\mathbf{q}}_n \\ \dot{\mathbf{q}}_{pn} &= -\frac{(1-\alpha_f)\gamma-\beta}{\beta}\dot{\mathbf{q}}_n - \frac{(1-\alpha_f)(\gamma-2\beta)}{2\beta}\Delta t\,\ddot{\mathbf{q}}_n\end{aligned} \tag{4.17}$$

We consider the global residual vector $\mathbf{R} = \begin{bmatrix}\mathbf{R}_m & \mathbf{R}_c\end{bmatrix}^{\mathrm{T}}$. The linearization process at the $(k+1)^{th}$ iteration writes:

$$\mathbf{R}(\mathbf{q}_{n+1}^k, \boldsymbol{\Lambda}_{n+1}^k) + \mathbf{A}_T \begin{bmatrix}\mathrm{d}\mathbf{q} \\ \mathrm{d}\boldsymbol{\Lambda}\end{bmatrix} = \mathbf{0} \tag{4.18}$$

where $\mathbf{A}_T(t_{n+1}, \mathbf{q}_{n+1}^k)$ represents the global tangent operator of the system defined as:

$$\mathbf{A}_T = (1-\alpha_f)\begin{bmatrix}\tilde{\mathbf{K}}_T - \mathbf{K}_L & -\mathbf{L}^{\mathrm{T}} \\ -\mathbf{L} & \mathbf{0}\end{bmatrix} \tag{4.19}$$

and $\tilde{\mathbf{K}}_T$ is the effective tangent stiffness matrix defined as:

$$\tilde{\mathbf{K}}_T(\Delta t, \mathbf{q}_{n+1}^k) = \frac{1-\alpha_m}{1-\alpha_f}\frac{1}{\beta\Delta t^2}\mathbf{M} + \frac{\gamma}{\beta\Delta t}\mathbf{C} + \mathbf{K}_T(\mathbf{q}_{n+1}^k) \tag{4.20}$$

In the above equations, $\mathbf{K}_T(\mathbf{q}_{n+1}^k)$ and $\mathbf{K}_L(t_{n+1}, \mathbf{q}_{n+1}^k)$ are respectively the global tangent stiffness matrix and the global loading tangent matrix as defined in Section 2.6. The solution at the $(k+1)^{th}$ iteration is updated as follows:

$$\begin{bmatrix}\Delta\mathbf{q}^{k+1}\\ \Delta\boldsymbol{\Lambda}^{k+1}\end{bmatrix} = \begin{bmatrix}\Delta\mathbf{q}^{k}\\ \Delta\boldsymbol{\Lambda}^{k}\end{bmatrix} + \begin{bmatrix}\mathrm{d}\mathbf{q}\\ \mathrm{d}\boldsymbol{\Lambda}\end{bmatrix}, \qquad \begin{bmatrix}\mathbf{q}^{k+1}\\ \boldsymbol{\Lambda}^{k+1}\end{bmatrix} = \begin{bmatrix}\mathbf{q}^{k}\\ \boldsymbol{\Lambda}^{k}\end{bmatrix} + \begin{bmatrix}\mathrm{d}\mathbf{q}\\ \mathrm{d}\boldsymbol{\Lambda}\end{bmatrix} \tag{4.21}$$

Adaptive time-step-size. In implicit solvers, it is common to adapt the time-step-size $\Delta t = t_{n+1} - t_n$ based on the convergence rate of the solution at t_n. In this present work, we employ the time-step-size function used in [114] as follows:

$$\Delta t_{min} \leq \Delta t = B(I_0, I_n)\Delta t_p \leq \Delta t_{max}, \quad B = \begin{cases} 2 - \left(\dfrac{I_n - 1}{I_0 - 1}\right), & I_n < I_0 \\ 1 - \dfrac{1}{2}\left(\dfrac{I_n - I_0}{N_{max} - I_0}\right), & I_n \geq I_0 \end{cases} \tag{4.22}$$

where Δt_p and I_n are the time-step-size and the number of iterations of the previous increment, Δt_{min} and Δt_{max} are the user-defined minimum and maximum time-step-size, and I_0 and N_{max} are the desired and the maximal allowed number of iterations. If the residual does not vanish after N_{max} iterations, the time step is re-computed with $\Delta t/2$. The algorithm of the Newton-Raphson iterative procedure for the time step $[t_n, t_{n+1}]$ is summarized in Algorithm 2.

The well-known principal advantage of the Newton-Raphson method is its significant convergence rate. The major disadvantage of the method lies in solving the linearized equation in Eq. (4.18). This process requires computing and factorizing the tangent operator for each iteration. Therefore, when the problem size increases, the computational cost of solving this linear equation increases significantly. This motivates the development of the implicit solver using the Asymptotic Numerical Method, which will be presented in Section 4.3.

Algorithm 2 Newton-Raphson procedure for the time step $[t_n, t_{n+1}]$, given the maximum number of iteration N_{max} and the tolerance for relative residual δ_{NR}

Require: Time-step-size Δt, solution at t_n : $(\cdot)_n$, tangent operator $\mathbf{A}_T = \mathbf{A}_T((\cdot)_n)$
  Set $(\cdot)^{(0)} = (\cdot)_n$
  Evaluate residual vector $\mathbf{R}^{(0)} = \mathbf{R}(t_{n+1}, (\cdot)^{(0)})$
  Set $k = 0$
  while $k \leq N_{max}$ **do**
    Evaluate $\begin{bmatrix} \mathrm{d}\mathbf{q} & \mathrm{d}\boldsymbol{\Lambda} \end{bmatrix}^{\mathrm{T}}$ from Eq. (4.18)
    Update the solution at $(k+1)^{th}$ iteration using Eq. (4.21)
    Loop on elements to evaluate:

$$\mathbf{K}_T = \mathbf{K}_T((\cdot)^{k+1}), \qquad \mathbf{f}_{\mathrm{int},n+1} = \mathbf{f}_{\mathrm{int}}((\cdot)^{k+1}), \qquad \mathbf{f}_{\mathrm{ext},n+1} = \mathbf{f}_{\mathrm{ext}}(t_{n+1}, (\cdot)^{k+1})$$

    Evaluate $\mathbf{R}^{k+1} = \mathbf{R}(t_{n+1}, (\cdot)^{k+1})$ using Eq. (4.14) and Eq. (4.15)
    Update $\mathbf{A}_T = \mathbf{A}_T(\Delta t, \mathbf{K}_T)$
    Evaluate relative error: $\delta = \| \mathbf{R}_m^{k+1} \| \, / \, \| \mathbf{f}_{\mathrm{int},n+1} \|$
    if $\delta \leq \delta_{NR}$ **then**
      break
    else
      $k = k + 1$
    end if
  end while
  if $\delta \leq \delta_{NR}$ **then**
    $(\cdot)_{n+1} = (\cdot)^{k+1}$
    Evaluate the new time-step-size using Eq.(4.22)
    Update $\mathbf{A}_T = \mathbf{A}_T(\Delta t, \tilde{\mathbf{K}}_T)$
  else
    Reduce time-step size: $\Delta t = \Delta t/2$
    if $\Delta t < \Delta t_{min}$ **then** break
    end if
    Update $\mathbf{A}_T = \mathbf{A}_T(\Delta t, \tilde{\mathbf{K}}_T)$ and restart the procedure
  end if

4.3 Asymptotic Numerical Method for Implicit Geometrically Nonlinear Dynamics

This section presents the Asymptotic Numerical Method (ANM) as an efficient alternative technique for buckling dynamic analysis. In this section, we consider the geometric nonlinearities, as well as the deformation-dependent pressure load. The central idea of ANM is rooted in perturbation theory, where the solution is approximated by a power series expansion in a small parameter ϵ. This parameter may be a physical scalar already present in the nonlinear problem or an artificially introduced scalar, called a homotopy parameter, used to control the degree of nonlinearity. Claude et al. [57] followed the first option, by using the time t as the parameter, thus the time step Δt was automatically adjusted during the simulation. However, the numerical tests revealed that the adjusted time steps were considerably smaller than those typically used in the NR solver. In this work, we adopt the second choice as originally done by Cochelin and Compain [60]. To illustrate the fundamental concept, let us consider a nonlinear equation of the form:

$$R(U) = C + L(U) + Q(U, U) = 0 \tag{4.23}$$

where U is the primary unknown, C denotes a constant term, $L(U)$ denotes the solvable linear part of the residual, and $Q(U)$ denotes the quadratic nonlinear contribution. Introducing a homotopy parameter ϵ to perturb the nonlinear part yields:

$$R(U) = C + L(U) + \epsilon\, Q(U, U) = 0 \tag{4.24}$$

The original nonlinear equation is recovered when $\epsilon = 1$. ANM approximates the solution U in the form of a power series in ϵ:

$$\begin{aligned} U = \sum_{p=1}^{\infty} \epsilon^{p-1}\, U_p &= \sum_{p=1}^{N} \epsilon^{p-1}\, U_p + \sum_{p=N+1}^{\infty} \epsilon^{p-1}\, U_p \\ &= \sum_{p=1}^{N} \epsilon^{p-1}\, U_p + \mathcal{O}(\epsilon^N) \end{aligned} \tag{4.25}$$

Here, U_p are the p-order terms in the power series, N is the truncated order, and $\mathcal{O}(\epsilon^N)$ denotes all terms of order higher than or equal to N in ϵ. Substituting the series in

Eq. (4.25) into Eq. (4.24), we obtain:

$$\begin{aligned} R(U) &= C + \sum_{p=1}^{\infty} \epsilon^{p-1} L(U_p) + \sum_{p=1}^{\infty} \sum_{r=1}^{\infty} \epsilon\, Q(\epsilon^{p-1} U_p, \epsilon^{r-1} U_r) \\ &= C + \sum_{p=1}^{\infty} \epsilon^{p-1} L(U_p) + \sum_{p=1}^{\infty} \sum_{r=1}^{\infty} \epsilon^{p+r-1} Q(U_p, U_r) \\ &= C + \sum_{p=1}^{N} \epsilon^{p-1} L(U_p) + \sum_{p=1}^{N} \left(\epsilon^{p-1} \sum_{r=1}^{p-1} Q(U_r, U_{p-r}) \right) + \mathcal{O}(\epsilon^N) \end{aligned} \tag{4.26}$$

Equating terms of the same power in ϵ yields a sequence of linear problems:

$$\begin{aligned} p = 1\,(\epsilon^0) &: C + L(U_1) = 0 \\ p \geq 2\,(\epsilon^{p-1}) &: L(U_p) + \sum_{r=1}^{p-1} Q(U_r, U_{p-r}) = 0 \end{aligned} \tag{4.27}$$

which can be solved successively, as all involve the same linear operator $L(\cdot)$. Once the solution series is obtained, the final approximation is computed by evaluating the series at $\epsilon = 1$, thus recovering the solution of the original nonlinear problem in Eq. (4.23).

In this section, we apply the above methodology to geometrically nonlinear dynamics. The goal is to develop a general ANM solver applicable to both three-dimensional solid elements and 7-parameter shell formulations, capable of accounting for linear kinematic constraints. We begin by formulating the power series expansion of the solution at the element level, considering first solid elements and then 7-parameter shell elements. Subsequently, the solution technique is then developed at the global discrete level, considering residual expressions defined in Eqs. (4.14) and (4.15). To complete the algorithmic framework, we introduce the convergence criteria and the control parameters for the proposed ANM solver. The section concludes with a comparative discussion of the ANM and the traditional Newton–Raphson method in terms of resolution strategy and computational efficiency.

4.3.1 ANM development for three-dimensional solid elements

This section considers solid elements formulated in Chapter 2 to construct the ANM solution using the methodology introduced previously. We focus solely on the geometrical nonlinearity in the internal virtual work. It is worth noting that we can also construct the ANM solution directly from the discrete form. However, we prefer to begin with the

continuous weak form to see how the perturbation technique can be applied to solve the geometric nonlinearity. Let us write the virtual internal work of a solid element evaluated at an arbitrary time t using its definition in Eq. (2.29) as follows:

$$\delta\Pi^e_{\text{int}}(\boldsymbol{u}(t), \boldsymbol{S}(t)) = \int_{\Omega^e} \delta\boldsymbol{E}(\delta\boldsymbol{u}, \boldsymbol{u}(t)) : \boldsymbol{S}(t)\, d\Omega \tag{4.28}$$

In Eq. (4.28), $\boldsymbol{u}$ is considered as the primary variable, whereas $\boldsymbol{S}$ is considered as the intermediate variable, which is treated only at the element level. We suppose that the solution at the initial time $\boldsymbol{u}_0 = \boldsymbol{u}(t = t_0)$ and $\boldsymbol{S}_0 = \boldsymbol{S}(t = t_0)$ are known. Consider the linear Saint-Venant-Kirchhoff material, the PK2 tensor is given as:

$$\boldsymbol{S}(t) = \boldsymbol{\mathcal{D}} : \boldsymbol{E}(\boldsymbol{u}(t)) \tag{4.29}$$

In the following, the symbols $(\cdot)^e$ and $(\cdot)(t)$ are omitted for clarity, and the symbol $(\cdot)_0$ denotes the known solution of $(\cdot)$ at the time $t = t_0$.

Linear and Quadratic parts. The first step is to express the internal virtual work in Eq. (4.28) in the form in Eq. (4.23), which means that we need to separate the linear and nonlinear parts in the internal virtual work. To achieve this, the strategy is to express the governing equations in terms of the known solution $(\cdot)$ and the increment $\Delta(\cdot) = (\cdot) - (\cdot)_0$. We start with the Green-Lagrange strain. Let us remind the strain-displacement relation as follows:

$$\boldsymbol{E}(\boldsymbol{u}) = \frac{1}{2}\left(\frac{\partial \boldsymbol{u}}{\partial \boldsymbol{X}} + \frac{\partial \boldsymbol{u}}{\partial \boldsymbol{X}}^{\mathrm{T}} + \frac{\partial \boldsymbol{u}}{\partial \boldsymbol{X}}^{\mathrm{T}} \cdot \frac{\partial \boldsymbol{u}}{\partial \boldsymbol{X}}\right) = \boldsymbol{E}^l(\boldsymbol{u}) + \boldsymbol{E}^{nl}(\boldsymbol{u}, \boldsymbol{u}) \tag{4.30}$$

where $\boldsymbol{E}^l(\boldsymbol{u})$ and $\boldsymbol{E}^{nl}(\boldsymbol{u}, \boldsymbol{u})$ denote the linear and quadratic parts of the Green-Lagrange strain tensor with respect to the displacement $\boldsymbol{u}$. Similarly, the variation of the Green-Lagrange strain tensor writes:

$$\delta\boldsymbol{E} = \frac{1}{2}\left(\frac{\partial \delta\boldsymbol{u}}{\partial \boldsymbol{X}} + \frac{\partial \delta\boldsymbol{u}}{\partial \boldsymbol{X}}^{\mathrm{T}} + \frac{\partial \delta\boldsymbol{u}}{\partial \boldsymbol{X}}^{\mathrm{T}} \cdot \frac{\partial \boldsymbol{u}}{\partial \boldsymbol{X}} + \frac{\partial \boldsymbol{u}}{\partial \boldsymbol{X}}^{\mathrm{T}} \cdot \frac{\partial \delta\boldsymbol{u}}{\partial \boldsymbol{X}}\right) = \delta\boldsymbol{E}^l(\delta\boldsymbol{u}) + \delta\boldsymbol{E}^{nl}(\boldsymbol{u}, \delta\boldsymbol{u}) \tag{4.31}$$

with:

$$\delta\boldsymbol{E}^{nl}(\boldsymbol{u}, \delta\boldsymbol{u}) = 2\boldsymbol{E}^{nl}(\boldsymbol{u}, \delta\boldsymbol{u}) \tag{4.32}$$

Thus, we can express the Green-Lagrange strain tensor measured by $\boldsymbol{u}$ in terms of the known solution $\boldsymbol{u}_0$ and the increment $\Delta\boldsymbol{u}$ as follows:

$$\begin{aligned}\boldsymbol{E} &= \boldsymbol{E}^l(\boldsymbol{u}_0+\Delta\boldsymbol{u}) + \boldsymbol{E}^{nl}(\boldsymbol{u}_0+\Delta\boldsymbol{u},\boldsymbol{u}_0+\Delta\boldsymbol{u})\\ &= \boldsymbol{E}^l(\boldsymbol{u}_0) + \boldsymbol{E}^{nl}(\boldsymbol{u}_0,\boldsymbol{u}_0) + \boldsymbol{E}^l(\Delta\boldsymbol{u}) + 2\boldsymbol{E}^{nl}(\boldsymbol{u}_0,\Delta\boldsymbol{u}) + \boldsymbol{E}^{nl}(\Delta\boldsymbol{u},\Delta\boldsymbol{u})\\ &= \boldsymbol{E}(\boldsymbol{u}_0) + \Delta\boldsymbol{E}(\boldsymbol{u}_0,\Delta\boldsymbol{u}) + \boldsymbol{E}^{nl}(\Delta\boldsymbol{u},\Delta\boldsymbol{u})\end{aligned} \tag{4.33}$$

Substituting the above relation into Eq.(4.29), the PK2 stress can be expressed as follows:

$$\boldsymbol{S} = \boldsymbol{S}_0 + \boldsymbol{\mathcal{D}} : \Delta\boldsymbol{E}(\boldsymbol{u}_0,\Delta\boldsymbol{u}) + \Delta\boldsymbol{S}^{nl} \tag{4.34}$$

with:

$$\Delta\boldsymbol{S}^{nl} = \boldsymbol{\mathcal{D}} : \boldsymbol{E}^{nl}(\Delta\boldsymbol{u},\Delta\boldsymbol{u}) \tag{4.35}$$

Similarly, let us express the variation $\delta\boldsymbol{E}(\delta\boldsymbol{u},\boldsymbol{u})$ in Eq. (4.31) in terms of the known solution $\boldsymbol{u}_0$ and the increment $\Delta\boldsymbol{u}$ as follows:

$$\begin{aligned}\delta\boldsymbol{E}(\delta\boldsymbol{u},\boldsymbol{u}_0+\Delta\boldsymbol{u}) &= \delta\boldsymbol{E}^l(\delta\boldsymbol{u}) + \delta\boldsymbol{E}^{nl}(\delta\boldsymbol{u},\boldsymbol{u}_0+\Delta\boldsymbol{u})\\ &= \delta\boldsymbol{E}(\delta\boldsymbol{u},\boldsymbol{u}_0) + \delta\boldsymbol{E}^{nl}(\delta\boldsymbol{u},\Delta\boldsymbol{u})\end{aligned} \tag{4.36}$$

Substituting Eq. (4.34) and Eq. (4.36) into Eq. (4.28), we can rewrite the continuous virtual internal work as follows:

$$\begin{aligned}\delta\Pi_{\text{int}} &= \int_\Omega \delta\boldsymbol{E}(\delta\boldsymbol{u},\boldsymbol{u}_0) : \boldsymbol{S}_0\, d\Omega \;\; ...\\ &\quad + \int_\Omega \left(\delta\boldsymbol{E}(\delta\boldsymbol{u},\boldsymbol{u}_0) : \boldsymbol{\mathcal{D}} : \Delta\boldsymbol{E}(\boldsymbol{u}_0,\Delta\boldsymbol{u}) + \delta\boldsymbol{E}^{nl}(\delta\boldsymbol{u},\Delta\boldsymbol{u}) : \boldsymbol{S}_0\right) d\Omega \;\; ...\\ &\quad + \int_\Omega \left(\delta\boldsymbol{E}(\delta\boldsymbol{u},\boldsymbol{u}_0) : \Delta\boldsymbol{S}^{nl} + \delta\boldsymbol{E}^{nl}(\delta\boldsymbol{u},\Delta\boldsymbol{u}) : \Delta\boldsymbol{S}\right) d\Omega\\ &= \delta\Pi_{\text{int},0} + \Delta\delta\Pi_{\text{int}}\end{aligned} \tag{4.37}$$

It can be observed in Eq. (4.37), the increment of the internal virtual work $\Delta\delta\Pi_{\text{int}} = \delta\Pi_{\text{int}} - \delta\Pi_{\text{int},0}$ is now separated into the linear and nonlinear quadratic parts with respect to $(\Delta\boldsymbol{u},\Delta\boldsymbol{S})$. It is worth noting that the above transformation is performed quite easily, thanks to the linearity of the material model.

Now, let us discretize the above development in space using finite solid elements as presented in Appendix A.1. We start with the PK2 stress vector:

$$\mathbf{S} = \mathbf{D}\left(\mathbf{B}^l\,\mathbf{q} + \frac{1}{2}\mathbf{B}^{nl}(\mathbf{q})\,\mathbf{q}\right) = \mathbf{S}_0 + \Delta\mathbf{S} \tag{4.38}$$

with:

$$\Delta\mathbf{S} = \mathbf{D}\,\bar{\mathbf{B}}(\mathbf{q}_0)\,\Delta\mathbf{q} + \Delta\mathbf{S}^{nl}\,, \qquad \Delta\mathbf{S}^{nl} = \frac{1}{2}\mathbf{D}\,\mathbf{B}^{nl}(\Delta\mathbf{q})\,\Delta\mathbf{q} \tag{4.39}$$

The transformation in Eq. (4.38) is obtained using the following relations:

$$\bar{\mathbf{B}}(\mathbf{q}) = \bar{\mathbf{B}}(\mathbf{q}_0) + \mathbf{B}^{nl}(\Delta\mathbf{q})\,, \qquad \mathbf{B}^{nl}(\Delta\mathbf{q})\,\mathbf{q}_0 = \mathbf{B}^{nl}(\mathbf{q}_0)\,\Delta\mathbf{q} \tag{4.40}$$

The discrete form of the internal virtual work in Eq. (4.37) writes:

$$\delta\Pi_{\text{int}} = \delta\mathbf{q}^{\mathrm{T}}\,\mathbf{f}_{\text{int}} = \delta\mathbf{q}^{\mathrm{T}}\Big(\mathbf{f}_{\text{int},0} + \mathbf{K}_T(\mathbf{q}_0)\,\Delta\mathbf{q} + \Delta\mathbf{F}^{nl}\Big) \tag{4.41}$$

or the element internal force vector writes:

$$\mathbf{f}_{\text{int}} = \int_\Omega \bar{\mathbf{B}}^{\mathrm{T}}(\mathbf{q}_0 + \Delta\mathbf{q})\;(\mathbf{S}_0 + \Delta\mathbf{S})\,d\Omega = \mathbf{f}_{\text{int},0} + \mathbf{K}_T(\mathbf{q}_0)\,\Delta\mathbf{q} + \Delta\mathbf{F}^{nl} \tag{4.42}$$

where $\mathbf{K}_T\,\Delta\mathbf{q}$ and $\Delta\mathbf{F}^{nl}$ denote the linear and nonlinear parts of the increment of the internal force vector, $\mathbf{K}_T$ is the element tangent stiffness matrix. The discrete form of the quadratic term $\Delta\mathbf{F}^{nl}$ is given as:

$$\Delta\mathbf{F}^{nl} = \int_\Omega \Big[\bar{\mathbf{B}}(\mathbf{q}_0)^{\mathrm{T}}\;\Delta\mathbf{S}^{nl} + \mathbf{B}^{nl}(\Delta\mathbf{q})^{\mathrm{T}}\;\Delta\mathbf{S}\Big]\,d\Omega \tag{4.43}$$

Perturbation. The second step is to perturb the nonlinear parts in the element internal force vector in Eq. (4.42). Along the lines of Eq. (4.24), let us introduce a homotopy parameter ϵ, and use it to perturb the nonlinear terms in Eq. (4.42) and Eq. (4.38) as follows:

$$\mathbf{f}_{\text{int}} = \mathbf{f}_{\text{int},0} + \mathbf{K}_T\,\Delta\mathbf{q} + \epsilon\Delta\mathbf{F}^{nl} \tag{4.44}$$

$$\Delta\mathbf{S} = \mathbf{D}\,\bar{\mathbf{B}}(\mathbf{q}_0)\,\Delta\mathbf{q} + \epsilon\Delta\mathbf{S}^{nl} \tag{4.45}$$

It is noted that the original internal force is obtained with $\epsilon = 1$. The homotopy parameter is then used to expand the variables into power series as done in Eq. (4.25). Thus, the increments $\Delta\mathbf{q}$ and $\Delta\mathbf{S}$ are approximated as follows:

$$\Delta\mathbf{q} = \sum_{p=1}^{N} \epsilon^{p-1}\Delta\mathbf{q}_p + \mathcal{O}(\epsilon^N)\,, \qquad \Delta\mathbf{S} = \sum_{p=1}^{N} \epsilon^{p-1}\Delta\mathbf{S}_p + \mathcal{O}(\epsilon^N) \tag{4.46}$$

It is noted that $\Delta\mathbf{S}$ is treated as an internal variable and is considered only at the element level. Substituting Eq. (4.46) and Eq. (4.39) into Eq. (4.45), we obtain the following equation:

$$\begin{aligned}\Delta\mathbf{S} &= \mathbf{D}\,\bar{\mathbf{B}}(\mathbf{q}_0)\sum_{p=1}^{N}\epsilon^{p-1}\Delta\mathbf{q}_p + \frac{1}{2}\epsilon\,\mathbf{D}\,\mathbf{B}^{nl}\left(\sum_{p=1}^{N}\epsilon^{p-1}\Delta\mathbf{q}_p\right)\sum_{r=1}^{N}\epsilon^{r-1}\Delta\mathbf{q}_p + \mathcal{O}(\epsilon^N)\\ &= \mathbf{D}\,\bar{\mathbf{B}}(\mathbf{q}_0)\sum_{p=1}^{N}\epsilon^{p-1}\Delta\mathbf{q}_p + \frac{1}{2}\mathbf{D}\sum_{p=1}^{N}\epsilon^{p-1}\sum_{r=1}^{p-1}\left(\mathbf{B}^{nl}(\Delta\mathbf{q}_r)\;\Delta\mathbf{q}_{p-r}\right) + \mathcal{O}(\epsilon^N)\\ &= \sum_{p=1}^{N}\epsilon^{p-1}\Delta\mathbf{S}_p + \mathcal{O}(\epsilon^N)\end{aligned} \tag{4.47}$$

Equating the above equation with respect to the power of ϵ, we get:

$$\Delta\mathbf{S}_p = \mathbf{D}\,\bar{\mathbf{B}}(\mathbf{q}_0)\;\Delta\mathbf{q}_p + \Delta\mathbf{S}_p^{nl} \tag{4.48}$$

with

$$\Delta\mathbf{S}_p^{nl} = \frac{1}{2}\mathbf{D}\sum_{r=1}^{p-1}\mathbf{B}^{nl}(\Delta\mathbf{q}_r)\;\Delta\mathbf{q}_{p-r} \tag{4.49}$$

Substituting Eq. (4.46) and Eq (4.39) into Eq (4.43), the term $\epsilon\Delta\mathbf{F}^{nl}$ is expanded as follows:

$$\epsilon\Delta\mathbf{F}^{nl} = \int_\Omega\left[\bar{\mathbf{B}}(\mathbf{q}_0)^{\mathrm{T}}\;\epsilon\Delta\mathbf{S}^{nl} + \epsilon\sum_{p=1}^{N}\epsilon^{p-1}\;\mathbf{B}^{nl}(\Delta\mathbf{q}_p)^{\mathrm{T}}\;\sum_{r=1}^{N}\epsilon^{r-1}\Delta\mathbf{S}_r + \mathcal{O}(\epsilon^N)\right]d\Omega \tag{4.50}$$

Thus, the power series of the element internal force vector in Eq. (4.44) writes:

$$\mathbf{f}_{\text{int}} = \mathbf{f}_{\text{int},0} + \sum_{p=1}^{N}\left[\epsilon^{p-1}\left(\mathbf{K}_T\,\Delta\mathbf{q}_p + \Delta\mathbf{F}_p^{nl}\right)\right] + \mathcal{O}(\epsilon^N) \tag{4.51}$$

where:

$$\Delta\mathbf{F}_p^{nl} = \int_\Omega\left[\bar{\mathbf{B}}(\mathbf{q}_0)^{\mathrm{T}}\;\Delta\mathbf{S}_p^{nl} + \sum_{r=1}^{p-1}\mathbf{B}^{nl}(\Delta\mathbf{q}_r)^{\mathrm{T}}\;\Delta\mathbf{S}_{p-r}\right]d\Omega \tag{4.52}$$

The element vector in Eq. (4.51) is used to construct the global internal vector as presented in Section 4.3.3. Let us summarize the element-level computation to construct

element vector $\Delta\mathbf{F}_p^{nl}$ and update internal variable $\Delta\mathbf{S}_p$ as follows:

$$\begin{aligned}\Delta\mathbf{S}_p^{nl} &= \frac{1}{2}\mathbf{D}\sum_{r=1}^{p-1}\mathbf{B}^{nl}(\Delta\mathbf{q}_r)\;\Delta\mathbf{q}_{p-r}\\ \Delta\mathbf{F}_p^{nl} &= \int_\Omega\left[\bar{\mathbf{B}}(\mathbf{q}_0)^{\mathrm{T}}\;\Delta\mathbf{S}_p^{nl}+\sum_{r=1}^{p-1}\mathbf{B}^{nl}(\Delta\mathbf{q}_r)^{\mathrm{T}}\;\Delta\mathbf{S}_{p-r}\right]d\Omega\\ \Delta\mathbf{S}_p &= \mathbf{D}\;\bar{\mathbf{B}}(\mathbf{q}_0)\;\Delta\mathbf{q}_p+\Delta\mathbf{S}_p^{nl}\end{aligned} \tag{4.53}$$

In the above equation, all the nonlinear terms vanish at order $p=1$.

4.3.2 ANM development for 7-parameter shell elements

This section considers the 7-parameter shell element formulated in Chapter 3. We applied the perturbation technique to handle the geometrical nonlinearity and also the deformation-dependent pressure load. The ANM development is quite similar to that for a solid element. Therefore, in this section, we present the finite element formulation directly. A significant remark here is that the internal virtual work of a 7-parameter shell element depends, in addition to the displacement field, on the EAS field, which is governed by the orthogonality condition. Let us remind ourselves of the discrete internal force vector of a 7-parameter shell element as follows:

$$\mathbf{f}_{\text{int}}=\int_\Omega\bar{\mathbf{B}}(\mathbf{q})^{\mathrm{T}}\;\mathbf{S}(\mathbf{E},\boldsymbol{\alpha})\;d\Omega \tag{4.54}$$

followed by the orthogonality condition that writes:

$$\mathbf{R}_\alpha=\int_\Omega\mathbf{B}_\alpha^{\mathrm{T}}\;S^{33}(\mathbf{E},\boldsymbol{\alpha})\;d\Omega=\mathbf{0} \tag{4.55}$$

The external pressure force vector writes:

$$\mathbf{f}_{\text{ext}}^e=\int_{-1}^{1}\int_{-1}^{1}k\,p\,\mathbf{N}^{\mathrm{T}}\;\mathbf{T}(\boldsymbol{g}_1)\;\boldsymbol{g}_2\;d\theta^1\,d\theta^2 \tag{4.56}$$

In the above equations, as well as in the following, for the sake of clarity, the symbol $(\cdot)^e$ is omitted, and the symbol $(\cdot)_0$ denotes the known solution at the time $t=t_0$.

Linear and Quadratic parts. As done with solid elements, we transform the internal force vector $\mathbf{f}_{\text{int}}(\mathbf{q})$ in terms of the known solution $(\cdot)$ and the increment $\Delta(\cdot)=(\cdot)-(\cdot)_0$.

Let us start with the PK2 vector:

$$\begin{aligned}\mathbf{S} &= \mathbf{D}\left(\mathbf{B}^{l}\,\mathbf{q} + \frac{1}{2}\mathbf{B}^{nl}(\mathbf{q})\,\mathbf{q}\right) + \mathbf{D}^{(:,3)}\,\mathbf{B}_{\alpha}\,\boldsymbol{\alpha} \\ &= \mathbf{S}_0 + \Delta\mathbf{S} + \mathbf{D}^{(:,3)}\,\mathbf{B}_{\alpha}\,\Delta\boldsymbol{\alpha}\end{aligned} \tag{4.57}$$

with:

$$\Delta\mathbf{S} = \mathbf{D}\,\bar{\mathbf{B}}(\mathbf{q}_0)\,\Delta\mathbf{q} + \Delta\mathbf{S}^{nl}\,, \qquad \Delta\mathbf{S}^{nl} = \frac{1}{2}\mathbf{D}\,\mathbf{B}^{nl}(\Delta\mathbf{q})\,\Delta\mathbf{q} \tag{4.58}$$

Concerning the orthogonality condition, we obtain the following expression by substituting Eq. (4.57) and Eq. (4.58) into Eq. (4.55):

$$\begin{aligned}&\mathbf{R}_{\alpha} = \mathbf{K}_{\alpha\alpha}\,\Delta\boldsymbol{\alpha} + \mathbf{K}_{\alpha u}\,\Delta\mathbf{q} + \Delta\mathbf{R}_{\alpha}^{nl} = \mathbf{0} \\ &\text{leading to: } \Delta\boldsymbol{\alpha} = -\mathbf{K}_{\alpha\alpha}^{-1}\left(\boldsymbol{K}_{\alpha u}\,\Delta\mathbf{q} + \Delta\mathbf{R}_{\alpha}^{nl}\right)\end{aligned} \tag{4.59}$$

with

$$\Delta\mathbf{R}_{\alpha}^{nl} = \int_{\Omega}\mathbf{B}_{\alpha}^{\mathrm{T}}\,\Delta S^{nl,33}\,d\Omega \tag{4.60}$$

where $\Delta S^{nl,33}$ is the third component in the vector $\Delta\mathbf{S}^{nl}$, or can be explicitly expressed as:

$$\Delta S^{nl,33} = \mathcal{D}^{33ij}\left(\frac{\partial\Delta\boldsymbol{u}}{\partial\theta^{i}}\cdot\frac{\partial\Delta\boldsymbol{u}}{\partial\theta^{j}}\right) \tag{4.61}$$

By substituting Eq. (4.57), Eq. (4.58), and Eq. (4.59) into Eq. (4.54), we can separate the linear and nonlinear parts in the element internal force as follows:

$$\mathbf{f}_{\mathrm{int}} = \mathbf{f}_{\mathrm{int},0} + \mathbf{K}_{T}(\mathbf{q}_0)\,\Delta\mathbf{q} + \Delta\mathbf{F}^{nl} \tag{4.62}$$

with:

$$\mathbf{K}_{T}(\mathbf{q}_0) = \mathbf{K}_{uu} - \mathbf{K}_{u\alpha}\,\mathbf{K}_{\alpha\alpha}^{-1}\mathbf{K}_{u\alpha}^{\mathrm{T}} \tag{4.63}$$

and:

$$\Delta\mathbf{F}^{nl} = \int_{\Omega}\left(\bar{\mathbf{B}}(\mathbf{q}_0)^{\mathrm{T}}\,\Delta\mathbf{S}^{nl} + \mathbf{B}^{nl}(\Delta\mathbf{q})^{\mathrm{T}}\,\Delta\mathbf{S}\right)\,d\Omega - \mathbf{K}_{u\alpha}\,\mathbf{K}_{\alpha\alpha}^{-1}\,\Delta\mathbf{R}_{\alpha}^{nl} \tag{4.64}$$

where:

$$\begin{aligned}\mathbf{K}_{uu} &= \int_\Omega \bar{\mathbf{B}}(\mathbf{q}_0)^{\mathrm{T}}\,\mathbf{D}\,\bar{\mathbf{B}}(\mathbf{q}_0)\,d\Omega \\ \mathbf{K}_{u\alpha} &= \int_\Omega \bar{\mathbf{B}}(\mathbf{q}_0)^{\mathrm{T}}\,\mathbf{D}^{(:,3)}\,\mathbf{B}_\alpha\,d\Omega \\ \mathbf{K}_{\alpha\alpha} &= \int_\Omega \mathbf{B}_\alpha^{\mathrm{T}}\,\mathcal{D}^{3333}\,\mathbf{B}_\alpha\,d\Omega\end{aligned} \tag{4.65}$$

More details on the finite discretization can be found in Appendix A.2.

Concerning the external pressure force in Eq. (4.56), let us write the following relation between the covariant in the current configuration $\boldsymbol{g}_\alpha$ and the known one $\boldsymbol{g}_{\alpha,0}$:

$$\begin{aligned}\boldsymbol{g}_1 &= \frac{\partial \boldsymbol{x}_0}{\partial\theta^1} + \frac{\partial \Delta\boldsymbol{u}}{\partial\theta^1} = \boldsymbol{g}_{1,0} + \frac{\partial \Delta\boldsymbol{u}}{\partial\theta^1} = \boldsymbol{g}_{1,0} + \mathbf{G}^{1:3}\,\Delta\mathbf{q} \\ \boldsymbol{g}_2 &= \frac{\partial \boldsymbol{x}_0}{\partial\theta^2} + \frac{\partial \Delta\boldsymbol{u}}{\partial\theta^2} = \boldsymbol{g}_{2,0} + \frac{\partial \Delta\boldsymbol{u}}{\partial\theta^2} = \boldsymbol{g}_{2,0} + \mathbf{G}^{4:6}\,\Delta\mathbf{q}\end{aligned} \tag{4.66}$$

Substituting the above equation into Eq. (4.56), we can rewrite the external pressure force vector as follows:

$$\mathbf{f}_{\text{ext}} = \mathbf{f}_{\text{ext}}(\mathbf{q}_0) + \mathbf{K}_L(\mathbf{q}_0)\,\Delta\mathbf{q} + \Delta\mathbf{L}^{nl} \tag{4.67}$$

where:

$$\mathbf{K}_L(\mathbf{q}_0)\,\Delta\mathbf{q} = \int_{-1}^{1}\int_{-1}^{1} k\,p\,\mathbf{N}^{\mathrm{T}}\,\left(\mathbf{T}(\boldsymbol{g}_{1,0})\,\mathbf{G}^{4:6} - \mathbf{T}(\boldsymbol{g}_{2,0})\,\mathbf{G}^{1:3}\right)\,\Delta\mathbf{q}\,d\theta^1\,d\theta^2 \tag{4.68}$$

and:

$$\Delta\mathbf{L}^{nl} = \int_{-1}^{1}\int_{-1}^{1} k\,p\,\mathbf{N}^{\mathrm{T}}\,\mathbf{T}\left(\mathbf{G}^{1:3}\,\Delta\mathbf{q}\right)\,\mathbf{G}^{4:6}\,\Delta\mathbf{q}\,d\theta^1\,d\theta^2 \tag{4.69}$$

Perturbation. Let us use the homotopy parameter to perturb the linear terms in Eq. (4.62), Eq. (4.59), and Eq. (4.67) as follows:

$$\begin{aligned}\mathbf{f}_{\text{int}} &= \mathbf{f}_{\text{int},0} + \mathbf{K}_T(\mathbf{q}_0)\,\Delta\mathbf{q} + \epsilon\Delta\mathbf{F}^{nl} \\ \mathbf{f}_{\text{ext}} &= \mathbf{f}_{\text{ext}}(\mathbf{q}_0) + \mathbf{K}_L(\mathbf{q}_0)\,\Delta\mathbf{q} + \epsilon\Delta\mathbf{L}^{nl}\end{aligned} \tag{4.70}$$

and:

$$\begin{aligned}\mathbf{S} &= \mathbf{S}_0 + \mathbf{D}\,\bar{\mathbf{B}}(\mathbf{q}_0)\,\Delta\mathbf{q} + \mathbf{D}^{(:,3)}\,\mathbf{B}_\alpha\,\Delta\boldsymbol{\alpha} + \epsilon\Delta\mathbf{S}^{nl} \\ \Delta\boldsymbol{\alpha} &= -\mathbf{K}_{\alpha\alpha}^{-1}\left(\mathbf{K}_{\alpha u}\,\Delta\mathbf{q} + \epsilon\Delta\mathbf{R}_\alpha^{nl}\right)\end{aligned} \tag{4.71}$$

The power series of the variable is given as:

$$\begin{aligned} \Delta\mathbf{q} &= \sum_{p=1}^{N} \epsilon^{p-1} \Delta\mathbf{q}_p + \mathcal{O}(\epsilon^N)\,, \qquad \Delta\mathbf{S} = \sum_{p=1}^{N} \epsilon^{p-1} \Delta\mathbf{S}_p + \mathcal{O}(\epsilon^N) \\ \Delta\boldsymbol{\alpha} &= \sum_{p=1}^{N} \epsilon^{p-1} \Delta\boldsymbol{\alpha}_p + \mathcal{O}(\epsilon^N) \end{aligned} \tag{4.72}$$

It is worth noting that $\Delta\mathbf{S}$ and $\Delta\boldsymbol{\alpha}$ are treated as internal variables and are considered only at the element level. Substituting the series in Eq. (4.72) into Eq. (4.70) yields:

$$\mathbf{f}_{\text{int}} = \mathbf{f}_{\text{int},0} + \sum_{p=1}^{N} \left[\epsilon^{p-1} \left(\mathbf{K}_T \, \Delta\mathbf{q}_p + \Delta\mathbf{F}_p^{nl} \right) \right] + \mathcal{O}(\epsilon^N) \tag{4.73}$$

with:

$$\begin{aligned} \Delta\mathbf{S}_p^{nl} &= \frac{1}{2}\mathbf{D} \sum_{r=1}^{p-1} \mathbf{B}^{nl}(\Delta\mathbf{q}_r) \, \Delta\mathbf{q}_{p-r}\,, \quad \Delta\mathbf{R}_{\alpha,p}^{nl} = \int_\Omega \mathbf{B}_\alpha^{\mathrm{T}} \, \Delta S_p^{nl,33} \, d\Omega \\ \Delta\mathbf{F}_p^{nl} &= \int_\Omega \left[\bar{\mathbf{B}}(\mathbf{q}_0)^{\mathrm{T}} \, \Delta\mathbf{S}_p^{nl} + \sum_{r=1}^{p-1} \mathbf{B}^{nl}(\Delta\mathbf{q}_r)^{\mathrm{T}} \, \Delta\mathbf{S}_{p-r} \right] d\Omega - \mathbf{K}_{\alpha u}^{\mathrm{T}} \, \mathbf{K}_{\alpha\alpha}^{-1} \, \Delta\mathbf{R}_{\alpha,p}^{nl} \\ \Delta\mathbf{S}_p &= \mathbf{D} \, \bar{\mathbf{B}}(\mathbf{q}_0) \, \Delta\mathbf{q}_p + \mathbf{D}^{(:,3)} \, \mathbf{B}_\alpha \, \Delta\boldsymbol{\alpha}_p + \Delta\mathbf{S}_p^{nl} \\ \Delta\boldsymbol{\alpha}_p &= -\mathbf{K}_{\alpha\alpha}^{-1} \left(\mathbf{K}_{\alpha u} \, \Delta\mathbf{q}_p + \Delta\mathbf{R}_{\alpha,p}^{nl} \right) \end{aligned} \tag{4.74}$$

The homotopic element external pressure force vector writes:

$$\mathbf{f}_{\text{ext}}(\mathbf{q}) = \mathbf{f}_{\text{ext}}(\mathbf{q}_0) + \mathbf{K}_L \, \Delta\mathbf{q} + \epsilon \Delta\mathbf{L}^{nl} \tag{4.75}$$

Substituting the series in Eq. (4.72) into the above equation, we expand the element external pressure force vector in a power series as follows:

$$\mathbf{f}_{\text{ext}}(\mathbf{q}) = \mathbf{f}_{\text{ext}}(\mathbf{q}_0) + \sum_{p=1}^{N} \left[\epsilon^{p-1} \left(\mathbf{K}_L \, \Delta\mathbf{q}_p + \Delta\mathbf{L}_p^{nl} \right) \right] + \mathcal{O}(\epsilon^N) \tag{4.76}$$

where:

$$\Delta\mathbf{L}_p^{nl} = \sum_{r=1}^{p-1} \int_{-1}^{1} \int_{-1}^{1} k \, p(t_{n+1}) \mathbf{N}^{\mathrm{T}} \, \mathbf{T} \left(\mathbf{G}^{1:3} \, \Delta\mathbf{q}_r \right) \, \mathbf{G}^{4:6} \, \Delta\mathbf{q}_{p-r} \, d\theta^1 \, d\theta^2 \tag{4.77}$$

It is noted that all nonlinear terms in Eq. (4.74) and Eq. (4.77) vanish at order $p = 1$.

4.3.3 ANM solver for geometrically nonlinear dynamics

In this section, we illustrate how the ANM solution for the global-level problem is constructed from the element-level ANM development presented previously. We focus on the residual of the governing equations presented in Eq. (4.14) and Eq. (4.15). In those governing equations, the solution at the time t_n is assumed to be known, and we seek the solution at the time t_{n+1}. Along the lines of the element-level development, the solution at the time t_{n+1} can be written in terms of incremental quantities and the known solution at the time t_n as follows:

$$\begin{Bmatrix} \mathbf{q}_{n+1} \\ \mathbf{\Lambda}_{n+1} \end{Bmatrix} = \begin{Bmatrix} \mathbf{q}_{n} \\ \mathbf{\Lambda}_{n} \end{Bmatrix} + \begin{Bmatrix} \Delta\mathbf{q} \\ \Delta\mathbf{\Lambda} \end{Bmatrix} \tag{4.78}$$

Linear and Quadratic parts in governing equations. Using the variable transformation in Eq. (4.78), we can rewrite the governing equations in Eq. (4.10) in terms of the incremental quantities and the known solution at time t_n. Let us first rewrite the linear terms in the equation of motion:

$$\begin{aligned} \ddot{\mathbf{q}}_{n+1-\alpha_m} &= \ddot{\mathbf{q}}_{pn} + \frac{(1-\alpha_m)}{\beta\Delta t^2}\,\Delta\mathbf{q} \\ \dot{\mathbf{q}}_{n+1-\alpha_f} &= \dot{\mathbf{q}}_{pn} + (1-\alpha_f)\,\frac{\gamma}{\beta\Delta t}\,\Delta\mathbf{q} \\ \mathbf{\Lambda}_{n+1-\alpha_f} &= \mathbf{\Lambda}_{n} + (1-\alpha_f)\,\Delta\mathbf{\Lambda} \end{aligned} \tag{4.79}$$

where $\ddot{\mathbf{q}}_{pn}$ and $\dot{\mathbf{q}}_{pn}$ are the predictor terms defined in Eq. (4.17).

For geometrically nonlinear problems, as shown in the element-level development in Eq. (4.42) and Eq. (4.62), the internal force vector at t_{n+1} can be expressed as:

$$\mathbf{f}_{\text{int},n+1} = \mathbf{f}_{\text{int},n} + \Delta\mathbf{f}_{\text{int}} = \mathbf{f}_{\text{int},n} + \mathbf{K}_{\text{T}}(\mathbf{q}_n)\,\Delta\mathbf{q} + \Delta\mathbf{F}^{\text{nl}}(\mathbf{q}_n, \Delta\mathbf{q}) \tag{4.80}$$

or at the generalized midpoint $t_{n+1-\alpha_f}$ as:

$$\mathbf{f}_{\text{int},n+1-\alpha_f} = \mathbf{f}_{\text{int},n} + (1-\alpha_f)\Big(\mathbf{K}_{\text{T}}(\mathbf{q}_n)\,\Delta\mathbf{q} + \Delta\mathbf{F}^{\text{nl}}(\mathbf{q}_n, \Delta\mathbf{q})\Big) \tag{4.81}$$

Here, $\mathbf{K}_{\text{T}}(\mathbf{q}_n)$ is the global tangent stiffness matrix evaluated at t_n, and $\Delta\mathbf{F}^{\text{nl}}$ represents the nonlinear increment of the internal force vector.

Similarly, the external pressure force is expressed as:

$$\mathbf{f}_{\text{ext}}(t_{n+1},\mathbf{q}_{n+1}) = \mathbf{f}_{\text{ext}}(t_{n+1},\mathbf{q}_n) + \mathbf{K}_{\text{L}}(t_{n+1},\mathbf{q}_n)\,\Delta\mathbf{q} + \Delta\mathbf{L}^{\text{nl}}(t_{n+1},\mathbf{q}_n,\Delta\mathbf{q}) \tag{4.82}$$

Substituting the above into Eq. (4.12), we obtain:

$$\begin{aligned}\mathbf{f}_{\text{ext},n+1-\alpha_f} &= (1-\alpha_f)\mathbf{f}_{\text{ext}}(t_{n+1},\mathbf{q}_n) + \alpha_f\mathbf{f}_{\text{ext}}(t_n,\mathbf{q}_n)\\ &\quad + (1-\alpha_f)\Big(\mathbf{K}_{\text{L}}(t_{n+1},\mathbf{q}_n)\,\Delta\mathbf{q} + \Delta\mathbf{L}^{\text{nl}}(t_{n+1},\mathbf{q}_n,\Delta\mathbf{q})\Big)\end{aligned} \tag{4.83}$$

Homotopy and Perturbation. Having separated the linear and quadratic parts in the governing equations, we introduce the homotopy parameter ϵ to perturb the nonlinear terms as follows:

$$(1-\alpha_f)\left[\left(\tilde{\mathbf{K}}_T(\mathbf{q}_n) - \mathbf{K}_L(t_{n+1},\mathbf{q}_n)\right)\,\Delta\mathbf{q} + \epsilon\left(\Delta\mathbf{F}^{\text{nl}} - \Delta\mathbf{L}^{\text{nl}}\right) - \mathbf{L}^{\text{T}}\,\Delta\mathbf{\Lambda}\right] = -\mathbf{f}_n \tag{4.84}$$

where $\tilde{\mathbf{K}}_T(\mathbf{q}_n)$ is the effective tangent stiffness matrix defined in Eq. (4.20) and the global vector $\mathbf{f}_n$ is given as:

$$\mathbf{f}_n = \mathbf{M}\,\ddot{\mathbf{q}}_{pn} + \mathbf{C}\,\dot{\mathbf{q}}_{pn} + \mathbf{f}_{\text{int},n} - (1-\alpha_f)\mathbf{f}_{\text{ext}}(t_{n+1},\mathbf{q}_n) - \alpha_f\mathbf{f}_{\text{ext}}(t_n,\mathbf{q}_n) - \mathbf{L}^{\text{T}}\,\mathbf{\Lambda}_n \tag{4.85}$$

As in Eq. (4.46), and Eq. (4.72), the variables are approximated as follows:

$$\begin{Bmatrix}\Delta\mathbf{q}\\ \Delta\mathbf{\Lambda}\end{Bmatrix} = \sum_{p=1}^{N}\epsilon^{p-1}\begin{Bmatrix}\Delta\mathbf{q}_p\\ \Delta\mathbf{\Lambda}_p\end{Bmatrix} + \mathcal{O}(\epsilon^N) \tag{4.86}$$

Substituting Eq. (4.86) into the perturbed system and the constraint equation, and collecting terms of equal powers in ϵ, we obtain a hierarchy of linear problems:

$$\begin{aligned} p=1\,(\epsilon^0) &: \mathbf{A}_T\begin{bmatrix}\Delta\mathbf{q}_1\\ \Delta\mathbf{\Lambda}_1\end{bmatrix} = -\begin{bmatrix}\mathbf{f}_n\\ (1-\alpha_f)(\mathbf{B}_{n+1}-\mathbf{B}_n)\end{bmatrix}\\ p\geq 2\,(\epsilon^{p-1}) &: \mathbf{A}_T\begin{bmatrix}\Delta\mathbf{q}_p\\ \Delta\mathbf{\Lambda}_p\end{bmatrix} = \begin{bmatrix}-\Delta\mathbf{F}_p^{\text{nl}} + \Delta\mathbf{L}_p^{\text{nl}}\\ \mathbf{0}\end{bmatrix}\end{aligned} \tag{4.87}$$

where the tangent operator $\mathbf{A}_T$ is defined as:

$$\mathbf{A}_T(t_{n+1}, \mathbf{q}_n) = (1 - \alpha_f) \begin{bmatrix} \tilde{\mathbf{K}}_T(\mathbf{q}_n) - \mathbf{K}_L(t_{n+1}, \mathbf{q}_n) & -\mathbf{L}^{\mathrm{T}} \\ -\mathbf{L} & \mathbf{0} \end{bmatrix} \tag{4.88}$$

and the high-order terms of the nonlinear increments are computed from the element level, as in Eq. (4.53) and Eq. (4.74), as functions of the lower-order computed solutions.

We can see that the original nonlinear system governed by Eq. (4.14) and Eq. (4.15) is now transformed into a set of linear systems in Eq. (4.87). These linear systems are characterized by the same tangent operator $\mathbf{A}_T$, and need to be solved sequentially. In general, the higher-order terms in the power series in Eq.(4.86) become successively smaller, which means that the power series converges to the solution. Assuming the sequential linear system is truncated at order $p = N$, the solution of the original nonlinear problem is computed using the power series in Eq.(4.86) with the homotopy parameter $\epsilon = 1$. The approximated solution at the t_{n+1} writes:

$$\begin{Bmatrix} \mathbf{q}_{n+1} \\ \mathbf{\Lambda}_{n+1} \end{Bmatrix} = \begin{Bmatrix} \mathbf{q}_n \\ \mathbf{\Lambda}_n \end{Bmatrix} + \sum_{p=1}^{N} \begin{Bmatrix} \Delta\mathbf{q}_p \\ \Delta\mathbf{\Lambda}_p \end{Bmatrix} + \mathcal{O}(\epsilon^N) \tag{4.89}$$

Here, a question naturally arises: how many orders does the power series need to provide an adequately accurate approximation of the solution?

Convergence criterion of the power series. The following condition can be used as the convergence criterion for the power series truncated at order N:

$$\delta = \frac{\| \Delta\mathbf{q}_N \|}{\sum_{p=1}^{N} \Delta\mathbf{q}_p} \leq \delta_{ANM} \tag{4.90}$$

where δ_{ANM} is a given tolerance. It is worth noting that we do not need to consider the series of Lagrange multipliers for the convergence criterion here, as the kinematic constraint is linear and the series converges easily at order 1.

The convergence criterion in Eq. (4.90) permits us to construct an order-adaptive algorithm. Indeed, in a given time step $[t_n, t_{n+1}]$, the order of the power series is increased until the convergence criterion is satisfied. Thus, we can easily adapt the order of the power series, which is also the number of linear problems, depending on the time step under consideration (i.e., the time-step size or the nonlinearity level).

Adaptive time-step-size Similar to the Newton-Raphson solver, it is desirable to adapt the time step based on the convergence rate. We employ here the time-step size function having the same form as the one in Eq. (4.22):

$$\Delta t_{min} \leq \Delta t = B(I_0, I_n)\Delta t_p \leq \Delta t_{max}, \quad B = \begin{cases} 2 - \left(\dfrac{I_n - 1}{I_0 - 1}\right), & I_n < I_0 \\ 1 - \dfrac{1}{2}\left(\dfrac{I_n - I_0}{N_{max} - I_0}\right), & I_n \geq I_0 \end{cases} \tag{4.91}$$

where Δt_p and I_n are the time-step size and the orders from the previous the increment, Δt_{min} and Δt_{max} are the user-defined minimum and maximum time-step-size, and I_0 and N_{max} are the desired and the maximal allowed power series orders. If the solution does not converge with N_{max} orders, the time step is re-computed with $\Delta t/2$. The algorithm of the ANM solver for the time step $[t_n, t_{n+1}]$ that we proposed is summarized in Algorithm 3.

Padé approximants The Padé approximants can be used to replace the power series, providing a better approximation of the solution. Several studies have employed this technique to improve the range of validity and to detect critical points [60, 8]. The Padé representation of the displacement $\mathbf{q}_{n+1}$ at order N is written as follows:

$$\mathbf{q}_{n+1} = \mathbf{q}_n + \sum_{p=1}^{N-1} \epsilon^{p-1} \frac{D_{N-p-1}}{D_{N-1}} \Delta \mathbf{q}_p + \mathcal{O}(\epsilon^{N-1}) \tag{4.92}$$

with D_i are the polynomials:

$$\begin{aligned} D_0 &= 1 \\ D_i &= D_0 + \sum_{k=1}^{i} \epsilon^k d_k = D_0 + \sum_{k=1}^{i} d_k \end{aligned} \tag{4.93}$$

where d_k, $k = 1, ..., i$ are the real coefficients determined by the Gram-Schmidt orthogonalization of the set of vectors $\{\Delta \mathbf{q}_1, \Delta \mathbf{q}_2, ..., \Delta \mathbf{q}_i\}$. The details of this technique can be found in [72].

Replacing the power series in Eq. (4.86) as well as Eq. (4.46) and Eq. (4.72) by the series in Eq. (4.92), we obtain the same set of linear problems in Eq.(4.87), and the same computation of internal variables in Eqs. (4.53), (4.74). The final solution is obtained using the series in Eq. (4.92) with the homotopy parameter $\epsilon = 1$. Thus, the convergence

criterion becomes:

$$\delta = \frac{\| \Delta \mathbf{q}_{N-1} \|}{\sum_{p=1}^{N-1} \frac{D_{N-p-1}}{D_{N-1}} \Delta \mathbf{q}_p} \leq \delta_{ANM} \tag{4.94}$$

Algorithm 3 ANM procedure for the time step $[t_n, t_{n+1}]$, given the maximum number of iteration N_{max} and the tolerance δ_{ANM}

Require: Time-step-size Δt, solution at t_n : $(\cdot)_n$, tangent operator $\mathbf{A}_T = \mathbf{A}_T((\cdot)_n)$
  Set $\Delta \mathbf{q} = \mathbf{0}$
  Set $p = 1$
  while $p \leq N_{max}$ **do**
    Solve the p-order linear problem in Eq. (4.87).
    Loop on elements: Compute internal variables $(\cdot)_p$ and $\Delta \mathbf{F}^{nl}_{p+1} - \Delta \mathbf{L}^{nl}_{p+1}$
    Evaluate convergence δ in Eq. (4.90) or Eq. (4.94)
    if $\delta \leq \delta_{ANM}$ **then**
      break
    else
      $p = p + 1$
    end if
  end while
  if $\delta \leq \delta_{ANM}$ **then**
    Evaluate solution: $(\cdot)_{n+1} = (\cdot)_n + \Delta(\cdot)$
    Evaluate the new time-step size using Eq.(4.22)
    Loop on elements: Evaluate internal variable $(\cdot)_{n+1}$ and $\mathbf{K}_T = \mathbf{K}_T((\cdot)_{n+1})$
    Evaluate $\mathbf{A}_T = \mathbf{A}_T(\Delta t, (\cdot)_{n+1})$
  else
    Reduce time-step-size: $\Delta t = \Delta t/2$
    Update $\mathbf{A}_T = \mathbf{A}_T(\Delta t, (\cdot)_n)$ and restart the procedure
  end if

4.3.4 Comparison between ANM and Newton–Raphson method

This section compares the ANM and the Newton–Raphson (NR) method in terms of solution strategy and discusses the advantage of the former, based on the algorithms developed in this work. The comparison of time-stepping efficiency and computational cost is conducted in the numerical tests of Chapter 5.

Resolution strategy. Conceptually, ANM approximates the solution by a power series, whereas NR iteratively predicts and corrects the solution to drive the residual to zero. Applying NR requires defining the residual and the tangent operator; the latter may

be approximate (modified NR or quasi-NR), at the cost of losing the convergence rate. This flexibility makes NR easily applicable to nonlinear material models or non-smooth nonlinearities (e.g., plasticity, contact).

By contrast, as outlined in Section 4.3, building an ANM approximation relies on two conditions: (i) the governing equations are smooth so their linear and nonlinear parts can be separated (Eq. (4.23)); and (ii) the nonlinear part is quadratic. If higher-order terms (e.g., cubic) are present, a generic ANM construction is not straightforward (as in classical perturbation techniques).

For nonlinear dynamics, these conditions are satisfied when only geometric nonlinearity is considered and the formulation is expressed in the reference configuration. For hyperelastic materials [126, 77], however, we cannot perform a general linear–quadratic split on the stress relations for all models. The difficulty increases with non-smooth nonlinearities (plasticity, contact), which typically require regularization [127, 7, 3].

Tangent and force evaluations. The main advantage of the ANM over the Newton-Raphson method is that, while solving a given time step, the ANM requires only one tangent operator, whereas the NR requires one per iteration. The trade-off is that ANM requires many evaluations of the force vector. Indeed, as seen in Eq. (4.53) and Eq. (4.74), the computation of the nonlinear term $\Delta\mathbf{F}_p^{nl}$ at order p involves $p(p-1)/2$ evaluations of $\int_\Omega \mathbf{B}^{nl}(\Delta\mathbf{q})^{\mathrm{T}}\,\Delta\mathbf{S}\,d\Omega$, whereas only the same one evaluation is required for the evaluation of the internal force vector. Therefore, if the order $N = 20$ is needed to obtain the solution in a given time step, it must be $N(N-1)(N+1)/6 = 1330$ evaluations of force vectors, which becomes significant over thousands of steps in a transient analysis.

Prior work by Guevel et al. [81] reported a speedup of 10 while using ANM solvers over a classical NR solver for transient Navier–Stokes with a constant time step (NR converging in roughly three iterations per step). In the present work, we compare NR and ANM in dynamic buckling with adaptive time stepping, measuring time-stepping efficiency (number of steps), solver workload (tangent operator/force vector evaluations), and CPU time (Section 5.3).

4.4 Explicit Nonlinear Dynamic Analysis

This section presents the algorithm of the explicit solver for nonlinear dynamics using the Central Difference (CD) scheme, with a focus on the 7-parameter shell elements. The global procedure of the explicit solver will first be presented in Section 4.4.1, considering not only geometrical and material nonlinearities but also kinematic ones,

such as rigid body motion constraints. We also present the multi-time-step explicit solver in Section 4.4.2. The issue lying in incorporating the orthogonality condition for the Enhanced Assumed Strain field within the explicit solver will be discussed in Section 4.4.3, in which we propose an efficient treatment of the orthogonality condition that maintains the accuracy and robustness of the explicit algorithm.

4.4.1 Explicit solver using Central Difference scheme

Let us write the fully discrete governing equations at the time step $[t_n, t_{n+1}]$ by considering the velocity at the mid-step to obtain the full explicit formulation [17]:

$$\begin{cases} \hat{\mathbf{M}}\,\ddot{\mathbf{q}}_{n+1} + \mathbf{C}\,\dot{\mathbf{q}}_{n+1/2} + \mathbf{f}_{\text{int},n+1} - \mathbf{f}_{\text{ext},n+1} - \mathbf{L}^{\mathrm{T}}\boldsymbol{\Lambda}_{n+1} = \mathbf{0} \\ \mathbf{L}\,\dot{\mathbf{q}}_{n+1} - \dot{\mathbf{B}}_{n+1} = \mathbf{0} \end{cases} \tag{4.95}$$

where $\hat{\mathbf{M}}$ is the diagonal Lumped Mass Matrix (LMM). The solution at the time t_{n+1} is solved using the Central Difference scheme which writes:

$$\begin{aligned} \dot{\mathbf{q}}_{n+1/2} &= \dot{\mathbf{q}}_n + 0.5\Delta t\,\ddot{\mathbf{q}}_n \\ \mathbf{q}_{n+1} &= \mathbf{q}_n + \Delta t\,\dot{\mathbf{q}}_{n+1/2} \\ \dot{\mathbf{q}}_{n+1} &= \dot{\mathbf{q}}_n + 0.5\Delta t\,\ddot{\mathbf{q}}_{n+1} \end{aligned} \tag{4.96}$$

The unknowns of our problem are the displacement, velocity, acceleration and the Lagrange multipliers at the time t_{n+1}. However, it can be seen that using the CD scheme in Eq. (4.96), the displacement at the considered time step $\mathbf{q}_{n+1}$ can be determined directly from the solution at the time t_n. Therefore, the unknowns in the linear system now are the acceleration $\ddot{\mathbf{q}}_{n+1}$, the velocity $\dot{\mathbf{q}}_{n+1}$, and the Lagrange multipliers $\boldsymbol{\Lambda}_{n+1}$. This is the reason why we express the kinematic constraint in Eq.(4.95) in terms of velocity instead of displacement. We can also express the kinematic constraint in terms of acceleration; however, it is demonstrated in [78] that the explicit algorithm is more stable when written in terms of velocity. Another important remark is that as the displacement $\mathbf{q}_{n+1}$ is known at the start of the considering time step $[t_n, t_{n+1}]$, it is easy to consider the nonlinearities that may rise from the kinematic constraints, such as rigid body motion (diaphragm) effects. Indeed, the nonlinear kinematic constraints can be written as follows:

$$\mathbf{L}(\mathbf{q}_{n+1})\,\dot{\mathbf{q}}_{n+1} - \dot{\mathbf{B}}_{n+1} = \mathbf{0} \tag{4.97}$$

In the following, we employ $\mathbf{L}$ for the sake of clarity, which is valid for both linear and nonlinear kinematic constraints.

Now let us develop the explicit algorithm to solve the problem in Eq. (4.95) by assuming that the internal force $\mathbf{f}_{\text{int},n+1}$ can be determined from the displacement $\mathbf{q}_{n+1}$. The unknowns in the linear system now are the acceleration $\ddot{\mathbf{q}}_{n+1}$, the velocity $\dot{\mathbf{q}}_{n+1}$, and the Lagrange multipliers $\mathbf{\Lambda}_{n+1}$. Using the equation of motion in Eq. (4.95), we express the acceleration in terms of the Lagrange multipliers as follows:

$$\begin{aligned}\ddot{\mathbf{q}}_{n+1} &= -\hat{\mathbf{M}}^{-1}\left(\mathbf{C}\,\dot{\mathbf{q}}_{n+1/2} + \mathbf{f}_{\text{int},n+1} - \mathbf{f}_{\text{ext},n+1}\right) + \hat{\mathbf{M}}^{-1}\,\mathbf{L}^{\mathrm{T}}\,\mathbf{\Lambda}_{n+1} \\ &= \ddot{\mathbf{q}}_{n+1,free} + \hat{\mathbf{M}}^{-1}\,\mathbf{L}^{\mathrm{T}}\,\mathbf{\Lambda}_{n+1}\end{aligned} \tag{4.98}$$

where $\ddot{\mathbf{q}}_{n+1,free}$ represents the "free" part of the acceleration that is independent of the kinematic constraint and can be evaluated. Thus, using Eq. (4.96), the relation between the velocity and the Lagrange multipliers writes:

$$\dot{\mathbf{q}}_{n+1} = \dot{\mathbf{q}}_{n+1/2} + 0.5\Delta t\left(\ddot{\mathbf{q}}_{n+1,free} + \hat{\mathbf{M}}^{-1}\mathbf{L}^{\mathrm{T}}\mathbf{\Lambda}_{n+1}\right) \tag{4.99}$$

Now, substituting Eq. (4.99) into the kinematic constraints in Eq. (4.95), we obtain the following equation:

$$\mathbf{H}\,\mathbf{\Lambda}_{n+1} = \dot{\mathbf{B}}_{n+1} - \mathbf{L}\,\left(\dot{\mathbf{q}}_{n+1/2} + 0.5\Delta t\,\ddot{\mathbf{q}}_{n+1,free}\right) \tag{4.100}$$

where

$$\mathbf{H} = 0.5\Delta t\,\mathbf{L}\,\hat{\mathbf{M}}^{-1}\,\mathbf{L}^{\mathrm{T}} \tag{4.101}$$

Using Eq. (4.100), we can compute the Lagrange multipliers. The acceleration and velocity can then be computed using Eqs. (4.98) and (4.99). We can observe that if the kinematic constraints are linear, meaning the matrix $\mathbf{L}$ is independent of the displacement, the matrix $\mathbf{H}$ can be evaluated and factorized before entering the solver. In contrast, $\mathbf{H}$ needs to be evaluated for each time step in cases where nonlinear kinematics constraints are considered. The algorithm of the solution process for a given time step using the CD scheme is presented in Algorithm 4. It can be seen that, except for the kinematic nonlinearity, the most time-consuming task in the algorithm is the loop over elements to compute the internal and external force vectors.

Algorithm 4 Central Difference (explicit) algorithm for nonlinear dynamics considering the time step $[t_n, t_{n+1}]$

Require: Time-step-size Δt, matrices $\mathbf{L}$ and $\mathbf{H}$ solution at t_n : $(\cdot)_n$
Compute $\mathbf{q}_{n+1}$ and $\dot{\mathbf{q}}_{n+1/2}$ using Eq. (4.96)
Loop on elements: Compute force vectors $\mathbf{f}_{\text{int},n+1}$ and $\mathbf{f}_{\text{ext},n+1}$
Compute $\ddot{\mathbf{q}}_{n+1,free}$ using Eq. (4.98)
Update $\mathbf{L}(\mathbf{q}_{n+1})$, $\mathbf{H}$ for nonlinear kinematic constraints
Compute $\mathbf{\Lambda}_{n+1}$ using Eq. (4.100)
Compute $\ddot{\mathbf{q}}_{n+1}$ and $\dot{\mathbf{q}}_{n+1}$ using Eq. (4.98) and Eq. (4.99)

4.4.2 Multi-time step explicit solver

In this section, we present the multi-time step explicit solver based on the Heterogeneous Asynchronous Time Integrator (HATI) method [78, 43] in the context of domain decomposition. To illustrate our development, let us consider the body Ω divided into $N_\Omega = 4$ subdomains, $\Omega = \bigcup_{s=1}^{N_\Omega=4} \Omega^{(s)}$ as displayed in Figure 4.4. The boundary of each subdomain consists of the Neumann and the Dirichlet boundaries as well as the interfaces with the adjacent subdomains $\Omega^{(v)}$, $\Gamma_N^{(s)} \cup \Gamma_D^{(s)} \cup \Gamma_h^{(sv)}$. As the Lagrange multipliers are introduced to account for the Dirichlet conditions as well as the coupling between subdomains, we consider 8 boundary Γ_l which regroup the four Dirichlet boundaries $\Gamma_D^{(s)}$ and the four interface boundaries $\Gamma_h^{(sv)}$ as summarized in Table 4.3.

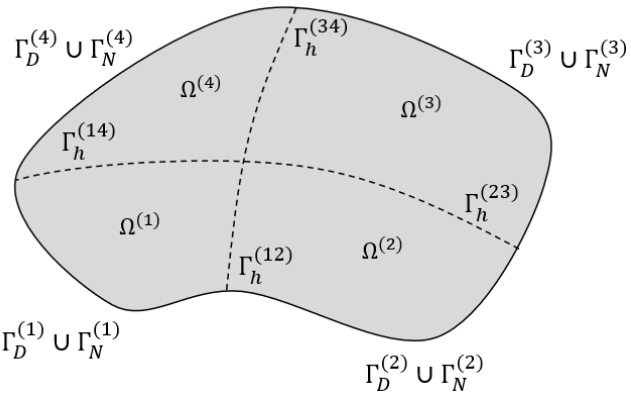

Figure 4.4 Coupling problem of four subdomains.

Concerning the time discretization, some of the four subdomains, denoted as $\Omega^{(a)}$, are discretized with a large time step Δt_m, and the others are discretized with a small time step $\Delta t_j = \Delta t_m / m$, where $m \in \mathbb{Z}^+$ denotes the time step ratio. In the following, we develop the algorithm to solve the problem in a large time step $[t_0; t_0 + \Delta t_m] = [t_0; t_m] = \cup_{j=1}^{j=m} [t_{j-1}; t_j]$ considering only linear Dirichlet conditions for subdomains $\Omega^{(a)}$. The case where the

Dirichlet conditions of subdomains $\Omega^{(a)}$ are nonlinear is discussed later. It is noted that the notation t_0 is used here for brevity, and does not refer to the initial instant $t = 0$.

Table 4.3 Summary of matrix

l	Boundary Γ_l	Matrix $\mathbf{L}_l^{(s)}$			
		$\mathbf{L}_l^{(1)}$	$\mathbf{L}_l^{(2)}$	$\mathbf{L}_l^{(3)}$	$\mathbf{L}_l^{(4)}$
1	$\Gamma_D^{(1)}$	$\mathbf{L}_D^{(1)}$	$\mathbf{0}$	$\mathbf{0}$	$\mathbf{0}$
2	$\Gamma_D^{(2)}$	$\mathbf{0}$	$\mathbf{L}_D^{(2)}$	$\mathbf{0}$	$\mathbf{0}$
3	$\Gamma_D^{(3)}$	$\mathbf{0}$	$\mathbf{0}$	$\mathbf{L}_D^{(3)}$	$\mathbf{0}$
4	$\Gamma_D^{(4)}$	$\mathbf{0}$	$\mathbf{0}$	$\mathbf{0}$	$\mathbf{L}_D^{(4)}$
5	$\Gamma_h^{(12)}$	$\mathbf{L}_h^{(12)}$	$\mathbf{L}_h^{(21)}$	$\mathbf{0}$	$\mathbf{0}$
6	$\Gamma_h^{(14)}$	$\mathbf{L}_h^{(14)}$	$\mathbf{0}$	$\mathbf{0}$	$\mathbf{L}_h^{(41)}$
7	$\Gamma_h^{(23)}$	$\mathbf{0}$	$\mathbf{L}_h^{(23)}$	$\mathbf{L}_h^{(32)}$	$\mathbf{0}$
8	$\Gamma_h^{(34)}$	$\mathbf{0}$	$\mathbf{0}$	$\mathbf{L}_h^{(34)}$	$\mathbf{L}_h^{(43)}$

Discrete governing equations. Let us write the discrete governing equations of the problem. The equation of motion of subdomains $\Omega^{(a)}$ at the time t_m is given as:

$$\mathbf{M}^{(a)}\,\ddot{\mathbf{q}}_m^{(a)} + \mathbf{C}^{(a)}\,\dot{\mathbf{q}}_{m-1/2}^{(a)} + \mathbf{f}_{\text{int},m}^{(a)} - \mathbf{f}_{\text{ext},m}^{(a)} - \sum_{l=1}^{N_\Gamma} \mathbf{L}_l^{(a)\text{T}}\,\mathbf{\Lambda}_{l,m} = \mathbf{0} \tag{4.102}$$

The one of subdomains $\Omega^{(b)}$ at the time t_j with $j = 1, ..., m$ writes:

$$\mathbf{M}^{(b)}\,\ddot{\mathbf{q}}_j^{(b)} + \mathbf{C}^{(b)}\,\dot{\mathbf{q}}_{j-1/2}^{(b)} + \mathbf{f}_{\text{int},j}^{(b)} - \mathbf{f}_{\text{ext},j}^{(b)} - \sum_{l=1}^{N_\Gamma} \mathbf{L}_l^{(b)\text{T}}\,\mathbf{\Lambda}_{l,j} = \mathbf{0} \tag{4.103}$$

In Eq. (4.102) and Eq. (4.103), $\mathbf{\Lambda}_l$ denote the Lagrange multipliers nodal vector corresponding to the boundary Γ_l, and $-\mathbf{L}_l^{(s)\text{T}}\,\mathbf{\Lambda}_l$ gives the reactions force from the boundary acting on the subdomain $\Omega^{(s)}$ subdomain $\Omega^{(s)}$ can be $\Omega^{(a)}$ or $\Omega^{(b)}$. The kinematic constraint at a given interface Γ_l (for instance, subscript l equal to $1, ...8$ in Table 4.3) is imposed at the small time step t_j:

$$\sum_{s=1}^{N_\Omega} \mathbf{L}_l^{(s)}\,\dot{\mathbf{q}}_j^{(s)} = \dot{\mathbf{B}}_{l,j} \tag{4.104}$$

In the above equation, $\mathbf{L}_l^{(s)}$ is the matrix related to the subdomain $\Omega^{(s)}$ and is given in Table 4.3, in which $\mathbf{L}_D^{(s)}\,\dot{\mathbf{q}}_j^{(s)} = \dot{\mathbf{B}}_j$ refers to the Dirichlet condition on $\Gamma_D^{(s)}$ as presented in Section 2.6, and $\mathbf{L}^{(sv)}\,\dot{\mathbf{q}}_j^{(s)} + \mathbf{L}^{(vs)}\,\dot{\mathbf{q}}_j^{(v)} = \mathbf{0}$ refers to the coupling condition at the interface $\Gamma_h^{(sv)}$ as presented in Section 3.7.2. It is worth noting that the Dirichlet condition of $\Omega^{(a)}$ can be treated at the large time step, if the following condition is satisfied:

$$\mathbf{L}_D^{(a)}\,\mathbf{L}_h^{(ab)\mathrm{T}} = \mathbf{0} \tag{4.105}$$

The above condition literally means that the degrees of freedom of the Lagrange multipliers for the $\Gamma_D^{(a)}$ are not overlapped with the ones for $\Gamma_h^{(ab)}$. This restriction is used to account for the nonlinear Dirichlet condition in subdomains $\Omega^{(a)}$ as discussed later.

Concerning the time integration, we employ the Central Difference scheme, with the large time step Δt_m for subdomains $\Omega^{(a)}$ and the small time step $\Delta t_j = \Delta t_m/m$ for subdomains $\Omega^{(b)}$:

$$\begin{cases} \dot{\mathbf{q}}_{m-1/2}^{(a)} &= \dot{\mathbf{q}}_0^{(a)} + 0.5\Delta t_m\,\ddot{\mathbf{q}}_0^{(a)} \\ \mathbf{q}_m^{(a)} &= \mathbf{q}_0^{(a)} + \Delta t_m\,\dot{\mathbf{q}}_{m-1/2}^{(a)} \\ \dot{\mathbf{q}}_m^{(a)} &= \dot{\mathbf{q}}_{m-1/2}^{(a)} + 0.5\Delta t_m\,\ddot{\mathbf{q}}_m^{(a)} \end{cases}, \qquad \begin{cases} \dot{\mathbf{q}}_{j-1/2}^{(b)} &= \dot{\mathbf{q}}_{j-1}^{(b)} + 0.5\Delta t_j\,\ddot{\mathbf{q}}_{j-1}^{(b)} \\ \mathbf{q}_j^{(b)} &= \mathbf{q}_j^{(b)} + \Delta t_j\,\dot{\mathbf{q}}_{j-1/2}^{(b)} \\ \dot{\mathbf{q}}_j^{(b)} &= \dot{\mathbf{q}}_{j-1/2}^{(b)} + 0.5\Delta t_j\,\ddot{\mathbf{q}}_j^{(b)} \end{cases} \tag{4.106}$$

Finally, in order to write the velocity and the Lagrange multipliers of the subdomains $\Omega^{(a)}$ at the small time step t_j, the following assumption is made [78, 43]:

$$\begin{aligned} \dot{\mathbf{q}}_j^{(a)} &= \left(1 - \frac{j}{m}\right)\dot{\mathbf{q}}_0^{(a)} + \frac{j}{m}\dot{\mathbf{q}}_m^{(a)} \\ \mathbf{\Lambda}_{l,j} &= \left(1 - \frac{j}{m}\right)\mathbf{\Lambda}_{l,0} + \frac{j}{m}\mathbf{\Lambda}_{l,m} \end{aligned} \tag{4.107}$$

Eqs. (4.102), (4.103), (4.104), (4.106) and (4.107) are the governing equations of the coupling problem. In the following, we employ the HATI [78, 43] to solve these equations. The principle of HATI is that the solution of each subdomain is decomposed into a *free part* which is free from the Lagrange multipliers, and a *link part* which concerns only the Lagrange multipliers. The free part of each subdomain can be solved independently from the others, and serves later to compute all the Lagrange multipliers (link part). The final solution of each subdomain is simply the sum of the free part and the link part.

Free part. We consider first the subdomains $\Omega^{(a)}$. From Eq. (4.102), the acceleration at the time t_m can be expressed as follows:

$$\begin{aligned}\ddot{\mathbf{q}}_m^{(a)} &= -\hat{\mathbf{M}}^{(a)-1}\left(\mathbf{C}^{(a)}\,\dot{\mathbf{q}}_{m-1/2}^{(a)} + \mathbf{f}_{\text{int},m}^{(a)} - \mathbf{f}_{\text{ext},m}^{(a)}\right) + \hat{\mathbf{M}}^{(a)-1}\sum_{l=1}^{N_\Gamma}\mathbf{L}_l^{(a)\mathrm{T}}\,\boldsymbol{\Lambda}_{l,m} \\ &= \ddot{\mathbf{q}}_{m,free}^{(a)} + \hat{\mathbf{M}}^{(a)-1}\sum_{l=1}^{N_\Gamma}\mathbf{L}_l^{(a)\mathrm{T}}\,\boldsymbol{\Lambda}_{l,m}\end{aligned} \tag{4.108}$$

where the free part of the acceleration $\ddot{\mathbf{q}}_{m,free}^{(a)}$ can be evaluated using the CD scheme in Eq. (4.106). The velocity at the time t_m is thus given as:

$$\begin{aligned}\dot{\mathbf{q}}_m^{(a)} &= \dot{\mathbf{q}}_{m-1/2}^{(a)} + 0.5\Delta t_m\left(\ddot{\mathbf{q}}_{m,free}^{(a)} + \hat{\mathbf{M}}^{(a)-1}\sum_{l=1}^{N_\Gamma}\mathbf{L}_l^{(a)\mathrm{T}}\,\boldsymbol{\Lambda}_{l,m}\right) \\ &= \dot{\mathbf{q}}_{m,free}^{(a)} + 0.5\Delta t_m\,\hat{\mathbf{M}}^{(a)-1}\sum_{l=1}^{N_\Gamma}\mathbf{L}_l^{(a)\mathrm{T}}\,\boldsymbol{\Lambda}_{l,m}\end{aligned} \tag{4.109}$$

It is worth noting that the above equation also holds for the previous time step:

$$\dot{\mathbf{q}}_0^{(a)} = \dot{\mathbf{q}}_{0,free}^{(a)} + 0.5\Delta t_m\,\hat{\mathbf{M}}^{(a)-1}\sum_{l=1}^{N_\Gamma}\mathbf{L}_l^{(a)\mathrm{T}}\,\boldsymbol{\Lambda}_{l,0} \tag{4.110}$$

Using the first equation in Eq. (4.107), we can express the velocity at the small time step t_j as follows:

$$\dot{\mathbf{q}}_j^{(a)} = \left(1 - \frac{j}{m}\right)\dot{\mathbf{q}}_0^{(a)} + \frac{j}{m}\left(\dot{\mathbf{q}}_{m,free}^{(a)} + 0.5\Delta t_m\,\hat{\mathbf{M}}^{(a)-1}\sum_{l=1}^{N_\Gamma}\mathbf{L}_l^{(a)\mathrm{T}}\,\boldsymbol{\Lambda}_{l,m}\right) \tag{4.111}$$

Substituting the second equation in Eq. (4.107) into the above equation, and using the relation in Eq. (4.110), the velocity at the small time step t_j becomes:

$$\begin{aligned}\dot{\mathbf{q}}_j^{(a)} &= \left(1 - \frac{j}{m}\right)\dot{\mathbf{q}}_{0,free}^{(a)} + \frac{j}{m}\dot{\mathbf{q}}_{m,free}^{(a)} + 0.5\Delta t\hat{\mathbf{M}}^{(a)-1}\sum_{l=1}^{N_\Gamma}\mathbf{L}_l^{(a)\mathrm{T}}\,\boldsymbol{\Lambda}_{l,j} \\ &= \dot{\mathbf{q}}_{j,free}^{(a)} + 0.5\Delta t_m\,\hat{\mathbf{M}}^{(a)-1}\sum_{l=1}^{N_\Gamma}\mathbf{L}_l^{(a)\mathrm{T}}\,\boldsymbol{\Lambda}_{l,j}\end{aligned} \tag{4.112}$$

The above equation expresses the velocity in terms of the free part $\dot{\mathbf{q}}_{j,free}^{(a)}$ that can be evaluated independently from other subdomains, and the link part, which depends on the Lagrange multipliers at the small time step t_j.

For the subdomains $\Omega^{(b)}$, following the procedure in Section 4.4.1, we can easily write the velocity as follows:

$$\begin{aligned}\dot{\mathbf{q}}_j^{(b)} &= \dot{\mathbf{q}}_{j-1/2}^{(b)} + 0.5\Delta t_j \left(\ddot{\mathbf{q}}_{j,free}^{(b)} + \hat{\mathbf{M}}^{(b)-1} \sum_{l=1}^{N_\Gamma} \mathbf{L}_l^{(b)\mathrm{T}} \boldsymbol{\Lambda}_{l,j} \right) \\ &= \dot{\mathbf{q}}_{j,free}^{(b)} + 0.5\Delta t_j \, \hat{\mathbf{M}}^{(b)-1} \sum_{l=1}^{N_\Gamma} \mathbf{L}_l^{(b)\mathrm{T}} \boldsymbol{\Lambda}_{l,j}\end{aligned} \tag{4.113}$$

Let us denote $\Delta t^{(s)}$ is the time step size of the subdomain $\Omega^{(s)}$, with $\Delta t^{(a)} = \Delta t_m$ and $\Delta t^{(b)} = \Delta t_j$. From Eqs. (4.112) and (4.113), we can express the velocity of a subdomain $\Omega^{(s)}$ at the small time step t_j in terms of a free part, which can be evaluated independently from other subdomains, and a link part related to the Lagrange multipliers:

$$\dot{\mathbf{q}}_j^{(s)} = \dot{\mathbf{q}}_{j,free}^{(s)} + 0.5\Delta t^{(s)} \, \hat{\mathbf{M}}^{(s)-1} \sum_{l=1}^{N_\Gamma} \mathbf{L}_l^{(s)\mathrm{T}} \boldsymbol{\Lambda}_{l,j} \tag{4.114}$$

Solution of link part. Substituting Eq. (4.114) into Eq. (4.104), the kinematic constraint at the boundary Γ_l becomes:

$$\sum_{s=1}^{N_\Omega} \mathbf{L}_l^{(s)} \left(\dot{\mathbf{q}}_{j,free}^{(s)} + 0.5\Delta t^{(s)} \, \hat{\mathbf{M}}^{(s)-1} \sum_{k=1}^{N_\Gamma} \mathbf{L}_k^{(s)\mathrm{T}} \boldsymbol{\Lambda}_{k,j} \right) = \dot{\mathbf{B}}_{l,j} \tag{4.115}$$

The above equation is then used to determine the Lagrange multipliers of all the boundaries Γ_k with $k = 1, ...N_\Gamma$ via the operator $\mathbf{H}$ as follows:

$$\sum_{k=1}^{N_\Gamma} \mathbf{H}_{lk} \boldsymbol{\Lambda}_{k,j} = \dot{\mathbf{B}}_{l,j} - \sum_{s=1}^{N_\Omega} \mathbf{L}_l^{(s)} \dot{\mathbf{q}}_{j,free}^{(s)} \tag{4.116}$$

where:

$$\mathbf{H}_{lk} = \sum_{s=1}^{N_\Omega} 0.5\Delta t^{(s)} \, \mathbf{L}_l^{(s)} \hat{\mathbf{M}}^{(s)-1} \mathbf{L}_k^{(s)\mathrm{T}} \tag{4.117}$$

From the implementation point of view, if $\mathbf{L}_l$ are Boolean matrices, the operator $\mathbf{H}$ is a diagonal matrix. Otherwise, the operator $\mathbf{H}$ is a dense matrix. If all the kinematic constraints are linear, the operator remains unchanged during the simulation and can thus be evaluated and factorized before entering the solver.

Once the Lagrange multipliers are solved at each small time step, the solution of subdomains $\Omega^{(b)}$ can be determined using Eq. (4.113), and used for the next small time step computation. At the end of the mth small time step, when $t_j = t_m$, the Lagrange

multipliers $\mathbf{\Lambda}_{l,j=m}$ is used to evaluate the total solution of subdomains $\Omega^{(a)}$. The resolution procedure for the large time step $[t_0, t_m]$ is summarized in Algorithm 5.

Algorithm 5 Algorithm of multi-time step explicit solver for nonlinear dynamics considering the time step $[t_0, t_m] = \bigcup_{j=1}^{m} [t_{j-1}; t_j]$

Loop on subdomains $\Omega^{(a)}$: compute $\mathbf{q}_m^{(a)}$ and the free part $\dot{\mathbf{q}}_{m,free}^{(a)}$
Set $j = 1$
while $j \leq m$ **do**
  Loop on subdomains $\Omega^{(b)}$: compute $\mathbf{q}_m^{(b)}$ and the free part $\dot{\mathbf{q}}_{j,free}^{(b)}$
  Loop on subdomains $\Omega^{(a)}$: compute the free part $\dot{\mathbf{q}}_{j,free}^{(a)}$
  Compute the Lagrange multipliers for all kinematic constraints
  Compute the final solution of subdomains $\Omega^{(b)}$ at the time t_j
  j = j+1
end while
Compute the final solution of subdomains $\Omega^{(a)}$ at the time t_m

Case of nonlinear kinematic constraints. The above multi-time step explicit algorithm is applicable when both linear and nonlinear kinematic constraints arise in subdomains $\Omega^{(b)}$, but only linear Dirichlet conditions in subdomains $\Omega^{(a)}$. This requirement permits the use of the linear assumption for the Lagrange multipliers in Eq. (4.107). Thus, to account for the nonlinear kinematic constraints in subdomains $\Omega^{(a)}$, the corresponding Lagrange multipliers need to be treated separately from the ones of linear constraints.

Let us divide the Dirichlet boundaries of subdomains $\Omega^{(a)}$ into a linear part, denoted as $\Gamma_D^{(a)}$, a nonlinear part, denoted as $\Gamma_{nl}^{(a)}$, with $\Gamma_{nl}^{(a)} \cap \Gamma_D^{(a)} = \Gamma_{nl}^{(a)} \cap \Gamma_h^{(as)} = \varnothing$. The linear kinematic constraints for subdomains $\Omega^{(a)}$ remains the same as in Eq. (4.104), and the nonlinear constraints writes:

$$\mathbf{L}_{nl}^{(a)} \, \dot{\mathbf{q}}_m^{(a)} = \dot{\mathbf{B}}_{nl}^{(a)} \tag{4.118}$$

where $\mathbf{L}_{nl}^{(a)} = \mathbf{L}_{nl}^{(a)}(\mathbf{q}_{n+1}^{(a)})$. Considering the above constraints leads to the introduction of the Lagrange multipliers $\mathbf{\Lambda}_{nl}^{(a)}$ in the equation of motion in Eq. (4.102):

$$\mathbf{M}^{(a)} \, \ddot{\mathbf{q}}_m^{(a)} + \mathbf{C}^{(a)} \, \dot{\mathbf{q}}_{m-1/2}^{(a)} + \mathbf{f}_{\text{int},m}^{(a)} - \mathbf{f}_{\text{ext},m}^{(a)} - \sum_{l=1}^{N_\Gamma} \mathbf{L}_l^{(a)\text{T}} \, \mathbf{\Lambda}_{l,m} - \mathbf{L}_{nl}^{(a)\text{T}} \, \mathbf{\Lambda}_{nl,m}^{(a)} = \mathbf{0} \tag{4.119}$$

Thus, we can write the velocity of subdomains $\Omega^{(a)}$ at the time t_m:

$$\dot{\mathbf{q}}_m^{(a)} = \dot{\mathbf{q}}_{m,free}^{(a)} + 0.5\Delta t_m \, \hat{\mathbf{M}}^{(a)-1} \sum_{l=1}^{N_\Gamma} \mathbf{L}_l^{(a)\text{T}} \, \mathbf{\Lambda}_{l,m} + 0.5\Delta t_m \, \hat{\mathbf{M}}^{(a)-1} \, \mathbf{L}_{nl}^{(a)\text{T}} \, \mathbf{\Lambda}_{nl,m}^{(a)} \tag{4.120}$$

and the small time step t_j:

$$\dot{\mathbf{q}}_j^{(a)} = \dot{\mathbf{q}}_{j,free}^{(a)} + 0.5\Delta t_j \, \hat{\mathbf{M}}^{(a)-1} \sum_{l=1}^{N_\Gamma} \mathbf{L}_l^{(a)\mathrm{T}} \, \boldsymbol{\Lambda}_{l,j} + 0.5 \frac{j}{m} \Delta t_m \, \hat{\mathbf{M}}^{(a)-1} \, \mathbf{L}_{nl}^{(a)\mathrm{T}} \, \boldsymbol{\Lambda}_{nl,m}^{(a)} \tag{4.121}$$

As discussed previously, to be able to treat the nonlinear kinematics separately from the linear ones, the condition $\Gamma_{nl}^{(a)} \cap \Gamma_D^{(a)} = \Gamma_{nl}^{(a)} \cap \Gamma_h^{(as)} = \varnothing$ must be satisfied not only in the continuous setting, but also in the discrete setting, which leads to:

$$\mathbf{L}_{nl}^{(a)} \, \mathbf{L}_D^{(a)\mathrm{T}} = \mathbf{L}_{nl}^{(a)} \, \mathbf{L}_h^{(as)\mathrm{T}} = \mathbf{0} \tag{4.122}$$

The above equation permits to cancel the terms $\mathbf{L}_{nl}^{(a)} \, \hat{\mathbf{M}}^{(a)-1} \, \mathbf{L}_l^{(a)\mathrm{T}}$ and $\mathbf{L}_l^{(a)} \, \hat{\mathbf{M}}^{(a)-1} \, \mathbf{L}_{nl}^{(a)\mathrm{T}}$ while substituting Eqs. (4.120) and (4.121) respectively into the nonlinear kinematic constraints in Eq. (4.118) and the linear ones in Eq. (4.104). Therefore, the Lagrange multipliers related to the linear constraints are handled as presented in the previous section, whereas the ones for the nonlinear constraints can be solved separately via the nonlinear operator $\mathbf{H}_{nl}^{(a)}$ as follows:

$$\mathbf{H}_{nl}^{(a)} \, \boldsymbol{\Lambda}_{nl,m}^{(a)} = \dot{\mathbf{B}}_{nl}^{(a)} - \mathbf{L}_{nl}^{(a)} \, \dot{\mathbf{q}}_{m,free}^{(a)} \tag{4.123}$$

where:

$$\mathbf{H}_{nl}^{(a)} = 0.5\Delta t_m \, \mathbf{L}_{nl}^{(a)\mathrm{T}} \hat{\mathbf{M}}^{(a)-1} \, \mathbf{L}_{nl}^{(a)\mathrm{T}} \tag{4.124}$$

4.4.3 Treatment of the EAS field in 7-parameter shell elements

The previously developed algorithms assume that the global internal force vector can be computed directly from a given displacement. This can be done for solid elements as presented in Chapter 2. However, for 7-parameter shell elements, due to the presence of the EAS field, this process is not straightforward. As presented in Section 3.3.1, by omitting the symbol $(\cdot)^e$, let us rewrite the element internal force vector as follows:

$$\mathbf{f}_{\mathrm{int},n+1} = \int_\Omega \bar{\mathbf{B}}^{\mathrm{T}} \, \mathbf{S}(\mathbf{q}_{n+1}, \boldsymbol{\alpha}_{n+1}) \, d\Omega \tag{4.125}$$

followed by the orthogonality condition:

$$\mathbf{R}_{\alpha,n+1} = \int_\Omega \mathbf{B}_\alpha^{\mathrm{T}} \, S^{33}(\mathbf{q}_{n+1}, \boldsymbol{\alpha}_{n+1}) \, d\Omega = \mathbf{0} \tag{4.126}$$

More details on the matrices in the above equations, as well as in the following, can be found in Appendix A.2.

It can be observed in Eq. (4.125) that the element internal force vector depends not only on the displacement but also on the EAS variable $\boldsymbol{\alpha}_{n+1}$. To determine $\boldsymbol{\alpha}_{n+1}$, we need to solve the orthogonality condition in Eq. (4.126). This process is referred as the static condensation in [160, 159]. Nevertheless, solving this equation makes the global algorithm less efficient, especially when nonlinear material models are considered, as also reported in [122, 123, 132].

To address this issue, we propose a particular treatment for the EAS field and the orthogonality condition. The treatment consists of first shifting the EAS variable from the end of the time step to the mid-step, as is classically done for velocity in the equation of motion in Eq. (4.95). Therefore, the internal force vector writes:

$$\mathbf{f}_{\text{int},n+1} = \int_{\Omega} \bar{\mathbf{B}}^{\mathrm{T}} \mathbf{S}(\mathbf{q}_{n+1}, \boldsymbol{\alpha}_{n+1/2})\, d\Omega \tag{4.127}$$

It can be seen in Eq.(4.127) that the internal force vector can now be determined directly assuming that $\boldsymbol{\alpha}_{n+1/2}$ is known. Next, $\boldsymbol{\alpha}_{n+3/2}$ needs to be updated for the next time step computation, which may be obtained from the first-order linearization of the orthogonality in Eq. (4.128) as follows:

$$\begin{aligned}
\mathbf{R}_{\alpha,n+3/2} &= \int_{\Omega} \mathbf{B}_{\alpha}^{\mathrm{T}}\, S^{33}(\mathbf{q}_{n+1}, \boldsymbol{\alpha}_{n+3/2})\, d\Omega \\
&= \mathbf{R}_{\alpha,n+1/2} + \left[\int_{\Omega} \mathbf{B}_{\alpha}^{\mathrm{T}} \frac{\partial S^{33}}{\partial E_{33}} \cdot \frac{\partial E_{33}}{\partial(\theta^3 \tilde{\beta}_{33})}\, d\Omega\right] \left(\boldsymbol{\alpha}_{n+3/2} - \boldsymbol{\alpha}_{n+1/2}\right) \\
&= \mathbf{R}_{\alpha,n+1/2} + \left[\int_{\Omega} \mathbf{B}_{\alpha}^{\mathrm{T}}\, \mathcal{D}^{3333}\, \mathbf{B}_{\alpha}\, d\Omega\right] \left(\boldsymbol{\alpha}_{n+3/2} - \boldsymbol{\alpha}_{n+1/2}\right) \\
&= \mathbf{R}_{\alpha,n+1/2} + \mathbf{K}_{\alpha\alpha} \left(\boldsymbol{\alpha}_{n+3/2} - \boldsymbol{\alpha}_{n+1/2}\right) = \mathbf{0}
\end{aligned} \tag{4.128}$$

which yields:

$$\boldsymbol{\alpha}_{n+3/2} = \boldsymbol{\alpha}_{n+1/2} - \mathbf{K}_{\alpha\alpha}^{-1} \mathbf{R}_{\alpha,n+1/2} \tag{4.129}$$

In Eq. (4.128), $\mathcal{D}^{3333} = \partial S^{33}/\partial E_{33}$ denotes the material modulus in the reference configuration as defined in Eq. (3.39). The above treatment is similar to the solution proposed by Pagani et al. [132] for linear solid-shell elements. In the case of linear material, the use of the above treatment leads to almost the same results as using the static condensation, as reported in [132, 123] or more recently by us in [54].

For nonlinear material, we make another simplification that is $\mathcal{D}^{3333}$ is set equal to value of the linear Saint-Venant-Kirchhoff model in Eq. (3.17) as follows:

$$\mathcal{D}^{3333} = \lambda G^{33} G^{33} + \mu (G^{33} G^{33} + G^{33} G^{33}) \tag{4.130}$$

Therefore, the matrix $\mathbf{K}_{\alpha\alpha}$ can be pre-computed before entering into the explicit solvers. It is also noted that by using the bilinear approximation as in Eq. (3.33) for the EAS field within an element, the matrix $\mathbf{K}_{\alpha\alpha}$ is diagonal.

Using Eq. (4.128) with the simplification on the material modulus $\mathcal{D}^{3333}$ to update the EAS field, we do not fully respect the orthogonality condition. However, it makes the algorithm straightforward and efficient. In the numerical tests, we will investigate if the proposed algorithm gives adequately accurate solutions. Furthermore, to quantify the error in the orthogonality condition, we introduce the following energy error:

$$\epsilon_{EAS}(t) = \frac{\mathrm{W}_{\mathrm{EAS}}(t)}{\max\limits_{t\in[t_0;T]} \mathrm{W}_{\mathrm{total}}(t)} \tag{4.131}$$

where $\mathrm{W}_{\mathrm{total}}$ denotes the total (mechanical) energy, as detailed in Appendix B, and $\mathrm{W}_{\mathrm{EAS}}$ denotes the energy generated by the assumed strain, which is supposed to be zero. The variation of the later within a time step $[t_n; t_{n+1}]$ is given as:

$$\Delta \mathrm{W}_{\mathrm{EAS}} = \left| \Delta \boldsymbol{\alpha}^{\mathrm{T}} \left(\mathbf{R}_{\alpha,n+3/2} - \mathbf{R}_{\alpha,n+1/2} \right) \right| \tag{4.132}$$

Conclusion of the chapter. This chapter presented the solvers for nonlinear dynamics, with emphasis on the 7-parameter shell elements: (i) the implicit Newton–Raphson (NR) solver, (ii) the implicit Asymptotic Numerical Method (ANM) solver, (iii) an explicit solver using the Central-Difference (CD) scheme, and (iv) a multi-time-step explicit scheme based on the GC method. Their accuracy and robustness will be investigated in Chapter 5.

The implicit solvers employ α-methods to introduce numerical dissipation—damping non-physical high-frequency modes—and use adaptive time stepping to improve time-integration efficiency. The NR solver accommodates both geometric and material nonlinearities, whereas the ANM is applied only to geometric nonlinearity. A comparison of computational efficiency in dynamic buckling of thin structures will be carried out in Chapter 5, based on time-stepping efficiency (number of time steps), solver workload (tangent assemblies and force evaluations), and CPU time.

The explicit solvers use the CD scheme, which is conditionally stable: the time step must remain below a critical value that is often thickness-controlled and therefore very small. The Selective Mass Scaling (SMS) technique can be applied to raise the critical step Δt_{cr}; its impact on accuracy is verified a posteriori via numerical tests. A further contribution is the explicit algorithm to treat the EAS field in 7-parameter shell elements. As shown in [54], it is accurate and efficient for geometrically nonlinear dynamics; Chapter 5 will assess its performance under impulsive loading with severe deformation and elasto-plasticity.

Chapter 5

Numerical validation

This chapter validates and investigates both the nonlinear dynamic solvers and the developments made for the 7-parameter shell formulation—including standard mortar coupling for shell–shell and shell–solid interfaces, and elasto-plasticity at finite strain. Thin shells are modeled with high-order quadrilateral elements under reduced integration; unless otherwise stated, 8-node quadrilaterals with 2×2 Gauss points on the mid-surface are employed. Reference solutions are obtained either from the literature or from 3D computations using 20-node hexahedral solid elements, with an identical in-plane mesh to that of the shell model. All computations, including the 3D solid ones, are carried out using an in-house MATLAB [121] code developed during the PhD.

The chapter is organized as follows. Section 5.1 presents the classical three-intersecting plate benchmark to assess conservation (mechanical energy, linear and angular momenta) and the dissipation properties of the different time integration schemes. Section 5.2 examines solver performance on the snap-through of a cylindrical roof, and concludes with shell–shell and shell–solid coupling tests that serve as a benchmark for the standard mortar approach. Section 5.3 compares the ANM-based solver with the Newton–Raphson solver in dynamic buckling through two dynamic post-buckling branch-switching problems: an axially loaded cylinder and a closed cylinder under not conservative loads (external pressure). Finally, Section 5.4 investigates the finite-strain elasto-plastic framework across six benchmarks (which are introduced within the section for brevity), thereby validating the NR-based implicit solver and, in particular, the explicit algorithm developed for the 7-parameter shell element.

It is worth noting that the shell-shell coupling strategies (pre-processing and standard mortar approach) were investigated in the context of thin-walled beams under quasi-static regime in Chau et al. [52]. The results are not discussed in the present work for the sake of conciseness. Similarly, other validations beyond those presented in this chapter for

the dynamic implicit ANM solver with geometrical nonlinearities can be found in Chau et al. [53]. Finally, additional investigation on explicit dynamics with elastic materials is available in Chau et al. [54].

5.1 Intersecting Plates

The three-intersecting plates problem, first examined by Simo and Tarnow [153] and later in [27, 26, 55], is used here as a benchmark case. It combines large rigid-body motions with bending, shear, and torsional deformations, making it a demanding test for verifying energy and momentum conservation in nonlinear shell dynamics. In this work, the plates are connected using the standard mortar method to assess its suitability for finite deformation problems and its ability to satisfy mechanical conservation laws.

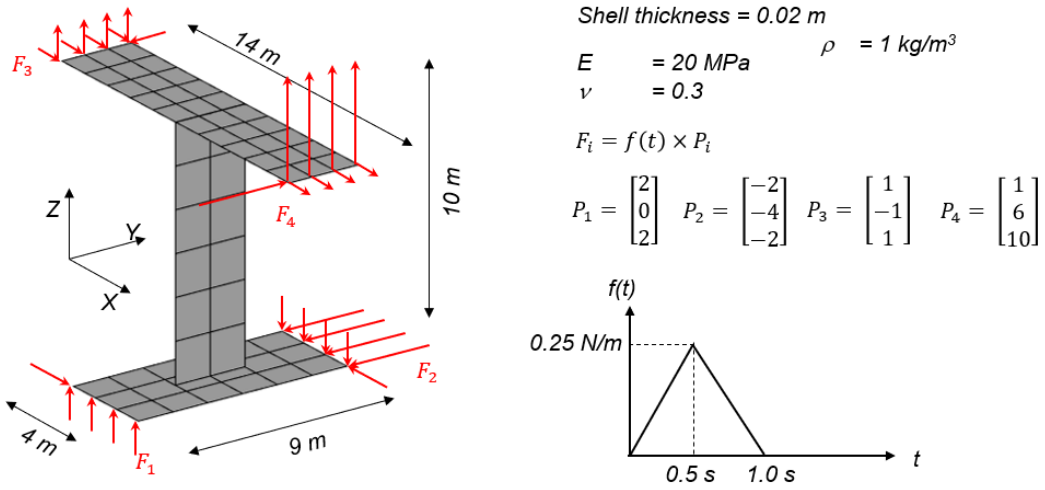

Figure 5.1 Three intersecting plates: problem description.

The geometry is shown in Figure 5.1. The structure is subjected to an impulsive load and undergoes large translations and rotations, as illustrated in Figure 5.2. The objective is to check how well the developed solvers conserve total energy and linear and angular momenta, using both implicit α–methods and the explicit Central Difference scheme.

Implicit computations We first perform simulations with implicit schemes using a constant time step of $\Delta t = 5.00\,\text{ms}$. Results from the Constant Average Acceleration (CAA) scheme are shown in Figure 5.3. The simulation stops at $t \approx 3.2\,\text{s}$ due to the known stability limit of CAA in geometrically nonlinear dynamics. Until this point, total energy and momenta remain nearly constant, showing excellent agreement with [27, 26].

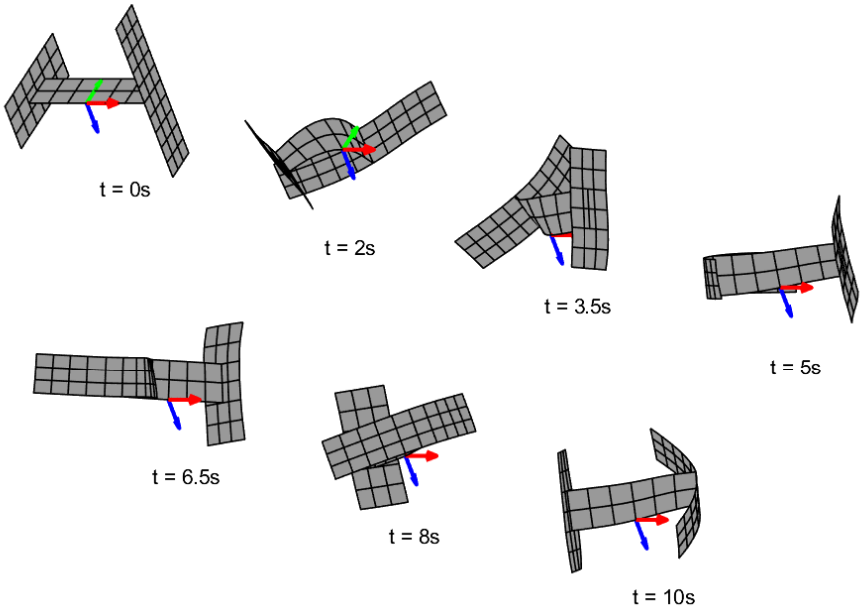

Figure 5.2 Snapshots during the motion of the three intersecting plates.

Figure 5.4 compares the internal, kinetic, and total energies obtained with the Hilber–α (HAM), Bossak–α (BAM), and Generalized–α (GAM) methods for different spectral-radius values ρ_∞. For HAM and BAM, reducing ρ_∞ increases numerical dissipation, as expected. Dissipation begins at the time $t \approx 3.0\,\mathrm{s}$, which also corresponds to the loss of stability of CAA. The sharp drop in total energy, also reported in [160], originates from the modified computation of the internal force $\mathbf{f}_{\mathrm{int},\,n+1-\alpha}$ in Eq. (4.12).

For $\rho_\infty = 0.95$ and 0.90, the GAM is unstable, while HAM and BAM remain stable for the entire run. Nevertheless, for $\rho_\infty = 0.85$, GAM becomes stable and dissipates less energy than HAM and BAM with $\rho_\infty = 0.95$. This is consistent with [112]: HAM and BAM could be stabilized with a smaller $1 - \rho_\infty$ than GAM, but GAM typically exhibits better conservation once stabilized.

Explicit computations Next, we perform multi-time-step explicit simulations. The structure is partitioned into two subdomains: the vertical plate, integrated with a coarse time step Δt_m, and the horizontal plates, integrated with a finer time step $\Delta t_j = \Delta t_m/m$, with $m \in \{1, 10, 35\}$.

Table 5.1 lists the Selective Mass Scaling (SMS) parameter β_0, the critical time step Δt_{cr}, and the chosen time step size for each subdomain. As discussed in Section 4.1.2,

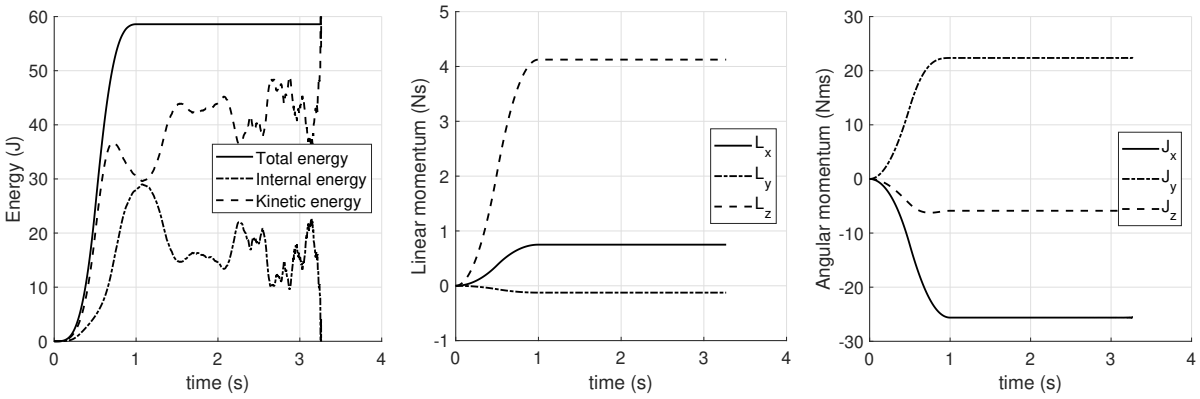

(a) Mechanical energies. (b) Liner momentum **L**. (c) Angular momentum **J**.

Figure 5.3 Three intersecting plates — implicit Constant Average Acceleration (CAA) computation with $\Delta t = 5.00\,\text{ms}$: time histories of mechanical energies, linear momentum, and angular momentum.

Table 5.1 Three intersecting plates – explicit computations: Summary of SMS parameter β_0, the critical time step $\Delta t_{\text{cr.}}$, and the chosen time step sizes for subdomain 1 (vertical plate) and subdomain 2 (horizontal plates).

	Subdomain 1 ($l^e/h^e = 37.5$)			**Subdomain 2** ($l^e/h^e = 25.0$)		
m	β_0	Δt_{cr} [μs]	Δt_m [μs]	β_0	Δt_{cr} [μs]	Δt_j [μs]
1	0.25	78.7	50.0	0.25	54.1	50.0
10	0.25	78.7	70.0	0.005	9.6	7.0
35	0.25	78.7	70.0		2.3	2.0

$\beta_0 = 0.25$ is the recommended value for 8-node square quadrilateral elements. Before applying SMS, both subdomains have the same critical time step, $\Delta t_{\text{cr}} = 2.3\,\mu\text{s}$, which is limited by the shell thickness. Given the characteristic length-to-thickness ratios of 37.5 and 25.0 for subdomains 1 and 2, respectively, SMS increases the critical time step sizes to 78.7 µs for subdomain 1 and 54.1 µs for subdomain 2.

Figure 5.5 shows the mechanical energy evolution for each case. All observed quantities remain stable. For $m = 1$, the total energy plateau is well preserved. It is worth noting that the multi-time-step computation with $m = 1$ provides the same results as the monolithic explicit computation. It is also important to underline that the use of the SMS technique ($\beta_0 = 0.25$ for both subdomains) has a negligible influence on the conservation of energy and momenta. For $m > 1$, a gradual loss of energy is observed. This is not due to the integration scheme itself, but to the assumed interpolation of the Lagrange multipliers between the coarse and fine steps [78]. This interpolation introduces

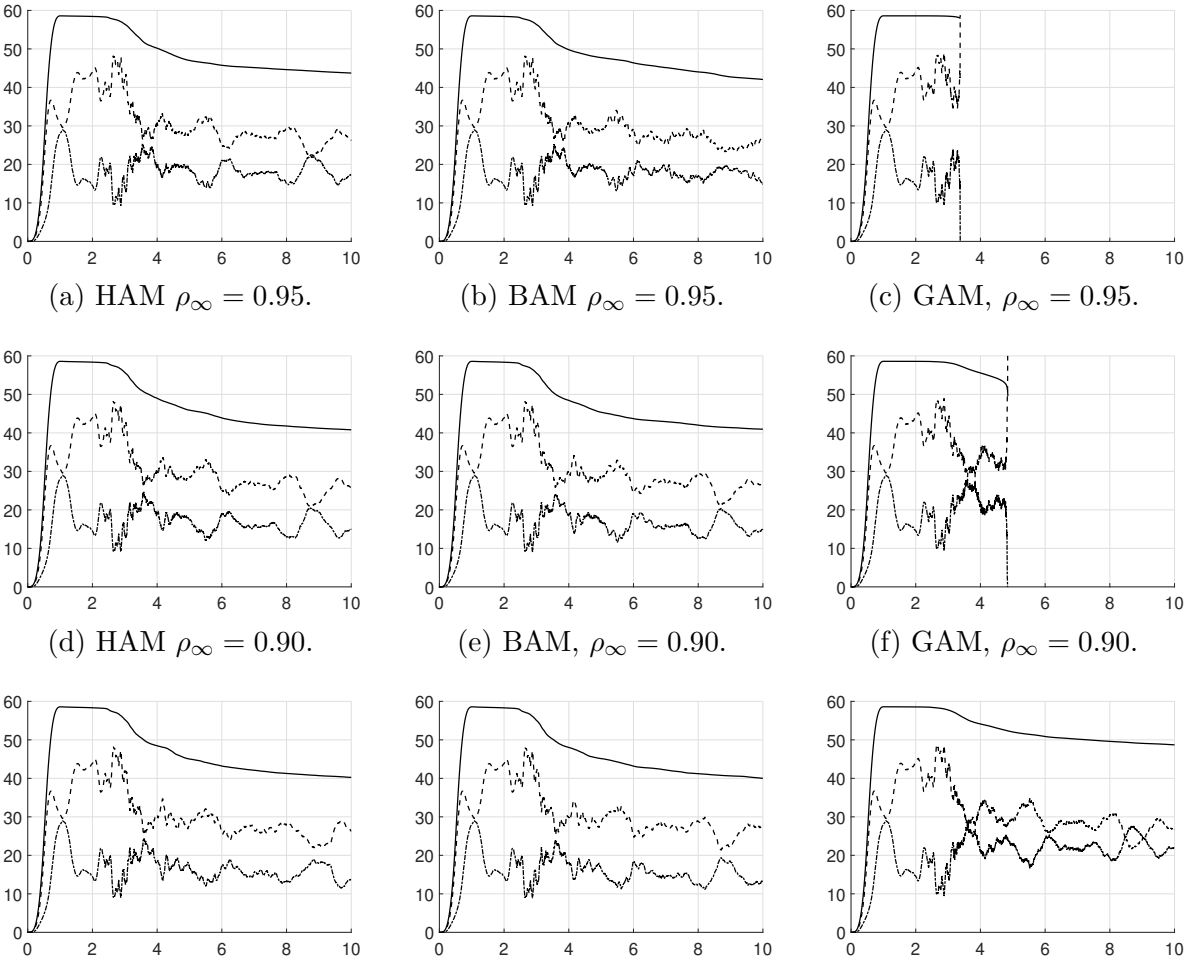

(a) HAM $\rho_\infty = 0.95$. (b) BAM $\rho_\infty = 0.95$. (c) GAM, $\rho_\infty = 0.95$.

(d) HAM $\rho_\infty = 0.90$. (e) BAM, $\rho_\infty = 0.90$. (f) GAM, $\rho_\infty = 0.90$.

(g) HAM, $\rho_\infty = 0.85$. (h) BAM, $\rho_\infty = 0.85$. (i) GAM, $\rho_\infty = 0.85$.

Figure 5.4 Three intersecting plates - Implicit computations using α–methods with $\Delta t = 5.00\,\text{ms}$: Energies $[J]$ versus time $[s]$ for different α–methods. Solid line: total energy, dashed: kinetic, dash-dot: internal energy.

small errors that accumulate over time, causing the observed energy loss. This drawback of the GC method is well-known, as well as the fact that the GC coupling between second-order accurate time integration schemes is only first-order accurate as soon as different time steps are considered. A new coupling algorithm has been proposed in [128], allowing the preservation of second-order accuracy. This new method has not been tested here. Moreover, in the light of previous results, it has to be noted that the drawback of the GC has to be nuanced: indeed, it can be seen that the loss of energy with GC multi-time step coupling for $m = 10$ is much lower than the loss of energy with α-generalized methods plotted in Figure 5.4.

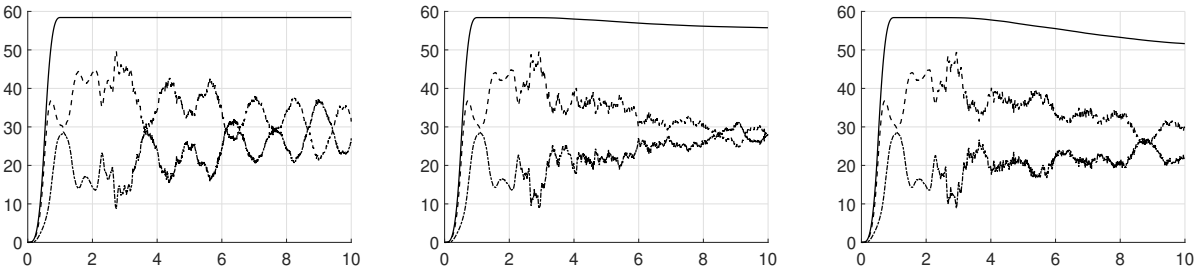

(a) $m = 1$ (b) $m = 10$ (c) $m = 35$

Figure 5.5 Three intersecting plates — multi-time-step explicit computations with $\Delta t_m = m\,\Delta t_j$: mechanical energies [J] vs time [s] for step ratios $m \in \{1, 10, 35\}$. Solid: total; dashed: kinetic; dash–dot: internal.

Conclusion. The benchmark of intersecting plates demonstrates that the developed implicit and explicit solvers, along with the standard mortar method, achieve good energy and momentum conservation. The results confirm the stability behavior of different α-methods and the multi-time step GC coupling algorithm. As underlined in the literature, the energy loss observed in the multi-time-step explicit solver using the GC method is retrieved.

5.2 Snap-through of Cylindrical Roof

We investigate the snap-through of a simply supported cylindrical roof, as illustrated in Figure 5.7. This problem, previously studied in [112, 57], is used here to evaluate solver robustness under fast stiffness changes, large displacements and post-buckling oscillations. The geometry and loading are shown in Figure 5.7, and typical deformed shapes during snap-through are presented in Figure 5.8.

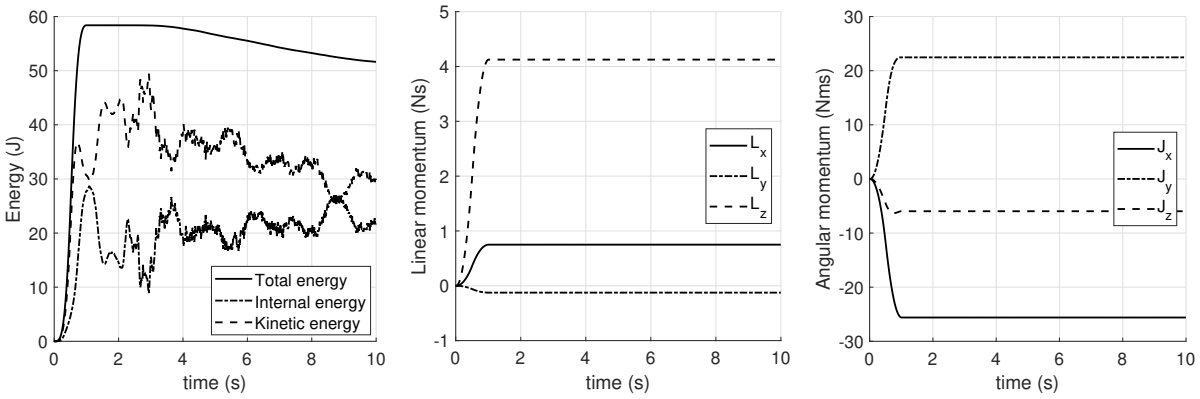

(a) Mechanical energies. (b) Linear momentum ***L***. (c) Angular momentum ***J***.

Figure 5.6 Three intersecting plates — multi-time-step explicit computations with $\Delta t_m = 35\,\Delta t_j = 70.0\,\mu s$: time histories of mechanical energies, linear momentum, and angular momentum.

The study first investigates implicit and explicit computations using a quarter-model of the structure, discretized with 4×4 8-node quadrilateral shell elements. The reference solution is obtained from a 3D model discretized by $4 \times 4 \times 2$ 20-node hexahedral elements. It is noted that two solid elements are used in the structure thickness to facilitate the assignment of the boundary condition at the mid-plane surface, as done in shell models. In the following, comparisons are made regarding displacement histories, energy, and energy error evolution. Subsequently, computations with standard mortar coupling are performed to evaluate the robustness and consistency of the mortar method.

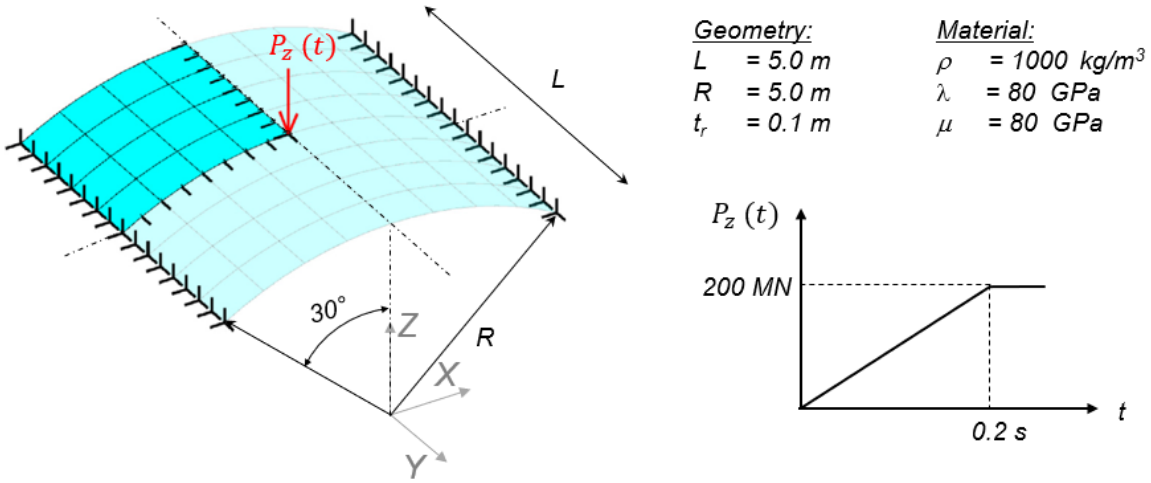

Figure 5.7 Cylindrical roof: Problem description (both sides of the roof are pinned).

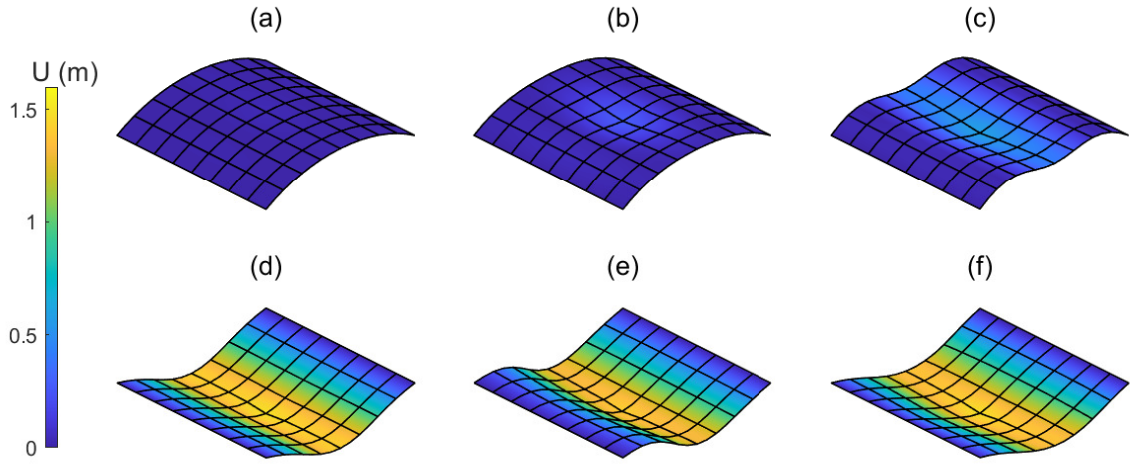

Figure 5.8 Cylindrical roof: Displacement U on the deformed configuration at different times: (a) $t = 0.01s$, (b) $t = 0.07s$, (c) $t = 0.14s$, (d) $t = 0.16s$, (e) $t = 0.20s$, (f) $t = 0.25s$.

5.2.1 Implicit computations

Constant time step

Using the Constant Average Acceleration (CAA) scheme with $\Delta t = 0.50\,\text{ms}$, both Newton–Raphson (NR) and Asymptotic Numerical Method (ANM) produce identical displacement histories (Figure 5.9(a)), matching the reference solid model. The 7-parameter shell accurately captures the buckling time ($t \approx 0.15\,\text{s}$), unlike the 6-parameter shell. Note that in [57], a mesh convergence test using ABAQUS [2] with the *S4R* element (a 4-node doubly curved shell element with reduced integration and hourglass control) confirms that the 4×4 7-parameter shell model and the 16×16 *S4R* shell model yield the same converged solution.

As seen in Figure 5.9(b), the number of ANM orders sharply rises in the post-buckling stage, where high-frequency modes are activated. ANM terminates earlier ($t \approx 0.18\,\text{s}$) due to the series order limit ($N_{\max} = 50$), while NR continues until instability at $t \approx 0.29\,\text{s}$, as highlighted by the dramatic growth of kinetic energy in Figure 5.10(a). With the Hilber–α method (HAM, $\rho_\infty = 0.8$), high-frequency oscillations are reduced, convergence improves, and both solvers again produce matching results (Figures 5.10–5.11). In summary, with fixed time steps, both solvers reproduce the reference response; HAM improves stability and efficiency, especially during the post-buckling stage.

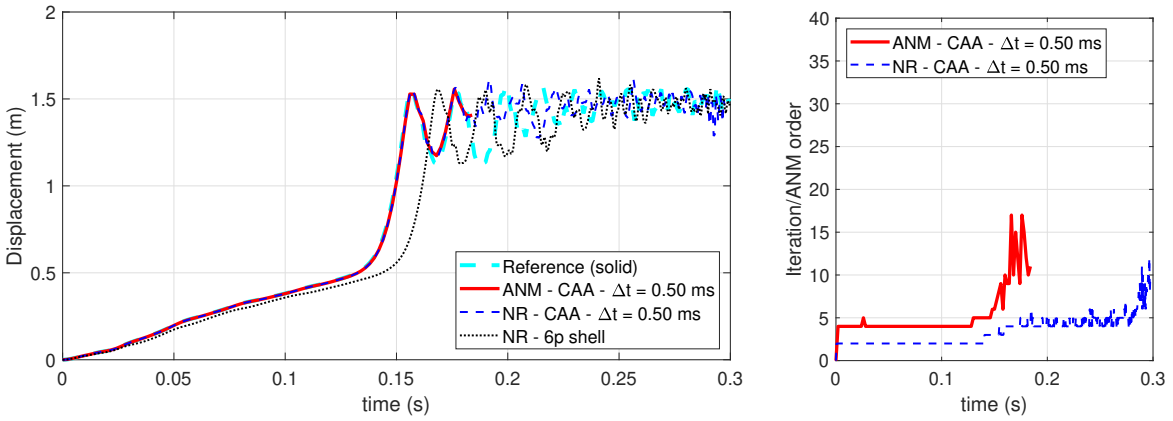

(a) Displacement of the loaded point. (b) Iteration / ANM order.

Figure 5.9 Cylindrical roof — CAA computations with $\Delta t = 0.50\,\text{ms}$: time history of the loaded-point displacement and the number of NR iterations / ANM order per step.

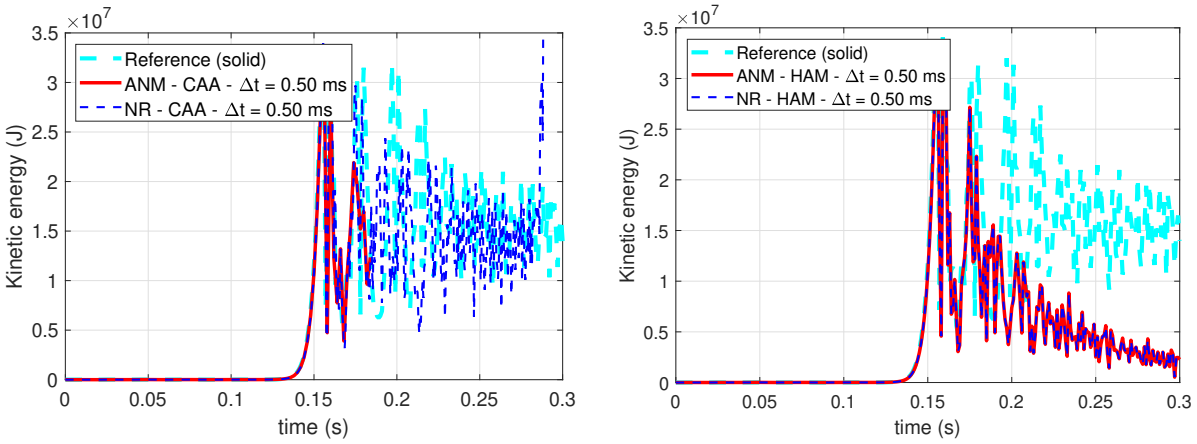

(a) CAA. (b) HAM.

Figure 5.10 Cylindrical roof — computations with $\Delta t = 0.50\,\text{ms}$: time history of the kinetic energy (CAA versus HAM).

Adaptive time stepping

We now perform computations using adaptive time steps with two maximum step sizes, $\Delta t_{\max} = 5.0\,\text{ms}$ and $\Delta t_{\max} = 2.5\,\text{ms}$. The time-stepping parameters are $I_n^{\text{NR}} = 8$ iterations and $I_n^{\text{ANM}} = 25$ orders; at each step, the solvers adjust the increment to remain within these limits.

The time history of the vertical displacement of the loaded point is shown in Figure 5.12(a). All solutions closely match the reference in the pre-buckling and buckling phases; however, in the post-buckling phase, the responses differ slightly from each other, unlike the constant-step case. In pre-buckling, both solvers take large steps close to $\Delta t_{\max}$

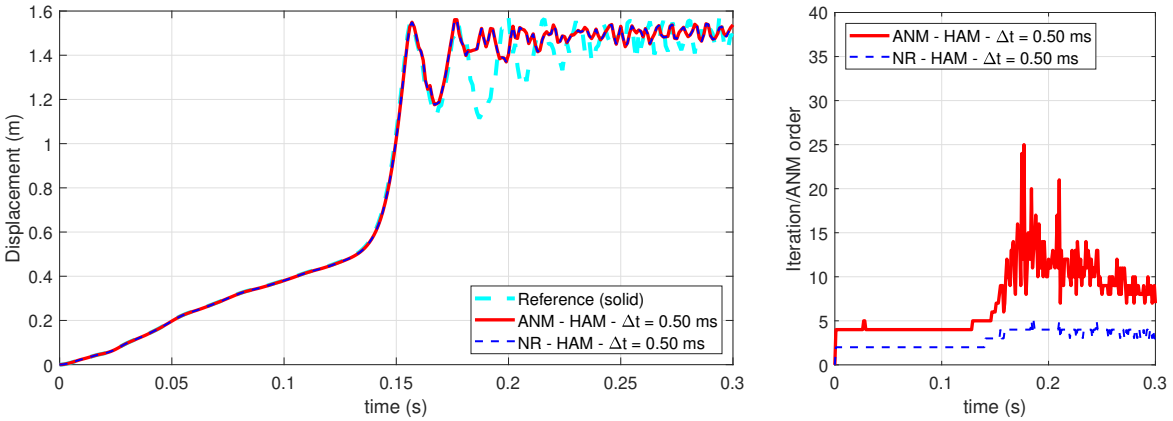

(a) Displacement of loaded point. (b) Iteration / ANM order.

Figure 5.11 Cylindrical roof — Hilber–α method (HAM, $\rho_\infty = 0.8$) with $\Delta t = 0.50\,\text{ms}$: time history of the loaded-point displacement and the number of NR iterations / ANM order per step.

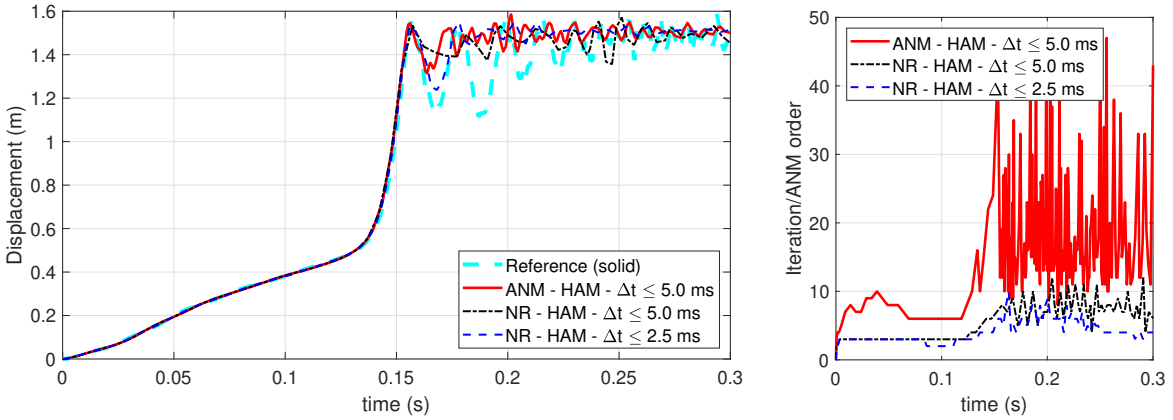

(a) Displacement of loaded point. (b) Iteration / ANM order.

Figure 5.12 Cylindrical roof - Hilber–α method computations with adaptive Δt: Time history of the displacement of the loaded point, and number of NR iterations / ANM order required for each time step.

(Figure 5.13(a)). During buckling, the step size decreases to capture the fast stiffness changes, and thereafter it adjusts itself to keep each solver near its target convergence rate during the post-buckling oscillations (Figure 5.12(b)). For $\Delta t_{\max} = 5.0\,\text{ms}$, the NR solver may increase the step size too quickly after buckling, leading to a non-physical increase in kinetic energy (Figure 5.13(b)). The maximum step of $\Delta t_{\max} = 2.5\,\text{ms}$—approximately one tenth of the fundamental period, as also recommended in [2]—prevents this issue.

The ANM solver allows for a more gradual time step adjustment and uses smaller steps in the post-buckling stage, which reduces the high-frequency energy dissipation

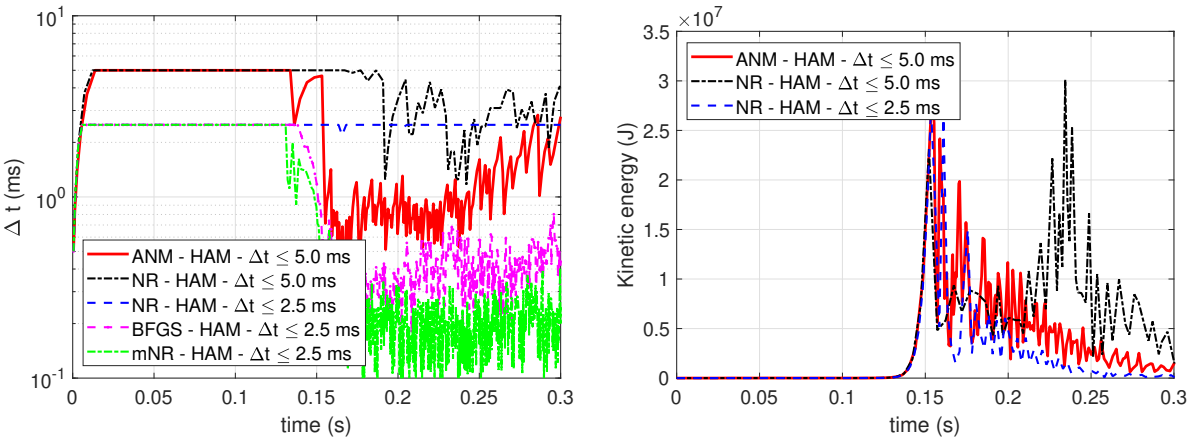

(a) time step size.

(b) Kinetic energy $W_{int.}$

Figure 5.13 Cylindrical roof - Hilber–α method computations with adaptive Δt: Time history of the time step size and the kinetic energy.

Table 5.2 Cylindrical roof — Time-stepping performance of implicit solvers.

Solver	$\Delta t_{\max}$	**Number of**			**Norm. CPU**
		Time steps	**Tangent matrices**	**Force vectors**	
ANM	5.0 ms	188	188	294×10^3	0.33
NR	5.0 ms	83	487	487	0.07
NR	2.5 ms	123	499	499	0.08
BFGS	2.5 ms	454	454	5235	0.52
mNR	2.5 ms	811	811	9307	1.00

(Figure 5.13(b)). However, Table 5.2 shows that NR converges more efficiently overall: ANM needs more time steps to complete the simulation, even though it requires fewer tangent operators (188 vs. 499 for NR). In contrast, ANM requires many more force-vector evaluations (294 862 vs. 499 for NR), increasing its computational time.

For comparison purposes, we also consider modified Newton–Raphson (mNR) and a quasi-Newton BFGS variant. In both cases, the exact tangent stiffness is evaluated at the beginning of each time step; in mNR, it is kept fixed across iterations, while in the quasi-Newton variant, it is updated by the BFGS algorithm [2]. Figure 5.13(a) and Table 5.2 indicate that the ANM outperforms both mNR and BFGS.

In summary, NR tends to achieve better time-stepping than ANM because it can take larger steps, making the effect of the α-methods more pronounced. When using NR, care must be taken in choosing $\Delta t_{\max}$ to avoid spurious kinetic-energy growth. The ANM advantage of fewer tangent assemblies is clear, but its large number of force evaluations makes it more expensive in this benchmark.

5.2.2 Explicit computations

We now consider explicit time integration for the snap-through of the cylindrical roof. The Central Difference scheme with lumped mass and the proposed treatment of the EAS field are used. As the ratio of the element characteristic length to the shell thickness $h_e/l_e \approx 3.0$, the use of the SMS permits us to increase the critical time step from 10.0 µs to 34.0 µs. In the following, all simulations are carried out with a time step of 30.0 µs. To control the oscillations in the post-buckling phase, Rayleigh damping is introduced via the Rayleigh matrix $\mathbf{C} = \alpha\,\hat{\mathbf{M}}$, where $\hat{\mathbf{M}}$ is the lumped mass matrix. The cases of $\alpha = 0.0$ (no damping) and $\alpha = 25.0$ are investigated. It is worth noting that the mass-proportional Rayleigh damping is usually preferred in explicit analyses as it does not alter the critical time step [2, 117]. Reference results are provided by implicit computation with solid elements.

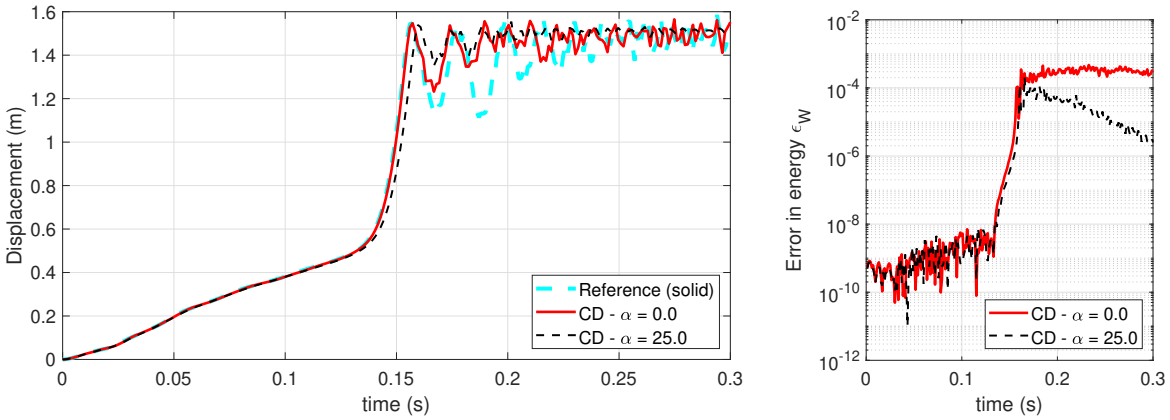

(a) Displacement of the loaded point.

(b) Energy error ϵ_W.

Figure 5.14 Cylindrical roof — explicit computations (with/without Rayleigh damping): time history of the loaded-point displacement and mechanical energy error ϵ_W.

In Figure 5.14(a), the undamped computation ($\alpha = 0$) matches the reference solution very well in both the pre-buckling and buckling phases. With mass-proportional Rayleigh damping ($\alpha = 25.0$), a slight shift in the predicted buckling time is observed, consistent with the introduced damping in low frequencies. The error norm in energy, whose calculation details can be found in Appendix B, is plotted in Figure 5.14(b). It confirms the accuracy of the explicit computations.

Figure 5.15 shows the time histories of the internal and kinetic energies and illustrates the expected energy decay under Rayleigh damping. A noteworthy observation is that, with $\alpha = 0$ (no Rayleigh damping), the computation using the proposed algorithm for the 7-parameter shell element exhibits a small amount of dissipation in the post-buckling phase

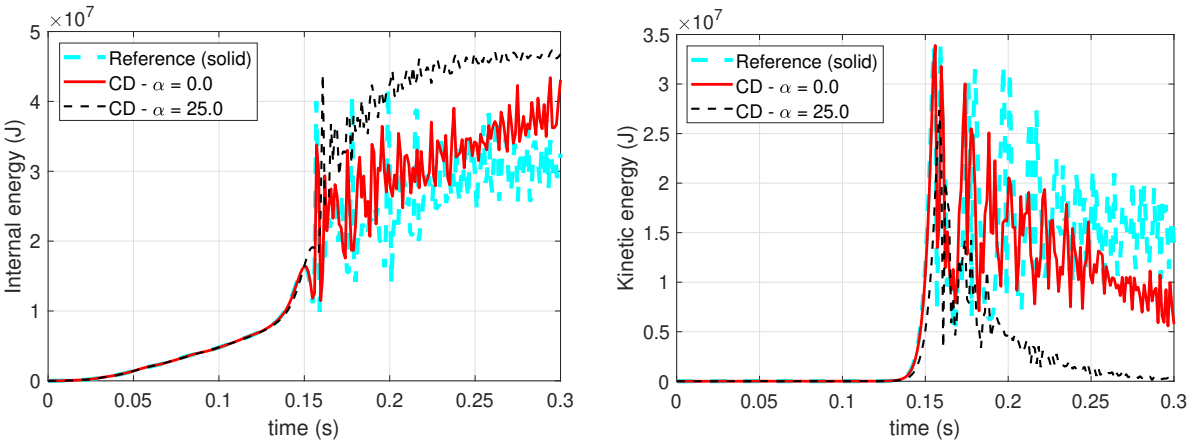

(a) Internal energy $W_{int.}$ (b) Kinetic energy $W_{kin.}$

Figure 5.15 Cylindrical roof — explicit computations (with/without Rayleigh damping): time histories of internal and kinetic energies.

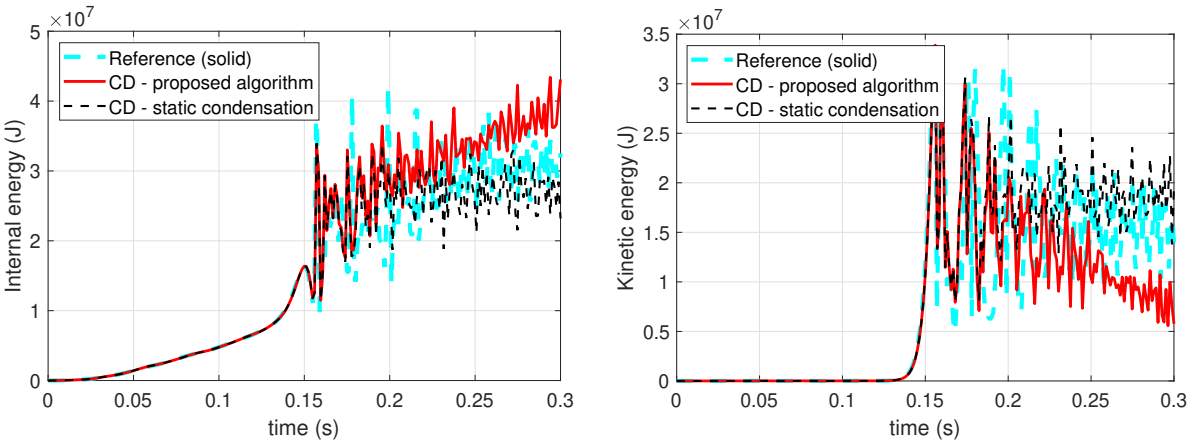

(a) Internal energy $W_{int.}$ (b) Kinetic energy $W_{kin.}$

Figure 5.16 Cylindrical roof — explicit computations with $\Delta t = 30\,\mu s$ and with no Rayleigh damping: time histories of internal and kinetic energies. Comparison between static condensation and the proposed EAS treatment.

when compared with the solid element computation. In contrast, the static-condensation treatment, corresponding to the EAS orthogonality condition solved for every element at each time step (see Section 4.4.3 and [54]), does not exhibit this dissipation, as seen in Figure 5.16. This phenomenon was not observed in the previous three-intersecting plates benchmark, suggesting that the proposed EAS treatment introduces some additional damping observed in the presence of high-frequency oscillations.

5.2.3 Computations with standard mortar coupling

We now consider the full cylindrical roof without exploiting symmetry. The structure is now divided into four subdomains, as displayed in Figure 5.17, each subdomain being discretized with a different element type. This test allows us to assess the robustness of mortar coupling between solid and shell elements both in implicit (NR and ANM) and explicit computations. The thin structure is decomposed into four subdomains listed below:

- Subdomain 1: 4×4 8-node quadrilateral shell elements,
- Subdomain 2: 6×6 6-node triangular shell elements,
- Subdomain 3: 3×3 fourth-order 25-node quadrilateral shell elements,
- Subdomain 4: $4 \times 4 \times 2$ 20-node hexahedral solid elements.

The coupling between subdomains is enforced using the standard mortar method. The current mesh breaks the symmetry of the problem, leading to an uncontrollable initial perturbation. Thus, we introduce a small lateral perturbation to the vertical load, $P_X = 0.1\, P_Z(t)$, to better control the perturbation. For the reference model, we use a full model with a uniform 8×8 mesh of 8-node quadrilateral shell elements. Reference results are provided adopting an implicit computation with a full shell model.

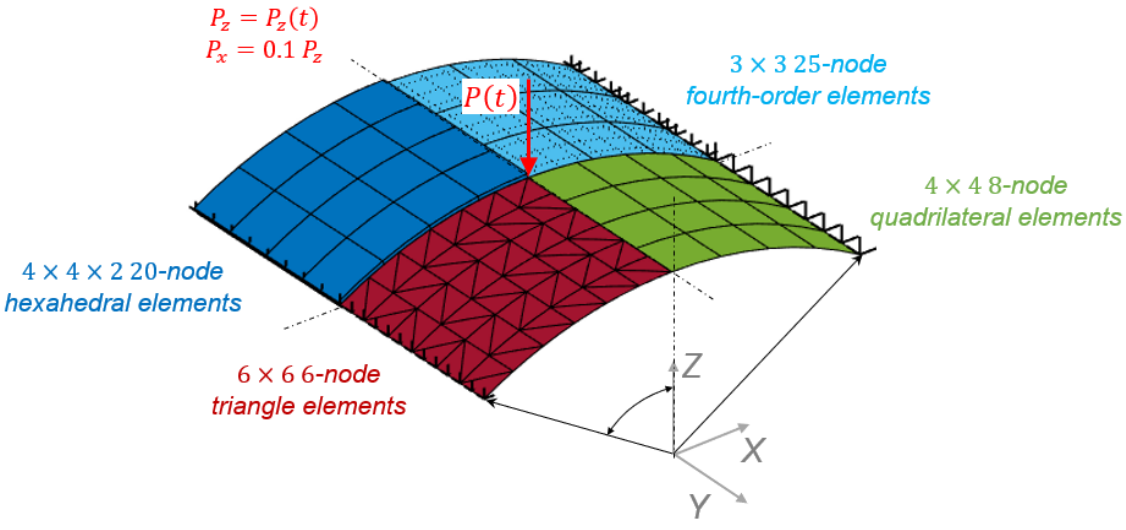

Figure 5.17 Cylindrical roof — subdomain partition and discretizations

For implicit computations, the NR solver produces displacement time history, plotted in Figure 5.19(a), in excellent agreement with the reference results. The ANM solver

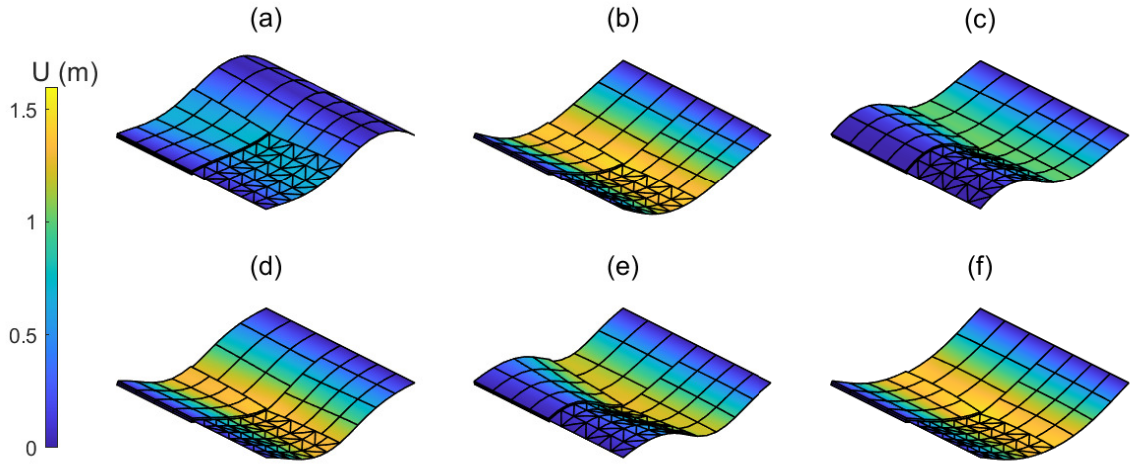

Figure 5.18 Cylindrical roof (asymmetric loading): snapshots of the displacement field U on the deformed configuration at selected times: (a) $t = 0.11\,\mathrm{s}$, (b) $t = 0.12\,\mathrm{s}$, (c) $t = 0.13\,\mathrm{s}$, (d) $t = 0.17\,\mathrm{s}$, (e) $t = 0.18\,\mathrm{s}$, (f) $t = 0.26\,\mathrm{s}$.

gives slightly different results in the high frequency oscillation stage, with a reduced time step as seen in Figure 5.19(b).

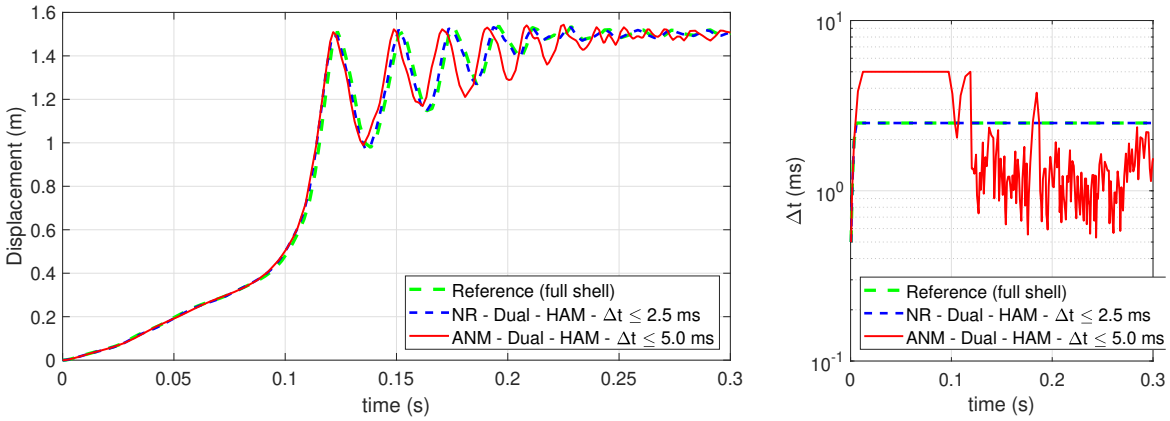

(a) Displacement of loaded point.

(b) time step size Δt.

Figure 5.19 Cylindrical roof — implicit computations with domain decomposition: time histories of the loaded-point displacement and the adaptive time step size.

For explicit computations, the multi-time-step explicit integrator is used: subdomains 1–2 employ a coarse time step $\Delta t_m = 25.0\,\mu\mathrm{s}$ (limited by subdomain 2), and subdomains 3–4 use a fine step $\Delta t_j = 2.5\,\mu\mathrm{s}$ (limited by the solid subdomain 4), yielding a step-size ratio $m = 10$. Mass-proportional Rayleigh damping is applied with $\mathbf{C} = 5.0\,\hat{\mathbf{M}}$. Results from the multi-time-step explicit computation, displayed in Figure 5.20(a), match

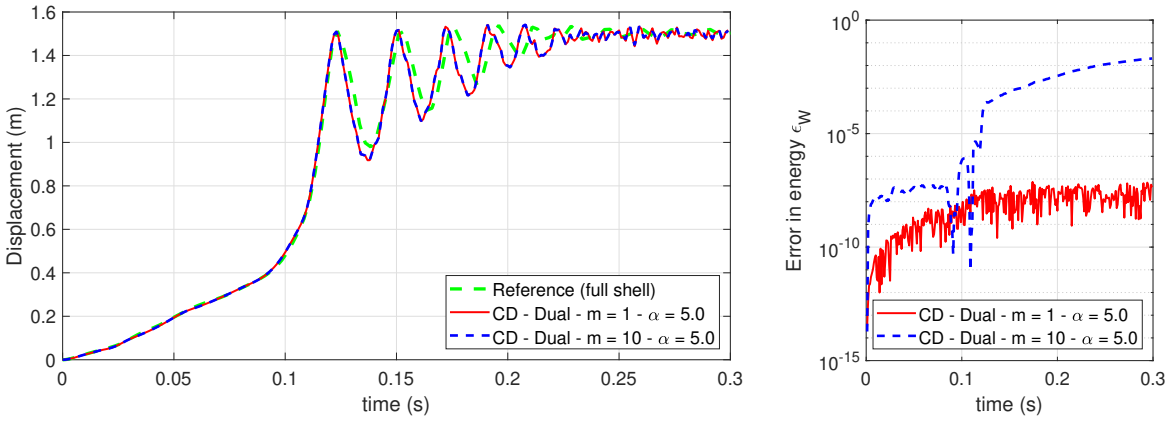

(a) Displacement of loaded point.

(b) Energy error ϵ_W.

Figure 5.20 Cylindrical roof — explicit computations with $\Delta t_m = 25.0\,\mu s$, $\Delta t_j = 2.5\,\mu s$ ($m = 10$) and Rayleigh damping $\mathbf{C} = 5.0\,\hat{\mathbf{M}}$: time histories of the loaded-point displacement and the mechanical-energy error ϵ_W.

the results obtained from the mono-time step computation ($m = 1$). Nonetheless, in Figure 5.20(b), as already observed in Section 5.1, the computation with $m = 10$ exhibits small energy dissipation, leading to an increase in energy error.

Overall conclusion . The snap-through benchmark confirms the excellent performance of the 7-parameter shell in triggering the snap-through buckling. For implicit computations with fixed time steps, the NR and ANM solvers yield identical results. Under adaptive time step setting, the NR allows for larger increments and is overall more efficient, but may spuriously increase kinetic energy unless $\Delta t_{\max}$ is chosen carefully. Whereas the ANM uses smaller time steps, assembles and factorizes fewer tangent matrices, but requires many force-vector evaluations.

The explicit computations provide excellent solutions compared to the reference. The use of mass-proportional Rayleigh damping slightly affects the solution. A small additional dissipation is observed with the proposed explicit EAS treatment in strongly oscillatory regimes; this is not present when using static condensation of the EAS field.

Finally, standard mortar coupling (shell–shell and shell–solid) preserves the accuracy of the single-domain solution. The explicit multi-time-step coupling ($m > 1$) exhibits energy loss as expected. Overall, this classical benchmark of the snap-through of the cylindrical roof, validates the accuracy, robustness, and efficiency of the developed solvers as well as the adopted coupling strategies. In the following, post-buckling branch-switching problems are investigated.

5.3 Implicit Buckling of Thin Shells

This section compares the Asymptotic Numerical Method (ANM) and the Newton–Raphson (NR) solvers on dynamic buckling problems. Two benchmarks are considered: an axially loaded cylinder and a closed cylinder under pressure load. In the latter, the tangent operator is non-symmetric due to the non-conservative loads. In all computations, the time-stepping parameters are $I_0^{\mathrm{NR}} = 8$ and $N_{\max}^{\mathrm{NR}} = 12$ for the NR solver, and $I_0^{\mathrm{ANM}} = 20$ and $N_{\max}^{\mathrm{ANM}} = 40$ for the ANM solver. We investigate snap-through timing, branch switching, and time-stepping performance.

5.3.1 Axially loaded cylinder

In this section, we consider the elastic buckling of a cylinder under axial compression. The benchmark is based on one of the experiments carried out by Yamaki [164], as illustrated in Figure 5.21. Numerical investigations of the benchmark were studied by [103, 114].

Figure 5.22 displays the specimen deformation and the load-displacement curve from [164]. These are grouped into two family curves —*Asymmetric* and *Symmetric*—defined with respect to the cross-section at mid-height. The asymmetric patterns were obtained by loading/unloading via edge axial displacement, whereas the symmetric patterns were induced by applying localized perturbations normal to the shell surface (finger taps). The results revealed a complex post-buckling branch-switching response, with abrupt, repeated changes in the number of circumferential waves n as loading progressed.

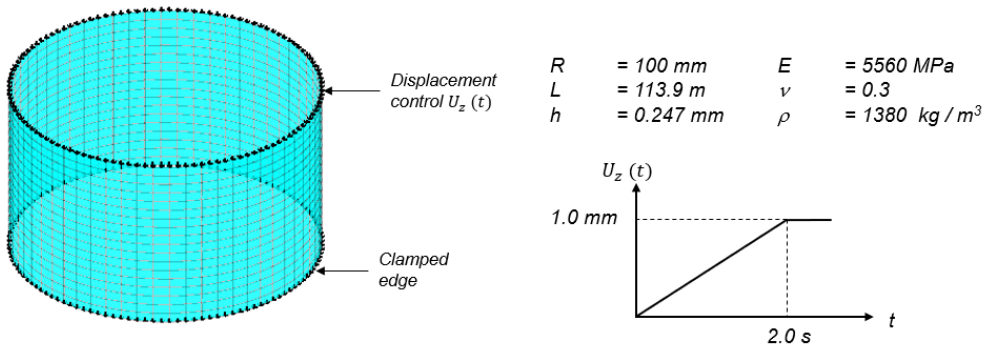

Figure 5.21 Axially loaded cylinder - problem description.

The model setup is illustrated in Figure 5.21. The cylinder is discretized with 200×40 8-node quadrilateral shell elements. In line with Lavrencic and Brank [114], we perturb

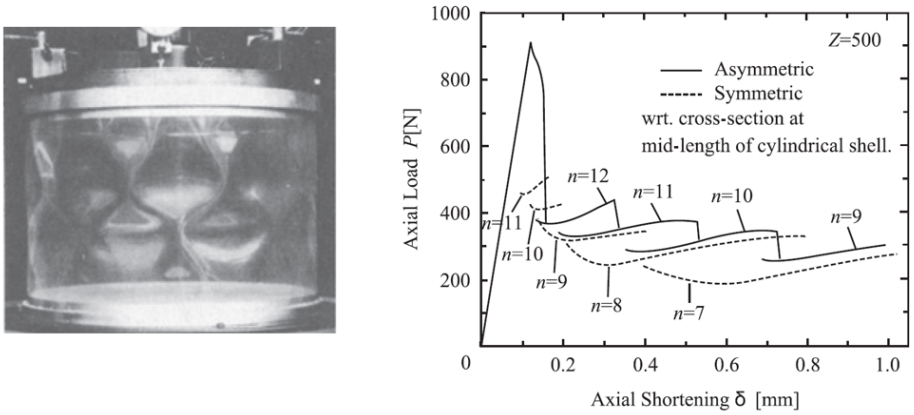

Figure 5.22 Axially loaded cylinder — experimental results [164]: deformation (left) and load–displacement curve (right). n denotes the number of circumferential waves.

the initial geometry using:

$$\Delta R(\phi, z) = \frac{h}{100}\left(\sum_{m=12}^{13} \sin\frac{m\pi z}{L} + \sum_{n=1}^{7} \sin(n\phi)\,\sin\frac{13\pi z}{L} + \sum_{n=1}^{9} \sin(n\phi)\,\sin\frac{12\pi z}{L}\right) \quad (5.1)$$

where ΔR is added to the radius, ϕ and z denote cylindrical coordinates, and $h = 0.247\,\text{mm}$ is the thickness. The map of ΔR is shown in Figure 5.23(a).

For the time discretization, we employ the Hilber–α method (HAM) with adaptive time-stepping $\Delta t \leq 0.01\,\text{s}$, and consider $\rho_\infty \in \{0.8, 0.6\}$. Strong numerical dissipation is required in this test and can affect the results, as reported in [114].

Figure 5.24 displays the imposed displacement–reaction force curve from our simulations versus the experimental results. All simulations predict the same first buckling load, which is lower than the experiment. The first buckling load is sensitive to the geometric perturbation: our value matches Lavrencic and Brank [114], which uses the same perturbation, whereas Kobayashi et al. [103] reported a higher load using a mode-based perturbation from a linear eigen-buckling analysis.

Table 5.3 Axially loaded cylinder — computational time-stepping workload (adaptive, $\Delta t \leq 0.01\,\text{s}$).

ρ_∞	Solver	Time steps	Tangent assemblies	Force evaluations	Norm. CPU
0.6	NR	620	4621	4621	0.21
0.8	NR	1026	8126	8126	0.36
0.6	ANM	2520	2520	1.54×10^6	1.00

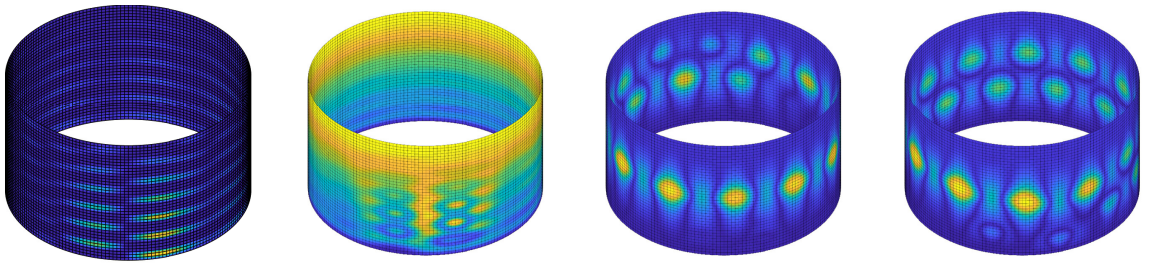

(a) Initial geometry (b) Pre-buckling (c) $n = 11$ (d) $n = 11/n = 12$

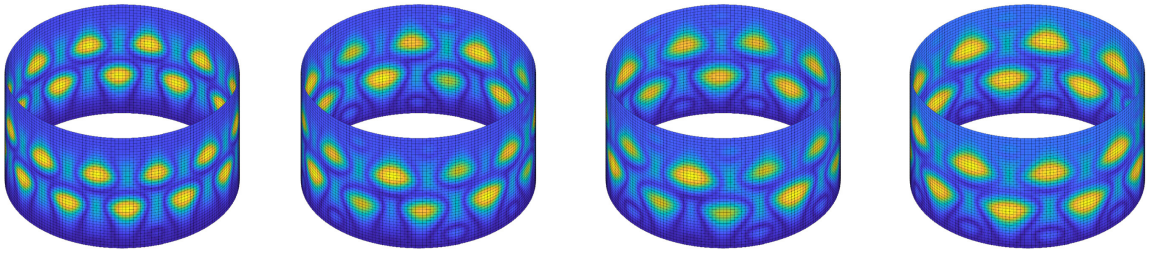

(e) $n = 12$ (f) $n = 11$ (g) $n = 10$ (h) $n = 9$

Figure 5.23 Axially loaded cylinder - Cartography of perturbation values ΔR (a) and deformed configurations (b-h) corresponding to the black points in Figure 5.24. n denotes the number of circumferential waves.

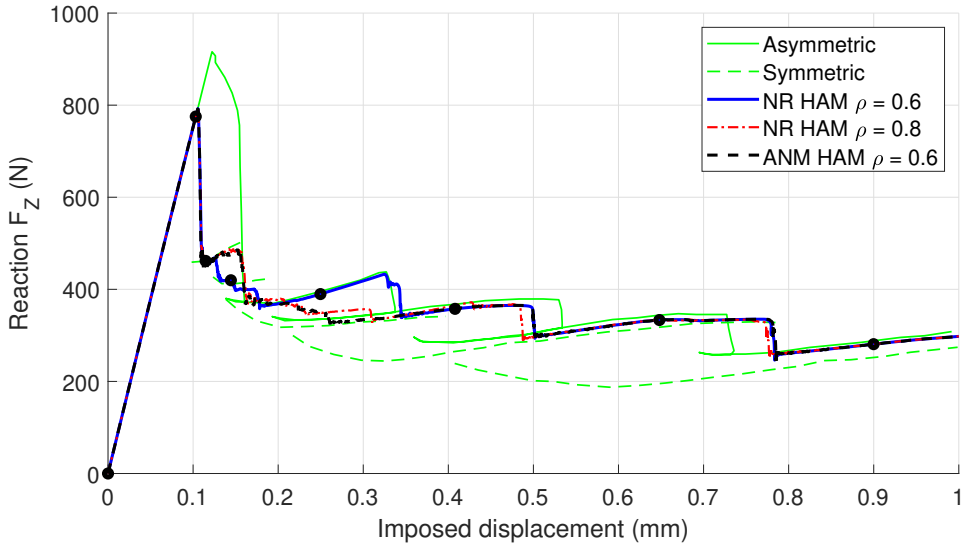

Figure 5.24 Axially loaded cylinder - Load-displacement curves from the experiment (Asymmetric and Symmetric curves) and the numerical solutions using NR and ANM solvers.

After the first buckling, the solution jumps to the configuration in Figure 5.23(c), matching a symmetric experimental mode with $n = 11$ (the deformed shape is not

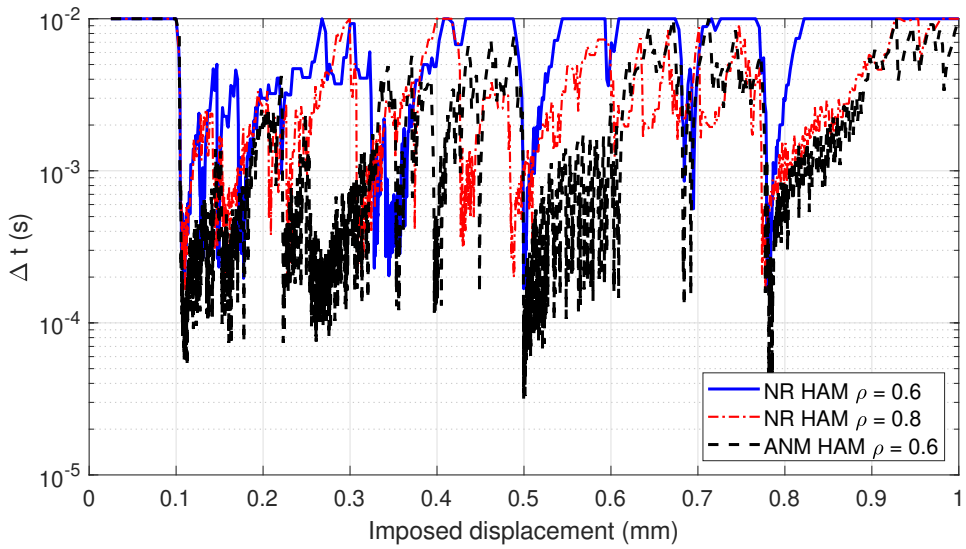

Figure 5.25 Axially loaded cylinder - Evolution of time step size during the simulation of NR and ANM solvers.

perfectly symmetric but exhibits 11 circumferential waves). From this point, different ρ_∞ values—hence different time step sizes (Figure 5.25) and inertial (kinetic) energy—lead NR to follow different post-buckling branches. In all cases, the load-displacement curves and the identified n values along the path (Figure 5.23) agree well with the experiments.

Figure 5.25 shows the time evolution of the time-step size, confirming the efficiency of the adaptive strategy. NR generally employs larger steps than ANM; consequently, numerical dissipation has less impact in the ANM computation, which explains the close agreement between ANM with $\rho_\infty = 0.6$ and NR with $\rho_\infty = 0.8$. Table 5.3 shows that ANM requires 2520 steps versus 1026 and 620 for NR; ANM assembles fewer tangents but many more force-vector evaluations, leading to higher CPU time. On average, the ANM solver evaluates about 600 force vectors for each time step.

5.3.2 Closed cylinder under pressure load

This benchmark examines the dynamic buckling of a thin closed cylindrical shell subjected to a (follower) pressure load. The case was investigated in the quasi-static regime by Ventura et al. [157]; here it serves to assess the solvers' ability to handle follower loads and multiple buckling paths. The problem setup is shown in Figure 5.26. By enforcing symmetry at mid-length, only one half of the cylinder is modeled, using 8-node quadrilateral shell elements.

A preliminary linear eigen-buckling analysis is performed, imposing constraints on the in-plane displacement at the center of the end disk and on the circumferential

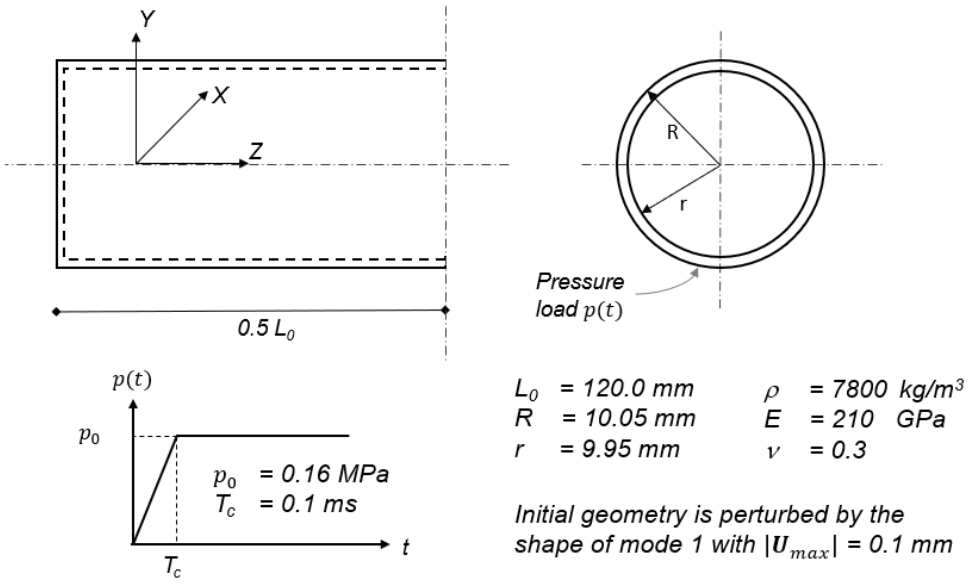

Figure 5.26 Closed cylinder under pressure load: problem description.

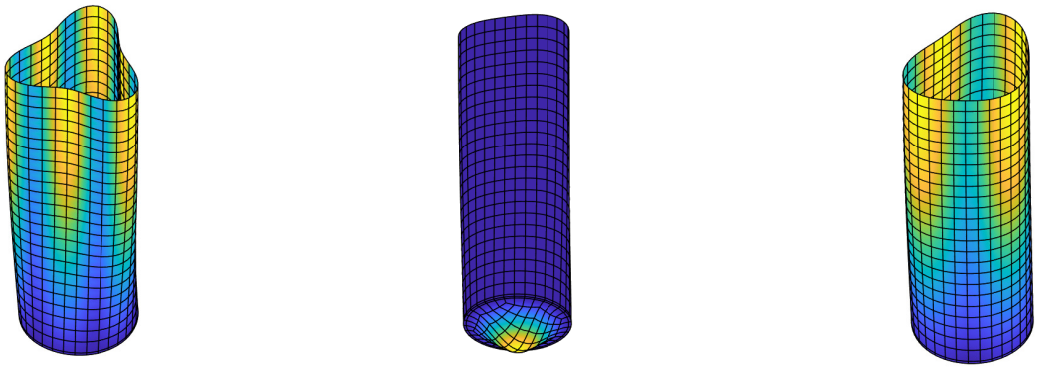

(a) Mode 1: $\lambda = 0.17$. (b) Mode 2: $\lambda = 0.18$. (c) Mode 3: $\lambda = 0.25$.

Figure 5.27 Closed cylinder under pressure load: The first three buckling modes obtained from the linear eigen-buckling analysis.

displacement at one point on the disk, in order to prevent the rigid-body modes. These constraints are not present in the subsequent dynamic simulations. The first three eigenmodes (most critical mode shapes) are shown in Figure 5.27. The shape of the first mode is used to perturb the initial geometry, with a maximum amplitude of 0.1 mm. All computations are performed using the Hilber–α method with a spectral radius of $\rho_\infty = 0.90$.

Computations with constant time step. With a fixed time step of $\Delta t = 0.01\,\text{ms}$, both NR and ANM produce identical solutions (Figure 5.28(a)). The evolution of the relative residual error in Figure 5.28(b) confirms the accuracy of the solutions, remaining less than 10^{-6}. Figure 5.28 also displays the results from the model with conservative load, showing that the buckling does not occur in this case, and highlighting the importance of correctly modeling the follower load.

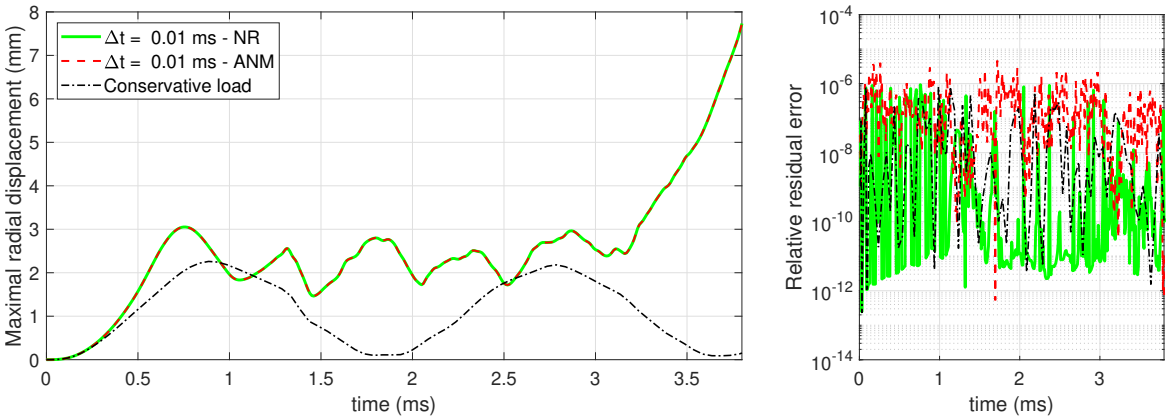

(a) Displacement of loaded point. (b) Relative residual error.

Figure 5.28 Closed cylinder under pressure load — implicit computations with $\Delta t = 0.01\,\text{ms}$: time histories of the maximal radial displacement and the relative residual error.

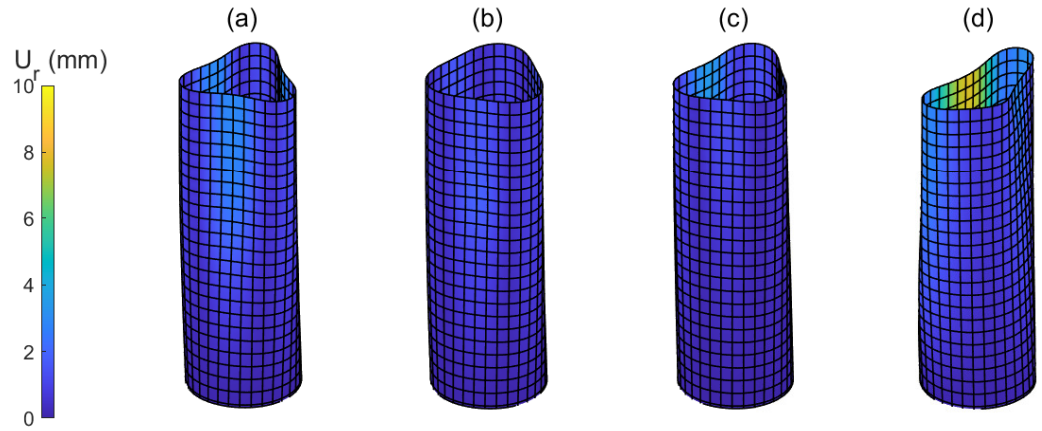

Figure 5.29 Closed cylinder under pressure load — maximal radial displacement on the deformed configuration at: (a) $t = 0.75\,\text{ms}$, (b) $t = 1.50\,\text{ms}$, (c) $t = 3.20\,\text{ms}$, (d) $t = 3.80\,\text{ms}$.

The time histories of displacement (Figure 5.28(a)) as well as the snapshot of deformed configurations (Figure 5.29) show that the first buckling event occurs at $t \approx 0.75\,\text{ms}$,

producing a three-lobe deformation consistent with the first eigenmode. The cylinder then oscillates about this post-buckling equilibrium, exciting high-frequency modes. A second buckling event occurs at $t \approx 3.2\,\text{ms}$, switching to a two-lobe pattern corresponding to the third eigenmode. The occurrence of the second buckling is linked to the asymmetric perturbation of the initial geometry caused by the boundary conditions used in the eigen-buckling analysis to suppress rigid-body motion. This asymmetry becomes more significant due to numerical errors, especially during the oscillation after the first buckling.

Computations with adaptive time step. Adaptive time step setting is now applied with a maximum step size of $\Delta t_{\max} = 0.05\,\text{ms}$. Figure 5.30(a) compares the displacement histories from NR and ANM against the constant time step result. Both solvers closely match the constant-time-step solution during the pre-buckling and first buckling phases ($t < 0.7\,\text{ms}$). Slight deviations appear in the post-buckling regime, more pronounced in NR due to its tendency to adopt larger steps when oscillations are present (Figure 5.30(b)).

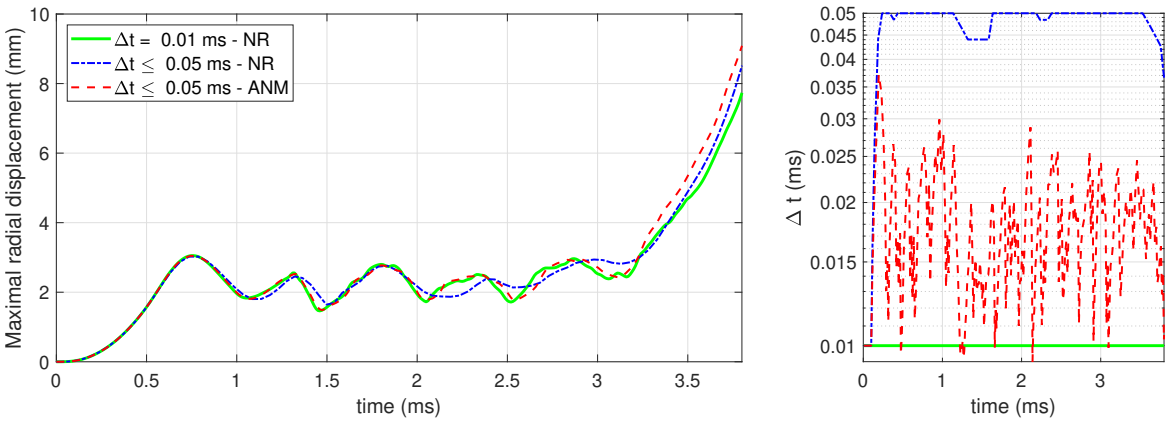

(a) Displacement of the loaded point. (b) Time step size.

Figure 5.30 Closed cylinder under pressure — implicit computations with $\Delta t \leq 0.05\,\text{ms}$: time histories of the maximal radial displacement and the time step size.

The computational performance for the different settings is summarized in Table 5.4. With $\Delta t_{\max} = 5.0\,\text{ms}$, NR completes the simulation in 98 steps, requiring 550 tangent-matrix factorizations, whereas ANM takes 266 steps with the same number of tangent evaluations, but many more force-vector computations, leading to a higher CPU time.

Use of symmetric tangent operator. For follower pressure loads, the exact tangent operator is non-symmetric due to the tangent matrix $\mathbf{K}_L$ presented in Section 3.5, thus demanding more computational time to be factorized. Here, we are interested

Table 5.4 Closed cylinder under pressure — computational time-stepping workload.

Time-step control (Δt)	Solver	Time steps	Tangent assemblies	Force evaluations	Norm. CPU
$\Delta t = 0.01$ ms	NR	401	1560	1560	0.49
	ANM	401	401	48 793	0.59
$\Delta t \leq 0.05$ ms	NR	98	550	550	0.25
	ANM	266	266	1.6×10^5	0.98
$\Delta t \leq 0.01$ ms, symmetrized tangent	NR	98	550	550	0.16
	ANM	264	264	1.7×10^5	1.00

Note: CPU is normalized by the ANM case with $\Delta t \leq 0.01$ ms and a symmetrized tangent.

in the performance of the solvers while using the symmetrized tangent operator. The symmetrization is carried out by replacing $\mathbf{K}_L$ by $\frac{1}{2}(\mathbf{K}_L + \mathbf{K}_L^{\mathrm{T}})$ in the computations.

Figure 5.31(a) shows that the displacement histories obtained with the symmetric tangent operator are identical to those from the exact-tangent formulation for both NR and ANM. Nevertheless, the evolution of the relative residual error in Figure 5.31(b) demonstrates that while NR maintains its accuracy, ANM results exhibit a noticeable loss of accuracy. This reduction in accuracy was expected: since an inexact symmetrized tangent operator is employed, the convergence of the displacement series does not guarantee the convergence of the residual.

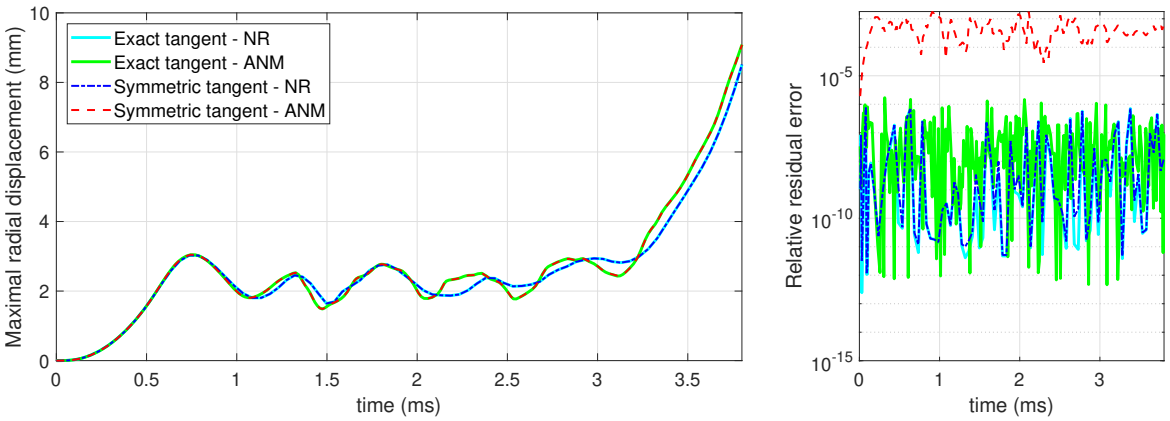

(a) Displacement of the loaded point. (b) Relative residual error.

Figure 5.31 Closed cylinder under pressure — implicit computations with $\Delta t \leq 0.05$ ms and a symmetric tangent operator: time histories of the maximal radial displacement and the relative residual error.

Table 5.4 reveals that using the symmetrized tangent operator does not change the number of time steps and tangent matrix factorizations for both NR and ANM solvers.

As expected, we observe a significant reduction in computational time in the NR solver when using the symmetrized tangent operator.

5.3.3 Conclusion

The two dynamic post-buckling branch-switching benchmarks—the axially loaded cylinder and the closed cylinder under follower pressure—together with the cylindrical roof in Section 5.2, confirm the accuracy and robustness of both Newton–Raphson (NR) and Asymptotic Numerical Method (ANM) implicit solvers for geometrically nonlinear dynamics. The numerical models perform very well in triggering buckling, capturing snap-through, the ensuing oscillatory response, and the relevant post-buckling branches.

The *Hilber–α* method (and related α-methods) and the *adaptive time-stepping* strategy play an essential role in implicit buckling analysis. The introduced numerical dissipation suppresses spurious high-frequency modes activated in the post-buckling oscillations, while preserving the accuracy of the primary buckling onset and the post-buckling branch selection. The adaptive time-stepping strategy further improves the solvers' efficiency and robustness: small time steps are used during and after buckling, and larger time steps are used in smooth phases.

The efficiency of the solvers is investigated by measuring time-stepping performance, solver workload (tangent/force evaluations), and CPU time. The investigation shows that ANM requires more time steps than NR. Although it assembles fewer tangent operators, the large number of force-vector evaluations makes ANM computationally more expensive. In the two benchmarks in this section, ANM performs on average about 600 force vector evaluations per time step; this figure can serve as a reference when assessing the feasibility and potential benefits of parallelizing the ANM solver implementation.

Overall, the implicit studies confirm that (i) both solvers are accurate and robust; (ii) the Hilber–α method turns out to be an efficient and reliable way to improve robustness in the post-buckling regime; and (iii) adaptive stepping is essential to balance stability, accuracy, and cost across smooth and highly nonlinear phases.

5.4 Finite-Strain Elasto-plastic Dynamics

The objectives of this section are threefold: (1) validate the finite-strain elasto-plastic framework for shell structures; (2) verify the accuracy and robustness of the implicit Newton–Raphson solver under combined material and geometric nonlinearities; and (3) assess the performance of the proposed explicit algorithm for 7-parameter shell elements.

Six benchmark problems are considered. The first is a quasi-static case that provides a baseline validation of the elasto-plastic framework under severe large deformation. The remaining five involve impulsive loading with significant dynamic effects. In all simulations, 8-node quadrilateral elements are used for shell models. In all dynamic benchmarks, three computations are performed: (i) an explicit run with the 6-parameter shell formulation, (ii) an implicit run with the 7-parameter shell formulation using the Newton–Raphson method, (iii) an explicit run with the proposed algorithm using the 7-parameter shell formulation. Reference solutions are taken either from the literature or from full 3D solid models using 20-node hexahedral elements, which have the same in-plane mesh as the shell model and a single element through the thickness.

In the computations of 6-parameter shell models, the enhanced strain variable $\tilde{\beta}_{33}$ is not included, so discrepancies are expected. By contrast, in the implicit 7-parameter shell computations, the orthogonality condition is fully satisfied. We employ the Hilber–α method with $\rho_\infty = 0.9$ and the adaptive time-step setting: the desired and maximal numbers of iterations are $I_0 = 6$ and $N_{\max} = 8$. To maintain focus on the performance of the explicit run of the 7-parameter shell models throughout this section, let us summarize here the workload of the implicit computations for all benchmarks in Table 5.5.

The explicit computation of the 6-parameter shell models and the implicit computations, as well as the references, permit us to evaluate the accuracy of the proposed explicit algorithm for 7-parameter shell elements. We also investigate the robustness of the explicit computations by observing the evolutions of the two error norms, in energy ϵ_W, and in the orthogonality condition ϵ_{EAS} (see Appendix B).

Table 5.5 Finite-strain elasto-plastic dynamics — time-stepping workload of *implicit NR* computations.

Benchmark (test case)	Time interval	Time steps	Tangent assemblies	Avg. NR iter./step
Quasi-static pinched hemisphere	$[0,1]\cup[1,0]$	20	109	5.45
Plate under pressure (Mesh 2)	$[0, 1.2\,\text{ms}]$	101	259	2.56
Roof under velocity impulse (Mesh 2)	$[0, 1.0\,\text{ms}]$	212	1387	6.54
Pinched cylinder	$[0, 1.0\,\text{ms}]$	706	4270	6.05
Twisted cylinder	$[0, 2.1\,\text{ms}]$	111	601	5.41
Stiffened roof	$[0, 50.0\,\text{ms}]$	118	617	5.24

Note: For the quasi-static run, the "time interval" denotes the load path (loading–unloading), and the load increment of 0.1 is fixed during the computation.

5.4.1 Quasi-static pinched hemisphere

We consider the classical pinched hemisphere benchmark, widely used to assess nonlinear shell formulations combining material and geometric effects [10, 101, 67, 50, 4, 118]. The model setup is illustrated in Figure 5.32(a): a thin hemispherical shell of radius $R = 100.0\,\text{mm}$ and thickness $t = 5.0\,\text{mm}$, made of a material with Young's modulus $E = 100\,\text{MPa}$, Poisson's ratio $\nu = 0.2$, and linear isotropic hardening $R(\xi) = 2+30\,\xi$ MPa. Two pairs of opposing point forces load the hemisphere, each with a magnitude of $2F = 2 \times 35$ N, applied at the bottom. Due to symmetry, only one quarter of the structure is modeled using 7-parameter shell elements. The analysis is performed using the Newton–Raphson solver and exact tangent matrices. The load is increased from 0.0 N to 35 N (loading) and then decreased to 0.0 N (unloading) in load increments of 3.5 N. The results are compared with the solution of NURBS-based Kirchhoff-Love shell reported in Ambati et al. [4].

Figure 5.32(b) shows the load–deflection curve at the loaded points. The 7-parameter shell closely reproduces the reference response, whereas the 6-parameter shell is noticeably stiffer. The evolution of the hardening variable at selected loading and unloading stages is illustrated in Figure 5.33. The workload of the 7-parameter shell model run is shown in Table 5.5, confirming the robustness of the implemented finite-strain elasto-plasticity framework and providing a solid foundation for the subsequent dynamic benchmarks.

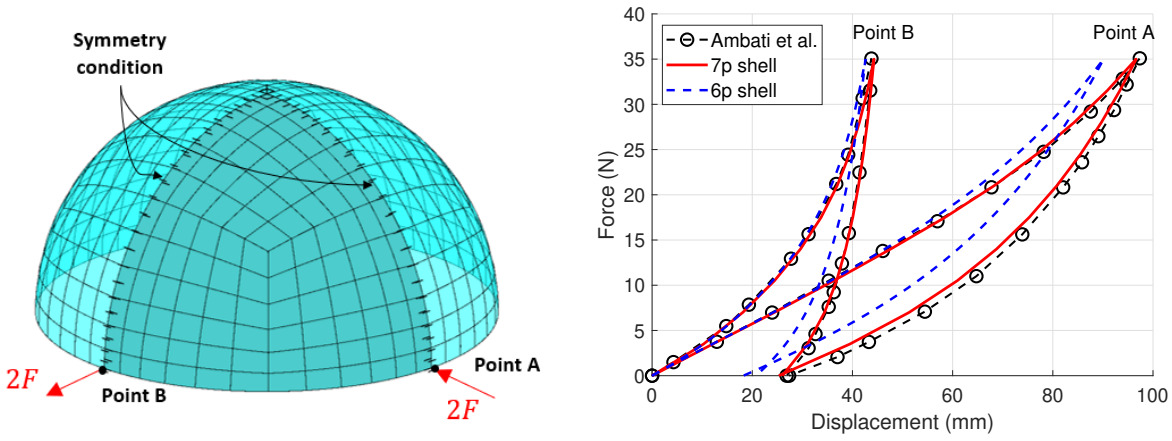

(a) Problem description.

(b) Force-displacement curve.

Figure 5.32 Pinched hemisphere: problem description and force-displacement curve

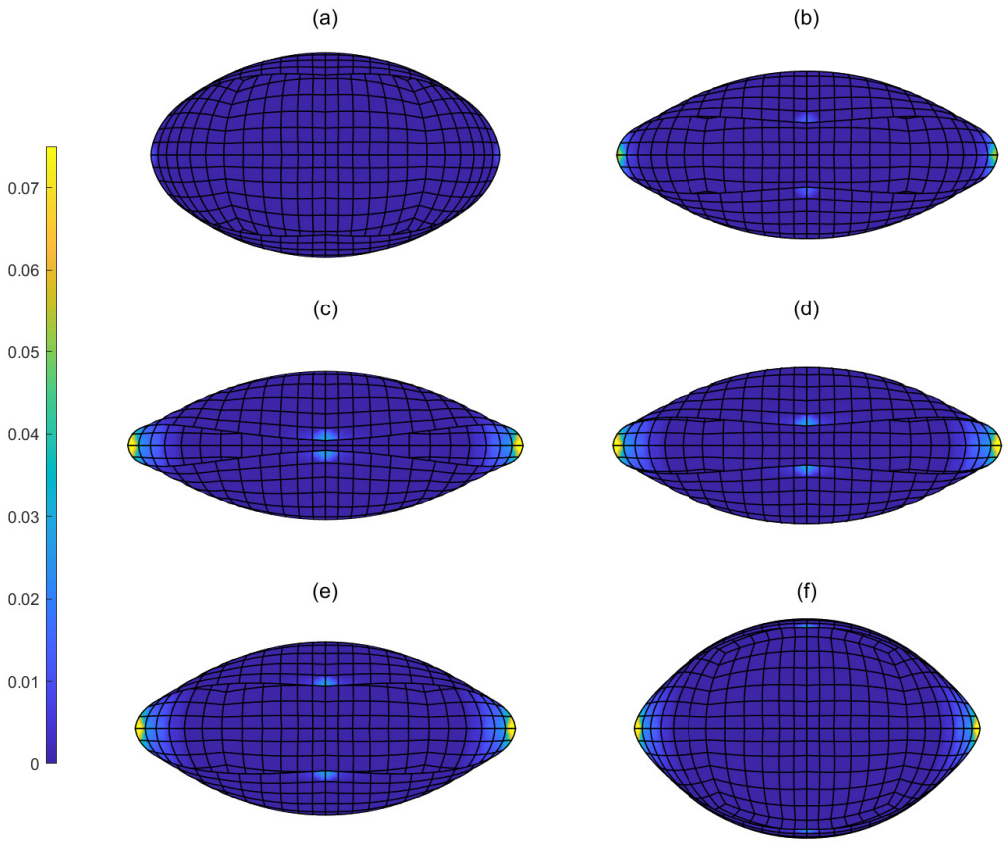

Figure 5.33 Pinched hemisphere: hardening variable ξ (at the midplane surface) at various loading stages on the deformed configuration. (a)–(c) loading with u_A = 42.0 mm, 77.7 mm, 96.5 mm; (d)–(f) unloading with u_A = 85.8 mm, 69.3 mm, 26.8 mm

.

5.4.2 Plate under uniform pressure

A simply supported square plate subjected to a suddenly applied uniform pressure load, as illustrated in Figure 5.34, is considered. This benchmark has been studied in [16, 21]. The pressure is applied instantaneously at $t = 0$ and remains constant for the entire simulation. The plate is modeled as an elastic–perfectly plastic material, and by symmetry, only one quarter of the domain is analyzed.

Two meshes are used: a coarse mesh of 8×8 elements (M1) and a fine mesh of 16×16 elements (M2). In both cases, since the characteristic element length is smaller than the thickness, we do not employ the SMS technique. The time steps used for the two meshes are respectively 0.3 µs and 0.6 µs. The reference is the computational result reported in [21], employing 32×32 Belytschko–Tsay shell elements [16].

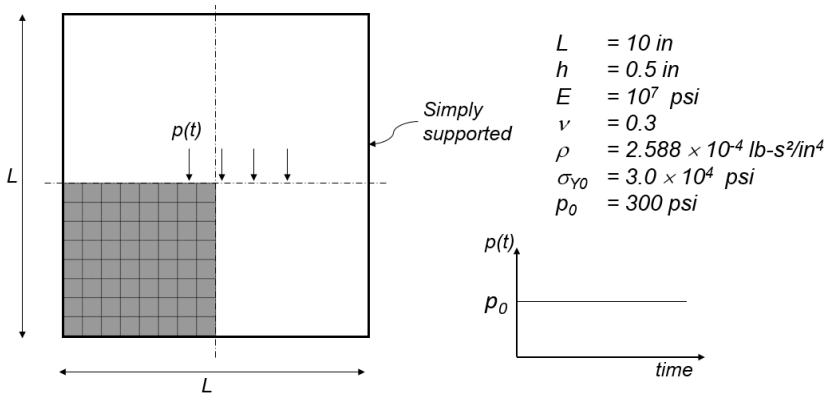

Figure 5.34 Plate under uniform pressure: problem description.

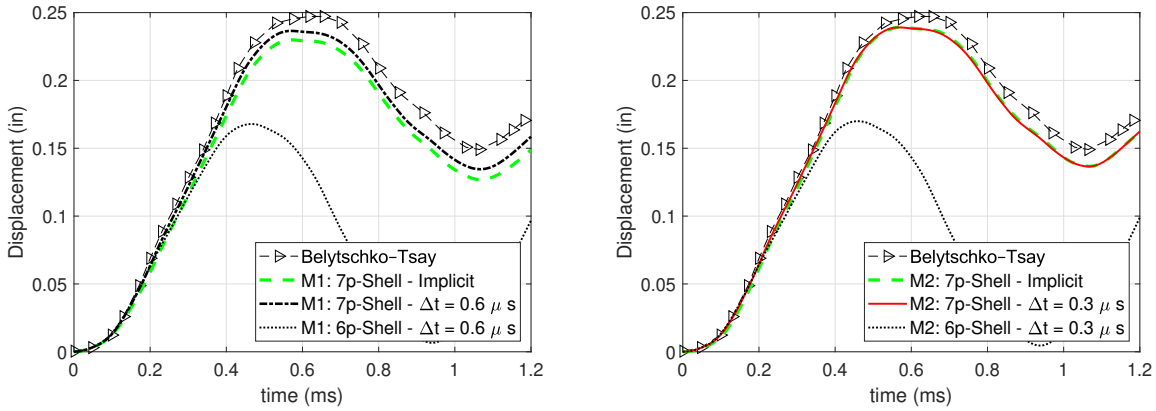

(a) Mesh 1. (b) Mesh 2.

Figure 5.35 Plate under uniform pressure: time histories of center point displacement obtained from the 8×8-element mesh (M1) and 16×16 element-mesh (M2).

Figure 5.35 shows the time histories of the central point displacement for all simulations versus the reference results. The 6-parameter shell formulation deviates significantly from the other solutions, as expected. In contrast, the 7-parameter shell results—both from implicit and explicit computations—are consistent between the two meshes and closely match the reference solution.

Figure 5.36 presents the evolution of the energy errors for explicit computations. The error ϵ_{EAS} remains bounded at approximately 2.5×10^{-3} and shows no sign of instability. Smaller time steps reduce ϵ_{EAS}. The energy error ϵ_W, remaining less than 10^{-6}, confirms the robustness and stability of the proposed explicit integration scheme.

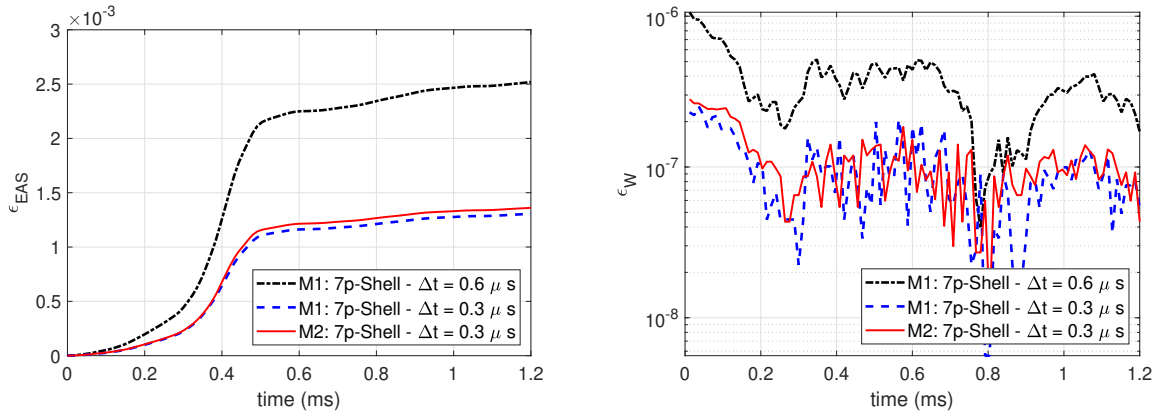

(a) ϵ_{EAS}. (b) ϵ_{W}.

Figure 5.36 Plate under uniform pressure: time histories of energy errors ϵ_{EAS} and ϵ_{W}

5.4.3 Roof loaded by velocity impulse

A 120° cylindrical panel subjected to an impulsive load is analyzed, as illustrated in Figure 5.37. This benchmark was also examined in [16, 21]. The geometry and material parameters are given in Figure 5.37. An initial velocity of 5650 in/s, normal to the shell surface, is applied over the region as specified in the Figure. Exploiting symmetry, only half of the panel is modeled. Two meshes are used: a coarse mesh of 8×16 elements (M1) and a fine mesh of 16×32 elements (M2). The reference results are reported in [21]: an experimental result and a numerical result obtained with a model of 4512 Belytschko–Tsay elements.

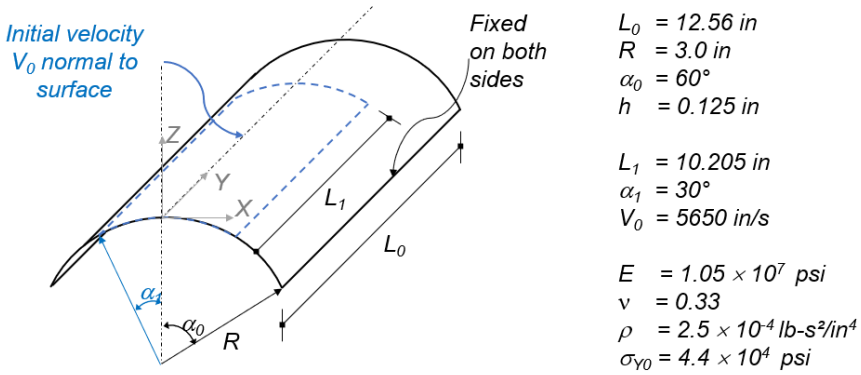

Figure 5.37 Cylindrical roof: problem description.

For the first mesh (M1), the ratio l_e/h_e is about 1.57, thus using the SMS technique with $\beta_0 = 0.125$ increases the critical time step from 0.29 µs to 0.45 µs. However, the initial velocity $V_0 = 5650$ in/s requires a time step of $\Delta t = 0.20$ µs for stability. Indeed,

as seen in Figure 5.38(a), the structure is significantly deformed very soon at about $t = 1.0\,\mu s$. If $V_0 = 565\,in/s$ is used, $\Delta t = 0.40\,\mu s$ is stable. The displacement time histories in Figure 5.39 show that the 6-parameter shell model fails to provide reliable results, whereas the 7-parameter shell results agree very well with the reference results. Regarding the peak displacement, the implicit computation is more accurate than the explicit one, as the orthogonality condition is not fully satisfied in the latter.

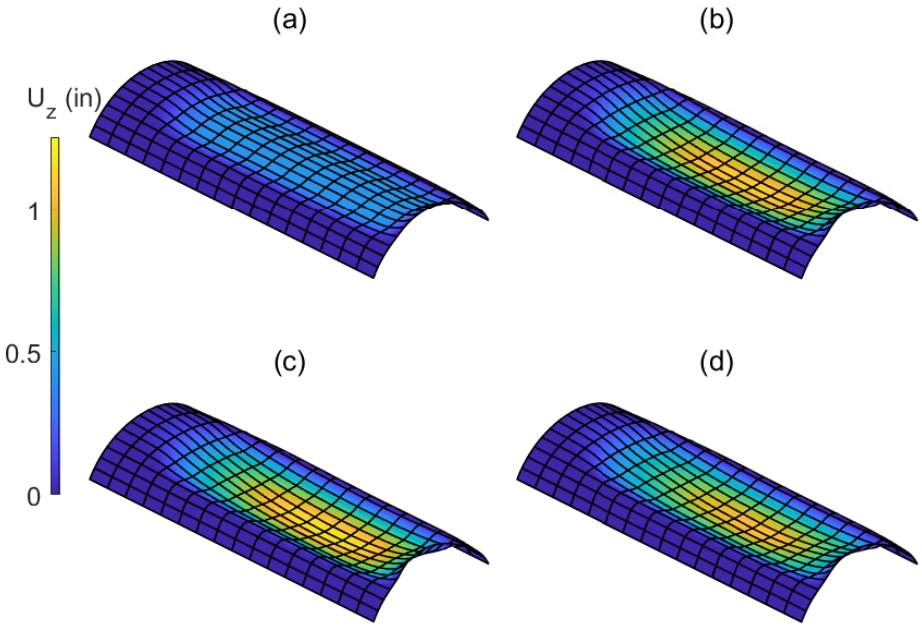

Figure 5.38 Cylindrical roof: vertical displacement U_z on the deformed configuration at selected times: (a) $t = 1.0\,\mu s$, (b) $t = 0.20\,ms$, (c) $t = 0.40\,ms$, (d) $t = 0.80\,ms$.

For the second mesh (M2), we do not apply the SMS technique, as the shell thickness exceeds the characteristic element length. The time step $\Delta t = 0.20\,\mu s$ is used (the critical time step is therefore about $0.22\,\mu s$). Figure 5.40(a) compares the reference results with the computational results. The implicit result is consistent with the M1 implicit case and the references. The explicit curve with $\Delta t = 0.20\,\mu s$ deviates slightly from the references but brings a strong improvement in comparison to the 6-parameter shell (Figure 5.39). This deviation can be explained by the fact that the time step $\Delta t = 0.20\,\mu s$ is too large, leading to a higher error in the EAS orthogonality condition, as shown by the evolution of the error norm ϵ_{EAS} in Figure 5.40(b). $\Delta t = 0.10\,\mu s$ yields a better solution, consistent with the implicit M1 result; the orthogonality error is reduced from 0.6 (for $\Delta t = 0.20\,\mu s$) to 0.03 (for $\Delta t = 0.10\,\mu s$). Deformed shapes of the panel are illustrated in Figure 5.38.

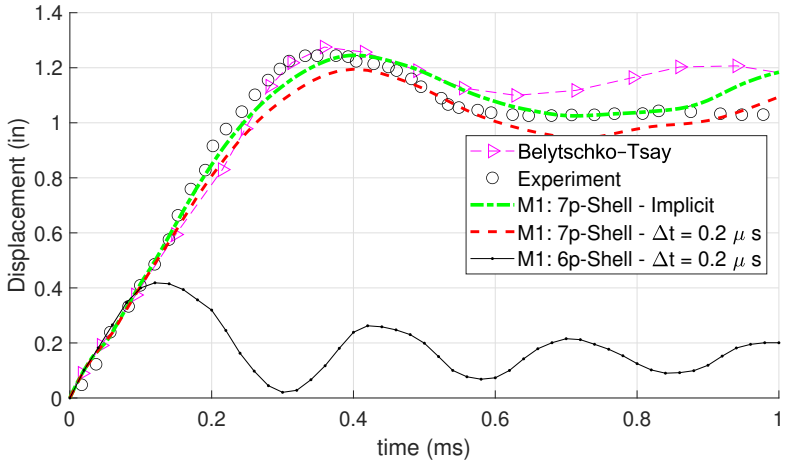

Figure 5.39 Cylindrical roof (Mesh 1): time history of the center-point displacement on the crown line for computations with Mesh 1.

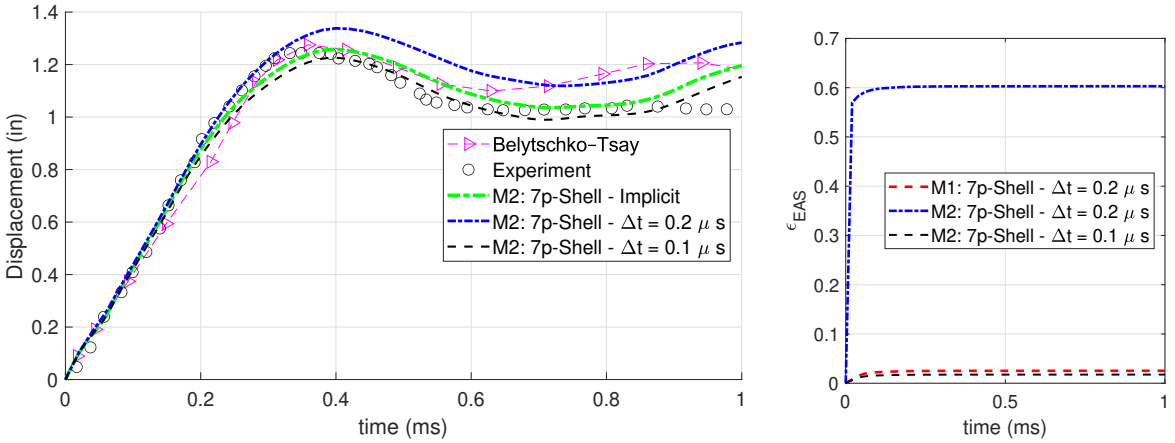

(a) Displacement. (b) EAS energy error.

Figure 5.40 Cylindrical roof (Mesh 2): time history of the center-point displacement on the crown line and the evolution of the EAS error ϵ_{EAS}.

5.4.4 Pinched cylinder

The problem setup is shown in Figure 5.41. A thick cylinder is subjected to an imposed displacement on the crown line. The geometry of the cylinder and the material parameters are given in Figure 5.41. The problem has been studied in [48, 144] under a quasi-static regime by considering a line load rather than an imposed displacement. In this test, the imposed displacement is controlled via the prescribed velocity–time history displayed in Figure 5.41, which ensures that the final displacement (for $t \geq T_c = 1.0\,\text{ms}$) is 10 cm. Exploiting symmetry, only one quarter of the structure is modeled with a mesh of 16×8 shell elements. Since the shell thickness exceeds the characteristic element length, we

do not apply the SMS technique. The reference solution is obtained from an explicit computation of a 3D model (20-node hexahedral elements).

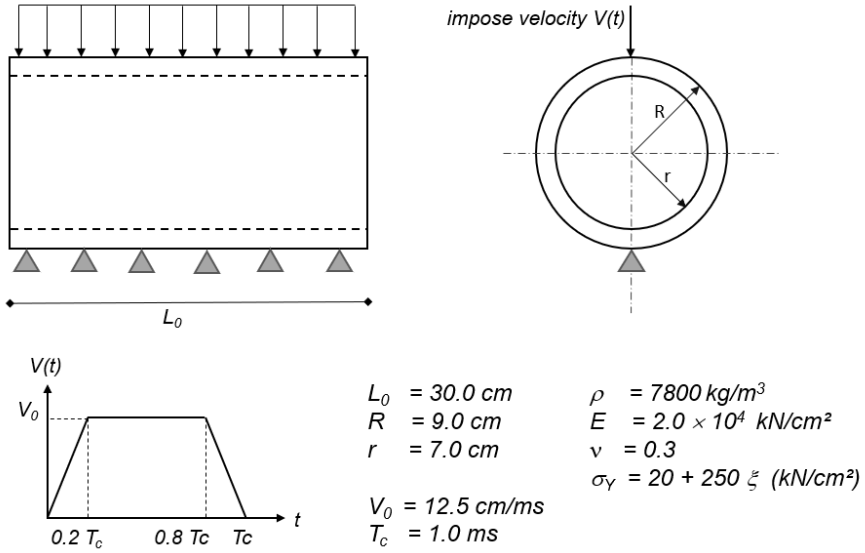

Figure 5.41 Pinched cylinder: problem description.

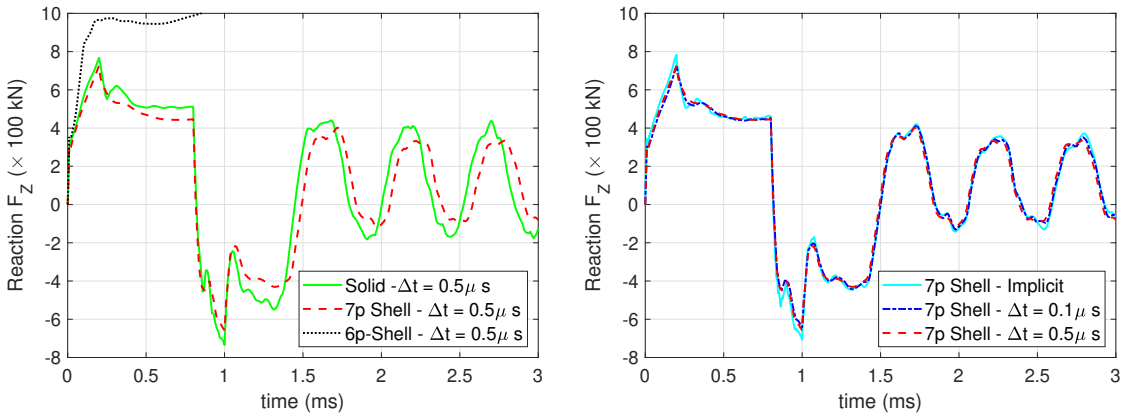

Figure 5.42 Pinched cylinder: time histories of the reaction force on the crown line obtained from different computations.

Figure 5.42 shows the time history of the reaction force on the crown line obtained from different computations. We can see that the cylinder goes through different snap-through stages (at $t \approx 0.25\,\text{ms}, 0.75\,\text{ms}, 1.20\,\text{ms}$), after which both solid model and implicit shell model exhibit oscillations. The 6-parameter shell element definitely fails to capture the buckling dynamic response in this case of nonlinear material law. The explicit computations using the 7-parameter shell model agree very well with the full solid computation, but show slightly reduced oscillation amplitudes. This is due to the

dissipative property of the proposed algorithm as observed in Section 5.2. It can also be seen that same results are obtained in explicit and implicit computations using the same 7-parameter shell model. Moreover, reducing the time step, from 0.1 µs to 0.5 µs, provides almost the same results in terms of vertical reactions. The evolutions of the energy-error norms ϵ_{EAS} and ϵ_W in Figure 5.43 confirm the stability of the proposed explicit algorithm for the 7-parameter shell elements. Reducing the time step leads to a decrease of the EAS error but this beneficial effect is negligible if we focus on previous global results (vertical reactions). Finally, energy errors remain very low in all the explicit computations. Selected deformed shapes in Figure 5.44 show very good agreement between the shell and solid models.

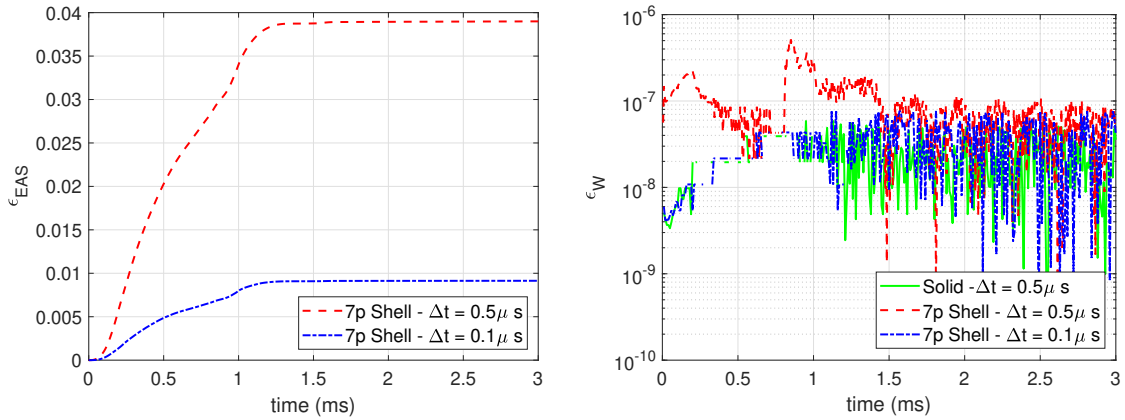

(a) δ_{EAS}. (b) δ_W.

Figure 5.43 Pinched cylinder: time histories of the EAS error ϵ_{EAS} and the mechanical-energy error ϵ_W obtained from different computations.

5.4.5 Twisted cylinder

A cylindrical shell with the boundary conditions and twisting load illustrated in Figure 5.45 is analyzed. This problem was studied in Ambati et al. [4] in a quasi-static regime; here it is considered under dynamic loading. The material follows a nonlinear hardening law as shown in Figure 5.45. The imposed twist angle is controlled via the prescribed angular-velocity history in Figure 5.45, reaching a final twist angle of 120° for $t \geq 2.0$ ms.

To trigger buckling, the initial meshes are perturbed by multiplying the coordinates X and Y by a coefficient c defined following [4, 21]:

$$c(\phi, Z) = \begin{cases} 1, & |Z| > 100 \text{ mm}, \\ 1 + 0.01 \cos(3\phi), & |Z| \leq 100 \text{ mm}. \end{cases} \tag{5.2}$$

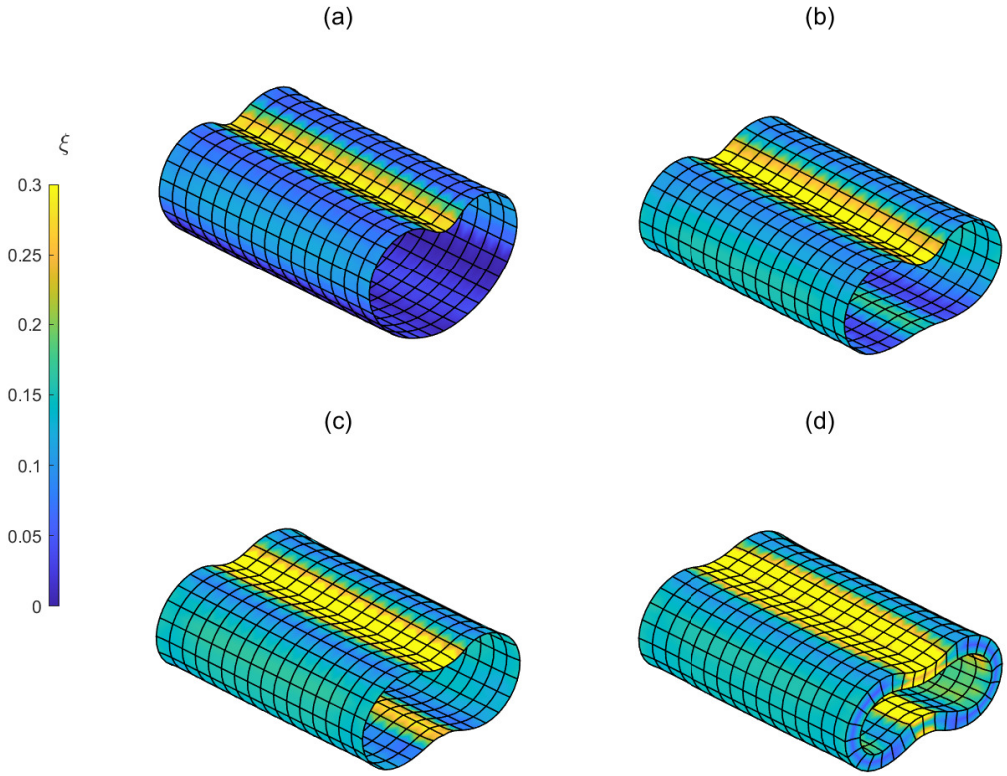

Figure 5.44 Pinched cylinder: hardening variable at various loading stages on the deformed configuration. (a–c) outer surface of the shell ($\theta^3 = 1$) from the 7-parameter shell explicit computation at $t = 0.6\,\text{ms}$, $1.0\,\text{ms}$, and $2.2\,\text{ms}$; (d) solid explicit computation at $t = 2.2\,\text{ms}$.

We use a 28×32-element mesh for shell models. Since the ratio of characteristic element length to thickness is about 3.5, using the SMS technique with $\beta_0 = 0.25$ increases the critical time step from $0.10\,\mu\text{s}$ to $0.35\,\mu\text{s}$. We choose $\Delta t = 0.25\,\mu\text{s}$ for the explicit computation with the 7-parameter shell model.

Figure 5.46(a) shows the norm of the total displacement, defined by $\text{U}_{\text{norm}} = \|\mathbf{q}\|_2/\sqrt{N}$, versus the twist angle, where $\mathbf{q}$ collects the nodal displacements and N is the number of nodes. The quasi-static reference solution from Ambati et al. [4] (NURBS-based Kirchhoff–Love shell) is included for comparison. The 7-parameter shell results differ slightly from the reference at the early stage, due to inertia effects that cause initial buckling near the twisted end of the cylinder rather than at mid-span as in the quasi-static case (Figure 5.47(a)). In the following loading stages, the agreement improves.

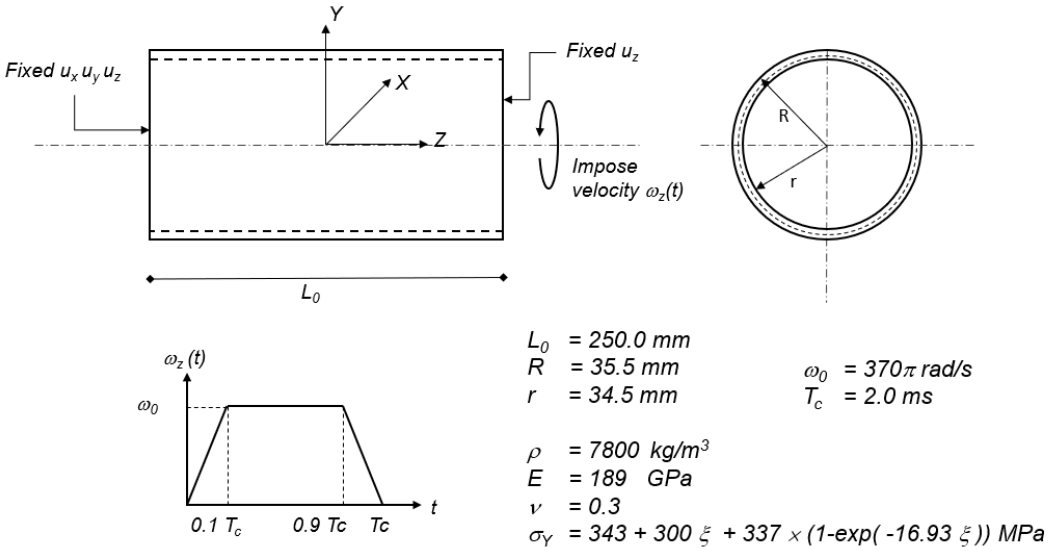

Figure 5.45 Twisted cylinder: problem description.

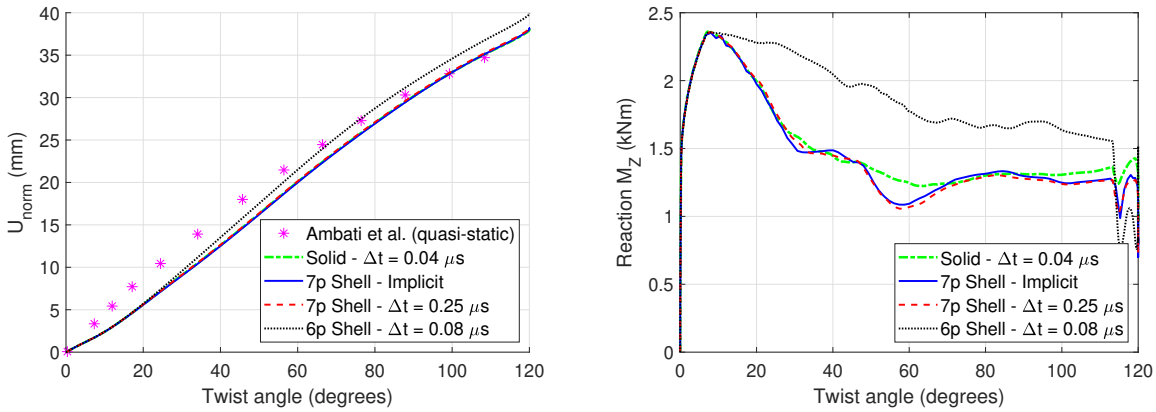

(a) Displacement versus twist angle.

(b) Reaction M_z versus twist angle.

Figure 5.46 Twisted cylinder: displacement U_{norm} and reaction versus twist angle.

Figure 5.46(b) presents the reaction moment M_z versus the twist angle. The results from the 7-parameter shell models, both implicit and explicit, match those from the solid model for displacement versus twist angle. The 6-parameter shell is noticeably stiffer than the 7-parameter shell and the solid results.

The evolution of the energy-error norms in Figure 5.48 confirms the stability of the explicit computations. Some EAS error for the explicit computations, associated with the orthogonality condition, can be observed, but the error in terms of energy remains less than the error related to the implicit computation, confirming the robustness of the explicit solver.

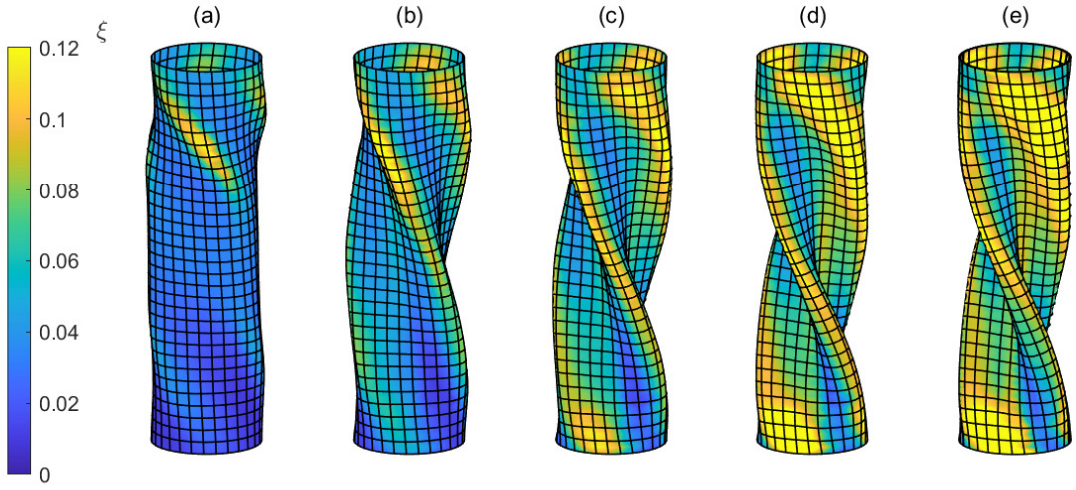

Figure 5.47 Twisted cylinder: hardening variable ξ at various twist angles on the deformed configuration. (a–d) mid-surface of the shell ($\theta^3 = 0$) from the 7-parameter shell explicit computation at $\phi = 30°, 60°, 90°, 120°$; (e) solid explicit computation at $\phi = 120°$.

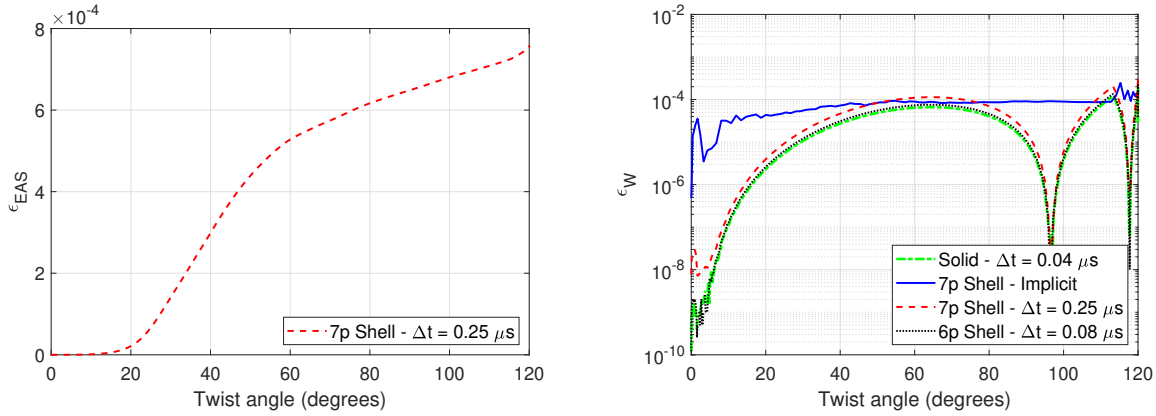

(a) ϵ_{EAS} (b) ϵ_W

Figure 5.48 Twisted cylinder: time histories of the EAS error ϵ_{EAS} and the mechanical-energy error ϵ_W obtained from different computations.

Snapshots of the hardening variable ξ on the deformed configurations for both shell and solid models are shown in Figure 5.47. The final twisted configuration at $\phi = 120°$ closely matches the reference results of Ambati et al. [4].

5.4.6 Stiffened roof

A stiffened cylindrical roof subjected to a vertical impulsive load is studied. The benchmark is described in Figure 5.49. This benchmark combines the main interesting

numerical aspects motivating the proposed development of implicit and multi-time-step explicit computations using advanced 7-parameter shell elements with mortar coupling for both nonlinear geometrical and material dynamics. This test case can be considered as a classical stiffened panel, such as in aerospace construction.

The load is applied over the area indicated in Figure 5.49. Two different materials with nonlinear hardening laws are considered for the roof and the stiffeners. Owing to symmetry, only one quarter of the structure is modeled. We investigate two models in which the structure is divided into two subdomains: the roof and the stiffeners. In the first model (M1), a coarse mesh of 16×16 elements is used for the roof (Figure 5.50(a)); in the second model (M2), a finer mesh of 32×32 elements is used for the roof (Figure 5.50(b)). In both models, each stiffener is discretized by 2×40 elements (Figure 5.50(c)). The roof and stiffeners are coupled using the standard mortar method.

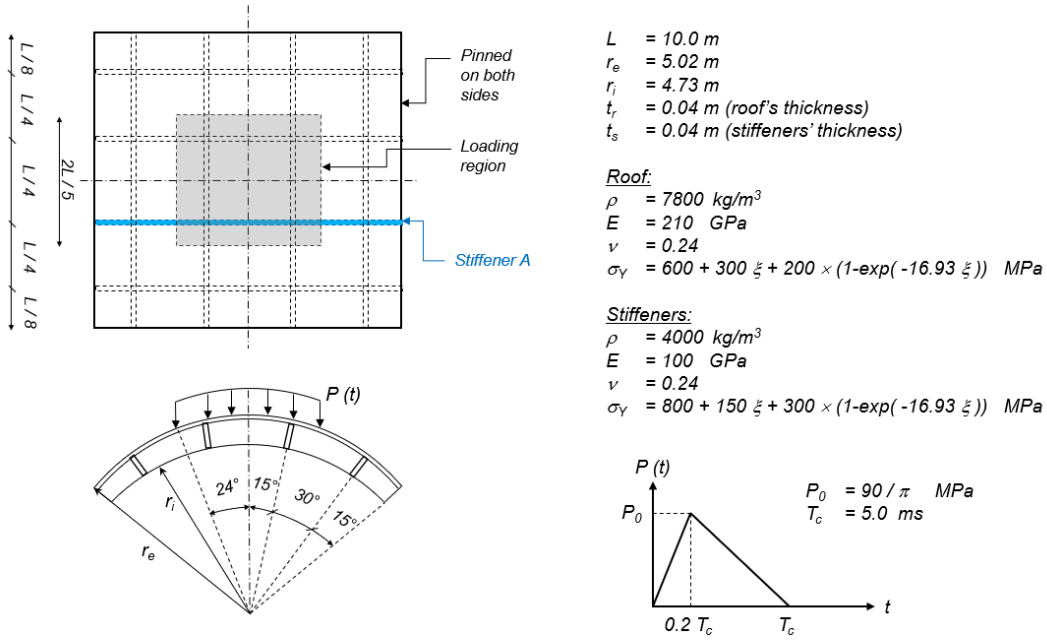

Figure 5.49 Stiffened roof: problem description.

For explicit computations, we use the multi-time-step strategy. For M1, the Selective Mass Scaling (SMS) technique is applied to increase the critical time step for the roof subdomain. The stiffener subdomain is computed with the fine time step $\Delta t_j = 2.0\,\mu s$, while the roof uses the coarse step $\Delta t_m = m\,\Delta t_j$. Two computations with $m = 3$ and $m = 6$ are carried out. For M2, the same time step $\Delta t = 2.0\,\mu s$ is used in both subdomains ($m = 1$). The reference result is obtained from an explicit full 3D solid model (20-node hexahedra) with $\Delta t = 2.0\,\mu s$. The solid mesh conforms between the roof and stiffeners,

so no mortar interface is required. The solid model consists of 42×42 elements for the roof and 2×42 elements for each stiffener.

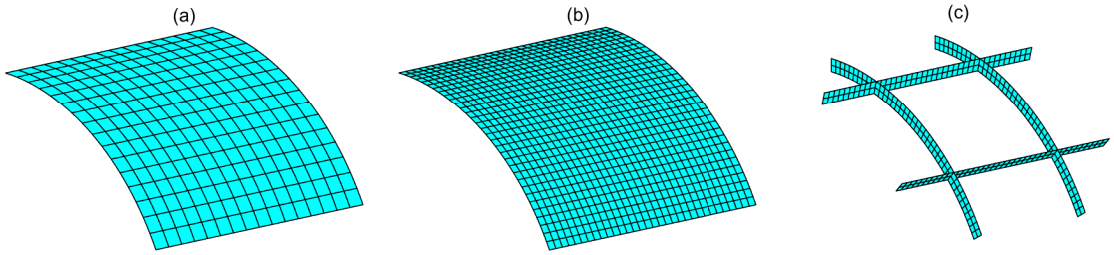

Figure 5.50 Stiffened roof: Meshes. (a) Roof mesh 16×16 (M1), (b) Roof mesh 32×32 (M2), (c) Mesh of 2×40 elements for each stiffener (both M1 and M2).

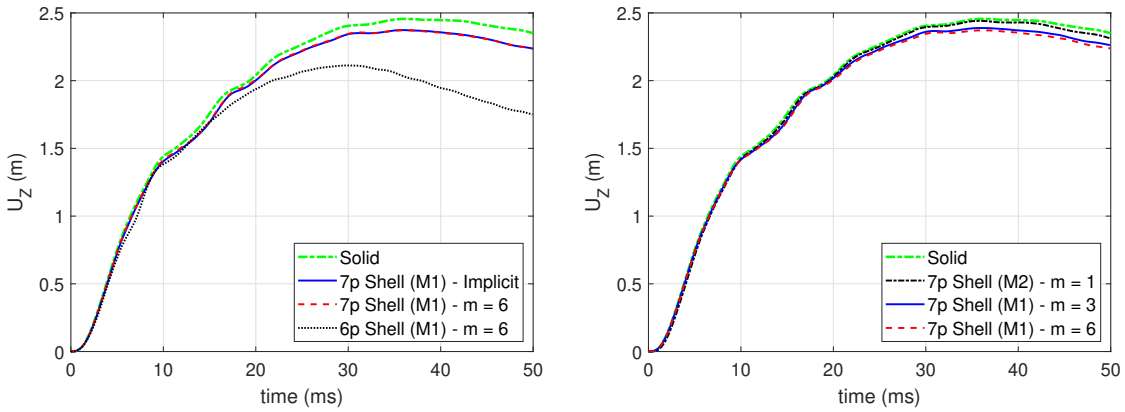

Figure 5.51 Stiffened roof: time histories of the center-point displacement on the crown line.

Figure 5.51 shows the time histories of the center-point displacement on the crown line for the different computations. Model M2 is closer to the reference than M1, owing to the finer mesh and smaller time step used for the roof. The evolution of the EAS error ϵ_{EAS} and the mechanical-energy error ϵ_W in Figure 5.52 confirms the stability and robustness of the proposed explicit algorithm in a multi-time-step explicit setting. It is highlighted that the error energy is very low for the reference solid computation as well as for the mono-time step shell computation. Using multi-time step explicit computation increases the energy error, but it remains less than 10^{-4}. Figures 5.53 and 5.54 present snapshots of the deformed configurations of the roof and of stiffener A (see Figure 5.49) with the hardening variable ξ, for both shell and reference solid models.

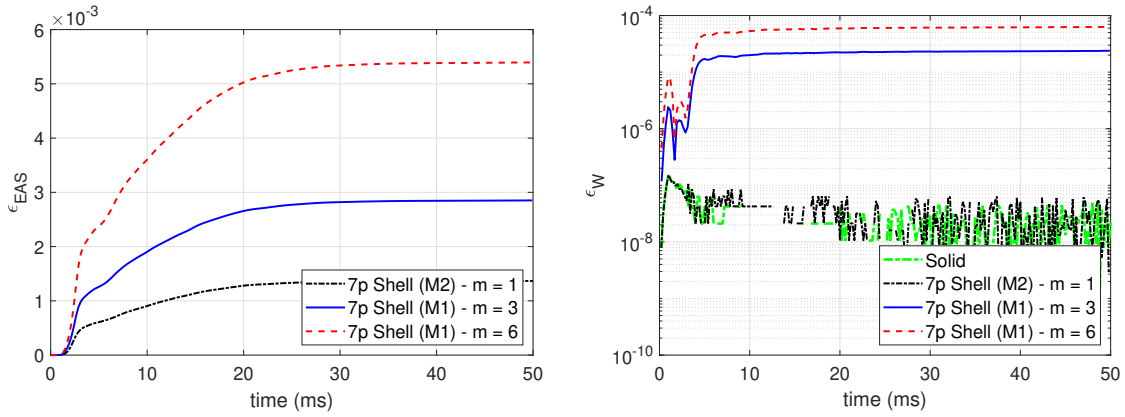

(a) δ_{EAS}. (b) δ_{W}.

Figure 5.52 Stiffened roof: time histories of the EAS error ϵ_{EAS} and the mechanical-energy error ϵ_W.

5.4.7 Conclusion

The benchmarks in this section show that the finite-strain elasto-plastic framework, combined with the 7-parameter shell formulation, delivers accurate and stable results under impulsive loading and severe deformation. All cases involve strong transients with significant inertial effects.

The 6-parameter shell systematically exhibits a stiffer response, confirming the importance of including the enhanced strain variable $\tilde{\beta}_{33}$. The implicit computations with the 7-parameter shell reproduce the reference solutions closely; the time-stepping results in Table 5.5 confirm the efficiency and robustness of the NR solver with the Hilber–α method and the adaptive time-stepping strategy.

The explicit computations with the 7-parameter shell also agree very well with the references, despite the error associated with the EAS field. This error decreases with smaller time steps; monitoring the norm ϵ_{EAS} (and the mechanical-energy error ϵ_W) provides a reliable check of solution quality. The stiffened-roof benchmark demonstrates that the multi-time-step strategy remains accurate and robust while accommodating heterogeneous mesh densities and disparate stable time steps. Finally, the Selective Mass Scaling technique increases the critical time step without altering the solution.

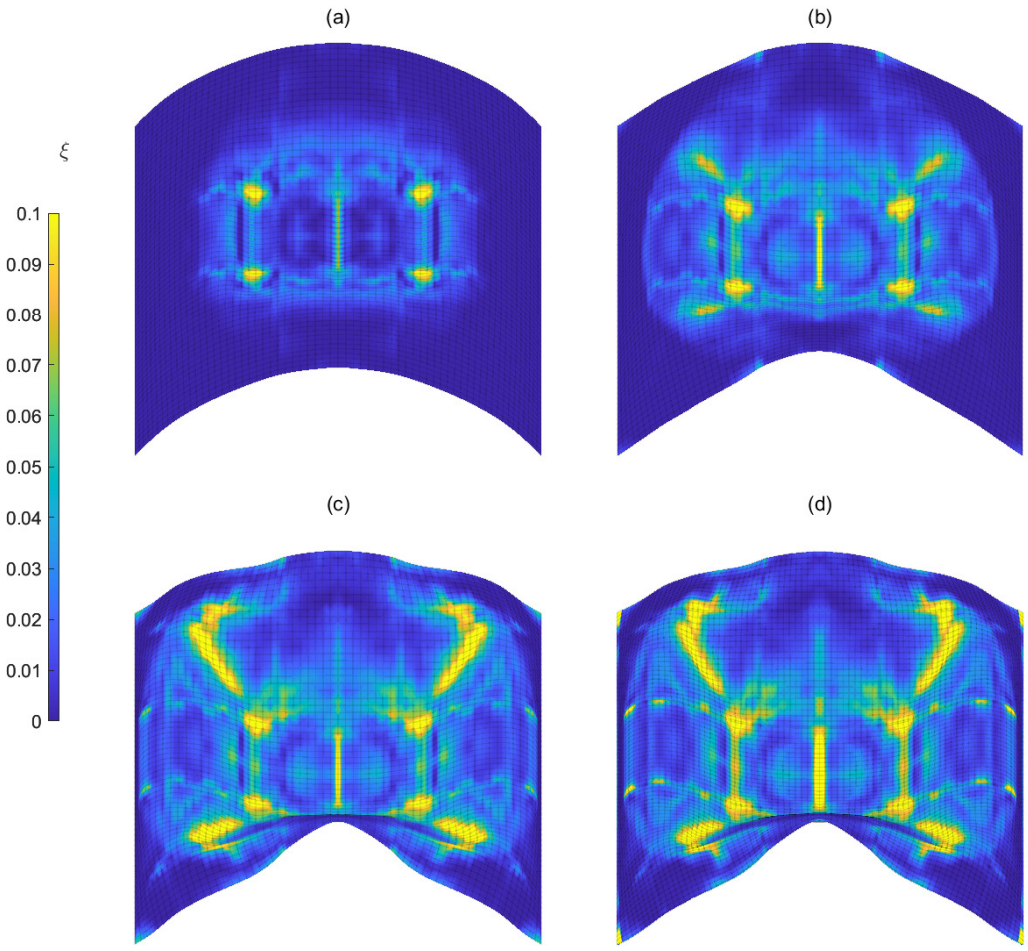

Figure 5.53 Stiffened roof: hardening variable ξ at different times on the deformed configuration of the roof. (a–c) outer surface ($\theta^3 = 1$) from 7-parameter shell explicit computation (M2) at $t = 5.0\,\text{ms}$, $10.0\,\text{ms}$, and $45.0\,\text{ms}$; (d) solid explicit computation at $t = 45.0\,\text{ms}$.

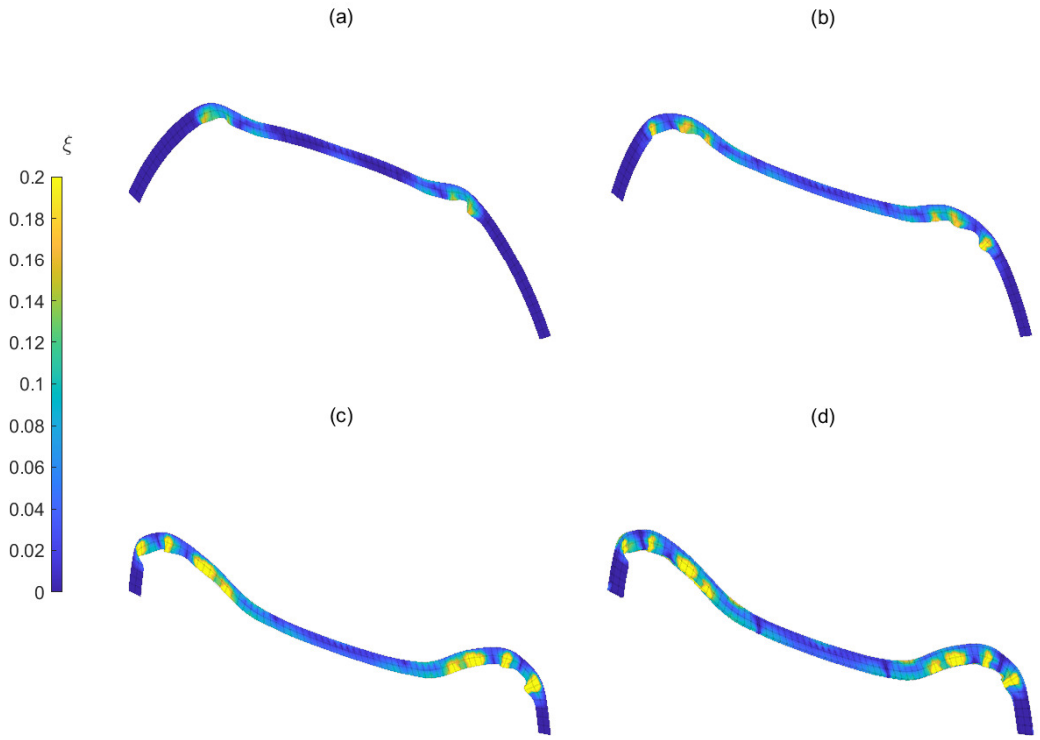

Figure 5.54 Stiffened roof: hardening variable ξ at different times on the deformed configuration of stiffener A (see Figure 5.49). (a–c) outer surface ($\theta^3 = 1$) from 7-parameter shell explicit computation (M2) at $t = 5.0\,\text{ms}$, $10.0\,\text{ms}$, and $45.0\,\text{ms}$; (d) solid explicit computation at $t = 45.0\,\text{ms}$.

Chapter 6

Spectral Element Perfectly Matched Layers for Transient Elastodynamics

As mentioned in Chapter 1, the study of Perfectly Matched Layers (PML) in this thesis represents a first step toward soil–structure interaction problems and computational efficiency. We employ the unsplit displacement-based PML formulation proposed by Basu and Chopra [14, 11] and implement it in `EFISPEC3D` [120, 64], a massively parallel open-source code for wave propagation based on the Spectral Element Method and the central-difference time scheme. This chapter begins with an introduction to the PML technique and the place of the adopted formulation in the literature. The continuous governing equations in the time domain are presented in Section 6.2, followed by the discrete displacement-based formulation with the Spectral Element Method in Section 6.3. Numerical investigations are reported in Section 6.4. It is worth noting that this work follows a previous paper in Chau et al. [51], focused on PML in 2D using isogeometric analysis (B-splines). Here, the project was to extend the 2D IGA-PML to the 3D Spectral Element and implement it in `EFISPEC3D`.

6.1 Introduction

The Perfectly Matched Layer is one of the most effective techniques for simulating wave propagation in unbounded domains. It was first proposed for electromagnetic waves by Bérenger [22]. The idea is to surround the physical domain with an artificial absorbing region of finite thickness that almost completely attenuates outgoing waves without producing spurious reflections at the interface. The construction of a PML relies on a stretching function that maps real coordinates in the PML region into complex values, transforming propagating waves of all incidence angles into exponentially decaying waves. Most formulations in elastodynamics are derived from the original

electromagnetic concept. Several PML formulations for elastodynamics have been developed in the frameworks of the Finite Element Method and the Spectral Element Method. Reviews are available in [110, 111] and more recently in [135]. In this work, we adopt the unsplit non-convolutional displacement-based formulation introduced by Basu and Chopra [12], originally developed for time-harmonic problems and later extended to transient elastodynamics [14, 13, 11].

In general, there are three main PML families in elastodynamics: the split-field PML, the unsplit-field convolutional PML (CPML), and the unsplit-field non-convolutional PML. In the first, the displacement (or velocity) field is split into perpendicular and tangential components relative to the boundary. In the second, the displacement field remains unified, but convolutions must be evaluated. In the third, first introduced by Basu and Chopra [12, 14, 13] and later by Kucukcoban and Kallivokas [110, 111], the convolutional terms are avoided.

In this third approach, the strong form of the governing equations in the frequency domain—modified by the stretching function—is transformed into the time domain by inverse Fourier transform, without evaluating convolution integrals as in CPML. This produces mixed displacement–stress semi-discrete equations. In particular, the semi-discrete equations in [14] and [110] are identical. For time integration, Kucukcoban and Kallivokas [110] proposed a mixed formulation with both displacement and stress as unknowns, which is advanced using implicit Newmark schemes. By contrast, Basu and Chopra [14] made a simplifying assumption for the strain-related fields, keeping the displacement field in a displacement-based form integrated with the Newmark method. This assumption may reduce accuracy when implicit schemes with large time steps are used, but it is adequate for explicit schemes [11].

The formulation adopted here by Basu and Chopra [14] employs the standard stretching function. In the continuous setting, this stretch absorbs waves of any incidence angle without reflections. However, in discrete computations, its performance deteriorates, and long-term simulations may show instability, especially for grazing-incidence waves. To improve stability, the complex-frequency-shifted (CFS) stretch was proposed, resulting in the CFS-PML, which can be naturally integrated into convolutional PMLs. In the non-convolutional unsplit-field approach, only the formulation of Kucukcoban and Kallivokas [111] has incorporated the CFS-PML, as in [76]. Still, as reported in [110, 111, 76], even a careful parameterization of the standard stretch cannot eliminate the long-term instability but can delay it.

In this thesis, we implement the displacement-based PML formulation of Basu and Chopra [14] in `EFISPEC3D`, exploiting the efficiency of the Spectral Element Method in

explicit simulations [105, 106]. Through numerical experiments involving a homogeneous half-space, a thin homogeneous half-space (waveguide), and a two-layered half-space, we study the effect of standard stretching parameters on the accuracy and long-term stability of the PML. In particular, it will be shown that increasing slightly the scaling parameter enables us to significantly delay the long-time instability drawback of the PML.

6.2 Time-domain Governing Equations

We consider a truncated domain $\Omega = \Omega_{\text{el}} \cup \Omega_{\text{PML}} \subset \mathbb{R}^3$, illustrated in Figure 6.1. Here, Ω_{el} denotes the elastic domain and Ω_{PML} the nonphysical PML region. The body Ω is bounded by $\Gamma = \Gamma^N \cup \Gamma^D$, where $\Gamma^N = \Gamma^N_{\text{el}} \cup \Gamma^N_{\text{PML}}$ is the Neumann boundary and $\Gamma^D = \Gamma^D_{\text{el}} \cup \Gamma^D_{\text{PML}}$ is the Dirichlet boundary. We assume that no external forces act within the PML and that displacements are fixed on its outer boundary.

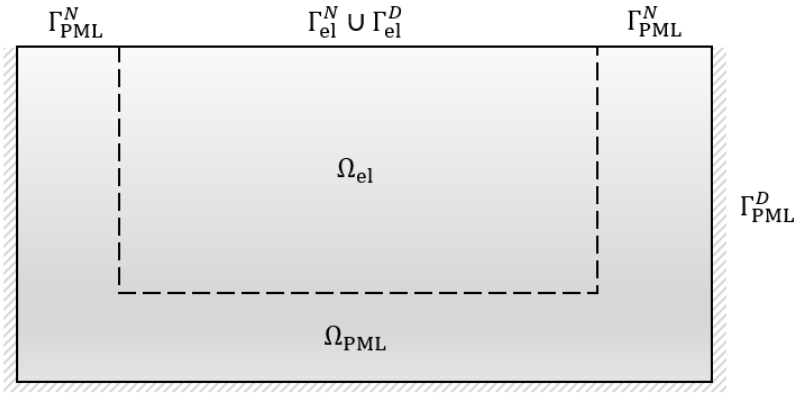

Figure 6.1 Truncated body Ω consisting of the elastic domain Ω_{el} and the nonphysical PML domain Ω_{PML}. The outer boundary of the PML is fixed.

6.2.1 Stretching function

The PML formulation used in this work follows Basu and Chopra [12, 14], Basu [11]. The governing equations are derived from the classical elastodynamic equations, modified by complex-valued stretching functions λ_I. These functions map real coordinates x_I into complex coordinates $\tilde{x}_I : \mathbb{R} \to \mathbb{C}$. In line with [110], we adopt the standard stretching function as follows:

$$\lambda_I(x_I) = \frac{\partial \tilde{x}_I}{\partial x_I} = \alpha_I(x_I) + \frac{\beta_I(x_I)}{i\omega}, \tag{6.1}$$

where ω is the circular frequency. The functions α_I and β_I are real, positive, and control the PML behavior. The attenuation function β_I (imaginary part) damps wave amplitudes inside the PML, while the scaling function α_I (real part) stretches the coordinates and ensures the decay of evanescent waves.

Two main requirements guide the definition of α_I and β_I. First, both must vanish at the interface between the elastic and PML domains to guarantee perfect matching. Second, they must vary smoothly across the PML thickness. Thud, a common choice is a polynomial profile:

$$\begin{aligned} \alpha_I(x_I) &= 1 + \alpha_{0I} \left(\frac{x_I - x_{0I}}{L_I} \right)^m, \\ \beta_I(x_I) &= \beta_{0I} \left(\frac{x_I - x_{0I}}{L_I} \right)^m, \end{aligned} \tag{6.2}$$

where x_I is the coordinate along the PML thickness, x_{0I} is the interface position, L_I is the PML thickness in direction I, and α_{0I}, β_{0I} are user-defined parameters.

To select β_{0I}, Kucukcoban and Kallivokas [111], Fathi et al. [74] studied one-dimensional wave propagation and introduced the logarithmic decrement of a wave inside the PML:

$$\delta = \int_{x_0}^{L} \frac{\beta(x)}{c_p} \, dx = \frac{\beta_0 L}{(n+1) c_p}, \tag{6.3}$$

where c_p is the wave velocity. The attenuation coefficient R is then given by:

$$R = e^{-2\delta}, \tag{6.4}$$

which accounts for the back-and-forth reflection inside the PML. From this relation, β_0 can be computed for a target R as:

$$\beta_0 = \frac{(n+1) c_p}{2L} \ln \left(\frac{1}{R} \right). \tag{6.5}$$

To obtain a similar form in the above equation, Kucukcoban and Kallivokas [111] propose the estimation of the parameter α_0 as follows:

$$\alpha_0 = \frac{(m+1)\, b}{2L} \ln \left(\frac{1}{R} \right), \tag{6.6}$$

where b is a characteristic length of the domain, such as the element size.

6.2.2 Strong form of governing equations

Elastic domain. We first recall the classical elastodynamic equations in the elastic domain Ω_{el}. They consist of the equation of motion, the constitutive relation, and the kinematic relation, which can be written as:

$$\begin{aligned} &\operatorname{div}\boldsymbol{\sigma} + \boldsymbol{b} = \rho\,\ddot{\boldsymbol{u}}, \\ &\boldsymbol{\sigma} = \boldsymbol{\mathcal{C}} : \boldsymbol{\epsilon}, \\ &\boldsymbol{\epsilon} = \frac{1}{2}\left(\nabla\boldsymbol{u} + \nabla\boldsymbol{u}^{\mathrm{T}}\right). \end{aligned} \tag{6.7}$$

Here, $\boldsymbol{u}$ denotes the displacement field, $\ddot{\boldsymbol{u}}$ the acceleration, $\boldsymbol{b}$ the body force per unit volume, $\boldsymbol{\sigma}$ the Cauchy stress tensor, $\boldsymbol{\epsilon}$ the infinitesimal strain tensor, and $\boldsymbol{\mathcal{C}}$ the fourth-order elasticity tensor. The first line in Eq. (6.7) corresponds to the balance of linear momentum, the second to Hooke's law of linear elasticity, and the third to the strain–displacement relation. The boundary and initial conditions associated with Eq. (6.7) are:

$$\begin{cases} \boldsymbol{u} = \mathbf{u}_d & \text{on } \Gamma_{\text{el}}^D, \\ \boldsymbol{\sigma}\,\boldsymbol{n} = \boldsymbol{t} & \text{on } \Gamma_{\text{el}}^N, \end{cases} \qquad \begin{cases} \boldsymbol{u}(t=0) = \mathbf{0}, \\ \dot{\boldsymbol{u}}(t=0) = \dot{\mathbf{u}}_0, \end{cases} \tag{6.8}$$

where $\mathbf{u}_d$ is the prescribed displacement, $\boldsymbol{t}$ is the prescribed traction on Γ_{el}^N and $\boldsymbol{n}$ is the outward unit normal vector.

PML equations in the frequency domain. The PML equations are obtained by replacing the real-valued coordinates $\boldsymbol{x}$ in Eq. (6.7) with the complex-stretched coordinates $\tilde{\boldsymbol{x}}$, using the stretching functions given in Eq. (6.1). Assuming that no body forces are applied in the PML region, the governing equations in the frequency domain become:

$$\begin{aligned} &\sum_{J=1}^{3} \frac{\partial \sigma_{IJ}}{\partial \tilde{x}_J} = \sum_{J=1}^{3} \frac{1}{\lambda_J} \frac{\partial \sigma_{IJ}}{\partial x_J} = -\,\omega^2 \rho\, u_I, \\ &\epsilon_{IJ} = \frac{1}{2}\left(\frac{\partial u_I}{\partial \tilde{x}_J} + \frac{\partial u_J}{\partial \tilde{x}_I}\right) = \frac{1}{2}\left(\frac{1}{\lambda_J}\frac{\partial u_I}{\partial x_J} + \frac{1}{\lambda_I}\frac{\partial u_J}{\partial x_I}\right). \end{aligned} \tag{6.9}$$

Note that the constitutive stress-strain relation of Eq. (6.7) remains unchanged in the PML domain.

PML equations in the time domain. Multiplying the equation of motion in Eq. (6.9) by the product $\lambda_1\lambda_2\lambda_3$, and then expanding each λ_I into its real and imaginary parts $\lambda_I = \alpha_I + \beta_I/(i\omega)$, leads to the following expression:

$$\operatorname{div}\left[\boldsymbol{\sigma}\left(\mathbf{F}^{ee} + \frac{1}{i\omega}\mathbf{F}^{ep} + \frac{1}{(i\omega)^2}\mathbf{F}^{pp}\right)\right] = -\omega^2\rho\left(f_M + \frac{f_C}{i\omega} + \frac{f_K}{(i\omega)^2} + \frac{f_H}{(i\omega)^3}\right)\boldsymbol{u} \tag{6.10}$$

In Eq. (6.10), the matrices $\mathbf{F}^{ee}$, $\mathbf{F}^{ep}$, and $\mathbf{F}^{pp}$ are diagonal and contain the contributions from the scaling and attenuation functions. They are defined as:

$$\begin{aligned}
\mathbf{F}^{pp} &= \begin{bmatrix} \beta_2\beta_3 & 0 & 0 \\ 0 & \beta_1\beta_3 & 0 \\ 0 & 0 & \beta_1\beta_2 \end{bmatrix}, \qquad \mathbf{F}^{ee} = \begin{bmatrix} \alpha_2\alpha_3 & 0 & 0 \\ 0 & \alpha_1\alpha_3 & 0 \\ 0 & 0 & \alpha_1\alpha_2 \end{bmatrix}, \\
\mathbf{F}^{ep} &= \begin{bmatrix} \alpha_2\beta_3 + \alpha_3\beta_2 & 0 & 0 \\ 0 & \alpha_1\beta_3 + \alpha_3\beta_1 & 0 \\ 0 & 0 & \alpha_1\beta_2 + \alpha_2\beta_1 \end{bmatrix}
\end{aligned} \tag{6.11}$$

The coefficients f_M, f_C, f_K, and f_H are scalar functions that result from the product of the scaling and attenuation functions in the three coordinate directions. They are given by:

$$\begin{aligned}
f_M &= \alpha_1\alpha_2\alpha_3, & f_C &= \alpha_1\alpha_2\beta_3 + \alpha_1\alpha_3\beta_2 + \alpha_2\alpha_3\beta_1, \\
f_K &= \beta_1\beta_2\alpha_3 + \beta_1\beta_3\alpha_2 + \beta_2\beta_3\alpha_1, & f_H &= \beta_1\beta_2\beta_3.
\end{aligned} \tag{6.12}$$

Similarly, by multiplying the strain–displacement relation in Eq. (6.9) by the product $\lambda_I\lambda_J$, one obtains the following kinematic condition:

$$\left(\alpha_I\alpha_J + \frac{\alpha_I\beta_J + \alpha_J\beta_I}{i\omega} + \frac{\beta_I\beta_J}{(i\omega)^2}\right)\epsilon_{IJ} = \frac{1}{2}\left[\left(\alpha_I + \frac{\beta_I}{i\omega}\right)\frac{\partial u_I}{\partial x_J} + \left(\alpha_J + \frac{\beta_J}{i\omega}\right)\frac{\partial u_J}{\partial x_I}\right] \tag{6.13}$$

Transformation into the time domain. To obtain the time-domain formulation, the inverse Fourier transform is applied to Eq. (6.10). This introduces additional history-dependent fields, and the equation of motion in the PML becomes:

$$\operatorname{div}\left(\boldsymbol{\sigma}\mathbf{F}^{ee} + \boldsymbol{\Sigma}\mathbf{F}^{ep} + \bar{\boldsymbol{\Sigma}}\mathbf{F}^{pp}\right) = \rho\left(f_M\,\ddot{\boldsymbol{u}} + f_C\,\dot{\boldsymbol{u}} + f_K\,\boldsymbol{u} + f_H\,\bar{\boldsymbol{u}}\right) \tag{6.14}$$

In Eq. (6.14), the auxiliary fields $\bar{\boldsymbol{u}}$, $\boldsymbol{\Sigma}$, and $\bar{\boldsymbol{\Sigma}}$ are time integrals of the displacement and stress fields. They are defined as:

$$\bar{\boldsymbol{u}}(t) = \int_0^t \boldsymbol{u}(\tau)\, d\tau, \qquad \boldsymbol{\Sigma}(t) = \int_0^t \boldsymbol{\sigma}(\tau)\, d\tau, \qquad \bar{\boldsymbol{\Sigma}}(t) = \int_0^t \boldsymbol{\Sigma}(\tau)\, d\tau \tag{6.15}$$

A similar procedure is applied to Eq. (6.13). Multiplying both sides by $i\omega$ and then transforming into the time domain gives:

$$\begin{aligned} \alpha_I \alpha_J\, \dot{\epsilon}_{IJ} + (\alpha_I \beta_J + \alpha_J \beta_I)\, \epsilon_{IJ} + \beta_I \beta_J\, E_{IJ} = \\ \frac{1}{2}\left(\alpha_I \frac{\partial \dot{u}_I}{\partial x_J} + \alpha_J \frac{\partial \dot{u}_J}{\partial x_I} + \beta_I \frac{\partial u_I}{\partial x_J} + \beta_J \frac{\partial u_J}{\partial x_I} \right) \end{aligned} \tag{6.16}$$

where the new field E_{IJ} is defined as:

$$E_{IJ}(t) = \int_0^t \epsilon_{IJ}(\tau)\, d\tau \tag{6.17}$$

Equations (6.14) and (6.16), together with the elastic constitutive relation of Eq. (6.7), form the governing equations of the PML in the time domain.

6.2.3 Continuous weak form of governing equations

Let $\delta\boldsymbol{u}$ be an arbitrary virtual displacement field. The weak form of the equations of motion over the whole domain Ω is obtained by applying the Principle of Virtual Work:

$$\delta\Pi_{\text{kin}} + \delta\Pi_{\text{int}} + \delta\Pi_{\text{PML}} - \delta\Pi_{\text{ext}} = 0 \tag{6.18}$$

In Eq. (6.18), the different contributions are given below. We first define the external virtual work, the virtual kinetic energy, and the internal virtual work in the elastic domain Ω_{el}. The external virtual work is:

$$\delta\Pi_{\text{ext}} = \int_{\Omega_{\text{el}}} \delta\boldsymbol{u} \cdot \boldsymbol{b}\, d\Omega + \int_{\Gamma_{\text{el}}^N} \delta\boldsymbol{u} \cdot \boldsymbol{t}\, d\Gamma = \int_{\Omega_{\text{el}}} \delta u_I\, b_I\, d\Omega + \int_{\Gamma_{\text{el}}^N} \delta u_I\, t_I\, d\Gamma \tag{6.19}$$

The virtual kinetic energy is:

$$\delta\Pi_{\text{kin}} = \int_{\Omega_{\text{el}}} \rho\, \delta\boldsymbol{u} \cdot \ddot{\boldsymbol{u}}\, d\Omega = \int_{\Omega_{\text{el}}} \rho\, \delta u_I\, \ddot{u}_I\, d\Omega \tag{6.20}$$

The internal virtual work in the elastic domain is:

$$\delta\Pi_{\text{int}} = \int_{\Omega_{\text{el}}} \delta\boldsymbol{\epsilon} : \boldsymbol{\sigma}\, d\Omega = \int_{\Omega_{\text{el}}} \nabla\delta\boldsymbol{u} : \boldsymbol{\sigma}\, d\Omega = \int_{\Omega_{\text{el}}} \frac{\partial \delta u_I}{\partial x_J}\, \sigma_{IJ}\, d\Omega \tag{6.21}$$

Next, we consider the contribution of the PML domain. The total PML virtual work $\delta\Pi_{\text{PML}}$ is split into the virtual work of inertial forces, denoted $\delta\Pi_{\text{PML},\rho}$, and the virtual work of internal stresses, denoted $\delta\Pi_{\text{PML},\sigma}$:

$$\delta\Pi_{\text{PML}} = \delta\Pi_{\text{PML},\rho} + \delta\Pi_{\text{PML},\sigma} \tag{6.22}$$

The virtual work of inertial forces in the PML domain is:

$$\begin{aligned} \delta\Pi_{\text{PML},\rho} &= \int_{\Omega_{\text{PML}}} \rho\, \delta\boldsymbol{u} \cdot \left(f_M \ddot{\boldsymbol{u}} + f_C \dot{\boldsymbol{u}} + f_K \boldsymbol{u} + f_H \bar{\boldsymbol{u}}\right)\, d\Omega \\ &= \int_{\Omega_{\text{PML}}} \rho\, \delta u_I \left(f_M \ddot{u}_I + f_C \dot{u}_I + f_K u_I + f_H \bar{u}_I\right)\, d\Omega \end{aligned} \tag{6.23}$$

The virtual work of internal stresses in the PML domain is:

$$\begin{aligned} \delta\Pi_{\text{PML},\sigma} &= \int_{\Omega_{\text{PML}}} \nabla\delta\boldsymbol{u} : \left(\boldsymbol{\sigma}\mathbf{F}^{ee} + \boldsymbol{\Sigma}\mathbf{F}^{ep} + \bar{\boldsymbol{\Sigma}}\mathbf{F}^{pp}\right)\, d\Omega \\ &= \int_{\Omega_{\text{PML}}} \frac{\partial \delta u_I}{\partial x_J} \left(\sigma_{IJ} F^{ee}_{JJ} + \Sigma_{IJ} F^{ep}_{JJ} + \bar{\Sigma}_{IJ} F^{pp}_{JJ}\right)\, d\Omega \end{aligned} \tag{6.24}$$

6.3 Displacement-based Spectral Element PML

6.3.1 Spectral element method

Before discretizing the continuous weak form of the governing equations, we briefly recall the main ingredients of the Spectral Element Method (SEM). The SEM can be regarded as a particular version of the Finite Element Method (FEM), designed for explicit computations, specifically in wave propagation problems.

Lagrangian polynomials. The main idea is to use high-order Lagrange interpolation polynomials associated with the Gauss–Lobatto–Legendre (GLL) points. Given a set of $p+1$ control points $\{\xi^\alpha\}_{\alpha=1}^{p+1}$ with $-1 \le \xi^\alpha \le 1$, the Lagrange basis polynomials of degree p are defined as:

$$L^\alpha(\xi) = \prod_{\substack{\beta=1 \\ \beta\neq\alpha}}^{p+1} \frac{\xi - \xi^\beta}{\xi^\alpha - \xi^\beta}, \qquad \alpha = 1, 2, \ldots, p+1 \tag{6.25}$$

These functions satisfy the Kronecker property:

$$L^{\alpha}(\xi^{\beta}) = \delta^{\alpha\beta} \tag{6.26}$$

The derivative of $L^{\alpha}(\xi)$ with respect to ξ can be written explicitly as:

$$\frac{dL^{\alpha}}{d\xi}(\xi) = L^{\alpha}(\xi) \sum_{\substack{\beta=1 \\ \beta\neq\alpha}}^{p+1} \frac{1}{\xi - \xi^{\beta}} \tag{6.27}$$

During the integration over elements, the Gauss-Lobatto-Legendre integration rule with $n+1$ GLL points is required. As we shall see in the following, this concept permits, first, the direct calculation of the diagonal mass matrix and, second, a matrix-free numerical implementation. These two advantages are crucial in explicit solvers.

Hexahedral spectral element. In this work, the order $p = 4$ of the Lagrange basis function is chosen. In three dimensions, the geometry of a hexahedral element is approximated using the tensor product of the one-dimensional basis functions. For $p = 4$, each element contains $(p+1)^3 = 125$ GLL nodes $\mathbf{X}^{\alpha\beta\gamma}$ with isoparametric coordinates $(\xi^{\alpha}, \eta^{\beta}, \zeta^{\gamma}) \in [-1, 1]^3$. A material point in the physical element is mapped as:

$$x_I(\xi, \eta, \zeta) = \sum_{\alpha,\beta,\gamma=1}^{p+1} L^{\alpha}(\xi)\, L^{\beta}(\eta)\, L^{\gamma}(\zeta)\, \mathrm{X}_I^{\alpha\beta\gamma} = \sum_{\alpha,\beta,\gamma=1}^{p+1} N^{\alpha\beta\gamma}(\xi, \eta, \zeta)\, \mathrm{X}_I^{\alpha\beta\gamma} \tag{6.28}$$

where $I = 1, 2, 3$ and $N^{\alpha\beta\gamma} = L^{\alpha} L^{\beta} L^{\gamma}$ are the tensor-product shape functions. Similarly, the displacement field is approximated via the nodal displacement $\mathrm{U}_I^{\alpha\beta\gamma}$ as:

$$u_I(\xi, \eta, \zeta) = \sum_{\alpha,\beta,\gamma=1}^{p+1} N^{\alpha\beta\gamma}(\xi, \eta, \zeta)\, \mathrm{U}_I^{\alpha\beta\gamma} \tag{6.29}$$

Using the chain rule, the gradient of the displacement field is given as:

$$\frac{\partial u_I}{\partial x_J} = \frac{\partial u_I}{\partial \xi}\frac{\partial \xi}{\partial x_J} + \frac{\partial u_I}{\partial \eta}\frac{\partial \eta}{\partial x_J} + \frac{\partial u_I}{\partial \zeta}\frac{\partial \zeta}{\partial x_J} \tag{6.30}$$

In the above equation, the derivatives $\partial\xi/\partial x_I$, $\partial\eta/\partial x_I$ and $\partial\zeta/\partial x_I$ can be obtained from the inverse of the Jacobian matrix $\mathbf{J}$ given as:

$$\mathbf{J} = \begin{bmatrix} \dfrac{\partial}{\partial \xi} & \dfrac{\partial}{\partial \eta} & \dfrac{\partial}{\partial \zeta} \end{bmatrix} \cdot \boldsymbol{x}(\xi, \eta, \zeta) \tag{6.31}$$

and the derivatives in the isoparametric space defined as:

$$\begin{aligned}
\frac{\partial u_I}{\partial \xi} &= \sum_{\alpha,\beta,\gamma=1}^{p+1} \frac{\partial L^\alpha}{\partial \xi}(\xi)\, L^\beta(\eta)\, L^\gamma(\zeta)\, \mathrm{U}_I^{\alpha\beta\gamma} \\
\frac{\partial u_I}{\partial \eta} &= \sum_{\alpha,\beta,\gamma=1}^{p+1} L^\alpha(\xi)\, \frac{\partial L^\beta}{\partial \eta}(\eta)\, L^\gamma(\zeta)\, \mathrm{U}_I^{\alpha\beta\gamma} \\
\frac{\partial u_I}{\partial \zeta} &= \sum_{\alpha,\beta,\gamma=1}^{p+1} L^\alpha(\xi)\, L^\beta(\eta)\, \frac{\partial L^\gamma}{\partial \zeta}(\zeta)\, \mathrm{U}_I^{\alpha\beta\gamma}
\end{aligned} \tag{6.32}$$

Integration over an element. Now, let us consider a function $f(\boldsymbol{x}(\xi,\eta,\zeta))$, the integral of the function over a spectral element using the Gauss-Lobatto-Legendre quadrature writes:

$$\int_{\Omega^e} f\, d\Omega = \sum_{\alpha,\beta,\gamma=1}^{p+1} \omega^\alpha \omega^\beta \omega^\gamma J^{\alpha\beta\gamma}\, f(\boldsymbol{x}(\xi^\alpha,\eta^\beta,\zeta^\gamma)) \tag{6.33}$$

where ω^α denoting the quadrature weights, and $J^{\alpha\beta\gamma}$ denotes the determinant of the Jacobian matrix $\mathbf{J}^{\alpha\beta\gamma}$ evaluated at the GLL point $(\xi^\alpha,\, \eta^\beta,\, \zeta^\gamma)$:

$$J^{\alpha\beta\gamma} = \det \mathbf{J}^{\alpha\beta\gamma} \quad \text{with} \quad \mathbf{J}^{\alpha\beta\gamma} = \begin{bmatrix} \dfrac{\partial}{\partial \xi} & \dfrac{\partial}{\partial \eta} & \dfrac{\partial}{\partial \zeta} \end{bmatrix} \cdot \boldsymbol{x}(\xi^\alpha,\eta^\beta,\zeta^\gamma) \tag{6.34}$$

6.3.2 Displacement-based weak form

We now discretize in space the continuous weak form in Eq. (6.18) using the concept of the Spectral Element Method presented above. To this end, the body Ω is partitioned into N^e non-overlapping subdomains Ω^e, called elements:

$$\Omega \approx \bigcup_{e=1}^{N^e} \Omega^e \tag{6.35}$$

This partitioning allows the integrals in the weak form to be computed as the sum of contributions from all elements:

$$\delta\Pi = \sum_{e=1}^{N^e} \left(\int_{\Omega^e} (\cdot)\, d\Omega + \int_{\Gamma^N \cap \partial\Omega^e} (\cdot)\, d\Gamma \right) = 0 \tag{6.36}$$

As in the classical Finite Element Method, the weak form is discretized at the element level and then assembled into the global weak form via an assembly operator. In the

following, we focus on the element-level contributions for elements in the elastic domain Ω^e_{el} and in the PML domain Ω^e_{PML}; and the notation $(\cdot)^{\alpha\beta\gamma} = (\cdot)(\xi^\alpha, \eta^\beta, \zeta^\gamma)$ is used.

Element in the elastic domain. Using the geometry approximation in Eq. (6.28) and the quadrature rule in Eq. (6.33), the discrete weak form of the virtual kinetic energy of an elastic element can be written as:

$$\begin{aligned}
\delta\Pi^e_{\text{kin}} &= \int_{\Omega^e_{\text{el}}} \rho\, \delta u_I\, \ddot{u}_I\, d\Omega = \sum_{I=1}^{3} \sum_{\alpha,\beta,\gamma=1}^{p+1} \omega^\alpha \omega^\beta \omega^\gamma J^{\alpha\beta\gamma}\, \rho^{\alpha\beta\gamma}\, \delta u_I^{\alpha\beta\gamma}\, \ddot{u}_I^{\alpha\beta\gamma} \\
&= \sum_{I=1}^{3} \sum_{\alpha,\beta,\gamma=1}^{p+1} \omega^\alpha \omega^\beta \omega^\gamma J^{\alpha\beta\gamma}\, \rho^{\alpha\beta\gamma}\, \delta \mathrm{U}_I^{\alpha\beta\gamma}\, \ddot{\mathrm{U}}_I^{\alpha\beta\gamma} \\
&= \sum_{I=1}^{3} \sum_{\alpha,\beta,\gamma=1}^{p+1} \mathrm{M}^{\alpha\beta\gamma}\, \delta \mathrm{U}_I^{\alpha\beta\gamma}\, \ddot{\mathrm{U}}_I^{\alpha\beta\gamma} = \delta \mathbf{U}^{e,\mathrm{T}}\, \mathbf{M}^e\, \ddot{\mathbf{U}}^e
\end{aligned} \tag{6.37}$$

where $\delta\mathbf{U}^e$ and $\ddot{\mathbf{U}}^e$ are, respectively, the element-level vectors of nodal virtual displacements and nodal accelerations. It follows from Eq. (6.37) that the mass distribution in the element is represented only through the nodal masses $\mathrm{M}^{\alpha\beta\gamma}$, which directly leads to the diagonal mass matrix $\mathbf{M}^e$. This property is one of the practical advantages of SEM in explicit computations.

For the virtual work of external forces, we assume that the boundary $\Gamma^N \cap \partial\Omega^e$ is defined by the control points $\mathbf{X}^{\alpha\beta\gamma_0}$, where γ_0 is fixed. The discrete virtual work of the external forces can then be written as:

$$\begin{aligned}
\delta\Pi^e_{\text{ext}} &= \int_{\Omega^e_{\text{el}}} b_I\, \delta u_I\, d\Omega + \int_{\gamma^N \cap \Omega^e_{el}} t_I\, \delta u_I\, d\Gamma \\
&= \sum_{I=1}^{3} \sum_{\alpha,\beta,\gamma=1}^{p+1} \omega^\alpha \omega^\beta \omega^\gamma J^{\alpha\beta\gamma}\, \delta \mathrm{U}_I^{\alpha\beta\gamma}\, b_I^{\alpha\beta\gamma} + \sum_{I=1}^{3} \sum_{\alpha,\beta=1}^{p+1} \omega^\alpha \omega^\beta J^{\alpha\beta\gamma_0}\, \delta \mathrm{U}_I^{\alpha\beta\gamma_0}\, t_I^{\alpha\beta\gamma_0} \\
&= \delta \mathbf{U}^{e,\mathrm{T}}\, \mathbf{f}^e_{\text{ext}}
\end{aligned} \tag{6.38}$$

where $\mathbf{f}^e_{\text{ext}}$ denotes the external force vector of the element.

Using the geometry approximation in Eq. (6.28) and the quadrature rule in Eq. (6.33), the discrete virtual internal energy of an elastic element writes:

$$\begin{aligned}\delta\Pi^e_{\text{int}} &= \sum_{I,J=1}^{3} \int_{\Omega^e_{\text{el}}} \frac{\partial \delta u_I}{\partial x_J}\,\sigma_{IJ}\,d\Omega = \sum_{I,J=1}^{3} \sum_{\alpha,\beta,\gamma=1}^{p+1} \int_{\Omega^e_{\text{el}}} \delta \mathrm{U}_I^{\alpha\beta\gamma}\,\frac{\partial (N^{\alpha\beta\gamma})}{\partial x_J}\sigma_{IJ}\,d\Omega \\ &= \sum_{I,J=1}^{3} \sum_{\alpha,\beta,\gamma=1}^{p+1} \delta \mathrm{U}_I^{\alpha\beta\gamma} \sum_{\alpha',\beta',\gamma'=1}^{p+1} \omega^{\alpha'}\omega^{\beta'}\omega^{\gamma'}\,J^{\alpha'\beta'\gamma'} \left(\frac{\partial (N^{\alpha\beta\gamma})}{\partial x_J}\,\sigma_{IJ}\right)^{\alpha'\beta'\gamma'}\end{aligned} \tag{6.39}$$

By applying the property of the Lagrange polynomials in Eq. (6.26), we obtain:

$$\begin{aligned}&\sum_{\alpha',\beta',\gamma'=1}^{p+1} \omega^{\alpha'}\omega^{\beta'}\omega^{\gamma'}\,J^{\alpha'\beta'\gamma'} \left(\frac{\partial (N^{\alpha\beta\gamma})}{\partial x_J}\,\sigma_{IJ}\right)^{\alpha'\beta'\gamma'} \\ &\qquad = \omega^{\beta}\,\omega^{\gamma} \sum_{\alpha'=1}^{p+1} \omega^{\alpha'}\,J^{\alpha'\beta\gamma}\,\frac{\partial L^{\alpha}(\xi^{\alpha'})}{\partial \xi} \left(\frac{\partial \xi}{\partial x_J}\,\sigma_{IJ}\right)^{\alpha'\beta\gamma} \\ &\qquad\quad + \omega^{\alpha}\,\omega^{\gamma} \sum_{\beta'=1}^{p+1} \omega^{\beta'}\,J^{\alpha\beta'\gamma}\,\frac{\partial L^{\beta}(\eta^{\beta'})}{\partial \eta} \left(\frac{\partial \eta}{\partial x_J}\,\sigma_{IJ}\right)^{\alpha\beta'\gamma} \\ &\qquad\quad + \omega^{\alpha}\,\omega^{\beta} \sum_{\gamma'=1}^{p+1} \omega^{\gamma'}\,J^{\alpha\beta\gamma'}\,\frac{\partial L^{\gamma}(\zeta^{\gamma'})}{\partial \zeta} \left(\frac{\partial \zeta}{\partial x_J}\,\sigma_{IJ}\right)^{\alpha\beta\gamma'}\end{aligned} \tag{6.40}$$

Thus, the discrete internal virtual energy in Eq. (6.39) becomes:

$$\delta\Pi^e_{\text{int}} = \sum_{I=1}^{3} \sum_{\alpha,\beta,\gamma=1}^{p+1} \delta \mathrm{U}_I^{\alpha\beta\gamma}\,(\mathbf{f}^e_{\text{int}})_I^{\alpha\beta\gamma} = \delta\mathbf{U}^{e,\mathrm{T}}\,\mathbf{f}^e_{\text{int}} \tag{6.41}$$

where $\mathbf{f}^e_{\text{int}}$ denotes the element internal force vector, and $(\mathbf{f}^e_{\text{int}})_I^{\alpha\beta\gamma}$ is its nodal contribution in direction I, defined as:

$$\begin{aligned}(\mathbf{f}^e_{\text{int}})_I^{\alpha\beta\gamma} &= \omega^{\beta}\,\omega^{\gamma} \sum_{\alpha'=1}^{p+1} \omega^{\alpha'}\,J^{\alpha'\beta\gamma}\,\frac{\partial L^{\alpha}(\xi^{\alpha'})}{\partial \xi}\,T_{\xi I} \\ &\quad + \omega^{\alpha}\,\omega^{\gamma} \sum_{\beta'=1}^{p+1} \omega^{\beta'}\,J^{\alpha\beta'\gamma}\,\frac{\partial L^{\beta}(\eta^{\beta'})}{\partial \eta}\,T_{\eta I} \\ &\quad + \omega^{\alpha}\,\omega^{\beta} \sum_{\gamma'=1}^{p+1} \omega^{\gamma'}\,J^{\alpha\beta\gamma'}\,\frac{\partial L^{\gamma}(\zeta^{\gamma'})}{\partial \zeta}\,T_{\zeta I}\end{aligned} \tag{6.42}$$

with the auxiliary vectors $\boldsymbol{T}_\theta$, for $\theta = \xi, \eta, \zeta$, defined as:

$$T_{\theta I} = \sum_{J=1}^{3} \frac{\partial \theta}{\partial x_J}\, \sigma_{IJ} \tag{6.43}$$

To summarize, the discrete total virtual work of an elastic element Ω^e_{el} is:

$$\delta\Pi^e_{\text{kin}} + \delta\Pi^e_{\text{int}} - \delta\Pi^e_{\text{ext}} = \delta\mathbf{U}^{e,\text{T}} \left(\mathbf{M}^e\, \ddot{\mathbf{U}}^e + \mathbf{f}^e_{\text{int}} - \mathbf{f}^e_{\text{ext}} \right) \tag{6.44}$$

Element in the PML domain. In line with the spatial discretization of $\delta\Pi^e_{\text{kin}}$ in Eq. (6.37), the discrete virtual work of the inertial forces in a PML element can be written as:

$$\delta\Pi^e_{\text{PML},\rho} = \sum_{I=1}^{3} \sum_{\alpha,\beta,\gamma=1}^{p+1} \delta \text{U}_I^{\alpha\beta\gamma} \left(\text{M}_\text{P}^{\alpha\beta\gamma}\, \ddot{\text{U}}_I^{\alpha\beta\gamma} + \text{C}_\text{P}^{\alpha\beta\gamma}\, \dot{\text{U}}_I^{\alpha\beta\gamma} + \text{K}_\text{P}^{\alpha\beta\gamma}\, \text{U}_I^{\alpha\beta\gamma} + \text{H}_\text{P}^{\alpha\beta\gamma}\, \bar{\text{U}}_I^{\alpha\beta\gamma} \right) \tag{6.45}$$

where the nodal coefficients are defined as:

$$\begin{aligned} \text{M}_\text{P}^{\alpha\beta\gamma} &= (\rho\, f_M)^{\alpha\beta\gamma}, \qquad & \text{C}_\text{P}^{\alpha\beta\gamma} &= (\rho\, f_C)^{\alpha\beta\gamma}, \\ \text{K}_\text{P}^{\alpha\beta\gamma} &= (\rho\, f_K)^{\alpha\beta\gamma}, \qquad & \text{H}_\text{P}^{\alpha\beta\gamma} &= (\rho\, f_H)^{\alpha\beta\gamma} \end{aligned} \tag{6.46}$$

Following the discretization of the virtual internal energy $\delta\Pi^e_{\text{int}}$, the discrete virtual work of the internal stresses of a PML element can be written as:

$$\delta\Pi^e_{\text{PML},\sigma} = \sum_{I=1}^{3} \sum_{\alpha,\beta,\gamma=1}^{p+1} \delta \text{U}_I^{\alpha\beta\gamma}\, \text{P}_I^{\alpha\beta\gamma} \tag{6.47}$$

with $\text{P}_I^{\alpha\beta\gamma}$ given by:

$$\begin{aligned} \text{P}_I^{\alpha\beta\gamma} = {} & \omega^\beta \omega^\gamma \sum_{\alpha'=1}^{p+1} \omega^{\alpha'}\, J^{\alpha'\beta\gamma}\, \frac{\partial L^\alpha(\xi^{\alpha'})}{\partial \xi}\, S_{\xi I}^{\alpha'\beta\gamma} \\ & + \omega^\alpha \omega^\gamma \sum_{\beta'=1}^{p+1} \omega^{\beta'}\, J^{\alpha\beta'\gamma}\, \frac{\partial L^\beta(\eta^{\beta'})}{\partial \eta}\, S_{\eta I}^{\alpha\beta'\gamma} \\ & + \omega^\alpha \omega^\beta \sum_{\gamma'=1}^{p+1} \omega^{\gamma'}\, J^{\alpha\beta\gamma'}\, \frac{\partial L^\gamma(\zeta^{\gamma'})}{\partial \zeta}\, S_{\zeta I}^{\alpha\beta\gamma'} \end{aligned} \tag{6.48}$$

where the auxiliary vectors $\boldsymbol{S}_\theta$, for $\theta = \xi, \eta, \zeta$, are defined as:

$$S_{\theta I} = \sum_{J=1}^{3} \frac{\partial \theta}{\partial x_J} \left(\sigma_{IJ} F^{ee}_{JJ} + \Sigma_{IJ} F^{ep}_{JJ} + \bar{\Sigma}_{IJ} F^{pp}_{JJ} \right) \tag{6.49}$$

Combining Eq. (6.45) and Eq. (6.47), the discrete virtual work of a PML element can be expressed as:

$$\delta \Pi^e_{\mathrm{PML}} = \delta \mathbf{U}^{e,\mathrm{T}} \left(\mathbf{M}^e_{\mathrm{PML}} \, \ddot{\mathbf{U}}^e + \mathbf{f}^e_{\mathrm{PML}} \right) \tag{6.50}$$

where $\mathbf{M}^e_{\mathrm{PML}}$ denotes the diagonal PML-element mass matrix defined as:

$$(\mathbf{M}^e_{\mathrm{PML}})^{\alpha\beta\gamma}_I = \mathrm{M}^{\alpha\beta\gamma}_{\mathrm{P}} \tag{6.51}$$

and $\mathbf{f}^e_{\mathrm{PML}}$ is the PML-element force vector defined as:

$$(\mathbf{f}^e_{\mathrm{PML}})^{\alpha\beta\gamma}_I = \mathrm{C}^{\alpha\beta\gamma}_{\mathrm{P}} \, \dot{\mathrm{U}}^{\alpha\beta\gamma}_I + \mathrm{K}^{\alpha\beta\gamma}_{\mathrm{P}} \, \mathrm{U}^{\alpha\beta\gamma}_I + \mathrm{H}^{\alpha\beta\gamma}_{\mathrm{P}} \, \bar{\mathrm{U}}^{\alpha\beta\gamma}_I + \mathrm{P}^{\alpha\beta\gamma}_I \tag{6.52}$$

Semi-discrete weak form at the global level. From the element-level discrete weak forms in Eq. (6.44) and Eq. (6.50), the semi-discrete displacement-based equation of motion for the whole body Ω is obtained by assembling all elements with the standard finite element procedure:

$$\mathbf{M} \, \ddot{\mathbf{U}} + \mathbf{f}_{\mathrm{int}} - \mathbf{f}_{\mathrm{ext}} = \mathbf{0} \tag{6.53}$$

Here, $\mathbf{M}$ denotes the diagonal global mass matrix, assembled from the mass matrices of both the elastic and PML elements. The internal force vector $\mathbf{f}_{\mathrm{int}}$ is the sum of contributions from elastic elements, $\mathbf{f}^e_{\mathrm{int}}$, and PML elements, $\mathbf{f}^e_{\mathrm{PML}}$. The external force vector $\mathbf{f}_{\mathrm{ext}}$ collects all nodal body forces and applied tractions on the Neumann boundary.

6.3.3 Explicit algorithm

We divide the time interval into discrete time steps of size Δt. At a generic time step $t_{n+1} = t_n + \Delta t$, the governing equations of the body Ω can be written as:

$$\begin{aligned} &\mathbf{M} \, \ddot{\mathbf{U}}_{n+1} + \mathbf{f}_{\mathrm{int},n+1} - \mathbf{f}_{\mathrm{ext},n+1} = \mathbf{0} \\ &\boldsymbol{\sigma}_{n+1} = \boldsymbol{\mathcal{C}} : \boldsymbol{\epsilon}_{n+1} \end{aligned} \tag{6.54}$$

where the kinematic conditions in Eq. (6.7) and Eq. (6.16) are applied, respectively, in the elastic and PML domains.

Central Difference scheme. The Central Difference (CD) scheme is used to integrate the equation of motion in time:

$$\begin{aligned} \mathbf{U}_{n+1} &= \mathbf{U}_n + \Delta t \left(\dot{\mathbf{U}}_n + \frac{\Delta t}{2} \ddot{\mathbf{U}}_n \right) \\ \dot{\mathbf{U}}_{n+1} &= \dot{\mathbf{U}}_n + \frac{\Delta t}{2} \left(\ddot{\mathbf{U}}_n + \ddot{\mathbf{U}}_{n+1} \right) \end{aligned} \tag{6.55}$$

Assuming that the solution at time t_n is known, Eq. (6.55) permits us to obtain explicitly the displacements at t_{n+1}. The elastic internal force vector $\mathbf{f}^e_{\text{int}}$ in Eq. (6.42) is then computed using the kinematic condition and the linear stress–strain relation. However, the computation of the PML force vector in Eq. (6.52) requires special treatment.

Explicit algorithm for the PML force vector. At time t_{n+1}, the PML force vector of an element can be written as:

$$(\mathbf{f}^e_{\text{PML}})^{\alpha\beta\gamma}_{I,n+1} = \mathrm{C}_{\mathrm{P}}^{\alpha\beta\gamma}\, \dot{\mathrm{U}}^{\alpha\beta\gamma}_{I,n+1/2} + \mathrm{K}_{\mathrm{P}}^{\alpha\beta\gamma}\, \mathrm{U}^{\alpha\beta\gamma}_{I,n+1} + \mathrm{H}_{\mathrm{P}}^{\alpha\beta\gamma}\, \bar{\mathrm{U}}^{\alpha\beta\gamma}_{I,n+1} + \mathrm{P}^{\alpha\beta\gamma}_{I,n+1} \tag{6.56}$$

where the velocity field is evaluated at $t_{n+1/2}$, as is usual in explicit schemes. The strain measure in Eq. (6.16) takes the form:

$$\begin{aligned} &\alpha_I \alpha_J\, \dot{\epsilon}_{IJ,n+1/2} + (\alpha_I \beta_J + \alpha_J \beta_I)\, \epsilon_{IJ,n+1} + \beta_I \beta_J\, E_{IJ,n+1} \\ &\qquad = \frac{1}{2} \left(\alpha_I \frac{\partial \dot{u}_{I,n+1/2}}{\partial x_J} + \alpha_J \frac{\partial \dot{u}_{J,n+1/2}}{\partial x_I} + \beta_I \frac{\partial u_{I,n+1}}{\partial x_J} + \beta_J \frac{\partial u_{J,n+1}}{\partial x_I} \right) \end{aligned} \tag{6.57}$$

Assumptions for explicit update. To compute the PML force vector, we need the values of $\bar{\mathbf{U}}_{n+1}$ and $\boldsymbol{\epsilon}_{n+1}$, which are not directly available. The following assumptions are therefore introduced to obtain an explicit update.

1. For the history variable $\bar{\mathbf{U}}$:

$$\bar{\mathbf{U}}_{n+1} = \bar{\mathbf{U}}_n + \Delta t\, \mathbf{U}_{n+1} \tag{6.58}$$

2. For the strain-related fields:

$$\begin{aligned} \boldsymbol{\epsilon}_{n+1} &= \boldsymbol{\epsilon}_n + \Delta t\, \dot{\boldsymbol{\epsilon}}_{n+1/2} \\ \boldsymbol{E}_{n+1} &= \boldsymbol{E}_n + \Delta t\, \boldsymbol{\epsilon}_{n+1} \\ \bar{\boldsymbol{E}}_{n+1} &= \bar{\boldsymbol{E}}_n + \Delta t\, \boldsymbol{E}_{n+1} \end{aligned} \tag{6.59}$$

Substituting Eq. (6.59) into Eq. (6.57), the strain rate at $t_{n+1/2}$ is obtained as:

$$\begin{aligned}\dot{\epsilon}_{IJ,n+1/2} = \Bigg[&\frac{1}{2}\Big(\alpha_I \frac{\partial \dot{u}_{I,n+1/2}}{\partial x_J} + \alpha_J \frac{\partial \dot{u}_{J,n+1/2}}{\partial x_I} + \beta_I \frac{\partial u_{I,n+1}}{\partial x_J} + \beta_J \frac{\partial u_{J,n+1}}{\partial x_I}\Big) \\ &- (\alpha_I\beta_J + \alpha_J\beta_I)\,\epsilon_{IJ,n} - \beta_I\beta_J\left(E_{IJ,n} + \Delta t\,\epsilon_{IJ,n}\right)\Bigg] \\ &\times \Big[\alpha_I\alpha_J + \Delta t\,(\alpha_I\beta_J + \alpha_J\beta_I) + \Delta t^2\,\beta_I\beta_J\Big]^{-1}\end{aligned} \tag{6.60}$$

Once $\dot{\boldsymbol{\epsilon}}_{n+1/2}$ is obtained, the strain fields $\boldsymbol{\epsilon}_{n+1}, \boldsymbol{E}_{n+1}, \bar{\boldsymbol{E}}_{n+1}$ are updated using Eq. (6.59), and the stress-like tensors $\boldsymbol{\sigma}_{n+1}$, $\boldsymbol{\Sigma}_{n+1}$, $\bar{\boldsymbol{\Sigma}}_{n+1}$ are computed from the constitutive law. Finally, the element-level PML force vector is obtained explicitly from Eq. (6.56). In the implementation, the fields $\boldsymbol{\epsilon}, \boldsymbol{E}, \bar{\boldsymbol{E}}$ are treated as internal variables and updated at each time step.

Consistency with the elastic case. When the PML parameters vanish ($\alpha_I = 1$, $\beta_I = 0$), Eq. (6.60) together with Eq. (6.59) reduces to:

$$\epsilon_{IJ,n+1} = \epsilon_{IJ,n} + \frac{\Delta t}{2}\left(\frac{\partial \dot{u}_{I,n+1/2}}{\partial x_J} + \frac{\partial \dot{u}_{J,n+1/2}}{\partial x_I}\right) \tag{6.61}$$

Expanding $\epsilon_{IJ,n}$ in terms of $u_{I,n}$ and using Eq. (6.55), this retrieves the classical kinematic condition:

$$\epsilon_{IJ,n+1} = \frac{1}{2}\left(\frac{\partial u_{I,n+1}}{\partial x_J} + \frac{\partial u_{J,n+1}}{\partial x_I}\right) \tag{6.62}$$

which confirms the consistency of the PML update scheme with the elastic case. The evaluation of the element-level PML internal force vector $(\mathbf{f}^e_{\text{PML}})^{\alpha\beta\gamma}_{I,n+1}$ is summarized in Algorithm 6.

Algorithm 6 Evaluation of the PML force vector at time t_{n+1}

Update the history variable $\bar{\mathbf{U}}_{n+1}$ using Eq. (6.58).
Compute the strain rate $\dot{\boldsymbol{\epsilon}}_{n+1/2}$ from Eq. (6.60).
Update the strain fields $\boldsymbol{\epsilon}_{n+1}, \boldsymbol{E}_{n+1}, \bar{\boldsymbol{E}}_{n+1}$ using Eq. (6.59).
Evaluate the stress-like tensors $\boldsymbol{\sigma}_{n+1}, \boldsymbol{\Sigma}_{n+1}, \bar{\boldsymbol{\Sigma}}_{n+1}$ from the constitutive relation.
Compute the nodal contributions $\mathrm{P}^{\alpha\beta\gamma}_{I,n+1}$ using Eq. (6.57).
Assemble the element PML force vector $(\mathbf{f}^e_{\text{PML}})^{\alpha\beta\gamma}_{I,n+1}$ with Eq. (6.56).

Critical time step. In explicit computations, the stability of the Central Difference scheme requires that the time step Δt satisfies the Courant–Friedrichs–Lewy (CFL) condition. For the Spectral Element Method, the critical time step is controlled by the smallest element size and the highest wave velocity in the domain. It can be estimated as:

$$\Delta t_{\text{crit}} = \frac{\ell_e}{(2p+1)\, c_{\max}} \tag{6.63}$$

where ℓ_e is the size of the smallest hexahedral element, $c_{\max}$ is the maximum wave velocity (typically the P-wave velocity), and p is the polynomial order of the spectral element. The factor $(2p+1)$ reflects the shorter nodal spacing introduced by higher-order spectral elements. In practice, Δt is usually set to $0.9\,\Delta t_{\text{crit}}$ to ensure numerical stability of the explicit time integration.

6.4 Numerical Validation

In this section, we evaluate the performance of the implemented PML in `EFISPEC3D` and investigate the impact of the stretching function parameters. The tests cover different configurations of the wave propagation problem: a 3D homogeneous medium, a pseudo-2D and 3D thin homogeneous medium (waveguide), and a 3D two-layered medium. In all tests, the spectral elements of order $p = 4$ are used for the discretization.

In all cases, the waves are generated by a concentrated surface load driven by a Ricker wavelet defined as:

$$\mathbf{f}(t) = \left[0, \quad 0, \quad -A\left(2\pi^2 \frac{(t-t_s)^2}{t_p^2} - 1\right) \exp\left(-\pi^2 \frac{(t-t_s)^2}{t_p^2}\right)\right]^{\mathrm{T}} \tag{6.64}$$

The Ricker wavelet is characterized by its fundamental period t_p, time shift t_s, and amplitude A. The values used here are $t_p = 0.2\,\text{s}$, $t_s = 0.3\,\text{s}$, and $A = 1\,\text{N}$.

As introduced in Section 6.2.1, the PML parameters are defined by six user-controlled values: α_{0I} and β_{0I} for $I = 1, 2, 3$ in the three spatial directions. In this work, β_{0I} is taken equal in all directions, while α_{0I} is chosen independently depending on the configuration. Different values of these parameters are tested, based on the design equations of Kucukcoban and Kallivokas [110] (Eq. (6.5) and Eq. (6.6)), with the polynomial order of the stretching functions fixed at $m = 2$. Unless otherwise stated (in the two-layered case), the mechanical properties of the medium are kept identical across all tests. For brevity, the notations $(\cdot)_{0X}$, $(\cdot)_{0Y}$, and $(\cdot)_{0Z}$ are used.

The accuracy of the PML models is evaluated by comparing the time histories of displacement at the receivers with those from a reference solution using an extended mesh. For this purpose, we define the relative error between PML models and the reference. The displacement error is defined over a time interval $[0, T]$ as follows:

$$\text{error} = \frac{\|\mathrm{U}_{I,PML} - \mathrm{U}_{I,ref}\|_{L^2([0,T])}}{\|\mathrm{U}_{I,ref}\|_{L^2([0,T])}} \tag{6.65}$$

where $\mathrm{U}_{I,PML}$ and $\mathrm{U}_{I,ref}$ are the displacement in direction I from the PML model the extended mesh, respectively. In addition, the long-term stability of the PML models is examined in the waveguide and two-layered medium tests.

6.4.1 Wave propagation in a homogeneous half-space

The PML model is illustrated in Figure 6.2. By symmetry, only one quarter of the half-space is modeled. The elastic domain has dimensions $100 \times 100 \times 100\,\mathrm{m}^3$ and is surrounded by a PML layer of thickness 15 m in all directions. The mechanical properties of the elastic medium are indicated in Figure 6.2. The mesh consists of $23 \times 23 \times 23$ spectral elements of order $p = 4$, which corresponds to three elements across the PML thickness. The stretching function parameters used in the five tested configurations (Models 1–5) are summarized in Table 6.1.

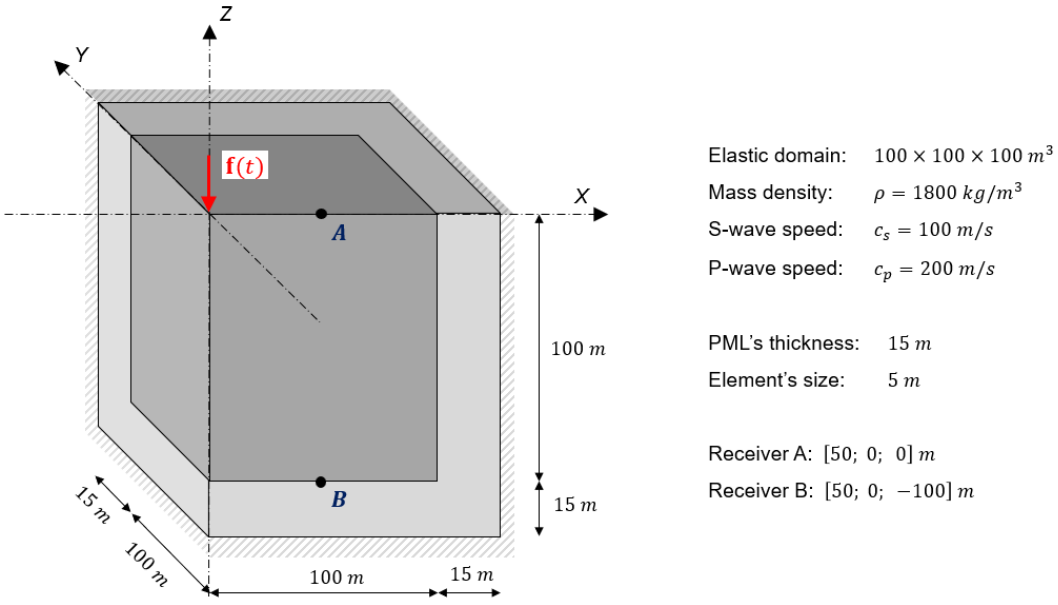

Figure 6.2 Homogeneous medium case: PML model description.

We first investigate the influence of the parameter β_0. In Models 1–3, α_{0I} was set to zero in all directions, while β_0 was increased from 100.0 to 180.0, corresponding to attenuation coefficients R ranging from 10^{-2} to 10^{-4}. As β_0 increases, the critical time step decreases from 2.5 ms (Model 1) to 2.0 ms (Models 2 and 3), whereas the critical time step of the elastic domain alone is 2.5 ms.

Table 6.1 Homogeneous medium case: stretching function parameters and the time-step-sizes for PML models

Model	α_{0X}	α_{0Y}	α_{0Z}	β_0	Δt (ms)
1	0	0	0	100.0	2.5
2	0	0	0	140.0	2.0
3	0	0	0	180.0	2.0
4	4.0	4.0	4.0	140.0	2.5
5	0	0	4.0	140.0	2.0

Table 6.2 Homogeneous medium case: relative error in displacement over the time interval $[0.0, 4.0\,\text{s}]$ at receiver A, located on the free surface at $[50, 0, 0]$ m, and receiver B, located at the PML–elastic interface at $[50, 0, -100]$ m

Model	**Point A**		**Point B**	
	u_X	u_Z	u_X	u_Z
1	0.57%	0.81%	1.16%	2.12%
2	0.38%	0.68%	1.17%	1.88%
3	0.43%	0.78%	1.34%	2.09%
4	1.14%	1.74%	0.95%	1.24%
5	0.39%	0.68%	1.02%	1.60%

Figure 6.4 presents the vertical displacement time histories recorded at receiver A, located on the free surface at $[50, 0, 0]$ m, and receiver B, located at the PML–elastic interface at $[50, 0, -100]$ m, for Model 1. The results from the PML model agree well with the reference solution obtained from an extended mesh. Snapshots of vertical displacement at $t = 1.5$ s are shown in Figure 6.3. P-waves are generated first and reach the PML very quickly. The displacement field is dominated by S-waves radiating outward into the medium and Rayleigh waves traveling along the free surface. The PML absorbs all wave types without spurious reflections back into the elastic domain.

The relative error norms at both receivers for all models are reported in Table 6.2. Increasing β_0 from 100.0 (Model 1) to 140.0 (Model 2) improves the accuracy of the

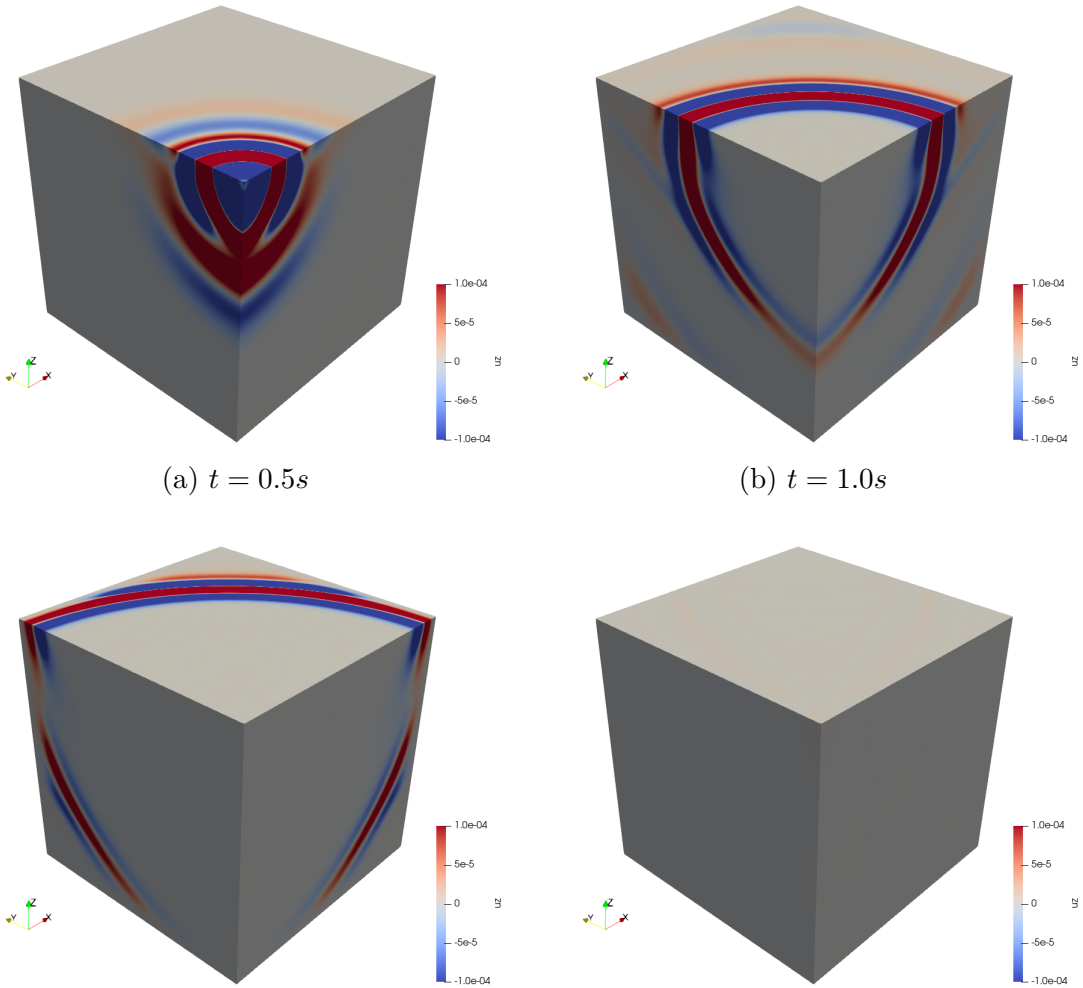

(a) $t = 0.5s$ (b) $t = 1.0s$

(c) $t = 1.5s$ (d) $t = 2.5s$

Figure 6.3 Homogeneous medium case: Snapshots of vertical displacement obtained from Model 1.

PML, as expected. However, further increasing β_0 to 180.0 (Model 3) does not lead to additional improvement. In this case, the stretching function exhibits an excessively steep gradient across the PML thickness, which enhances spurious wave generation due to spatial dispersion.

The parameter $\beta_0 = 140.0$ was therefore retained to examine the effect of α_{0I} in Models 4 and 5. In Model 4, $\alpha_{0I} = 4.0$, corresponding to the attenuation coefficient of $R = 10^{-3}$, was applied in all directions, while in Model 5, only α_{0Z} was set to 4.0. Since $\alpha_{0I} > 0$ adds effective mass to the PML, the critical time step of Model 4 increases accordingly. Table 6.2 shows that using α_{0Z} alone (Model 5) improves accuracy, especially at receiver B, located at the PML–elastic interface. By contrast, setting α_{0X} and α_{0Y} in

addition to α_{0Z} (Model 4) generates more spurious waves, deteriorating the accuracy at receiver A on the free surface. This is also confirmed in Figure 6.5, which plots the time history of the kinetic energy on a logarithmic scale obtained from different models. This difference is attributed to the presence of evanescent waves at the lower interface.

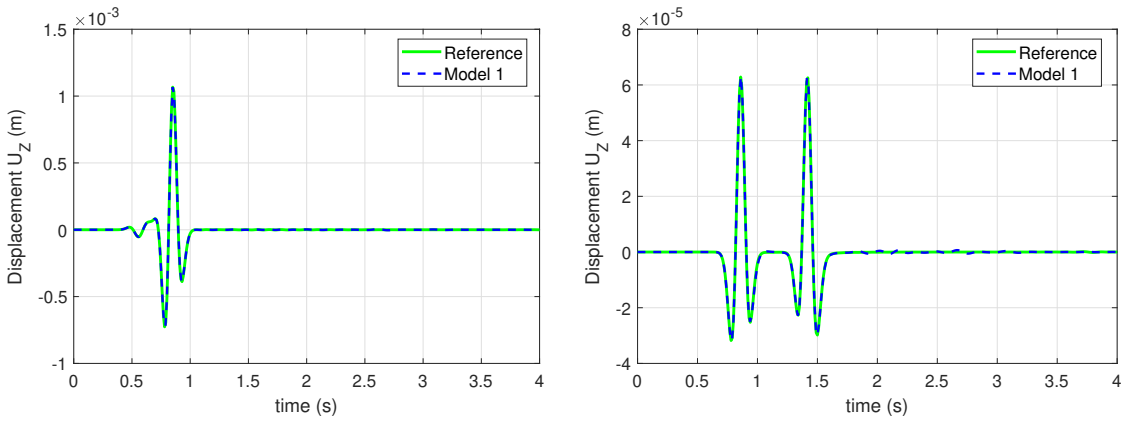

(a) Receiver A. (b) Receiver B.

Figure 6.4 Homogeneous medium case: Time history of the vertical displacement at receiver A [50.0; 0.0; 0.0] and receiver B [50.0; 0.0; −100.0], obtained from Model 1.

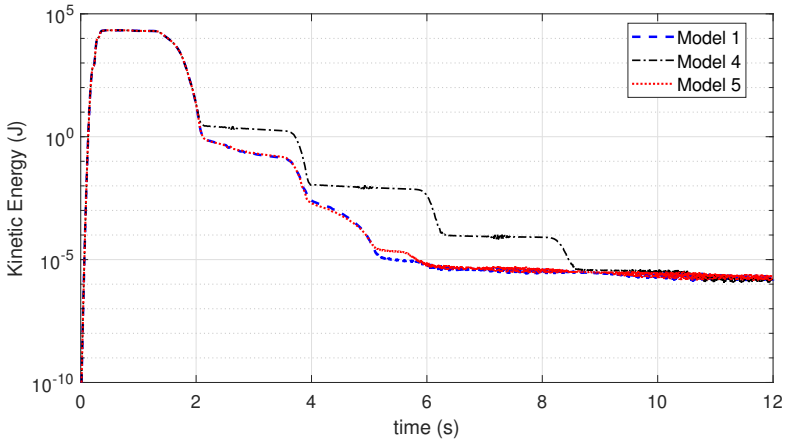

Figure 6.5 Homogeneous medium case: Time histories of kinetic energy in the elastic domain from different PML models.

To summarize, the homogeneous half-space test confirms the effectiveness of the implemented PML. The results show that an appropriate choice of the attenuation parameter β_0 is essential for accuracy, while excessively large values can degrade performance due to numerical dispersion. The scaling parameter α_{0I} must be carefully chosen for each direction. In this case, only α_{0Z} is required to attenuate the evanescent waves at the lower PML–elastic interface.

6.4.2 Homogeneous waveguide

To investigate the performance of the PML model in attenuating waves at near-grazing incidence, we consider the homogeneous waveguide problem. Two cases are studied: the pseudo-2D case, similar to the 2D case investigated in [75, 76], and the full 3D case.

Pseudo-2D homogenenous waveguide

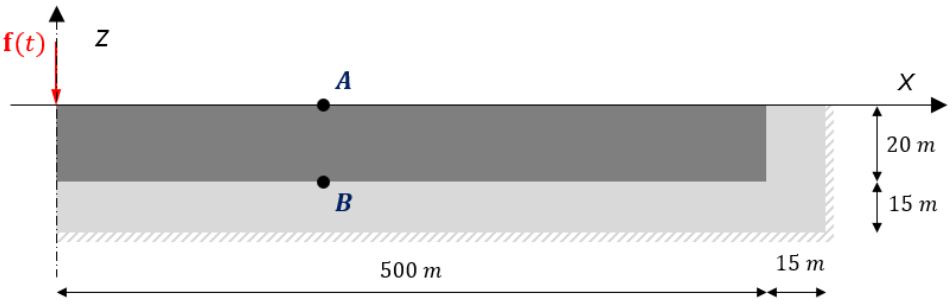

Elastic domain:	$500 \times 20\ m^2$	PML's thickness:	$15\ m$
Mass density:	$\rho = 1800\ kg/m^3$	Element's size:	$5\ m$
S-wave speed:	$c_s = 100\ m/s$	Receiver A:	$[200;\ 0;\ 0]\ m$
P-wave speed:	$c_p = 200\ m/s$	Receiver B:	$[200;\ 0;\ -20]\ m$

Figure 6.6 Pseudo-2D homogeneous waveguide: PML model description.

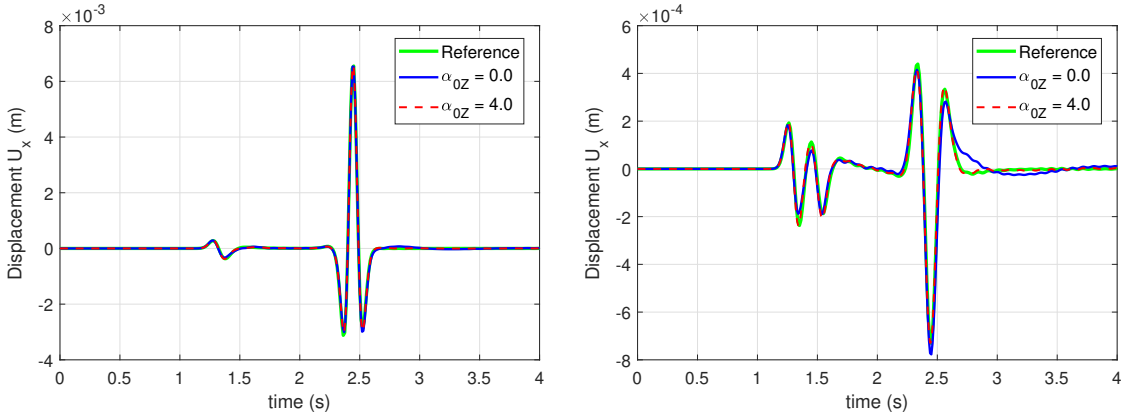

(a) Receiver A. (b) Receiver B.

Figure 6.7 Pseudo-2D homogeneous waveguide: Time history of the horizontal displacements at receiver A [200.0; 0.0; 0.0] and receiver B [200.0; 0.0; −20.0] from the PML models with $\alpha_{0X} = 0.0$ and $\alpha_{0X} = 4.0$.

The 2D PML model is illustrated in Figure 6.6. Exploiting symmetry, the elastic domain of 500 m length and 20 m depth is surrounded by a 15 m-thick PML. The elastic–

PML domain was discretized using 103×7 elements of size 5 m. A pseudo-2D scenario was obtained by blocking the nodal displacements in the Y-direction for all nodes located at the extremities in Y.

Table 6.3 Pseudo-2D homogeneous waveguide: relative error in displacement over the time interval $[0.0, 4.0\,\text{s}]$ at receiver A $[200, 0, 0]$ m, and receiver B $[200, 0, -20]$ m

Model	**Point A**		**Point B**	
	u_X	u_Z	u_X	u_Z
$\alpha_{0z} = 0.0$	4.15%	3.76%	21.93%	17.61%
$\alpha_{0z} = 1.0$	3.32%	3.17%	14.24%	13.99%
$\alpha_{0z} = 2.0$	2.91%	2.86%	11.94%	11.95%
$\alpha_{0z} = 3.0$	2.66%	2.64%	11.04%	10.03%
$\alpha_{0z} = 4.0$	2.50%	2.50%	10.26%	8.42%

For the PML, we set $\beta_0 = 140.0$ and $\alpha_{0X} = 0.0$, while α_{0Z} was varied between 0.0 and 4.0. Thus, the time step size for all the computations is $\Delta t = 2.0$ ms, as explained in the previous test. Figure 6.7 shows the displacement time histories at receiver A (free surface, $[100, 0, 0]$ m) and receiver B (PML–elastic interface, $[100, 0, -20]$ m) for $\alpha_{0Z} = 0.0$ and $\alpha_{0Z} = 4.0$. In both cases, the results agree well with the reference solution. It can be seen that the PML model with $\alpha_{0Z} = 4.0$ provides a better solution than the one with $\alpha_{0Z} = 0.0$, especially at receiver B. Table 6.3 reveals that increasing α_{0Z} improves accuracy at both receivers.

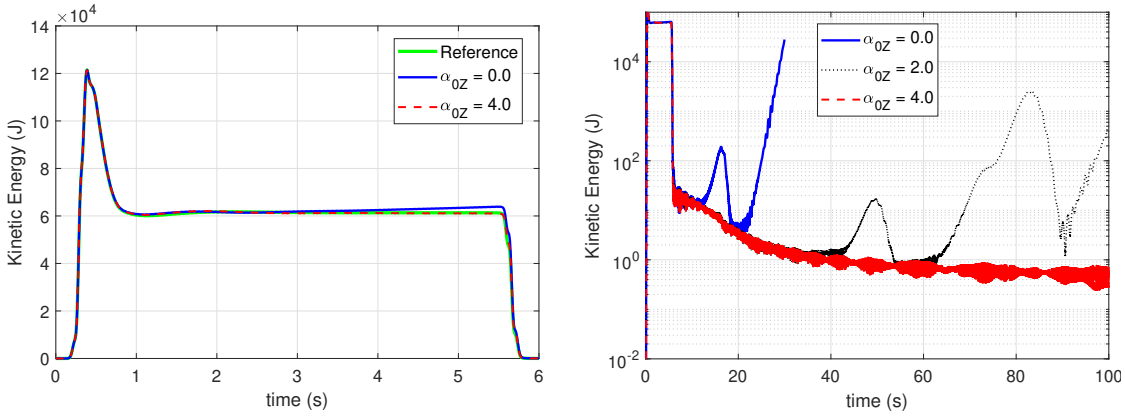

(a) Kinetic energy. (b) Kinetic energy.

Figure 6.8 Pseudo-2D homogeneous waveguide: Time history of the kinetic energy in the elastic domain from the PML models with $\alpha_{0X} = 0.0$, $\alpha_{0X} = 2.0$, and $\alpha_{0X} = 4.0$.

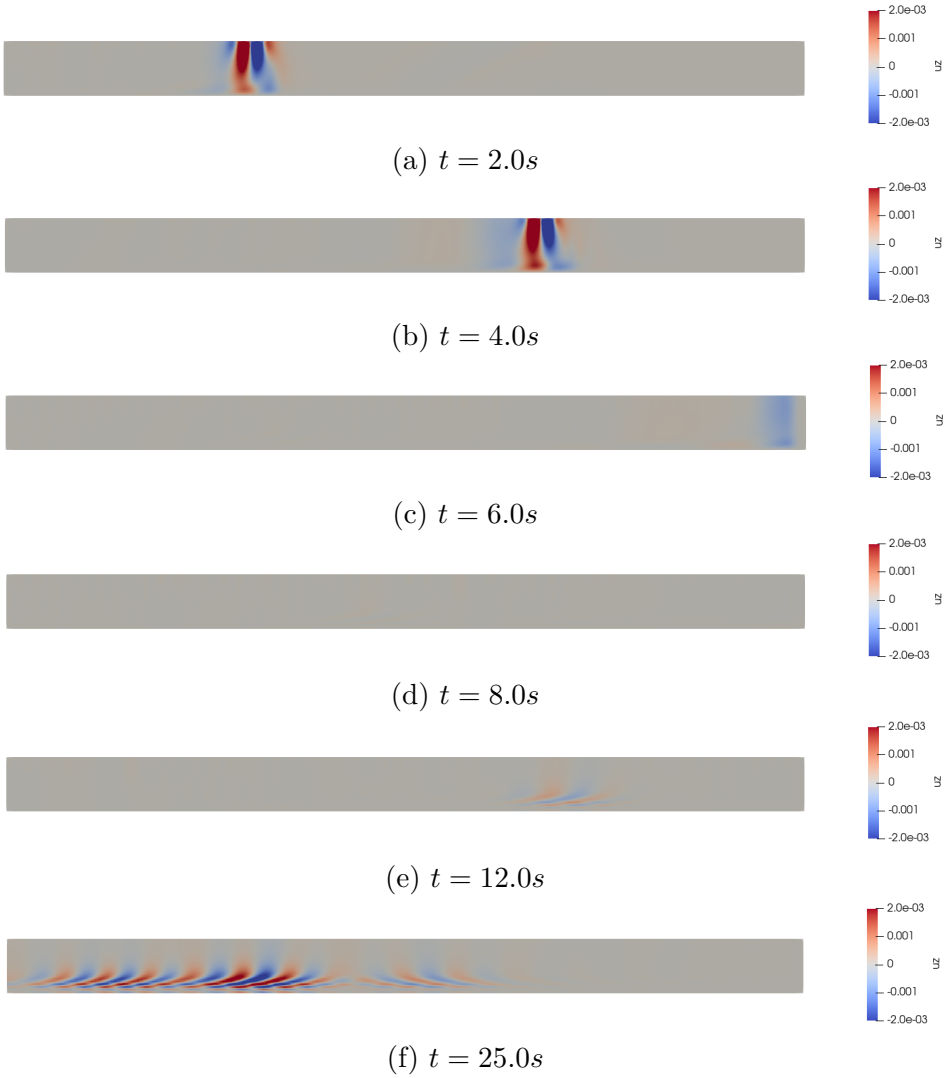

(a) $t = 2.0s$

(b) $t = 4.0s$

(c) $t = 6.0s$

(d) $t = 8.0s$

(e) $t = 12.0s$

(f) $t = 25.0s$

Figure 6.9 Pseudo-2D homogeneous waveguide: Snapshots of vertical displacement obtained from Model 1.

The evolution of kinetic energy in the elastic domain is plotted in Figure 6.8. For $\alpha_{0Z} = 0.0$, spurious waves generated at the lower PML region during the first 6.0 s cause a slight increase in the total kinetic energy (Figure 6.8(a)), which also degrades the response at receiver B as observed in Table 6.3. A longer simulation shows that instability begins at about $t = 12.0$ s and grows rapidly after $t = 25.0$ s. This behavior is also visible in the displacement snapshots of Figure 6.9. Setting $\alpha_{0Z} > 0$ cannot eliminate this instability, but delays its onset, as seen in Figure 6.8(b). It is highlighted that the scaling parameter $\alpha_{0Z} = 0.4$ enables us to improve the accuracy in terms of displacement and achieves to delay the onset of instability beyond $100s$.

3D homogeneous waveguide

The PML model for the 3D waveguide problem is illustrated in Figure 6.10. Exploiting symmetry, the elastic domain measures 500 m in length, 100 m in width, and 20 m in depth, and is surrounded by a PML of 15 m thickness in all directions. The full domain is discretized into $103 \times 23 \times 7$ elements of size 5.0 m. For brevity, the absorbing layers in the three directions are denoted as PML-X, PML-Y, and PML-Z. In this 3D configuration, both PML-Y and PML-Z must absorb waves at nearly grazing incidence.

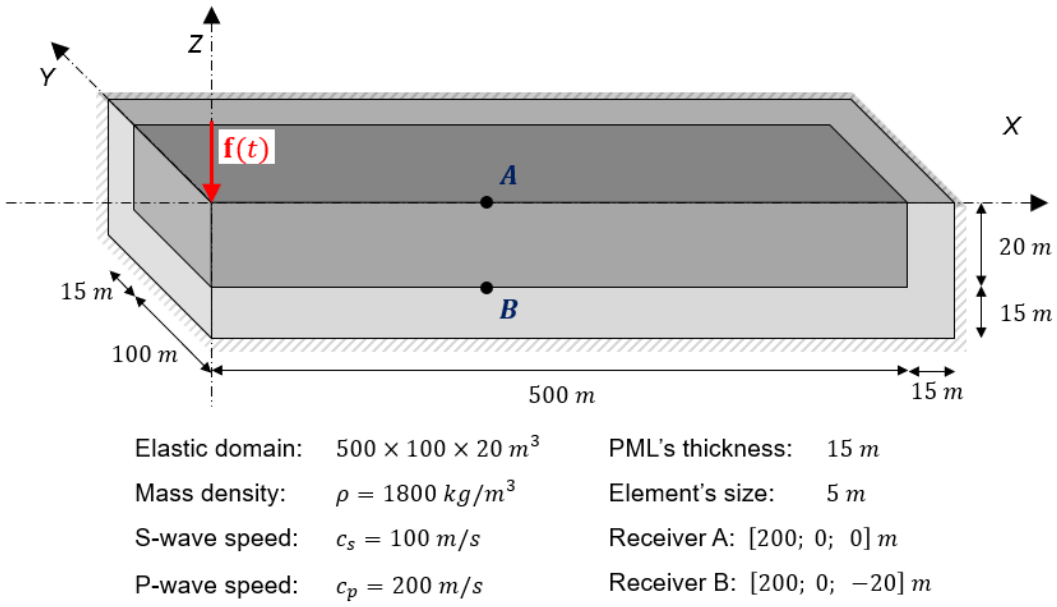

Figure 6.10 3D homogeneous waveguide: PML model description.

Table 6.4 3D homogeneous waveguide: relative error in displacement over the time interval $[0, 4.0\,\text{s}]$ at receiver A $[200, 0, 0]$ m, and receiver B $[200, 0, -20]$ m

Model	**Point A**		**Point B**	
	u_X	u_Z	u_X	u_Z
$\alpha_{0Y} = 0.0$	3.41%	3.98%	12.86%	13.68%
$\alpha_{0Y} = 1.0$	3.19%	3.58%	12.77%	13.60%
$\alpha_{0Y} = 2.0$	3.08%	3.37%	12.72%	13.55%
$\alpha_{0Y} = 3.0$	3.03%	3.28%	12.69%	13.51%
$\alpha_{0Y} = 4.0$	3.02%	3.30%	12.68%	13.49%

Building on the pseudo-2D investigation, the PML was parameterized with $\beta_0 = 140.0$, $\alpha_{0X} = 0.0$, and $\alpha_{0Z} = 4.0$, while α_{0Y} was varied from 0.0 to 4.0. Figure 6.11 shows

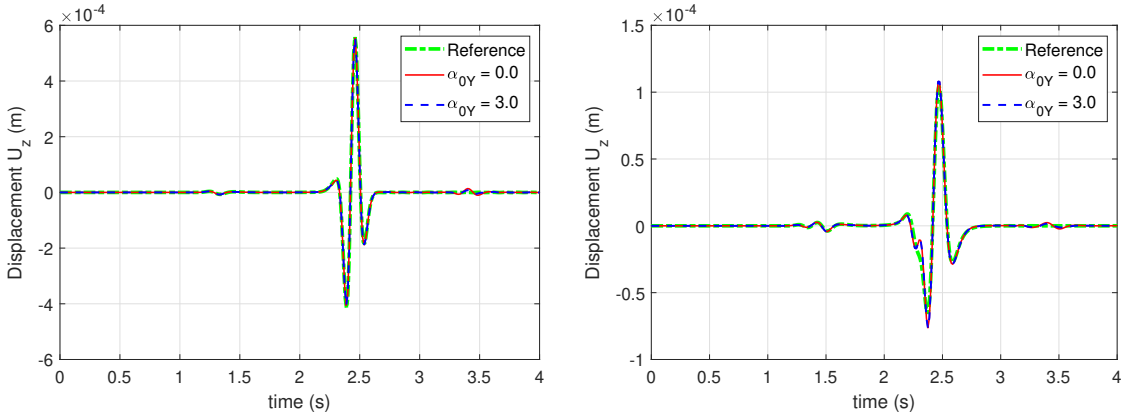

(a) Receiver A. (b) Receiver B.

Figure 6.11 3D homogeneous waveguide: Time history of the displacement at receiver A [100.0; 0.0; 0.0] and receiver B $[200, 0, -20]$ m from PML models with $\alpha_{0Y} = 0.0$ and $\alpha_{0Y} = 3.0$

the vertical displacement time histories at receiver A (free surface, $[200, 0, 0]$ m) and receiver B (PML-Z–elastic interface, $[200, 0, -20]$ m) for $\alpha_{0Y} = 0.0$ and $\alpha_{0Y} = 4.0$. In both cases, the results are consistent with the reference solution. The error norms at the two receivers, summarized in Table 6.4, indicate that increasing α_{0Y} slightly improves accuracy at both observation points.

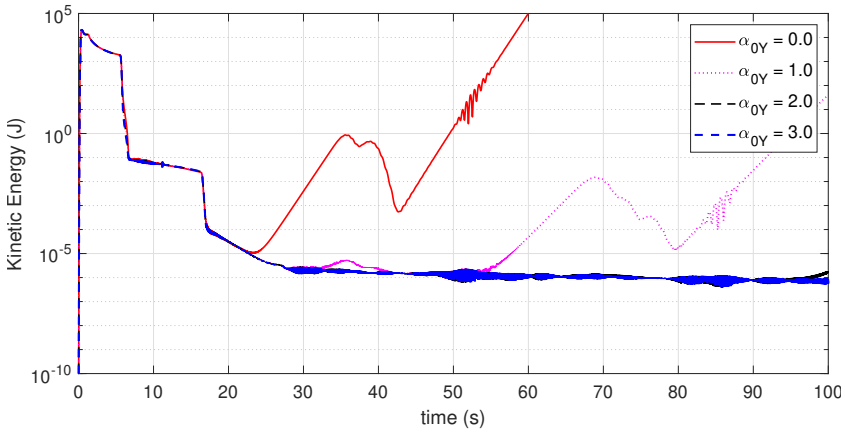

Figure 6.12 3D homogeneous waveguide: Energy in the elastic domain.

As in the pseudo-2D case, however, the PML exhibits long-term instability. This can be seen in the kinetic energy histories of the elastic domain (Figure 6.12) and in the displacement snapshots (Figure 6.13) obtained from the model with $\alpha_{0Y} = 0.0$. The latter indicates that the instability originates from the PML-Y at approximately $t = 56.0$ s. As seen in Figure 6.12, larger values of α_{0Y} help delay the onset of instability.

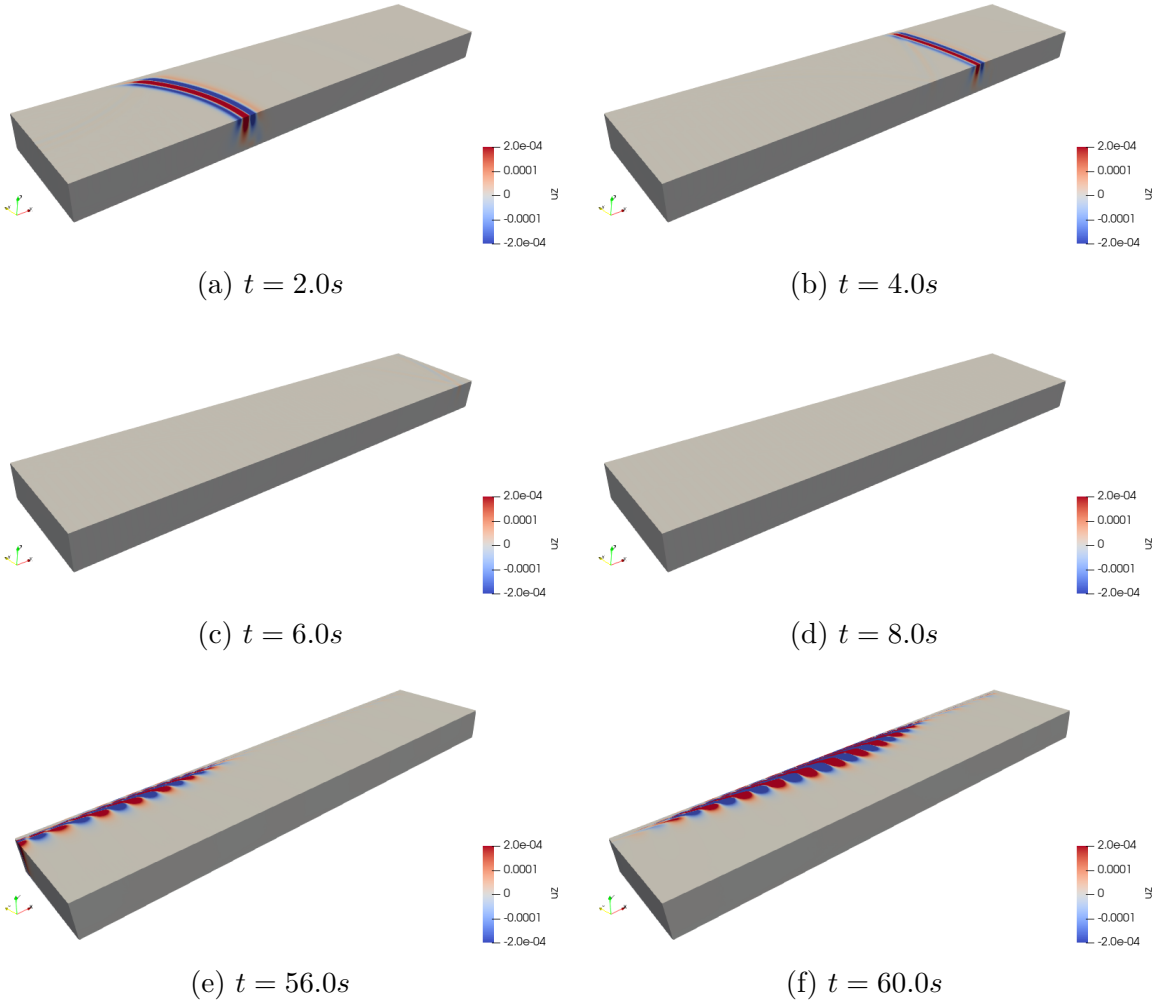

(a) $t = 2.0s$ (b) $t = 4.0s$

(c) $t = 6.0s$ (d) $t = 8.0s$

(e) $t = 56.0s$ (f) $t = 60.0s$

Figure 6.13 3D homogeneous waveguide: Snapshots of vertical displacement obtained from PML model with $\alpha_{0Y} = 0.0$.

6.4.3 Two-layered half-space

We now consider wave propagation in a heterogeneous half-space composed of two layers. The upper surface layer is 10 m thick. As shown in Figure 6.16, the P- and S-wave velocities in the lower layer are three times larger than those in the upper layer. This contrast in material properties leads to multiple reflections and refractions at the interface, which can trigger instabilities in long-term simulations [76].

The PML setup is illustrated in Figure 6.14, and the mesh is shown in Figure 6.15. The upper layer of 10 m depth (including both elastic and PML regions) is discretized with uniform spectral elements of size 5 m. Below this, a transition row of mesh-adaptive elements is introduced to increase the element size gradually. This adaptation allows

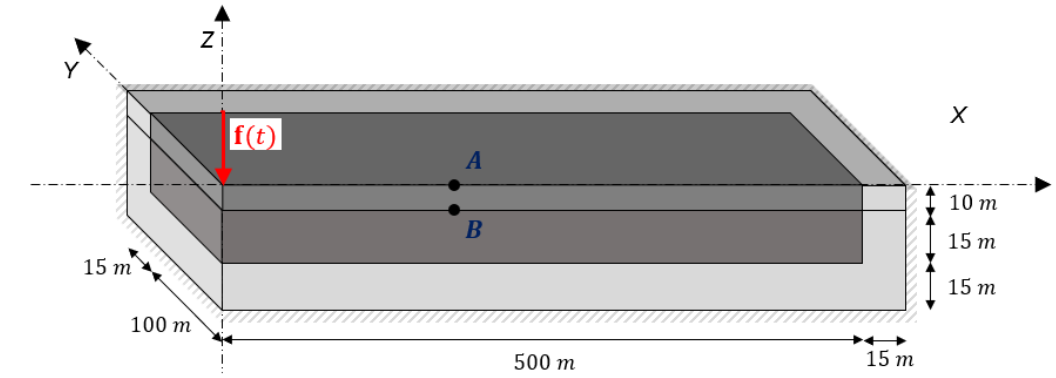

Elastic domain 1:	$500 \times 100 \times 10\ m^3$	Elastic domain 2:	$500 \times 100 \times 15\ m^3$	PML's thickness:	$15\ m$
Mass density:	$\rho_1 = 1800\ kg/m^3$	Mass density:	$\rho_2 = 2200\ kg/m^3$	Receiver A:	$[200;\ 0;\ 0]\ m$
S-wave speed:	$c_{s1} = 100\ m/s$	S-wave speed:	$c_{s2} = 300\ m/s$	Receiver B:	$[200;\ 0;\ -10]\ m$
P-wave speed:	$c_{p1} = 200\ m/s$	P-wave speed:	$c_{p2} = 600\ m/s$		

Figure 6.14 Two-layered half-space: PML model description.

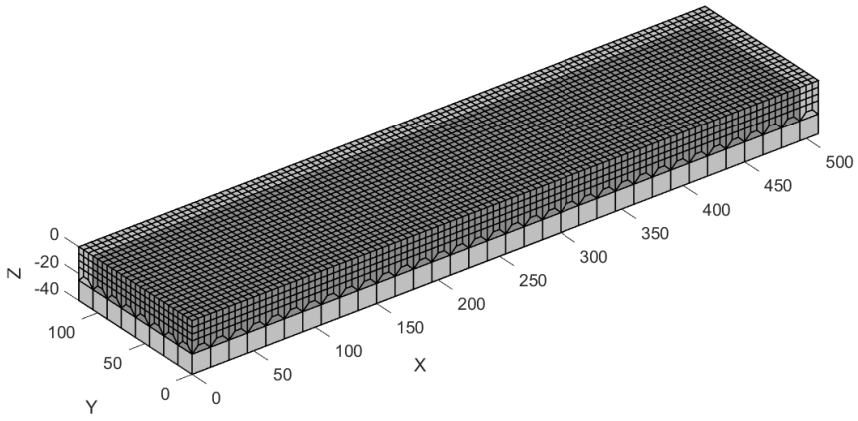

Figure 6.15 Two-layered half-space: Mesh of PML model.

the lower PML of 15 m thickness to be represented with coarser 15 m elements (only one element across the thickness). Such a meshing strategy is commonly used in `EFISPEC3D` to avoid unnecessarily small elements in stiff layers. It is worth noting that during wave propagation, the energy remains mainly in the surface layer due to the significant stiffness difference between the two layers; thus, only one element in the PML-Z thickness is sufficient to obtain good results.

Table 6.5 Two-layered half-space: relative error in displacement over the time interval $[0, 10.0\,\mathrm{s}]$ at receiver A $[200, 0, 0]\,\mathrm{m}$, and receiver B $[200, 0, -10]\,\mathrm{m}$

Model	Point A		Point B	
	u_X	u_Z	u_X	u_Z
$\alpha_{0X} = 0.0$	3.02%	1.71%	13.55%	5.82%
$\alpha_{0X} = 1.0$	3.01%	1.71%	13.51%	5.82%
$\alpha_{0X} = 2.0$	3.01%	1.71%	13.46%	5.82%
$\alpha_{0X} = 3.0$	3.01%	1.71%	13.43%	5.82%
$\alpha_{0X} = 4.0$	3.05%	1.74%	13.42%	5.82%

Based on the previous investigations, the PML was parameterized as follows: $\beta_0 = 140.0$ and $\alpha_{0Z} = \alpha_{0Y} = 4.0$, while α_{0X} was varied from 0.0 to 4.0. The chosen time step size for all the computations is $\Delta t = 0.4\,\mathrm{ms}$. This small value is due to the small mesh-adapting elements in the stiffer layer.

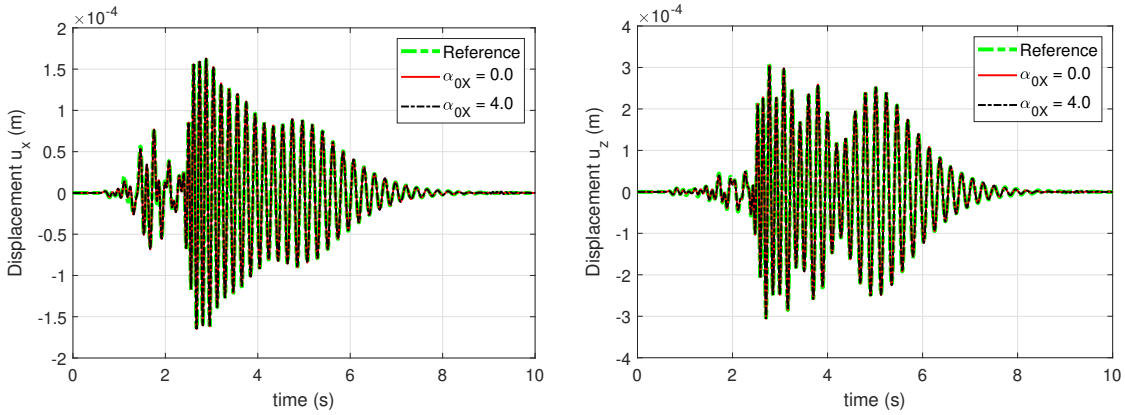

(a) Horizontal displacement u_X. (b) Vertical displacement u_Z.

Figure 6.16 Two-layered half-space: Time history of the displacement at receiver A [200.0; 0.0; 0.0] from the PML models with $\alpha_{0X} = 0.0$ and $\alpha_{0X} = 4.0$.

Figures 6.16 and 6.17 present the displacement time histories at receiver A (free surface, $[200, 0, 0]\,\mathrm{m}$) and receiver B (interface between the two elastic layers, $[200, 0, -10]\,\mathrm{m}$) for $\alpha_{0X} = 0.0$ and $\alpha_{0X} = 4.0$. In both cases, the results agree well with the reference solution. The error norms in displacement at the receivers, summarized in Table 6.5, confirm that varying α_{0X} has little influence on accuracy.

However, the use of $\alpha_{0X} \leq 1.0$ leads to instability, as shown by the kinetic energy evolution in the elastic domain (Figure 6.18). Snapshots of vertical displacement at

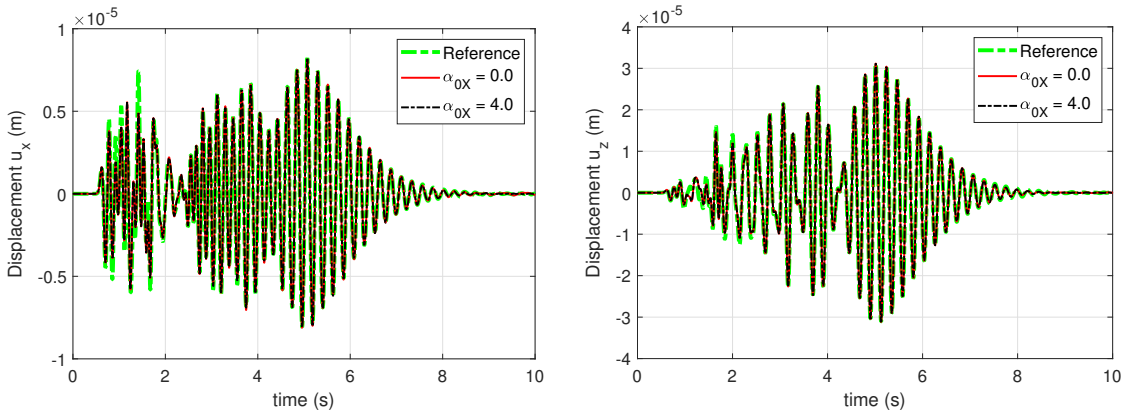

(a) Horizontal displacement u_X. (b) Vertical displacement u_Z.

Figure 6.17 Two-layered half-space: Time history of the displacement at point B [200.0; 0.0; −10.0] from the PML models with $\alpha_{0X} = 0.0$ and $\alpha_{0X} = 4.0$.

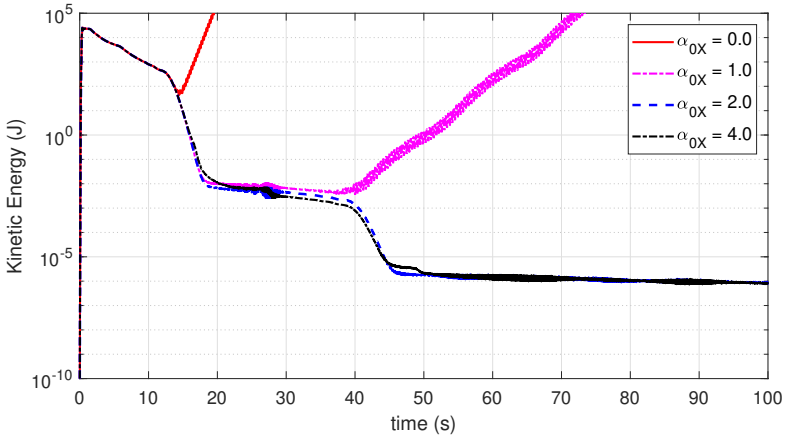

Figure 6.18 Two-layered half-space: Time histories of kinetic energy in the elastic domain from PML models.

$t = 12.0\,\mathrm{s}$ for $\alpha_{0X} = 0.0$ (Figure 6.19) confirm that the instability originates from PML-X. By contrast, setting $\alpha_{0X} \geq 2.0$ delays the onset of instability in long-term simulations.

6.5 Conclusion

This chapter presented an unsplit, non-convolutional, displacement-based Perfectly Matched Layer (PML) within the Spectral Element Method (SEM) to model unbounded domains. We adopted the formulation of Basu [11] together with the standard stretching function of Kucukcoban and Kallivokas [110], and derived the discrete weak form using fourth-order spectral elements ($p = 4$). Owing to its displacement-based structure, the

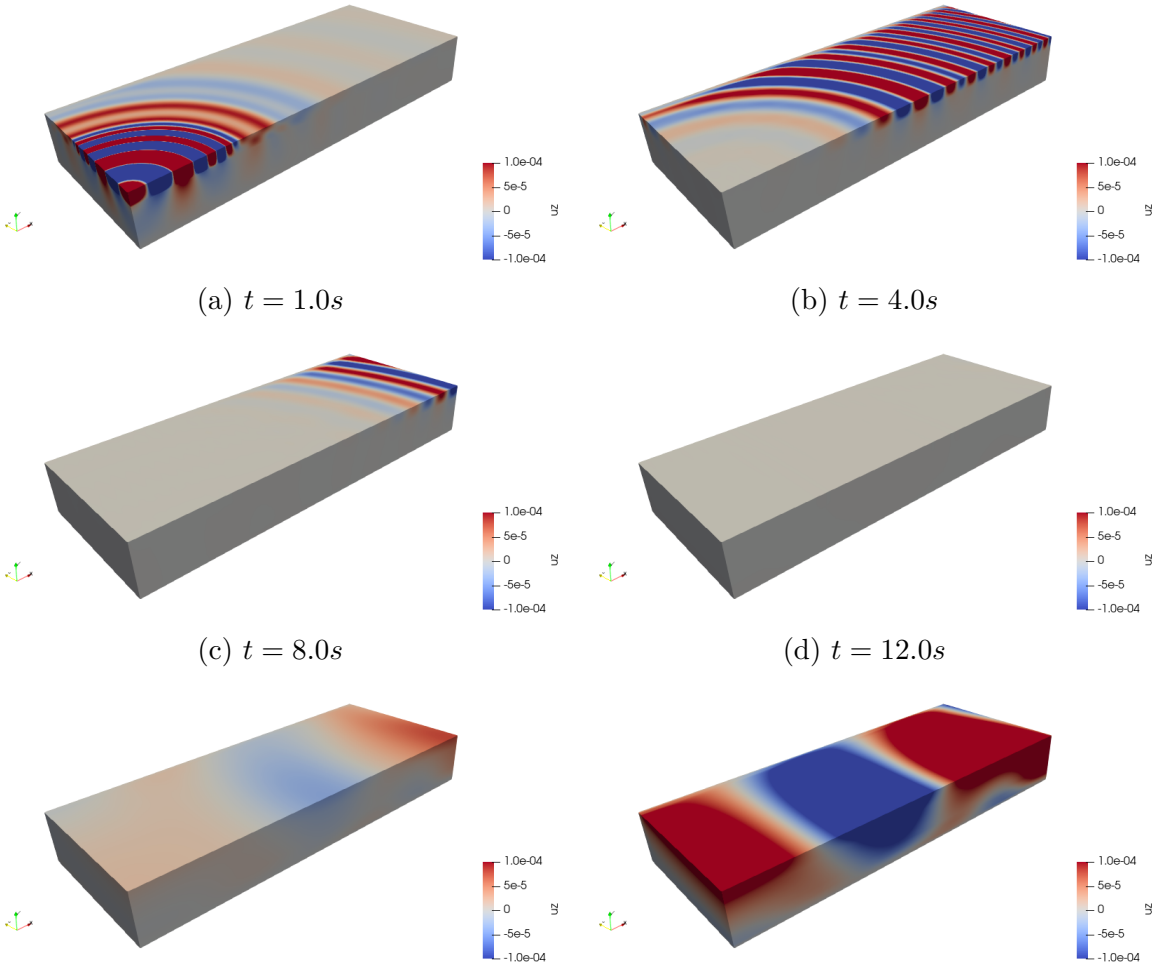

(a) $t = 1.0s$ (b) $t = 4.0s$

(c) $t = 8.0s$ (d) $t = 12.0s$

(e) $t = 18.0s$ (f) $t = 20.0s$

Figure 6.19 Two-layered half-space: Snapshots of vertical displacement obtained from PML model with $\alpha_{0X} = 0.0$.

PML integrates readily into `EFISPEC3D` [120, 64], a massively parallel open-source code for wave propagation.

The accuracy of the PML was assessed by benchmarks against extended-mesh reference solutions. The results show that careful design of the stretching function—particularly the parameter α_{0I}—is required to obtain the best performance. We also examined long-term stability using pseudo-2D and 3D waveguides and a two-layer half-space. In line with prior studies [110, 111, 76], tuning the PML parameters cannot entirely suppress the long-term instability, but it can significantly delay its onset in order to be perfectly suitable for seismology applications or other dynamic situations such as buckling or wrinkling of thin film connected to a 3D substrate.

Chapter 7

Conclusions and Perspectives

This chapter provides a synthesis of the theoretical developments, numerical strategies, and validation studies presented in the thesis, and evaluates them in light of the objectives introduced in Chapter 1. The work has addressed the nonlinear dynamic analysis of thin-shell structures by combining the 7-parameter shell formulation with robust implicit and explicit solvers, mortar coupling, and PML modeling for unbounded media. In the following, we summarize the main results, discuss their scope and limitations, and outline future research directions.

7.1 Summary of the thesis work

7-parameter shell elements. We adopt the displacement-based 7-parameter shell elements of Büchter et al. [48] to model thin-shell structures. The enhanced variational formulation is derived in the reference (undeformed) configuration. It involves six nodal kinematic unknowns, including three components of the mid-surface motion and three components describing the change of the shell directors (vectorial differences) in the global equations, together with a scalar enhanced-assumed-strain variable controlled at the element level by an orthogonality condition to alleviate Poisson thickness locking.

To extend our investigation to material nonlinearity, we adopt the isotropic finite-strain elasto-plastic framework in [147]. We first express the shell formulation in the current (deformed) configuration, which facilitates its incorporation. We then propose a method to account for the EAS field within the nonlinear material framework and make it compatible with the variational shell formulation.

We use the standard mortar method for shell–shell and shell–solid couplings. This complements pre-processing shell-shell connection strategies discussed in [31] and later investigated in [52] under quasi-static setting. The shell-shell mortar coupling is par-

ticularly useful when common shell directors cannot be enforced at the interface (e.g., shell–stiffener connections). As a reference solution for shell elements and coupling strategies, the solid element formulation is developed in parallel. A displacement-based finite element formulation that accounts for linear kinematic constraints (Dirichlet boundary conditions and mortar coupling) by introducing Lagrange multipliers is derived, enabling shell and solid elements to coexist in a monolithic global model.

Implicit solvers. For nonlinear dynamic analysis, we develop two implicit solvers: the Newton–Raphson (NR) and Asymptotic Numerical Method (ANM) solvers. Both solvers employ α-methods (e.g., the Hilber–α method or the Generalized–α method) to damp high-frequency modes, permitting larger time steps. An adaptive time-stepping algorithm is also employed to optimize the workload. The NR solver handles both geometric and material nonlinearities and serves as a reference for the ANM and explicit solvers.

In line with the expertise of *Laboratory LEM3*, we employ ANM to solve geometrically nonlinear dynamic problems with non-conservative pressure loading. The algorithm is derived from homotopy and perturbation techniques, as in [60], for both solid and shell elements at the element level. At the global level, the governing equations are transformed into a sequence of linear systems characterized by the same tangent operator, so only one tangent factorization is needed per time step. Based on the convergence criteria of the solution series, we propose an order-adaptive time-step algorithm that allows to adopt the optimal number of linear systems to be solved.

Explicit solvers. We develop two explicit solvers using the central-difference scheme as an alternative to implicit solvers, especially for highly nonlinear, fast dynamics. Both solvers can account for geometric, material, and kinematic nonlinearities. Although nonlinear kinematic constraints, such as contact conditions, are not discussed in the thesis work, they can be incorporated into the developed explicit solvers. The first solver is the classical monolithic scheme, whereas the second implements a multi-time-step strategy based on the GC approach [78, 43]. The latter is derived in the context of domain decomposition and allows for different time steps depending on subdomains.

When using 7-parameter shell elements in the explicit solvers, two issues arise: the thickness-controlled critical time step and the treatment of the orthogonality condition at the element level. To address the first issue, Selective Mass Scaling [58] (SMS) is adapted for the proposed 7-parameter shells thanks to a controllable parameter. To address the second, we propose an explicit algorithm for the orthogonality condition, similar to that in [132], which preserves the computational efficiency of explicit methods.

We also propose a posteriori checks to verify solution quality, through the tracking of the error related to the orthogonality condition.

Numerical investigations. We conduct three numerical campaigns to validate the developed shell formulation and solvers. The first campaign consists of two academic benchmarks—the three-intersecting plates and the snap-through of a cylindrical roof—and confirms the robustness and accuracy of the developed solvers, as well as the mortar coupling approach and the SMS technique.

The second campaign consists of two dynamic post-buckling branch-switching benchmarks. The ANM and NR solvers are compared in terms of computational efficiency by measuring the number of time steps and the solver workload (number of tangent operators and force-vector evaluations). It is shown that the NR solver can use larger time steps, but this can lead to nonphysical solutions if the maximum time step is not carefully controlled. ANM performs slower time stepping, requires fewer tangent operators but many force-vector evaluations, and turns out to be more computationally expensive. It is due to the excessive weight of the large number of force-vector evaluations in comparison to the weight related to the factorization of the tangent operator. It is expected that this weight could be significantly reduced in other environments than MATLAB. Indeed, it is well known that, in implicit computations, the cost of the construction and factorization of the tangent operator is dominant for large industrial cases (Cochelin et al. [62]). For non-conservative pressure loads, using a symmetrized tangent does not affect NR convergence or accuracy, but significantly degrades ANM accuracy as expected.

The third campaign consists of six benchmarks under impulsive load, severe deformation, and material plasticity. The investigation confirmed the accuracy and robustness of the adopted finite-strain elasto-plasticity framework, the Newton-Raphson implicit solver, and the classical and multi-time step explicit solvers. For the explicit runs of shell models, our proposed 7-parameter shell element algorithm performs very well in terms of accuracy and stability. The proposed post-processing check in terms of energy and error related to the orthogonality condition demonstrates its reliability in ensuring solution accuracy.

Spectral element Perfectly Matched Layers. As a first step towards the soil-structure interaction problem and explicit computational efficiency, we extend the thesis work to study the Perfectly Matched Layers. We adapt the unsplit non-convolutional displacement-based PML formulation proposed in [11] in the framework of the Spectral Element Method and implemented it in `EFISPEC3D` [120, 64], a massively parallel open-

source code for wave propagation problems. The numerical investigation, comprising the homogeneous Lamb's test, waveguides, and a two-layer half-space, demonstrates the very good performance of our PML model in absorbing outgoing waves, even under grazing incidence. We also show that the PML parameters are critical for accuracy and long-term stability.

To conclude, the finite element formulations and solvers for nonlinear dynamics are included in an in-house software developed during the thesis work. This software is ready for academic research and medium-scale engineering applications, and serves as a foundation for high-performance computing codes.

7.2 Perspectives

Building on the results of this thesis, several developments can be pursued to turn the current framework into a more powerful simulation tool for solid mechanics.

Contact mechanics. Incorporating contact is essential to deal with a great variety of applications (e.g., metal forming, biomechanics, fluid–structure interaction with contact). By incorporating contact problems into the mortar coupling, contact problems can be formulated using the Lagrange multiplier method. The dual approach can be considered for computational efficiency. The problem can be solved using the developed explicit solvers, whereas the augmented Lagrange multiplier method must be used with the Newton-Raphson implicit solver.

An ongoing exploratory project focuses on predicting flatness defects during the cold-rolling process, using the MATLAB code developed during the PhD, in collaboration with ArcelorMittal. We aim to study the effect of the dynamic buckling after the roll bite. The frictional-contact algorithm using the Lagrange multiplier method was employed in the roll bite, and the problem was solved using the developed explicit solvers.

High-performance explicit code. Since the current MATLAB code is structured to serve both implicit and explicit solvers, a lean, element-centric explicit code would improve parallel efficiency. This can be done in MATLAB (with MEX for kernels) or in Julia [28]. The 7-parameter shell is compatible with matrix-free implementations using either linear elements (with ANS or $\bar{B}$ to mitigate locking) or spectral elements; for the latter, the impact of polynomial order and Gauss–Lobatto integration can be assessed with the existing code.

High-performance implicit solvers. In the current MATLAB code, the evaluation and factorization of the tangent operator are effectively parallelized, enabling the NR solver to run on multiple processors. However, as noted in the manuscript, the parallel computing for force vector evaluations is less effective. A promising path for ANM is the Schur–Dual domain decomposition, which enables parallel computation of both the tangent operators and the force-vector evaluations.

Soil–structure interaction (SSI). A natural extension of the present framework is the analysis of SSI for thin-walled structures, e.g., storage tanks under seismic conditions. The idea is to couple the shell subsystem (7-parameter formulation) with a 3D soil continuum discretized by spectral elements and truncated by a displacement-based PML. The mortar-coupling approach couples the shell structure to the soil. This approach can also be extended to a contact problem to consider the partial uplift or slide of the shell structure. The dynamic wrinkling problem of thin film bonded to a 3D compliant substrate is also a very interesting future application for the developed numerical tools.

The multi-time-step explicit solver is a promising approach, allowing the use of different time step sizes in the shell structures and the soil. If necessary, the developed multi-time-step explicit solver can be naturally extended to accommodate more than two time steps. One of the main interests of explicit computations lies in their ability to be massively parallelized, as in the seismology simulation code `EFISPEC3D`. Finally, the implicit/explicit multi-time-step strategy can also be employed, in which the shell subdomain is integrated by a large time step with an implicit scheme, whereas the soil subdomain uses an explicit small time step.

Bibliography

[1] (2007). Eurocode 3: Design of steel structures – Part 1-6: Strength and stability of shell structures. EN 1993-1-6:2007 + A1:2017.

[2] ABAQUS (2014). *(2014) Theory Manual, Version 6.14*. Dassaults Systemes Simulia, Inc.

[3] Aggoune, W., Zahrouni, H., and Potier-Ferry, M. (2006). Asymptotic numerical method for unilateral contact. *International Journal for Numerical Methods in Engineering*, 68:605–631.

[4] Ambati, M., Kiendl, J., and Lorenzis, L. D. (2018). Isogemetric Kirchhoff-Love shell formulation for elasto-plasticity. *Computer Methods in Applied Mechanics and Engineering*, 340:320–339.

[5] Armero, F. and Romero, I. (2001a). On the formulation of high-frequency dissipative time-stepping algorithms for nonlinear dynamics. Part i: low-order methods for two model problems and nonlinear elastodynamics. *Computer Methods in Applied Mechanics and Engineering*, 190(20):2603–2649.

[6] Armero, F. and Romero, I. (2001b). On the formulation of high-frequency dissipative time-stepping algorithms for nonlinear dynamics. Part II: second-order methods. *Computer Methods in Applied Mechanics and Engineering*, 190(51):6783–6824.

[7] Assidi, M., Zahrouni, H., Damil, N., and Potier-Ferry, M. (2009). Regularization and perturbation technique to solve plasticity problems. *International Journal of Material Forming*, 2:1–14.

[8] Baguet, S. (2011). *PhD Thesis: Stabilité des structures minces et sensibilité aux imperfections par la Méthode Asymptotique Numérique*.

[9] Baguet, S. and Cochelin, B. (2003). On the behaviour of the ANM continuation in the presence of bifurcation. *Communication in Numerical Methods in Engineering*, 19:459–471.

[10] Basar, Y. and Itskov, M. (1999). Constitutive model and finite element formulation for large strain elasto-plastic analysis of shells. *Computational Mechanics*, 23(5):466–481.

[11] Basu, U. (2009). Explicit finite element perfectly matched layer for transient three-dimensional elastic waves. *International Journal for Numerical Methods in Engineering*, 77:151–176.

[12] Basu, U. and Chopra, A. (2003). Perfectly matched layers for time-harmonic elastodynamics of unbounded domains: theory and finite-element implementation. *Computer Methods in Applied Mechanics and Engineering*, 192:1337–1375.

[13] Basu, U. and Chopra, A. (2004a). Erratum to: Perfectly matched layers for transient elastodynamics of unbounded domains. *International Journal for Numerical Methods in Engineering*, 61:156–157.

[14] Basu, U. and Chopra, A. (2004b). Perfectly matched layers for transient elastodynamics of unbounded domains. *International Journal for Numerical Methods in Engineering*, 59:1039–1074.

[15] Bathe, K. and Dvorkin, E. N. (1985). A four-node plate bending element based on Mindlin/Reissner plate theory and a mixed interpolation. *International Journal for Numerical Methods in Engineering*, 21:367–383.

[16] Belytschko, T., Lin, J. I., and Tsay, C.-S. (1984). Explicit algorithms for the nonlinear dynamics of shell. *Computer Methods in Applied Mechanics and Engineering*, 42:225–251.

[17] Belytschko, T., Liu, W., and Moran, B. (2006). *Nonlinear Finite Elements for Continua and Structures*. Wiley.

[18] Belytschko, T., Stolarski, H., Liu, W., Carpenter, N., and Ong, J. (1985). Stress projection for membrane and shear locking in shell finite elements. *Computer Methods in Applied Mechanics and Engineering*, 51:221–258.

[19] Belytschko, T., Wong, L., and Chiang, H. (1992). Advances in one-point quadrature shell elements. *Computer Methods in Applied Mechanics and Engineering*, 98:93–107.

[20] Benson, D. (2017). Explicit finite element methods for large deformation problems in solid mechanics. *Encyclopedia of Computational Mechanics*, pages 1–43.

[21] Benson, D. J., Bazilevs, Y., Hsu, M. C., and Hughes, T. J. R. (2010). Isogeometric shell analysis: The Reissner-Mindlin Shell. *Computer Methods in Applied Mechanics and Engineering*, 199:276–289.

[22] Bérenger, J. (1994). A perfectly matched layer for the absorption of electromagnetic waves. *Journal of Computational Physics*, 114:185–200.

[23] Bernardi, C., Debit, N., and Maday, Y. (1990). Coupling finite element with spectral methods: first results. *Mathematics of computation*, pages 21–39.

[24] Bernardi, C., Maday, Y., and Patera, A. (1994). A new noncorforming approach to domain decomposition: The mortar element method. *Nonlinear partial differential equations and their applications: Collège de France Seminar*, 299:13–51.

[25] Betsch, P., Gruttmann, F., and Stein, E. (1996). A 4-node finite shell element for the implementation of general hyperelastic 3d-elasticity at finite strain. *Computer Methods in Applied Mechanics and Engineering*, 130:57–79.

[26] Betsch, P. and Janz, A. (2016). An energy–momentum consistent method for transient simulations with mixed finite elements developed in the framework of geometrically exact shells. *International Journal for Numerical Methods in Engineering*, 108:423–455.

[27] Betsch, P. and Sänger, N. (2009). On the use of geometrically exact shells in a conserving framework for flexible multibody dynamics. *Computer Methods in Applied Mechanics and Engineering*, 198:1609–1630.

[28] Bezanson, J., Edelman, A., Karpinski, S., and Shah, V. B. (2017). Julia: A fresh approach to numerical computing. *SIAM review*, 59(1):65–98.

[29] Bischoff, M. and Ramm, E. (1997). Shear deformable shell elements for large strains and rotations. *International Journal for Numerical Methods in Engineering*, 40:4427–4449.

[30] Bischoff, M. and Ramm, E. (2000). On the physical significance of higher order kinematic and static variables in a three-dimensional shell formulation. *International Journal of Solids and Structures*, 37:6933–6960.

[31] Bischoff, M., Wall, W., Bletwinger, K.-U., and Ramm, E. (2004). Models and Finite Elements for Thin-Walled Structures. *Encyclopedia of Computational Mechanics*, 2:59–137.

[32] Bletzinger, K., Bischoff, M., and Ramm, E. (2000). A unified approach for shear-locking-free triangular and rectangular shell finite elements. *Computers and Structures*, 75:321–334.

[33] Bouclier, R., Elguedj, T., and Combescure, A. (2013). Efficient isogeometric NURBS-based solid-shell elements: Mixed formulation and b-bar method. *Computer Methods in Applied Mechanics and Engineering*, 267:86–110.

[34] Bouclier, R., Elguedj, T., and Combescure, A. (2015a). An isogeometric locking-free NURBS-based solid-shell element for geometrically nonlinear analysis. *International Journal for Numerical Methods*, 101:774–808.

[35] Bouclier, R., Elguedj, T., and Combescure, A. (2015b). Development of a mixed displacement-stress formulation for the analysis of elastoplastic structures under small strains: Application to a locking-free, NURBS-based solid-shell element. *Computer Methods in Applied Mechanics and Engineering*, 295:543–561.

[36] Boutmir, S., Braikat, B., Jamal, M., Damil, N., Cochelin, B., and Potier-Ferry, M. (2004). Des solveurs implicites d'ordre supérieur pour les problèmes de dynamique non linéaire des structures. *Revue Européenne des Éléments Finis*, 13:449–460.

[37] Boutyour, E., Zahrouni, H., Potier-Ferry, M., and Boudi, M. (2004). Bifurcation points and bifurcation branches by asymptotic-numerical method and Padé approximants. *International Journal for Numerical Methods in Engineering*, 60:1987–2012.

[38] Brank, B. (2005). Nonlinear shel models with seven kinematic parameters. *Computer Methods in Applied Mechanics and Engineering*, 194:2336–2362.

[39] Brank, B., Briseghella, L., Tonelo, N., and Damjanic, F. B. (1998). On non-linear dynamics of shells: implementation of energy-momentum conserving algorithm for a finite rotation shell model. *International Journal for Numerical Methods in Engineering*, 42:409–442.

[40] Brank, B., Korelc, J., and Ibrahimbegovic, A. (2002). Nonlinear shell problem formulation accounting for through-the-thickness stretching and its finite element implementation. *Computers and Structures*, 80:699–717.

[41] Brank, B., Korelc, J., and Ibrahimbegović, A. (2003). Dynamics and time-stepping schemes for elastic shells undergoing finite rotations. *Computers and Structures*, 81(12):1193–1210. Advanced Computational Models and Techniques in Dynamics.

[42] Braun, M., Bischoff, M., and Ramm, E. (1994). Nonlinear shell formulations for complete three-dimensional constitutive laws including composites and laminates. *Computational Mechanics*, 15:1–18.

[43] Brun, M., Gravouil, A., Combescure, A., and Limam, A. (2015). Two FETI-based heterogeneous time step coupling methods for Newmark and α-schemes derived from the energy method. *Computer Methods in Applied Mechanics and Engineering*, 283:130–176.

[44] Brun, M., Martin, F. D., and Richart, N. (2021). Asynchronous SEM/FEM co-simulation for seismic analysis of concrete gravity dams. *Computers and Structures*, 245:106459.

[45] Brun, M., Zafati, E., Djeran-Maigre, I., and Prunier, F. (2016). Hybrid Asynchronous Perfectly Matched layer for seismic wave propagation in unbounded domains. *Finite Elements in Analysis & Design*, 122:1–15.

[46] Büchter, N. and Ramm, E. (1992a). 3d-extension of nonlinear shell equations based on the enhanced assumed strain concept. *Computational Methods in Applied Sciences*, pages 55–62.

[47] Büchter, N. and Ramm, E. (1992b). Shell theory versus degeneration. *International Journal for Numerical Methods in Engineering*, 34:39–59.

[48] Büchter, N., Ramm, E., and Roehl, D. (1994). Three-dimensional extension of non-linear shell formulation based on the enhanced assumed strain concept. *International Journal for Numerical Methods in Engineering*, 37:2551–2568.

[49] Caseiro, J. F., Valente, R. A. F., Reali, A., Kiendl, J., F.Auricchio, and de Sousa, R. J. A. (2014). On the Assumed Strain Method to alleviate locking in solid-shell NURBS-based finite elements. *Computer Methods in Applied Mechanics and Engineering*, 53(6):1341–1353.

[50] Caseiro, J. F., Valente, R. A. F., Reali, A., Kiendl, J., F.Auricchio, and de Sousa, R. J. A. (2015). Assumed natural strain NURBS-based solid-shell element for the analysis of large deformation elasto-plastic thin-shell structures. *Computer Methods in Applied Mechanics and Engineering*, 284:861–880.

[51] Chau, A.-K., Brun, M., and Elguedj, T. (2023). Hybrid Asynchronous Isogeometric Perfectly Matched Layer for transient elastodynamics. *Computers and Geotechnics*, 158:105387.

[52] Chau, A.-K., Brun, M., Ventura, P., Zahrouni, H., and Potier-Ferry, M. (2024). Non-linear buckling analysis of thin-walled beams modeled with 7-parameter shell elements. *Thin-Walled Structures*, 201:111994.

[53] Chau, A.-K., Brun, M., Ventura, P., Zahrouni, H., and Potier-Ferry, M. (2025a). Asymptotic numerical method for dynamic buckling of shell structures with follower pressure. *International Journal of Solids and Structures*, 308:113135.

[54] Chau, A.-K., Brun, M., Ventura, P., Zahrouni, H., and Potier-Ferry, M. (2025b). Explicit dynamics and buckling simulations with 7-p shell elements and enhanced assumed strain. *Finite Elements in Analysis and Design*, 247:104346.

[55] Chroscielewski, J. and Witkowski, W. (2010). Discrepancies of energy values in dynamics of three intersecting plates. *International Journal for Numerical Methods in Biomedical Engineering*, 26:1188–1202.

[56] Chung, J. and Hulbert, G. M. (1993). A time integration algorithm for structural dynamics with improved numerical dissipation - the generalized-alpha method. *J. Appl. Mech.-Trans*, ASME 60:371–375.

[57] Claude, B., Girault, G., Leblé, B., and Cadou, J.-M. (2023). On the use of high order perturbation method for numerical time integration in structural dynamics. *Comptes Rendus Mécanique*, 351:227–245.

[58] Cocchetti, G., Pagani, M., and Perego, U. (2013). Selective mass scaling and critical time-step estimate for explicit dynamics analyses with solid-shell elements. *Computers and Structures*, 127:39–52.

[59] Cochelin, B. (1994). A path-following technique via an asymptotic-numerical method. *Computers and Structures*, 53:1181–1192.

[60] Cochelin, B. and Compain, C. (2000). An Asymptotic Numerical Method for non-linear transient dynamics. *Revue européenne des éléments finis*, 9:113–128.

[61] Cochelin, B., Damil, N., and Potier-Ferry, M. (1994). Asymptotic-numerical method and Padé approximants for non-linear elastic structures. *International Journal for Numerical Methods in Engineering*, 37:1187–1213.

[62] Cochelin, B., Damil, N., and Potier-Ferry, M. (2007). *Méthode asymptotique numérique*. Hermès-Lavoisier, Paris.

[63] Crisfield, M. (1981). A fast Incremental/Iteration Solution Procedure that Handles 'snap-through'. *Computers and Structures*, 13:55–62.

[64] De Martin, F., Chaljub, E., Thierry, P., Sochala, P., Dupros, F., Maufroy, E., Hadri, B., Benaichouche, A., and Hollender, F. (2021). Influential parameters on 3-d synthetic ground motions in a sedimentary basin derived from global sensitivity analysis. *Geophysical Journal International*, 227(3):1795–1817.

[65] de Sousa, R. A., Cardoso, R., Valente, R., Yoon, J.-W., Gracio, J., and Joge, R. (2005). A new one-point quadrature enhanced assumed strain (eas) solid-shell element with multiple integration points along thickness. *International Journal for Numerical Methods in Engineering*, 62:952–977.

[66] Dornisch, W. and Klinkel, S. (2014). Treatment of Reissner-Mindlin shells with kinks without the need for drilling rotation stabilization in an isogeometric framework. *Computer Methods in Applied Mechanics and Engineering*, 276:35–66.

[67] Dujc, J. . and Brank, B. (2012). Stress resultant plasticity for shells revisited. *Computer Methods in Applied Mechanics and Engineering*, 247:146–165.

[68] Dvorkin, E. and Bathe, K. (1984). Continuum mechanics-based four-node shell element for general nonlinear analysis. *Eng Comput*, 11:77–78.

[69] Echter, R. and Bischoff, M. (2010). Numerical efficiency, locking and unlocking of NURBS finite elements. *Computer Methods in Applied Mechanics and Engineering*, 199:374–382.

[70] Echter, R., Oesterle, B., and Bischoff, M. (2013). A hierarchic family of isogeometric shell finite elements. *Computer Methods in Applied Mechanics and Engineering*, 254:170–180.

[71] Elguedj, T., Jan, Y., Combesure, A., Leblé, B., and Barras, G. (2018). X-FEM analysis of dynamic crack growth under transient loading thick shells. *International Journal of Impact Engineering*, 122:228–250.

[72] Elhage-Hussein, A., Potier-Ferry, M., and Damil, N. (2000). A numerical continuation method based on Padé approximants. *International Journal of Solids and Structures*, 37:6981–7001.

[73] F. Auricchio, R. L. T. (1999). A return-map algorithm for general associative isotropic elasto-plastic materials in large deformation regimes. *International Journal of Plasticity*, 15:1359–1378.

[74] Fathi, A., Poursartip, B., and Kallivokas, L. (2015). Time-domain hybrid formulations for wave simulations in three-dimensional PML-truncated heterogeneous media. *International Journal for Numerical Methods in Engineering*, 101:165–198.

[75] Festa, G. and Vilotte, J. P. (2006). The newmark scheme as velocity-stress time staggering: an efficient pml implementation for spectral element simulations of elastodynamics. *Geophys. J. Int.*, 161:789–812.

[76] François, S., Goh, H., and Kallivokas, L. (2021). Non-convolutional second-order complex-frequency-shifted perfectly matched layers for transient elastic wave propagation. *Computer Methods in Applied Mechanics and Engineering*, 377:113704.

[77] Fu, C., Wang, T., Xu, F., Huo, Y., and Potier-Ferry, M. (2019). A modeling and resolution framework for wrinkling in hyperelastic sheets at finite membrane strain. *Journal of the Mechanics and Physics of Solids*, 124:446–470.

[78] Gravouil, A. and Combescure, A. (2001). A multi-time-step explicit-implicit method for non-linear structural dynamics. *International Journal for Numerical Methods in Engineering*, 50:199–225.

[79] Gruttmann, F., Stein, E., and Wriggers, P. (1989). Theory and numerics of thin elastic shells with finite rotations. *Ing Arch*, 59:54–67.

[80] Guevel, Y., Girault, G., and Cadou, J. (2014). Parametric analysis of steady bifurcations in 2d incompressible viscous flow with high order algorithm. *Computers & Fluids*, 100:185–195.

[81] Guevel, Y., Girault, G., and Cadou, J. (2015). Numerical comparisons of high-order nonlinear solvers for the transient Navier–Stokes equations based on homotopy and perturbation techniques. *Journal of Computational and Applied Mathematics*, 289:356–370.

[82] Guevel, Y., Girault, G., and Cadou, J. (2018). Numerical bifurcation analysis for 3-dimensional sudden expansion fluid dynamic problem. *International Journal for Numerical Methods in Fluids*, 87:1–26.

[83] Hauptmann, R. and Schweizerhof, K. (1998). A systematic development of 'solid-shell' element formulation for linear and nonlinear analyses employing only displacement degrees of freedom. *International Journal for Numerical Methods in Engineering*, 42:49–69.

[84] Hilber, H. M., Hughes, T. J. R., and Taylor, R. L. (1977). Improved numerical dissipation for the time integration algorithms in structural dynamics. *Earthquake Engineering and Structural Dynamics*, 5:283–292.

[85] Hoffmann, M., Tkachuk, A., Bischoff, M., and Oesterle, B. (2023). Finite element technology-based selective mass scaling for explicit dynamic analyses of thin-walled structures using solid element. *COMPDYN 2023*.

[86] Hoffmann, M., Tkachuk, A., Bischoff, M., and Oesterle, B. (2025). Comparaison of Selective Mass Scalling for thin solids. *COMPDYN 2025*.

[87] Hosseino, S., Remmers, J., Verhoosel, C., and de Borst, R. (2013). An isogeometric solid-like shell element for nonliner analysis. *Int. J. Numer. Methods. Eng.*, 95(3):238–256.

[88] Hughes, T. (1987). *The Finite Element Method, Linear Static and Dynamic Finite Element Analysis*. Prentice-Hall.

[89] Hughes, T., Cottrell, J., and Bawilevs, Y. (2005). Isogeometric analysis: CAD, finite elements, NURBS, exact geometry and mesh refinement. *Comput. Methods. Appl. Mech.*, 194:4135–4195.

[90] Hughes, T. and Liu, W. (1981). Nonlinear finite element analysis of shells: Part i Three-dimensional shells. *Comput. Methods. Appl. Mech.*, 26:331–362.

[91] Ibrahimbegovic, A. (1994). Stress resultant geometrically nonlinear shell theory with drilling rotations - Part i: A consistent formulation. *Computer Methods in Applied Mechanics and Engineering*, 118:265–284.

[92] Ibrahimbegovic, A. (1997). Stress resultant geometrically nonlinear shell theory for finite rotations and its finite element implementation. *Applied Mechanics Reviews*, 50:199–226.

[93] Ibrahimbegovic, A. and Frey, F. (1994). Stress resultant geometrically nonlinear shell theory with drilling rotations - Part II: Computational aspects. *Computer Methods in Applied Mechanics and Engineering*, 118:285–308.

[94] Iwicki, P., Tejchman, J., and Chróścielewski, J. (2014). Dynamic FE simulations of buckling process in thin-walled cylindrical metal silos. *Thin-Walled Structures*, 84:344–359.

[95] Jamal, M., Braikat, B., Boutmir, S., Damil, N., and Potier-Ferry, M. (2002). A high order implicit algorithm for solving nonlinear problems. *Computational Mechanics*, 28:375–390.

[96] Kamensky, D., Hsu, M.-C., Schillinger, D., Evans, J. A., Aggarwal, A., Bazilevs, Y., Sacks, M. S., and Hughes, T. J. (2015). An immersogeometric variational framework for fluid–structure interaction: Application to bioprosthetic heart valves. *Computer Methods in Applied Mechanics and Engineering*, 284:1005–1053.

[97] Kiendl, J., Bletzinger, K.-U., Linhard, J., and Wüchner, R. (2009). Isogeometric shell analysis with Kirchhoff-Love elements. *Computer Methods in Applied Mechanics and Engineering*, 198:3902–3914.

[98] Kiendl, J., Hsu, M.-C., Wu, M., and Reali, A. (2015). Isogeometric Kirchhoff-Love shell formulation for general hyperelastic materials. *Computer Methods in Applied Mechanics and Engineering*, 291:280–303.

[99] Kirchhoff, G. (1850). Über das Gleichgewicht und die Bewegung einer elastischen Scheibe. *Journal für die reine und angewandte Mathematik*, 40:51–88.

[100] Klinkel, S., Gruttmann, F., and Wagner, W. (1999). A continuum based three-dimensional shell element for laminated structures. *Computers and Structures*, 71(1):43–62.

[101] Klinkel, S., Gruttmann, F., and Wagner, W. (2006). A robust nonlinear solid shell element based on a mixed variational formulation. *Computer Methods in Applied Mechanics and Engineering*, 195(1-3):179–201.

[102] Kloppel, T., Gee, M. W., and Wall, W. A. (2011). A scaled thickness conditioning for solid- and solid-shell discretizations of thin-walled structures. *Computer Methods in Applied Mechanics and Engineering*, 200:1301–1310.

[103] Kobayashi, T., Mihara, Y., and Fujii, F. (2012). Path-tracing analysis for post-buckling process of elastic cylindrical shells under axial compression. *Thin-Walled Structures*, 61:180–187.

[104] Komatisch, D. and Martin, R. (2007). An unsplit convolutional perfectly matched layer improved at grazing incidence seismic wave equation. *Geophysics*, 72.

[105] Komatisch, D. and Tromp, J. (1999). Introduction to the spectral element method for three-dimensional seismic wave propagation. *Geophys. J. Int.*, 139:806–822.

[106] Komatisch, D. and Tromp, J. (2002). Spectral-element simulations of global seismic wave propagation-i. validation. *Geophys. J. Int.*, 149:390–412.

[107] Komatisch, D. and Tromp, J. (2003). A perfectly matched layer absorbing boundary condition for the second-order seismic wave equation. *Geophys. J. Int.*, 154:146–153.

[108] Koschnick, F., Bischoff, M., Camprubi, N., and Bletzinger, K.-U. (2004). The discrete strain gap method and membrane locking. *Computer Methods in Applied Mechanics and Engineering*, 194:2444–2463.

[109] Kubiak, T. (2007). Criteria of dynamic buckling estimation of thin-walled structures. *Thin-Walled Structures*, 45(10):888–892.

[110] Kucukcoban, S. and Kallivokas, L. F. (2011). Mixed Perfectly-Matched-Layers for direct transient analysis in 2D elastic heterogeneous media. *Computer Methods in Applied Mechanics and Engineering*, 200:57–76.

[111] Kucukcoban, S. and Kallivokas, L. F. (2013). A symmetric hybrid formulation for transient wave simulations in PML-truncated heterogeneous media. *Wave Motion*, 50:57–79.

[112] Kuhl, D. and Crisfield, M. A. (1999). Energy-conserving and decaying algorithms in non-linear structural dynamics. *International Journal for Numerical Methods in Engineering*, 45:569–599.

[113] Kuhl, D. and Ramm, E. (1999). Generalized Energy–Momentum Method for non-linear adaptive shell dynamics. *Computer Methods in Applied Mechanics and Engineering*, 178(3):343–366.

[114] Lavrencic, M. and Brank, B. (2018). Simulation of shell buckling by implicit dynamics and numerically dissipative schemes. *Thin-Walled Structures*, 132:682–699.

[115] Lee, E. H. (1969). Elastic-plastic deformation at finite strains. *Journal of Applied Mechanics*, 36:1–6.

[116] Li, S., Brun, M., Djeran-Maigre, I., and Kuznetsov, S. (2021). Benchmark for three-dimensional explicit asynchronous absorbing layers for ground wave propagation and wave barriers. *Computers and Geotechnics*, 131(2021):103808.

[117] Li, S., Brun, M., Gravouil, A., and Fekak, F.-E. (2023). Explicit/implicit multi-time step simulation of bridge crane under earthquake with frictional contacts and high-frequency rayleigh damping. *Finite Elements in Analysis and Design*, 220:103946.

[118] Liu, N., Hsu, M.-C., Lua, J., and Pham, N. (2022). A large deformation isogeometric continuum shell formulation incorporating finite strain elastoplasticity. *Computational Mechanics*, 70(5):1–12.

[119] Love, A. E. H. (1888). The Small Free Vibrations and Deformation of a Thin Elastic Shell. *Physical Transactions of the Royal Society of Lodon*, 179:491–546.

[120] Martin, F. D. (2011). Verification of a Spectral-Element Method Code for the Southern California Earthquake Center LOH.3 viscoelastic case. *Bulletin od Seismological Society of America*, 101:2855–65.

[121] MATLAB (2022). *version 9.13.0 (R2022b)*. The MathWorks Inc., Natick, Massachusetts.

[122] Mattern, S., Schmied, C., and Schweizerhof, K. (2011). Highly efficient solid-shell finite elements for explicit dynamic analysis using symbolic. *EURODYN 2011*.

[123] Mattern, S., Schmied, C., and Schweizerhof, K. (2015). Highly efficient solid and solid-shell finite elements with mixed strain–displacement assumptions specifically set up for explicit dynamic simulations using symbolic programming. *Computers and Structures*, 154:210–225.

[124] Mindlin, R. D. (1951). Influence of rotatory inertia and shear on flexural motions of isotropic elastic plates. *Journal of Applied Mechanics*, 18:31–38.

[125] Najah, A., Cochelin, B., Damil, N., and Potier-Ferry, M. (1998). A critical review of asymptotic numerical methods. *Archives of Computational Methods in Engineering*, 5:3–22.

[126] Nezamabadi, S., Yvonnet, J., and Zahrouni, H. (2011). Solving hyperelastic material problems by asymptotic numerical method. *Computational Mechanics*, 47:77–92.

[127] Nezamabadi, S., Yvonnet, J., Zahrouni, H., and Potier-Ferry, M. (2010). A multiscale finite element approach for buckling analysis of elastoplastic long fiber composites. *International Journal for Multiscale Computational Engineering*, 8.

[128] Notre, Y. L., Brun, M., Grenat, C., and Gravouil, A. (2025). A new micro HATI second order preserving for transient dynamics. *Advanced Modeling and Simulation in Engineering Sciences*, 12:9.

[129] Oesterle, B., Tkachuk, A., and Bischoff, M. (2023). Finite element technology-based selective mass scaling for shear-deformable structural element formulations. *COMPDYN 2023*.

[130] Olovsson, L., Simonsson, K., and Unosson, M. (2005). Selective mass scaling for explicit finite element analyses. *International Journal for Numerical Methods in Engineering*, 63:1436–1445.

[131] Olovsson, L., Unosson, M., and Simonsson, K. (2004). Selective mass scaling for thin-walled structures modelled with tri-linear solid elements. *Computational Mechanics*, 34:134–136.

[132] Pagani, M., Reese, S., and Perego, U. (2014). Computationally efficient explicit nonlinear analyses using reduced integration-based solid-shell finite elements. *Computer Methods in Applied Mechanics and Engineering*, 268:141–159.

[133] Parish, H. (1991). Investigation of a finite rotation four node assumed strain shell element. *Int Journal Numer Methods Eng*, 31:127–150.

[134] Parish, H. (1995). A continuum-based shell theory for nonlinear applications. *Int Journal Numer Methods Eng*, 38:1855–1883.

[135] Pled, F. and Desceliers, C. (2022). Review and Recent Developments on the Perfectly Matched Layer (PML) Method for the Numerical Modeling and Simulation of Elastic Wave Propagation in Unbounded Domains. *Arch Computat Methods Eng*, 29:471–518.

[136] Popp, A. (2012). *Mortar Methods for Computational Contact Mechanics and General Interface Problems*. PhD thesis, Technische Unversitat Munchen.

[137] Powell, G. and Simons, J. (1981). Improved Iterative Strategy for Nonlinear Structures. *Int Journal Numer Methods Eng*, 17:1455–1467.

[138] Ramm, E. (1981). Strategies for Tracing the Nonlinear Response Near Limit Points. In Wunderlich, W., Stein, E., and Bathe, K. J., editors, *Nonlinear Finite Element Analysis in Structural Mechanics*, pages 63–89. Springer-Verlag, Berlin, Germany.

[139] Ramm, E. and Matzenmiller, A. (1986). Large deformation shell analysis based on the degenerate concept. *Finite Element Method for Plates and Shells*, 60:365 – 393.

[140] Ramm, E. and Wall, W. (2004). Shell structures - a sensitive interrelation between physics and numerics. *International Journal for Numerical Methods in Engineering*, 60:381 – 427.

[141] Reese, S. (2005). On a physically stabilized one point finite element formulation for three-dimensional finite elasto-plasticity. *Computer Methods in Applied Mechanics and Engineering*, 194:4685–4715.

[142] Reissner, E. (1945). The effect of transverse shear deformation on the bending of elastic plates. *ASME Journal of Applied Mechanics*, 12:69–77.

[143] Reissner, E. (1947). On bending of elastic plates. *Quartely of Applied Mathematics*, 5:55–68.

[144] Roehl, D. and Ramm, E. (1996). Large elasto-plastic finite element analysis of solids and shells with the enhanced assumed strain concept. *International Journal of Solids and Structures*, 33:3215–3237.

[145] Sansour, C. and Bufler, H. (1992). Exact finite rotation shell theory, its mixed variational formulation and its finite element implementation. *Int J Numer Methods Eng*, 34:73–115.

[146] Simo, J. (1988). A framework for finite strain elastoplasticity based on maximum plastic dissipation and the multiplicative decomposition. part ii: Computational aspects. *Computer Methods in Applied Mechanics and Engineering*, 68:1–31.

[147] Simo, J. (1992). Algorithms for static and dynamic multiplicative plasticity that preserve the classical return mapping schemes of the infinitesimal theory. *Computer Methods in Applied Mechanics and Engineering*, 99:61–112.

[148] Simo, J. and Fox, D. (1989). On a stress resultant geometrically exact shell model. Part i: Formulation and optimal parametrization. *Computer Methods in Applied Mechanics and Engineering*, 72:267–304.

[149] Simo, J., Fox, D., and Rifai, M. S. (1989). On a stress resultant geometrically exact shell model. Part II: The linear theory, computational aspects. *Computer Methods in Applied Mechanics and Engineering*, 73:53–92.

[150] Simo, J., Fox, D., and Rifai, M. S. (1990). On a stress resultant geometrically exact shell model. Part III: Computational aspects of the nonlinear theory. *Computer Methods in Applied Mechanics and Engineering*, 79:21–70.

[151] Simo, J. and Rifai, M. (1990). A class of mixed assumed strain methods and the method of incompatible modes. *International Journal for Numerical Methods in Engineering*, 29:1595–1638.

[152] Simo, J., Rifai, M. S., and Fox, D. (1992). On a stress resultant geometrically exact shell model. Part VI. Conserving algorithms for nonlinear dynamics. *International Journal for Numerical Methods in Engineering*, 34:117–164.

[153] Simo, J. and Tarnow, N. (1994). A new energy and momentum conserving algorithm for the nonlinear dynamics of shells. *International Journal for Numerical Methods in Engineering*, 37:2527–2549.

[154] Simo, J. and Taylor, R. (1991). Quasi-incompressible finite elasticity in principal stretches: continuum basis and numerical algorithms. *Computer Methods in Applied Mechanics and Engineering*, 85:273–310.

[155] Simo, J. C. and Hughes, T. J. (1998). *Computational inelasticity*. Springer.

[156] Tan, X. and Vu-Quoc, L. (2005). Efficient and accurate multilayer solid-shell element: Nonlinear materials at finite strain. *International Journal for Numerical Methods in Engineering*, 63:2124–2170.

[157] Ventura, P., Azzayani, H., Zahrouni, H., and Potier-Ferry, M. (2023). Buckling of pressurized cylindrical shells using the Asymptotic Numerical Method. *Thin-Walled Structures*, 188:110835.

[158] Vu-Quoc, L. and Tan, X. G. (2001). Geometrically exact sandwich shells: The dynamic case. *Comput. Methods Appl. Mech. Engrg*, 190:2825–2873.

[159] Vu-Quoc, L. and Tan, X. G. (2003a). Optimal solid shells for non-linear analyses of multilayer composites. i. Statics. *Comput. Methods Appl. Mech. Engrg*, 192:1017–1059.

[160] Vu-Quoc, L. and Tan, X. G. (2003b). Optimal solid shells for non-linear analyses of multilayer composites. II. Dynamics. *Comput. Methods Appl. Mech. Engrg*, 192:1017–1059.

[161] Wall, W., Gee, M., and Ramm, E. (2000). The challenge of a three-dimensional shell formulation - the conditioning problem. *Proc. IASS IACM 2000 - Fourth International Colloquium for Shells and Spatial Structures, IASS-IACM, Chania-Crete, Greece*.

[162] Wood, W. L., Bossak, M., and Zienkiewicz, O. C. (1980). An alpha modification of Newmark's method. *International Journal for Numerical Methods in Engineering*, 15:1562–1566.

[163] Xu, J., Hu, H., Liu, Q.-H., and Han, B. (2023). A high-order perfectly matched layer scheme for second-order spectral-element time-domain elastic wave modelling. *International Journal for Numerical Methods in Engineering*, 491:112373.

[164] Yamaki, N. (1984). *Elastic stability of circular cylindrical shells*, volume 27. Elsevier.

[165] Zahrouni, H. (1998). *PhD Thesis: Asymptotic numerical method for shells with large rotations*.

[166] Zahrouni, H., Cochelin, B., and Poiter-Ferry, M. (1999). Computing finite rotations of shells by an asymptotic-numerical method. *Computer Methods in Applied Mechanics and Engineering*, 175:71–85.

[167] Zhang, W., Seylabi, E. E., and Taciroglu, E. (2018). Time-domain pml formulation for modeling viscoelastic waves with rayleigh-type damping in an unbounded domain: Theory and application in abaqus. *Finite Elements in Analysis and Design*, 152:1–16.

[168] Zhang, W., Seylabi, E. E., and Taciroglu, E. (2019). An ABAQUS toolbox for soil-structure interaction analysis. *Computers and Geotechnics*, 114:103143.

[169] Zhang, W. and Taciroglu, E. (2021). A novel rayleigh-type viscoelastic perfectly-matched-layer for wave propagation analysis: Formulation, implementation and application. *Computer Methods in Applied Mechanics and Engineering*, 383:113913.

[170] Zienkiewicz, O. C. and Taylor, R. L. (2006). *The Finite Element Method*. Elsevier.

Appendix A

FINITE ELEMENT DISCRETIZATION FOR PROBLEMS AT FINITE STRAIN

A.1 Three-dimensional elements

A.1.1 Matrix form

For finite element implementation, it is common to introduce the matrix form of the stress, strain, and variation of strain. We define the Voigt notation for the PK2 stress,

$$\mathbf{S} = \Big[S_{11}, \quad S_{22}, \quad S_{33}, \quad S_{12}, \quad S_{23}, \quad S_{13},\Big]^{\mathrm{T}} \tag{A.1}$$

and the Green-Lagrange strain,

$$\mathbf{E} = \Big[E_{11}, \quad E_{22}, \quad E_{33}, \quad 2E_{12}, \quad 2E_{23}, \quad 2E_{13},\Big]^{\mathrm{T}} \tag{A.2}$$

The same notation is applied for any stress-like and strain-like quantities.

A.1.2 Spatial discretization

Let us rewrite the spatial approximation of the initial geometry and the displacement field as presented in Section 2.6 in the isoparametric setting:

$$\begin{aligned} \boldsymbol{X}^h(\boldsymbol{\xi}) &= \sum_m^{n^e} \mathbf{N}^{(m)}(\boldsymbol{\xi})\, \mathbf{X}^{(m)} = \mathbf{N}(\boldsymbol{\xi})\, \mathbf{X} \\ \boldsymbol{u}^h(\boldsymbol{\xi}, t) &= \sum_m^{n^e} \mathbf{N}^{(m)}(\boldsymbol{\xi})\, \mathbf{q}^{(m)} = \mathbf{N}(\boldsymbol{\xi})\, \mathbf{q} \end{aligned} \tag{A.3}$$

In the above equation, $\boldsymbol{\xi} = [\xi_1, \xi_2, \xi_3]^{\mathrm{T}}$ are the element's isoparametric coordinates, $\mathbf{N}^{(m)} = \mathbf{I}\, N^{(m)}$ denotes the nodal shape function matrix of the mth node, where $\mathbf{I}$ is the 3×3 identity matrix, and $\mathbf{N}$ is the element shape function matrix gathering the nodal shape function matrices. Similarly, $(\cdot)^h$ denotes the approximated quantities, $(\cdot)^{(m)}$ are the nodal quantities of the mth node, n^e is the number of nodes belonging to the eth element, $\mathbf{X}^e$ and $\mathbf{q}^e$ are vectors gathering the corresponding nodal quantities of all elements' nodes.

The deformed geometry is then obtained as:

$$\boldsymbol{x}^h(\boldsymbol{\xi}) = \boldsymbol{X}^h(\boldsymbol{\xi}) + \boldsymbol{u}^h(\boldsymbol{\xi}) = \sum_m \mathbf{N}^{(m)}(\boldsymbol{\xi})\, (\mathbf{X}^{(m)} + \mathbf{q}^{(m)}) = \mathbf{N}\left(\mathbf{X}^e + \mathbf{q}^e\right) \tag{A.4}$$

The approximations also apply to variations and time derivatives of the displacement field, which are all interpolated using the same basis.

Concerning the approximation of the Lagrange multipliers, the approximation used for the displacement is employed:

$$\boldsymbol{\lambda}^h(\boldsymbol{\xi}) = \sum_m^{n^e} \mathbf{N}^{(m)}(\boldsymbol{\xi})\, \boldsymbol{\lambda}^{(m)} = \mathbf{N}\, \boldsymbol{\Lambda}^e \tag{A.5}$$

In the following, the above approximations are used to approximate the element contributions $\delta\Pi^e$ to the global weak form as shown in Eq. (6.36), in both reference and current configurations. Indices $(\cdot)^h$ and $(\cdot)^e$ are omitted, and the summation convention is used.

A.1.3 Finite element formulation in the reference configuration

Virtual kinetic energy. The approximation of the element virtual kinetic energy writes:

$$\begin{aligned} \delta\Pi_{\mathrm{kin}} &= \int_\Omega \rho_0\, \delta\boldsymbol{u} \cdot \ddot{\boldsymbol{u}}\, d\Omega \\ &= \int_\Omega \rho_0\, (\mathbf{N}\, \delta\mathbf{q})^{\mathrm{T}}\, (\mathbf{N}\, \ddot{\mathbf{q}})\, d\Omega = (\delta\mathbf{q})^{\mathrm{T}}\, \mathbf{M}\, \ddot{\mathbf{q}} \end{aligned} \tag{A.6}$$

where $\mathbf{M}$ is the element consisitent mass matrix (CMM).

Considering the quadratic 20-node hexahedral elements, the lumped mass matrix is given as:

$$(\hat{\mathbf{M}})_{ij} = \eta\, \delta_{ij}\, (\mathbf{M})_{ij} \tag{A.7}$$

where η is the scaling parameter to ensure the mass conservation of the lumped mass matrix, computed as the ratio of the sum of all components of the CMM (which is equal to 3 times the total mass of the element) to the sum of the main diagonal components of the CMM.

Virtual external work. The approximation of the element external work writes:

$$\begin{aligned}\delta\Pi_{\text{ext}} &= \int_{\Omega} \rho_0 \, \delta\boldsymbol{u} \cdot \boldsymbol{b} \, d\Omega + \int_{\Gamma} \delta\boldsymbol{u} \cdot \boldsymbol{T} \, d\Gamma \\ &= \int_{\Omega} (\mathbf{N}\,\delta\mathbf{q})^{\mathrm{T}} \, \boldsymbol{b} \, d\Omega + \int_{\Gamma} (\mathbf{N}\,\delta\mathbf{q})^{\mathrm{T}} \, \boldsymbol{T} \, d\Gamma = (\delta\mathbf{q})^{\mathrm{T}} \, \mathbf{f}_{\text{ext}}\end{aligned} \tag{A.8}$$

where $\mathbf{f}_{\text{ext}}$ denotes the element external force vector.

Virtual work due to Lagrange multipliers The approximation of the virtual work due to the Lagrange multipliers writes:

$$\delta\Pi_{\text{cons}} = \int_{\Gamma_D} \delta\boldsymbol{u} \cdot \boldsymbol{\lambda} \, d\Gamma = \delta\mathbf{q}^{\mathrm{T}} \left(\int_{\Gamma_D} \mathbf{N}^{\mathrm{T}} \mathbf{N} \, d\Gamma \right) \boldsymbol{\Lambda} = \delta\mathbf{q}^{\mathrm{T}} \, \mathbf{L} \, \boldsymbol{\Lambda} = \delta\mathbf{q}^{\mathrm{T}} \, \mathbf{f}_{\text{cons}} \tag{A.9}$$

Similarly, the discrete weak form of the Dirichlet boundary condition writes:

$$\int_{\Gamma_D} \delta\boldsymbol{\lambda} \cdot \left(\boldsymbol{u} - \hat{\boldsymbol{u}}_D \right) d\Gamma = \delta\boldsymbol{\Lambda}^{\mathrm{T}} \left(\mathbf{L}\,\mathbf{q} - \mathbf{B} \right) = 0 \tag{A.10}$$

with

$$\mathbf{B} = \int_{\Gamma_D} \mathbf{N}^{\mathrm{T}} \, \hat{\boldsymbol{u}}_D \, d\Gamma \tag{A.11}$$

Virtual internal work. Before approximating the element's virtual internal work, let us compute the derivatives of the shape functions with respect to $\boldsymbol{X}$, which can be computed using the chain rule:

$$\frac{\partial N^{(m)}}{\partial \boldsymbol{X}} = \frac{\partial N^{(m)}(\boldsymbol{\xi})}{\partial \boldsymbol{\xi}} \, \frac{\partial \boldsymbol{\xi}}{\partial \boldsymbol{X}} = \frac{\partial N^{(m)}(\boldsymbol{\xi})}{\partial \boldsymbol{\xi}} \, \boldsymbol{J}^{-1} \tag{A.12}$$

where the derivatives and the Jacobian matrix $\boldsymbol{J}$ in the above equation are defined as:

$$\frac{\partial N^{(m)}}{\partial \boldsymbol{\xi}} = \begin{pmatrix} \dfrac{\partial N^{(m)}}{\partial \xi_1} \\ \dfrac{\partial N^{(m)}}{\partial \xi_2} \\ \dfrac{\partial N^{(m)}}{\partial \xi_3} \end{pmatrix}^{\mathrm{T}} \quad ; \quad \frac{\partial N^{(m)}}{\partial \boldsymbol{X}} = \begin{pmatrix} \dfrac{\partial N^{(m)}}{\partial X_1} \\ \dfrac{\partial N^{(m)}}{\partial X_2} \\ \dfrac{\partial N^{(m)}}{\partial X_3} \end{pmatrix}^{\mathrm{T}} \quad ; \quad \boldsymbol{J} = \begin{pmatrix} \dfrac{\partial X_1}{\partial \xi_1} & \dfrac{\partial X_1}{\partial \xi_2} & \dfrac{\partial X_1}{\partial \xi_3} \\ \dfrac{\partial X_2}{\partial \xi_1} & \dfrac{\partial X_2}{\partial \xi_2} & \dfrac{\partial X_2}{\partial \xi_3} \\ \dfrac{\partial X_3}{\partial \xi_1} & \dfrac{\partial X_3}{\partial \xi_2} & \dfrac{\partial X_3}{\partial \xi_3} \end{pmatrix} \tag{A.13}$$

Now, we can write the variation of the Green-Lagrange strain components:

$$\delta \mathbf{E} = \left(\mathbf{B}^{(m)} + \mathbf{B}_{\mathrm{nl}}^{(m)} \right) \delta \mathbf{q}^{(m)} = \left(\mathbf{B} + \mathbf{B}_{\mathrm{nl}} \right) \delta \mathbf{q} = \bar{\mathbf{B}} \, \delta \mathbf{q} \tag{A.14}$$

where $\mathbf{B}$ and $\mathbf{B}_{\mathrm{nl}}$ gathering the corresponding elementary matrices $(\cdot)^{(m)}$ with $m = 1, ..., n^e$:

$$\mathbf{B}^{(m)} = \begin{bmatrix} N_{,X_1}^{(m)} & 0 & 0 \\ 0 & N_{,X_2}^{(m)} & 0 \\ 0 & 0 & N_{,X_3}^{(m)} \\ N_{,X_2}^{(m)} & N_{,X_1}^{(m)} & 0 \\ 0 & N_{,X_3}^{(m)} & N_{,X_2}^{(m)} \\ N_{,X_3}^{(m)} & 0 & N_{,X_1}^{(m)} \end{bmatrix}, \qquad \mathbf{B}_{\mathrm{nl}}^{(m)} = \begin{bmatrix} \boldsymbol{u}_{,X_1}^{\mathrm{T}} \, N_{,X_1}^{(m)} \\ \boldsymbol{u}_{,X_2}^{\mathrm{T}} \, N_{,X_2}^{(m)} \\ \boldsymbol{u}_{,X_3}^{\mathrm{T}} \, N_{,X_3}^{(m)} \\ \boldsymbol{u}_{,X_1}^{\mathrm{T}} \, N_{,X_2}^{(m)} + \boldsymbol{u}_{,X_2}^{\mathrm{T}} \, N_{,X_1}^{(m)} \\ \boldsymbol{u}_{,X_2}^{\mathrm{T}} \, N_{,X_3}^{(m)} + \boldsymbol{u}_{,X_3}^{\mathrm{T}} \, N_{,X_2}^{(m)} \\ \boldsymbol{u}_{,X_1}^{\mathrm{T}} \, N_{,X_3}^{(m)} + \boldsymbol{u}_{,X_3}^{\mathrm{T}} \, N_{,X_1}^{(m)} \end{bmatrix} \tag{A.15}$$

where the notation $(.)_{,X_I} = \dfrac{\partial (.)}{\partial X_I}$ is used. Then, we can rewrite the variational form of the strain energy as:

$$\delta \Pi_{int} = \int_\Omega \delta E_{IJ} \, S_{IJ} \, d\Omega = \int_\Omega \delta \mathbf{E}^{\mathrm{T}} \, \mathbf{S} \, d\Omega = \delta \mathbf{q}^{\mathrm{T}} \int_\Omega \bar{\mathbf{B}}^{\mathrm{T}} \, \mathbf{S} \, d\Omega = \delta \mathbf{q}^{\mathrm{T}} \, \mathbf{f}_{\mathrm{int}} \tag{A.16}$$

Tangent stiffness. The matrix form of the material tangent stiffness is written as:

$$\begin{aligned} \int_\Omega \delta E_{IJ} \, \mathcal{D}_{IJKL} \, \mathrm{d}E_{KL} \, d\Omega &= \int_\Omega \delta \mathbf{E}^T \, \mathbf{D} \, \mathrm{d}\mathbf{E} \, d\Omega \\ &= \int_\Omega (\bar{\mathbf{B}} \, \delta \mathbf{q})^T \mathbf{D} \, (\bar{\mathbf{B}} \, \mathrm{d}\mathbf{q}) \, d\Omega = \delta \mathbf{q}^T \, \mathbf{K}_M \, \mathrm{d}\mathbf{q} \end{aligned} \tag{A.17}$$

where the material moduli matrix $\mathbf{D}$ is given as:

$$\mathbf{D} = \begin{bmatrix} \mathcal{D}_{1111} & \mathcal{D}_{1122} & \mathcal{D}_{1133} & \mathcal{D}_{1112} & \mathcal{D}_{1123} & \mathcal{D}_{1113} \\ \mathcal{D}_{2211} & \mathcal{D}_{2222} & \mathcal{D}_{2233} & \mathcal{D}_{2212} & \mathcal{D}_{2223} & \mathcal{D}_{2213} \\ \mathcal{D}_{3311} & \mathcal{D}_{3322} & \mathcal{D}_{3333} & \mathcal{D}_{3312} & \mathcal{D}_{3323} & \mathcal{D}_{3313} \\ \mathcal{D}_{1211} & \mathcal{D}_{1222} & \mathcal{D}_{1233} & \mathcal{D}_{1212} & \mathcal{D}_{1223} & \mathcal{D}_{1213} \\ \mathcal{D}_{2311} & \mathcal{D}_{2322} & \mathcal{D}_{2333} & \mathcal{D}_{2312} & \mathcal{D}_{2323} & \mathcal{D}_{2313} \\ \mathcal{D}_{1311} & \mathcal{D}_{1322} & \mathcal{D}_{1333} & \mathcal{D}_{1312} & \mathcal{D}_{1323} & \mathcal{D}_{1313} \end{bmatrix} \tag{A.18}$$

The geometric stiffness is given as:

$$\begin{aligned} \int_\Omega \mathrm{d}\delta E_{IJ}\, S_{IJ}\, d\Omega &= \int_\Omega \delta \boldsymbol{u}_{,X_I} \cdot S_{IJ}\, \mathrm{d}\boldsymbol{u}_{,X_J}\, d\Omega \\ &= \int_\Omega (\mathbf{G}\,\delta\mathbf{q})^{\mathrm{T}}\, \mathbf{H}(\mathbf{S})\, (\mathbf{G}\,\mathrm{d}\mathbf{q})\, d\Omega = \delta\mathbf{q}^T\, \mathbf{K}_S\, \mathrm{d}\mathbf{q} \end{aligned} \tag{A.19}$$

where $\mathbf{G}$ is the element matrix gathering the nodal matrix $\mathbf{G}^{(m)}$. The matrices $\mathbf{G}^{(m)}$ and $\mathbf{H}(\mathbf{S})$ are defined as:

$$\mathbf{G}^{(m)} = \begin{bmatrix} \mathbf{I}\, N^{(m)}_{,X_1} \\ \mathbf{I}\, N^{(m)}_{,X_2} \\ \mathbf{I}\, N^{(m)}_{,X_3} \end{bmatrix}, \qquad \mathbf{H}(\mathbf{S}) = \begin{bmatrix} \mathbf{I}\, S_{11} & \mathbf{I}\, S_{12} & \mathbf{I}\, S_{13} \\ \mathbf{I}\, S_{12} & \mathbf{I}\, S_{22} & \mathbf{I}\, S_{23} \\ \mathbf{I}\, S_{13} & \mathbf{I}\, S_{23} & \mathbf{I}\, S_{33} \end{bmatrix} \tag{A.20}$$

Thus, the tangent stiffness matrix writes:

$$\mathbf{K}_T = \mathbf{K}_M + \mathbf{K}_S \tag{A.21}$$

A.1.4 Finite element formulation in the current configuration

Virtual internal work. Before approximating the element's virtual internal work, let us compute the derivatives of the shape functions associated with the mth node with respect to $\boldsymbol{x}$, which can be computed using the chain rule:

$$\frac{\partial N^{(m)}}{\partial \boldsymbol{x}} = \frac{\partial N^{(m)}(\boldsymbol{\xi})}{\partial \boldsymbol{\xi}}\, \frac{\partial \boldsymbol{\xi}}{\partial \boldsymbol{x}} = \frac{\partial N^{(m)}(\boldsymbol{\xi})}{\partial \boldsymbol{\xi}}\, \boldsymbol{J}_x^{-1} \tag{A.22}$$

where the derivatives and the Jacobian matrix $\boldsymbol{J}$ in the above equation are defined as:

$$\frac{\partial N^{(m)}}{\partial \boldsymbol{\xi}} = \begin{pmatrix} \dfrac{\partial N^{(m)}}{\partial \xi_1} \\ \dfrac{\partial N^{(m)}}{\partial \xi_2} \\ \dfrac{\partial N^{(m)}}{\partial \xi_3} \end{pmatrix}^{\mathrm{T}} \quad ; \quad \frac{\partial N^{(m)}}{\partial \boldsymbol{x}} = \begin{pmatrix} \dfrac{\partial N^{(m)}}{\partial x_1} \\ \dfrac{\partial N^{(m)}}{\partial x_2} \\ \dfrac{\partial N^{(m)}}{\partial x_3} \end{pmatrix}^{\mathrm{T}} \quad ; \quad \boldsymbol{J}_x = \begin{pmatrix} \dfrac{\partial x_1}{\partial \xi_1} & \dfrac{\partial x_1}{\partial \xi_2} & \dfrac{\partial x_1}{\partial \xi_3} \\ \dfrac{\partial x_2}{\partial \xi_1} & \dfrac{\partial x_2}{\partial \xi_2} & \dfrac{\partial x_2}{\partial \xi_3} \\ \dfrac{\partial x_3}{\partial \xi_1} & \dfrac{\partial x_3}{\partial \xi_2} & \dfrac{\partial x_3}{\partial \xi_3} \end{pmatrix} \tag{A.23}$$

Now, we can write the variation of the engineering strain components:

$$\delta\boldsymbol{\epsilon} = \bar{\mathbf{B}}^{(m)}\, \delta\mathbf{q}^{(m)} = \bar{\mathbf{B}}\, \delta\mathbf{q} \tag{A.24}$$

with

$$\bar{\mathbf{B}}^{(m)} = \begin{bmatrix} N^{(m)}_{,x_1} & 0 & 0 \\ 0 & N^{(m)}_{,x_2} & 0 \\ 0 & 0 & N^{(m)}_{,x_3} \\ N^{(m)}_{,x_2} & N^{(m)}_{,x_1} & 0 \\ 0 & N^{(m)}_{,x_3} & N^{(m)}_{,x_2} \\ N^{(m)}_{,x_3} & 0 & N^{(m)}_{,x_1} \end{bmatrix} \tag{A.25}$$

where the notation $(.)_{,x_I} = \dfrac{\partial(.)}{\partial x_I}$ is used. Then, we can rewrite the variational form of the strain energy as:

$$\begin{aligned} \delta\Pi_{int} &= \int_\omega \delta\boldsymbol{\epsilon}^{\mathrm{T}}\, \boldsymbol{\sigma}\, d\omega = \delta\mathbf{q}^{\mathrm{T}} \int_\omega \bar{\mathbf{B}}^{\mathrm{T}}\, \boldsymbol{\sigma}\, d\omega \\ &= \int_\Omega \delta\boldsymbol{\epsilon}^{\mathrm{T}}\, \boldsymbol{\tau}\, d\Omega = \delta\mathbf{q}^{\mathrm{T}} \int_\Omega \bar{\mathbf{B}}^{\mathrm{T}}\, \boldsymbol{\tau}\, d\Omega \\ &= \delta\mathbf{q}^{\mathrm{T}}\, \mathbf{f}_{\mathrm{int}} \end{aligned} \tag{A.26}$$

Tangent operators. The matrix form of the material tangent operator is given as:

$$\begin{aligned} \int_\Omega \delta\epsilon_{IJ}\, \mathcal{C}_{IJKL}\, \mathrm{d}\epsilon_{KL}\, d\Omega &= \int_\Omega \delta\boldsymbol{\epsilon}^T\, \mathbf{C}\, \mathrm{d}\boldsymbol{\epsilon}\, d\Omega \\ &= \int_\Omega (\bar{\mathbf{B}}\, \delta\mathbf{q})^T \mathbf{C}\, (\bar{\mathbf{B}}\, \mathrm{d}\mathbf{q})\, d\Omega = \delta\mathbf{q}^T\, \mathbf{K}_M\, \mathrm{d}\mathbf{q} \end{aligned} \tag{A.27}$$

where matrix $\mathbf{C}$ is organized in the same manner as matrix $\mathbf{D}$ in Eq. (A.18).

The geometric stiffness is given as:

$$\begin{aligned}\int_\Omega \mathrm{d}\delta\epsilon_{IJ}\,\sigma_{IJ}\,d\omega &= \int_\omega \delta\boldsymbol{u}_{,x_I}\cdot\sigma_{IJ}\,\mathrm{d}\boldsymbol{u}_{,x_J}\,d\omega = \int_\omega (\mathbf{G}_x\,\delta\mathbf{q})^{\mathrm{T}}\,\mathbf{H}(\boldsymbol{\sigma})\,(\mathbf{G}_x\,\mathrm{d}\mathbf{q})\,d\omega \\ &= \int_\Omega \delta\boldsymbol{u}_{,x_I}\cdot\tau_{IJ}\,\mathrm{d}\boldsymbol{u}_{,x_J}\,d\Omega = \int_\Omega (\mathbf{G}_x\,\delta\mathbf{q})^{\mathrm{T}}\,\mathbf{H}(\boldsymbol{\tau})\,(\mathbf{G}_x\,\mathrm{d}\mathbf{q})\,d\Omega \\ &= \delta\mathbf{q}^T\,\mathbf{K}_S\,\mathrm{d}\mathbf{q}\end{aligned} \tag{A.28}$$

where $\mathbf{G}_x$ is the element matrix gathering the nodal matrix $\mathbf{G}_x^{(m)}$. The matrices $\mathbf{G}_x^{(m)}$ and $\mathbf{H}((\cdot))$ are defined as:

$$\mathbf{G}_x^{(m)} = \begin{bmatrix}\mathbf{I}\,N^{(m)}_{,x_1}\\ \mathbf{I}\,N^{(m)}_{,x_2}\\ \mathbf{I}\,N^{(m)}_{,x_3}\end{bmatrix}, \qquad \mathbf{H}((\cdot)) = \begin{bmatrix}\mathbf{I}\,(\cdot)_{11} & \mathbf{I}\,(\cdot)_{12} & \mathbf{I}\,(\cdot)_{13}\\ \mathbf{I}\,(\cdot)_{12} & \mathbf{I}\,(\cdot)_{22} & \mathbf{I}\,(\cdot)_{23}\\ \mathbf{I}\,(\cdot)_{13} & \mathbf{I}\,(\cdot)_{23} & \mathbf{I}\,(\cdot)_{33}\end{bmatrix} \tag{A.29}$$

Thus, the tangent stiffness matrix writes:

$$\mathbf{K}_T = \mathbf{K}_M + \mathbf{K}_S \tag{A.30}$$

A.2 7-parameter shell formulation

A.2.1 Matrix form

For finite element implementation, it is common to introduce the matrix form of the stress, strain, and variation of strain. We define the Voigt notation for the PK2 stress tensor as follows:

$$\mathbf{S} = \begin{bmatrix}S^{11}, & S^{22}, & S^{33}, & S^{12}, & S^{23}, & S^{13}\end{bmatrix}^{\mathrm{T}} \tag{A.31}$$

and the Green-Lagrange strain,

$$\mathbf{E} = \begin{bmatrix}E_{11}, & E_{22}, & E_{33}, & 2E_{12}, & 2E_{23}, & 2E_{13},\end{bmatrix}^{\mathrm{T}} \tag{A.32}$$

The same notation is applied for any stress-like and strain-like quantities.

A.2.2 Spatial discretization

Considering a shell element, the spatial approximation of the initial geometry and the displacement field, as presented in Section 3.1, in the isoparametric setting is given as:

$$\begin{aligned} \boldsymbol{X}^h(\boldsymbol{\theta}) &= \sum_m^{n^e} \mathbf{N}^{(m)}(\theta^1,\theta^2)\,\mathbf{R}^{(m)} + \theta^3 \mathbf{N}^{(m)}(\theta^1,\theta^2)\,\mathbf{A}_3^{(m)} \;= \mathbf{N}(\boldsymbol{\theta})\,\mathbf{X}^e \\ \boldsymbol{u}^h(\boldsymbol{\theta}) &= \sum_m^{n^e} \mathbf{N}^{(m)}(\theta^1,\theta^2)\,\mathbf{v}^{(m)} + \theta^3 \mathbf{N}^{(m)}(\theta^1,\theta^2)\,\mathbf{w}^{(m)} \;= \mathbf{N}(\boldsymbol{\theta})\,\mathbf{q}^e \end{aligned} \tag{A.33}$$

In the above equation, $\boldsymbol{\theta} = [\theta^1, \theta^2, \theta^3]^{\mathrm{T}}$ are the element's curvilinear coordinates, $\mathbf{N}^{(m)} = \mathbf{I}\, N^{(m)}$ denotes the nodal shape function matrix of the mth node, where $\mathbf{I}$ is the 3×3 identity matrix, and $\mathbf{N}$ is the element shape function matrix gathering the nodal shape function matrices. Similarly, $(\cdot)^h$ denotes the approximated quantities, $(\cdot)^{(m)}$ are the nodal quantities of the mth node, n^e is the number of nodes belonging to the eth element, $\mathbf{X}^e$ and $\mathbf{q}^e$ are vectors gathering the corresponding nodal quantities of the element.

The deformed geometry is then obtained as:

$$\boldsymbol{x}^h(\boldsymbol{\theta}) = \boldsymbol{X}^h(\boldsymbol{\theta}) + \boldsymbol{u}^h(\boldsymbol{\xi}) = \mathbf{N}\left(\mathbf{X}^e + \mathbf{q}^e\right) \tag{A.34}$$

The approximations also apply to variations and time derivatives of the displacement field, which are all interpolated using the same basis.

Concerning the EAS field, let us rewrite the bilinear approximation of the field within an element as follows:

$$\begin{aligned} \tilde{E}_{33} &= \theta^3\, \tilde{\beta}_{33} \\ &= \theta^3 \begin{bmatrix} 1 & \theta^1 & \theta^2 & \theta^1\theta^2 \end{bmatrix} \begin{bmatrix} \alpha_1 & \alpha_2 & \alpha_3 & \alpha_4 \end{bmatrix}^T \\ &= \mathbf{B}_\alpha\, \boldsymbol{\alpha} \end{aligned} \tag{A.35}$$

In the following, the above approximations are used to approximate the element contributions $\delta\Pi^e$ to the global weak form as shown in Eq. (6.36), in both reference and current configurations. Indices $(\cdot)^h$ and $(\cdot)^e$ are omitted, and the summation convention is used.

A.2.3 Finite element formulation in the reference configuration

Virtual kinetic energy. The approximation of the element virtual kinetic energy writes:

$$\delta\Pi_{\text{kin}} = \int_\Omega \rho_0\, \delta\boldsymbol{u}\cdot\ddot{\boldsymbol{u}}\; d\Omega = \int_\Omega \rho_0\, (\mathbf{N}\,\delta\mathbf{q})^{\mathrm{T}}\,(\mathbf{N}\,\ddot{\mathbf{q}})\; d\Omega = (\delta\mathbf{q})^{\mathrm{T}}\,\mathbf{M}\,\ddot{\mathbf{q}} \tag{A.36}$$

where $\mathbf{M}$ is the element consistent mass matrix (CMM). We can also express the CMM in terms of the mass associated with the mid-plane motion $\mathbf{M}_{\mathbf{v}}$ and the one associated with the change of the shell director $\mathbf{M}_{\mathbf{w}}$ as follows:

$$\begin{aligned}\delta\Pi_{\text{kin}} &= \int_\Omega \rho_0\, (\mathbf{N}^{(m)}\,\delta\mathbf{v}^{(m)} + \theta^3\mathbf{N}^{(m)}\,\delta\mathbf{w}^{(m)})^{\mathrm{T}}\,(\mathbf{N}^{(n)}\,\mathbf{v}^{(n)} + \theta^3\mathbf{N}^{(n)}\,\mathbf{w}^{(n)})\; d\Omega \\ &= \delta\mathbf{v}^{(m)}\,\mathbf{M}_{\mathbf{v}}^{(mn)}\,\ddot{\mathbf{v}}^{(n)} + \delta\mathbf{w}^{(m)}\,\mathbf{M}_{\mathbf{w}}^{(mn)}\,\ddot{\mathbf{w}}^{(n)}\end{aligned} \tag{A.37}$$

In the above equation, the following integral vanishes:

$$\int_\Omega \theta^3\,\mathbf{N}^{(m),\mathrm{T}}\,\mathbf{N}^{(n)}\; d\Omega = \mathbf{0} \tag{A.38}$$

Considering the quadratic 8-node quadrilateral element, the lumped mass matrix $\hat{\mathbf{M}}$ is obtained in the same manner as done in Eq. (A.7).

Virtual internal work. Let us first approximate the local covariant base vectors as follows

$$\begin{pmatrix}\boldsymbol{G}_1\\ \boldsymbol{G}_2\\ \boldsymbol{G}_3\end{pmatrix} = \mathbf{G}^{(m)}\,\mathbf{X}^{(m)} = \mathbf{G}\,\mathbf{X} \tag{A.39}$$

with

$$\mathbf{G}^{(m)} = \begin{bmatrix} N^{(m)}_{,\theta^1} & 0 & 0 & \theta^3 N^{(m)}_{,\theta^1} & 0 & 0 \\ 0 & N^{(m)}_{,\theta^1} & 0 & 0 & \theta^3 N^{(m)}_{,\theta^1} & 0 \\ 0 & 0 & N^{(m)}_{,\theta^1} & 0 & 0 & \theta^3 N^{(m)}_{,\theta^1} \\ N^{(m)}_{,\theta^2} & 0 & 0 & \theta^3 N^{(m)}_{,\theta^2} & 0 & 0 \\ 0 & N^{(m)}_{,\theta^2} & 0 & 0 & \theta^3 N^{(m)}_{,\theta^2} & 0 \\ 0 & 0 & N^{(m)}_{,\theta^2} & 0 & 0 & \theta^3 N^{(m)}_{,\theta^2} \\ 0 & 0 & 0 & N^{(m)} & 0 & 0 \\ 0 & 0 & 0 & 0 & N^{(m)} & 0 \\ 0 & 0 & 0 & 0 & 0 & N^{(m)} \end{bmatrix} \tag{A.40}$$

where the notation $(.)_{,\theta^i} = \dfrac{\partial(.)}{\partial\theta^i}$ is used. Similarly, we can use matrix $\mathbf{G}$ to compute the derivatives of displacement $\boldsymbol{u}$ with respect to $(\theta^1, \theta^2, \theta^3)$ as follows:

$$\begin{pmatrix} \boldsymbol{u}_{,\theta^1} \\ \boldsymbol{u}_{,\theta^2} \\ \boldsymbol{u}_{,\theta^3} \end{pmatrix} = \mathbf{G}^{(m)}\,\mathbf{q}^{(m)} = \mathbf{G}\,\mathbf{q} \tag{A.41}$$

We introduce the matrices $\mathbf{R}$ and $\mathbf{A}(\mathbf{q})$ given as:

$$\mathbf{R} = \begin{bmatrix} \boldsymbol{G}_1^{\mathrm{T}} & \mathbf{0} & \mathbf{0} \\ \mathbf{0} & \boldsymbol{G}_2^{\mathrm{T}} & \mathbf{0} \\ \mathbf{0} & \mathbf{0} & \boldsymbol{G}_3^{\mathrm{T}} \\ \boldsymbol{G}_2^{\mathrm{T}} & \boldsymbol{G}_1^{\mathrm{T}} & \mathbf{0} \\ \mathbf{0} & \boldsymbol{G}_3^{\mathrm{T}} & \boldsymbol{G}_2^{\mathrm{T}} \\ \boldsymbol{G}_3^{\mathrm{T}} & \mathbf{0} & \boldsymbol{G}_1^{\mathrm{T}} \end{bmatrix}, \qquad \mathbf{A}(\mathbf{q}) = \begin{bmatrix} \boldsymbol{u}_{,\theta^1}^{\mathrm{T}} & \mathbf{0} & \mathbf{0} \\ \mathbf{0} & \boldsymbol{u}_{,\theta^2}^{\mathrm{T}} & \mathbf{0} \\ \mathbf{0} & \mathbf{0} & \boldsymbol{u}_{,\theta^3}^{\mathrm{T}} \\ \boldsymbol{u}_{,\theta^2}^{\mathrm{T}} & \boldsymbol{u}_{,\theta^1}^{\mathrm{T}} & \mathbf{0} \\ \mathbf{0} & \boldsymbol{u}_{,\theta^3}^{\mathrm{T}} & \boldsymbol{u}_{,\theta^2}^{\mathrm{T}} \\ \boldsymbol{u}_{,\theta^3}^{\mathrm{T}} & \mathbf{0} & \boldsymbol{u}_{,\theta^1}^{\mathrm{T}} \end{bmatrix} \tag{A.42}$$

Using the above matrices, the approximation of the Green-Lagrange strain components from Eq. (3.11) writes:

$$\mathbf{E} = \left(\mathbf{R} + \frac{1}{2}\mathbf{A}(\mathbf{q})\right)\mathbf{G}\,\mathbf{q} = \left(\mathbf{B}^l + \frac{1}{2}\mathbf{B}^{nl}(\mathbf{q})\right)\mathbf{q} \tag{A.43}$$

The variation of the Green-Lagrange strain components in Eq. (3.30) writes:

$$\delta\mathbf{E} = \left(\mathbf{R} + \mathbf{A}(\mathbf{q})\right)\mathbf{G}\,\delta\mathbf{q} = \left(\mathbf{B}^l + \mathbf{B}^{nl}(\mathbf{q})\right)\delta\mathbf{q} = \bar{\mathbf{B}}(\mathbf{q})\,\delta\mathbf{q} \tag{A.44}$$

Then, the discrete form of the virtual internal work writes:

$$\delta\Pi_{int} = \int_\Omega \delta\mathbf{E}^{\mathrm{T}}\,\mathbf{S}\,d\Omega = \delta\mathbf{q}^{\mathrm{T}}\int_\Omega \bar{\mathbf{B}}^{\mathrm{T}}\,\mathbf{S}\,d\Omega = \delta\mathbf{q}^{\mathrm{T}}\,\mathbf{f}_{\mathrm{int}} \tag{A.45}$$

followed by the orthogonality condition:

$$\delta\Pi_{EAS} = \delta\boldsymbol{\alpha}^{\mathrm{T}}\int_{\Omega^e}\mathbf{B}_\alpha^{\mathrm{T}}\,S^{33}(\boldsymbol{u}, \tilde{\beta}_{33})\,d\Omega = \delta\boldsymbol{\alpha}^{\mathrm{T}}\,\mathbf{R}_\alpha = 0 \tag{A.46}$$

Tangent stiffness. Let us rewrite the continuous weak form of the linearized internal virtual work in Eq. (3.38):

$$\mathrm{d}\delta\Pi_{\mathrm{int}} = \int_\Omega \delta E_{ij}\,\mathcal{D}^{ijkl}\,\mathrm{d}E_{kl}\,d\Omega + \int_\Omega \mathrm{d}\delta E_{ij}\,S^{ij}\,d\Omega + \int_\Omega \delta E_{ij}\,\mathcal{D}^{ij33}\,\theta^3\mathrm{d}\tilde{\beta}_{33}\,d\Omega \tag{A.47}$$

followed by linearization of the orthogonality condition:

$$\mathrm{d}\delta\Pi_{\mathrm{EAS}} = \int_\Omega \delta\tilde{\beta}_{33}\theta^3\,\mathcal{D}^{33kl}\,\mathrm{d}E_{kl}\,d\Omega + \int_\Omega \delta\tilde{\beta}_{33}\theta^3\,\mathcal{D}^{3333}\,\theta^3\mathrm{d}\tilde{\beta}_{33}\,d\Omega = 0 \tag{A.48}$$

The matrix form of the material tangent stiffness is written as:

$$\begin{aligned}\int_\Omega \delta E_{ij}\,\mathcal{D}^{ijkl}\,\mathrm{d}E_{kl}\,d\Omega &= \int_\Omega \delta\mathbf{E}^T\,\mathbf{D}\,\mathrm{d}\mathbf{E}\,d\Omega \\ &= \int_\Omega (\bar{\mathbf{B}}\,\delta\mathbf{q})^T\mathbf{D}\,(\bar{\mathbf{B}}\,\mathrm{d}\mathbf{q})\,d\Omega = \delta\mathbf{q}^T\,\mathbf{K}_M\,\mathrm{d}\mathbf{q}\end{aligned} \tag{A.49}$$

where the material moduli matrix $\mathbf{D}$ is given as:

$$\mathbf{D} = \begin{bmatrix} \mathcal{D}^{1111} & \mathcal{D}^{1122} & \mathcal{D}^{1133} & \mathcal{D}^{1112} & \mathcal{D}^{1123} & \mathcal{D}^{1113} \\ \mathcal{D}^{2211} & \mathcal{D}^{2222} & \mathcal{D}^{2233} & \mathcal{D}^{2212} & \mathcal{D}^{2223} & \mathcal{D}^{2213} \\ \mathcal{D}^{3311} & \mathcal{D}^{3322} & \mathcal{D}^{3333} & \mathcal{D}^{3312} & \mathcal{D}^{3323} & \mathcal{D}^{3313} \\ \mathcal{D}^{1211} & \mathcal{D}^{1222} & \mathcal{D}^{1233} & \mathcal{D}^{1212} & \mathcal{D}^{1223} & \mathcal{D}^{1213} \\ \mathcal{D}^{2311} & \mathcal{D}^{2322} & \mathcal{D}^{2333} & \mathcal{D}^{2312} & \mathcal{D}^{2323} & \mathcal{D}^{2313} \\ \mathcal{D}^{1311} & \mathcal{D}^{1322} & \mathcal{D}^{1333} & \mathcal{D}^{1312} & \mathcal{D}^{1323} & \mathcal{D}^{1313} \end{bmatrix} \tag{A.50}$$

It is worth noting that the components of the matrix $\mathbf{D}$ in the above equation are defined in the local curvilinear coordinates of the shell surface, which are different from those in Eq. (A.18) expressed in the global Cartesian coordinates. In case that the components obtained from the material library are provided in Cartesian coordinates, they can be converted to curvilinear coordinates as follows:

$$\mathbf{D}_{\mathrm{curvi}} = \mathbf{T}^{-1}\,\mathbf{D}_{\mathrm{Cartesian}}\,\mathbf{T}^{-\mathrm{T}} \tag{A.51}$$

where $\mathbf{T}$ is defined as:

$$\mathbf{T} = \begin{bmatrix} J_{11}^2 & J_{12}^2 & J_{13}^2 & 2J_{11}J_{12} & 2J_{12}J_{13} & 2J_{11}J_{13} \\ J_{21}^2 & J_{22}^2 & J_{23}^2 & 2J_{21}J_{22} & 2J_{22}J_{23} & 2J_{21}J_{23} \\ J_{31}^2 & J_{32}^2 & J_{33}^2 & 2J_{31}J_{32} & 2J_{32}J_{33} & 2J_{31}J_{33} \\ J_{11}J_{21} & J_{12}J_{22} & J_{13}J_{23} & J_{11}J_{22}+J_{12}J_{21} & J_{12}J_{23}+J_{13}J_{22} & J_{11}J_{23}+J_{13}J_{21} \\ J_{21}J_{31} & J_{22}J_{32} & J_{23}J_{33} & J_{21}J_{32}+J_{22}J_{31} & J_{22}J_{33}+J_{23}J_{32} & J_{21}J_{33}+J_{23}J_{31} \\ J_{11}J_{31} & J_{12}J_{32} & J_{13}J_{33} & J_{11}J_{32}+J_{12}J_{31} & J_{12}J_{33}+J_{13}J_{32} & J_{11}J_{33}+J_{13}J_{31} \end{bmatrix} \tag{A.52}$$

with:

$$J_{Kl} = \frac{\partial X_K}{\partial \theta^l} \tag{A.53}$$

The geometric stiffness is given as:

$$\begin{aligned}\int_\Omega \mathrm{d}\delta E_{ij}\, S^{ij}\, d\Omega &= \int_\Omega \delta \boldsymbol{u}_{,\theta^i} \cdot S^{ij}\, \mathrm{d}\boldsymbol{u}_{,\theta^j}\, d\Omega \\ &= \int_\Omega (\mathbf{G}\,\delta\mathbf{q})^{\mathrm{T}}\, \mathbf{H}(\boldsymbol{S})\, (\mathbf{G}\,\mathrm{d}\mathbf{q})\, d\Omega = \delta\mathbf{q}^T\, \mathbf{K}_S\, \mathrm{d}\mathbf{q}\end{aligned} \tag{A.54}$$

where the matrix $\mathbf{H}(\mathbf{S})$ is defined as:

$$\mathbf{H}(\boldsymbol{S}) = \begin{bmatrix} \mathbf{I}\, S^{11} & \mathbf{I}\, S^{12} & \mathbf{I}\, S^{13} \\ \mathbf{I}\, S^{12} & \mathbf{I}\, S^{22} & \mathbf{I}\, S^{23} \\ \mathbf{I}\, S^{13} & \mathbf{I}\, S^{23} & \mathbf{I}\, S^{33} \end{bmatrix} \tag{A.55}$$

The third integral in Eq. (A.47) writes:

$$\int_\Omega \delta E_{ij}\, \mathcal{D}^{ij33}\, \theta^3 \mathrm{d}\tilde{\beta}_{33}\, d\Omega = \delta\mathbf{q}^{\mathrm{T}} \left(\int_\Omega \bar{\mathbf{B}}^{\mathrm{T}}\, \mathbf{D}^{(:,3)}\, \mathbf{B}_\alpha\, d\Omega \right) \mathrm{d}\boldsymbol{\alpha} = \delta\mathbf{q}^{\mathrm{T}}\, \mathbf{K}_{u\alpha}\, \mathrm{d}\boldsymbol{\alpha} \tag{A.56}$$

Thus, the discrete form of the increment of the virtual internal works writes:

$$\begin{aligned}\mathrm{d}\delta\Pi_{\mathrm{int}} &= \delta\mathbf{q}^{\mathrm{T}}\, (\mathbf{K}_M\, \mathrm{d}\mathbf{q} + \mathbf{K}_S\, \mathrm{d}\mathbf{q} + \mathbf{K}_{u\alpha}\, \mathrm{d}\boldsymbol{\alpha}) \\ &= \delta\mathbf{q}^{\mathrm{T}}\, (\mathbf{K}_{uu}\, \mathrm{d}\mathbf{q} + \mathbf{K}_{u\alpha}\, \mathrm{d}\boldsymbol{\alpha})\end{aligned} \tag{A.57}$$

In Eq. (3.46), we note $\mathbf{K}_{uu} = \mathbf{K}_M + \mathbf{K}_S$.

Similarly, the discrete form of Eq. (A.48) writes:

$$\mathrm{d}\delta\Pi_{\mathrm{EAS}} = \delta\boldsymbol{\alpha}^{\mathrm{T}} \left(\mathbf{K}_{\alpha\alpha}\, \mathrm{d}\boldsymbol{\alpha} + \mathbf{K}_{u\alpha}^{\mathrm{T}}\, \mathrm{d}\mathbf{q} \right) = \mathbf{0} \tag{A.58}$$

where

$$\mathbf{K}_{\alpha\alpha} = \int_\Omega \mathbf{B}_\alpha^{\mathrm{T}}\, \mathcal{D}^{3333}\, \mathbf{B}_\alpha\, d\Omega \tag{A.59}$$

A.2.4 Finite element formulation in the current configuration

Virtual internal work. Let us approximate the local covariant base vectors in the current configuration using the matrix $\mathbf{G}$ defined in Eq. (A.40) as follows:

$$\begin{pmatrix} \boldsymbol{g}_1 \\ \boldsymbol{g}_2 \\ \boldsymbol{g}_3 \end{pmatrix} = \mathbf{G}^{(m)}\, (\mathbf{X}^{(m)} + \mathbf{q}^{(m)}) = \mathbf{G}\, (\mathbf{X} + \mathbf{q}) \tag{A.60}$$

The component of the strain variation in Eq. (3.50) is approximated as follows:

$$\delta\boldsymbol{\epsilon} = \mathbf{R}\,\mathbf{G}\,\delta\mathbf{q} = \bar{\mathbf{B}}\,\delta\mathbf{q} \tag{A.61}$$

where

$$\mathbf{R} = \begin{bmatrix} \boldsymbol{g}_1^{\mathrm{T}} & \mathbf{0} & \mathbf{0} \\ \mathbf{0} & \boldsymbol{g}_2^{\mathrm{T}} & \mathbf{0} \\ \mathbf{0} & \mathbf{0} & \boldsymbol{g}_3^{\mathrm{T}} \\ \boldsymbol{g}_2^{\mathrm{T}} & \boldsymbol{g}_1^{\mathrm{T}} & \mathbf{0} \\ \mathbf{0} & \boldsymbol{g}_3^{\mathrm{T}} & \boldsymbol{g}_2^{\mathrm{T}} \\ \boldsymbol{g}_3^{\mathrm{T}} & \mathbf{0} & \boldsymbol{g}_1^{\mathrm{T}} \end{bmatrix} \tag{A.62}$$

Thus, the discrete form of the virtual internal work writes:

$$\delta\Pi_{int} = \int_\Omega \delta\boldsymbol{\epsilon}^{\mathrm{T}}\,\boldsymbol{\tau}\,d\Omega = \delta\mathbf{q}^{\mathrm{T}} \int_\Omega \bar{\mathbf{B}}^{\mathrm{T}}\,\boldsymbol{\tau}\,d\Omega = \delta\mathbf{q}^{\mathrm{T}}\,\mathbf{f}_{\mathrm{int}} \tag{A.63}$$

followed by the orthogonality condition:

$$\delta\Pi_{EAS} = \delta\boldsymbol{\alpha}^{\mathrm{T}} \int_\Omega \mathbf{B}_\alpha^{\mathrm{T}}\,\tau^{33}(\boldsymbol{u}, \tilde{\beta}_{33})\,d\Omega = \delta\boldsymbol{\alpha}^{\mathrm{T}}\,\mathbf{R}_\alpha = 0 \tag{A.64}$$

Tangent stiffness. Let us rewrite the continuous weak form of the linearized internal virtual work in Eq. (3.38):

$$\mathrm{d}\delta\Pi_{\mathrm{int}} = \int_\Omega \delta\epsilon_{ij}\,\mathcal{C}^{ijkl}\,\mathrm{d}\epsilon_{kl}\,d\Omega + \int_\Omega \mathrm{d}\delta\epsilon_{ij}\,\tau^{ij}\,d\Omega + \int_\Omega \delta\epsilon_{ij}\,\mathcal{C}^{ij33}\,\theta^3\mathrm{d}\tilde{\beta}_{33}\,d\Omega \tag{A.65}$$

followed by linearization of the orthogonality condition:

$$\mathrm{d}\delta\Pi_{\mathrm{EAS}} = \int_\Omega \delta\tilde{\beta}_{33}\theta^3\,\mathcal{C}^{33kl}\,\mathrm{d}\epsilon_{kl}\,d\Omega + \int_\Omega \delta\tilde{\beta}_{33}\theta^3\,\mathcal{C}^{3333}\,\theta^3\mathrm{d}\tilde{\beta}_{33}\,d\Omega = 0 \tag{A.66}$$

The matrix form of the material tangent stiffness is written as:

$$\begin{aligned} \int_\Omega \delta\epsilon_{ij}\,\mathcal{C}^{ijkl}\,\mathrm{d}\epsilon_{kl}\,d\Omega &= \int_\Omega \delta\boldsymbol{\epsilon}^T\,\mathbf{C}\,\mathrm{d}\boldsymbol{\epsilon}\,d\Omega \\ &= \int_\Omega (\bar{\mathbf{B}}\,\delta\mathbf{q})^T\mathbf{C}\,(\bar{\mathbf{B}}\,\mathrm{d}\mathbf{q})\,d\Omega = \delta\mathbf{q}^T\,\mathbf{K}_M\,\mathrm{d}\mathbf{q} \end{aligned} \tag{A.67}$$

where the material moduli matrix $\mathbf{C}$ is given as:

$$\mathbf{C} = \begin{bmatrix} \mathcal{C}^{1111} & \mathcal{C}^{1122} & \mathcal{C}^{1133} & \mathcal{C}^{1112} & \mathcal{C}^{1123} & \mathcal{C}^{1113} \\ \mathcal{C}^{2211} & \mathcal{C}^{2222} & \mathcal{C}^{2233} & \mathcal{C}^{2212} & \mathcal{C}^{2223} & \mathcal{C}^{2213} \\ \mathcal{C}^{3311} & \mathcal{C}^{3322} & \mathcal{C}^{3333} & \mathcal{C}^{3312} & \mathcal{C}^{3323} & \mathcal{C}^{3313} \\ \mathcal{C}^{1211} & \mathcal{C}^{1222} & \mathcal{C}^{1233} & \mathcal{C}^{1212} & \mathcal{C}^{1223} & \mathcal{C}^{1213} \\ \mathcal{C}^{2311} & \mathcal{C}^{2322} & \mathcal{C}^{2333} & \mathcal{C}^{2312} & \mathcal{C}^{2323} & \mathcal{C}^{2313} \\ \mathcal{C}^{1311} & \mathcal{C}^{1322} & \mathcal{C}^{1333} & \mathcal{C}^{1312} & \mathcal{C}^{1323} & \mathcal{C}^{1313} \end{bmatrix} \tag{A.68}$$

where $\mathbf{C}$ is constructed in the same samner as matrix $\mathbf{D}$. In case that the components obtained from the material library are provided in Cartesian coordinates, they can be converted to curvilinear coordinates as follows:

$$\mathbf{C}_{\text{curvi}} = \mathbf{T}^{-1}\,\mathbf{C}_{\text{Cartesian}}\,\mathbf{T}^{-\text{T}} \tag{A.69}$$

where $\mathbf{T}$ is defined as:

$$\mathbf{T} = \begin{bmatrix} J_{11}^2 & J_{12}^2 & J_{13}^2 & 2J_{11}J_{12} & 2J_{12}J_{13} & 2J_{11}J_{13} \\ J_{21}^2 & J_{22}^2 & J_{23}^2 & 2J_{21}J_{22} & 2J_{22}J_{23} & 2J_{21}J_{23} \\ J_{31}^2 & J_{32}^2 & J_{33}^2 & 2J_{31}J_{32} & 2J_{32}J_{33} & 2J_{31}J_{33} \\ J_{11}J_{21} & J_{12}J_{22} & J_{13}J_{23} & J_{11}J_{22}+J_{12}J_{21} & J_{12}J_{23}+J_{13}J_{22} & J_{11}J_{23}+J_{13}J_{21} \\ J_{21}J_{31} & J_{22}J_{32} & J_{23}J_{33} & J_{21}J_{32}+J_{22}J_{31} & J_{22}J_{33}+J_{23}J_{32} & J_{21}J_{33}+J_{23}J_{31} \\ J_{11}J_{31} & J_{12}J_{32} & J_{13}J_{33} & J_{11}J_{32}+J_{12}J_{31} & J_{12}J_{33}+J_{13}J_{32} & J_{11}J_{33}+J_{13}J_{31} \end{bmatrix} \tag{A.70}$$

with:

$$J_{Kl} = \frac{\partial x_K}{\partial \theta^l} \tag{A.71}$$

The geometric stiffness is given as:

$$\begin{aligned} \int_\Omega \mathrm{d}\delta\epsilon_{ij}\,\tau^{ij}\,d\Omega &= \int_\Omega \delta\boldsymbol{u}_{,\theta^i}\cdot\tau^{ij}\,\mathrm{d}\boldsymbol{u}_{,\theta^j}\,d\Omega \\ &= \int_\Omega (\mathbf{G}\,\delta\mathbf{q})^{\text{T}}\,\mathbf{H}(\boldsymbol{\tau})\,(\mathbf{G}\,\mathrm{d}\mathbf{q})\,d\Omega = \delta\mathbf{q}^T\,\mathbf{K}_S\,\mathrm{d}\mathbf{q} \end{aligned} \tag{A.72}$$

where the matrix $\mathbf{H}(\boldsymbol{\sigma})$ is defined as:

$$\mathbf{H}(\boldsymbol{\tau}) = \begin{bmatrix} \mathbf{I}\,\tau^{11} & \mathbf{I}\,\tau^{12} & \mathbf{I}\,\tau^{13} \\ \mathbf{I}\,\tau^{12} & \mathbf{I}\,\tau^{22} & \mathbf{I}\,\tau^{23} \\ \mathbf{I}\,\tau^{13} & \mathbf{I}\,\tau^{23} & \mathbf{I}\,\tau^{33} \end{bmatrix} \tag{A.73}$$

The third integral in Eq. (A.65) writes:

$$\int_\Omega \delta\epsilon_{ij}\, \mathcal{C}^{ij33}\, \theta^3 \mathrm{d}\tilde{\beta}_{33}\, d\Omega = \delta\mathbf{q}^{\mathrm{T}} \left(\int_\Omega \bar{\mathbf{B}}^{\mathrm{T}}\, \mathbf{C}^{(:,3)}\, \mathbf{B}_\alpha\, d\Omega \right) \mathrm{d}\boldsymbol{\alpha} = \delta\mathbf{q}^{\mathrm{T}}\, \mathbf{K}_{u\alpha}\, \mathrm{d}\boldsymbol{\alpha} \tag{A.74}$$

Thus, the discrete form of the increment of the virtual internal works writes:

$$\mathrm{d}\delta\Pi_{\mathrm{int}} = \delta\mathbf{q}^{\mathrm{T}}\, (\mathbf{K}_M\, \mathrm{d}\mathbf{q} + \mathbf{K}_S\, \mathrm{d}\mathbf{q} + \mathbf{K}_{u\alpha}\, \mathrm{d}\boldsymbol{\alpha}) \tag{A.75}$$

Similarly, the discrete form of Eq. (A.66) writes:

$$\mathrm{d}\delta\Pi_{\mathrm{EAS}} = \delta\boldsymbol{\alpha}^{\mathrm{T}} \left(\mathbf{K}_{\alpha\alpha}\, \mathrm{d}\boldsymbol{\alpha} + \mathbf{K}_{u\alpha}^{\mathrm{T}}\, \mathrm{d}\mathbf{q} \right) = \mathbf{0} \tag{A.76}$$

where

$$\mathbf{K}_{\alpha\alpha} = \int_\Omega \mathbf{B}_\alpha^{\mathrm{T}}\, \mathcal{C}^{3333}\, \mathbf{B}_\alpha\, d\Omega \tag{A.77}$$

Appendix B

MECHANICAL ENERGY AND MOMENTUM

B.1 Discrete mechanical energy

Let us present in the following the energy quantities of a discretized deformable body.

Mechanical energy. The mechanical (total) energy is the sum of the kinetic energy and internal energy:

$$\mathrm{W}_{\mathrm{total}} = \mathrm{W}_{\mathrm{kin}} + \mathrm{W}_{\mathrm{int}} \tag{B.1}$$

Considering a time step $[t_n; t_{n+1}] = [t_n; t_n + \Delta t]$, the evolution of the mechanical energy is given as:

$$\mathrm{W}_{(\cdot)}(t_{n+1}) = \mathrm{W}_{(\cdot)}(t_n) + \Delta \mathrm{W}_{(\cdot)}\,, \qquad \Delta \mathrm{W}_{\mathrm{total}} = \Delta \mathrm{W}_{\mathrm{kin}} + \Delta \mathrm{W}_{\mathrm{int}} \tag{B.2}$$

where the $\Delta \mathrm{W}_{(\cdot)}$ denotes the variation of the energy within the considered time step, $\Delta \mathrm{W}_{\mathrm{kin}}$ and $\Delta \mathrm{W}_{\mathrm{int}}$ are the discrete variations of kinetic and internal energy:

$$\Delta \mathrm{W}_{\mathrm{kin}} = \left(\frac{1}{2} \dot{\mathbf{q}}^{\mathrm{T}} \mathbf{M} \dot{\mathbf{q}} \right) \Bigg|_{n}^{n+1}, \qquad \Delta \mathrm{W}_{\mathrm{int}} = \frac{1}{2} \Delta \mathbf{q}^{\mathrm{T}} \left(\mathbf{f}_{\mathrm{int,n}} + \mathbf{f}_{\mathrm{int,n+1}} \right) \tag{B.3}$$

where $\mathbf{M}$ is the mass matrix used in the equation of motion. Thus, it can be the consistent mass matrix in implicit solvers or the lumped diagonal mass matrix in explicit solvers.

In explicit solvers, when the Rayleigh damping is used, the discrete variation of internal energy writes:

$$\Delta \mathrm{W}_{\mathrm{int}} = \frac{1}{2} \Delta \mathbf{q}^{\mathrm{T}} \left(\mathbf{C}\, \dot{\mathbf{q}}_{n-1/2} + \mathbf{f}_{\mathrm{int,n}} + \mathbf{C}\, \dot{\mathbf{q}}_{n+1/2} + \mathbf{f}_{\mathrm{int,n+1}} \right) \tag{B.4}$$

External energy. The external energy, denoted as $\mathrm{W}_{\mathrm{ext}}$, consists of the work from external forces and the work from the displacement boundaries (Dirichlet boundary and interface coupling boundary) $\mathrm{W}_{\mathrm{cons}}$. Its variation within the considered time step writes:

$$\Delta \mathrm{W}_{\mathrm{ext}} = \frac{1}{2}\Delta \mathbf{q}^{\mathrm{T}} \left(\mathbf{f}_{\mathrm{ext,n}} + \mathbf{f}_{\mathrm{ext,n+1}}\right) + \frac{1}{2}\Delta \mathbf{q}^{\mathrm{T}} \left(\mathbf{f}_{\mathrm{cons,n}} + \mathbf{f}_{\mathrm{cons,n+1}}\right) \tag{B.5}$$

Energy error. Based on the weak form of the body motion in Eq. (2.33), we introduce an energy error ϵ_{W} as follows:

$$\epsilon_W(t_{n+1}) = \frac{|\mathrm{W}_{\mathrm{total}}(t_{n+1}) - \mathrm{W}_{\mathrm{ext}}(t_{n+1})|}{\max\limits_{t\in[t_0,T]} \mathrm{W}_{\mathrm{total}}(t)} \tag{B.6}$$

B.2 Linear and angular momentum

The vectors of linear momentum $\boldsymbol{L}$ and angular momentum $\boldsymbol{J}$ of the body ω in the current configuration are given as follows:

$$\begin{aligned} \boldsymbol{L}(t) &= \int_{\omega} \rho\, \dot{\boldsymbol{u}}(t)\, d\omega = \int_{\Omega} \rho_0\, \dot{\boldsymbol{u}}(t)\, d\Omega \\ \boldsymbol{J}(t) &= \int_{\omega} \boldsymbol{x} \times \rho\, \dot{\boldsymbol{u}}(t)\, d\omega = \int_{\Omega} \boldsymbol{x} \times \rho_0\, \dot{\boldsymbol{u}}(t)\, d\Omega \end{aligned} \tag{B.7}$$

The above equation considers that the mass is distributed in the body, $\rho = \rho(\boldsymbol{x})$, and can be used for both solid and shell elements. In explicit solvers, as the lumped mass matrix $\hat{\mathbf{M}}$ is used in the equation of motion instead of the consistent one, the mass distribution $\rho = \rho(\boldsymbol{x})$ does not hold. We propose the following discrete form of the linear and angular momentum, accounting for the lumped mass matrix for solid elements as follows:

$$\boldsymbol{L}(t) \approx \sum_{m=1}^{N} \hat{\mathbf{M}}^{(m)}\, \dot{\mathbf{u}}^{(m)} = \hat{\mathbf{M}}\, \dot{\mathbf{q}}\,, \qquad \boldsymbol{J}(t) \approx \sum_{m=1}^{N} \mathbf{x}^{(m)} \times \hat{\mathbf{M}}^{(m)}\, \dot{\mathbf{u}}^{(m)} \tag{B.8}$$

For shell elements, assuming that the motion of the body is dominated by the mid-plane motion, the discrete linear and angular momenta become:

$$\boldsymbol{L}(t) \approx \sum_{m=1}^{N} \hat{\mathbf{M}}_{\mathbf{v}}^{(m)}\, \mathbf{v}^{(m)}\,, \qquad \boldsymbol{J}(t) \approx \sum_{m=1}^{N} \mathbf{r}^{(m)} \times \hat{\mathbf{M}}_{\mathbf{v}}^{(m)} \mathbf{v}^{(m)} \tag{B.9}$$